Transport and Deposition Problems in Blood Flow

Edwina Yeo
Wadham College
University of Oxford

A thesis submitted for the degree of
Doctor of Philosophy in Mathematics

Long Vacation 2022

For my mum, I know she would be so proud.

Acknowledgements

I would firstly like to wholeheartedly thank my supervisors Sarah Waters and James Oliver for their support during this DPhil. Under their guidance I have learnt some truly fascinating mathematics and grown so much as a researcher. They have instilled in me way of seeking out interesting problems which are also useful to researchers outside of mathematics. Most importantly, although sometimes this took a while to get through to me, they have showed me when to stop digging and appreciate the work you have done. I would like to especially thank them both for their support during this last year.

I would like to thank Alicia El Haj and Netanel Korin for sharing their experimental data, insight and expertise which has allowed me to work on such interesting problems.

I would not have made it though this DPhil without the support of my extended office mates: Michael Negus, Helen Saville, Amy Kent, Matt Shirley and Arkady Wey. They have listed to me during my most difficult moments. I will miss the late nights in the Mathematical Institute, the OCIAM pub trips and the afternoon walks.

I would like to thank my Dad and my two sisters, who have supported me through the most difficult times in my life. Their support during these years and especially in the recent months has helped me finish this DPhil and I will be forever grateful.

I would like to thank Henry for his camaraderie during the recent long nights, for his perspective and for all the proof reading. Finally, I would like to thank Mats, for too many things to list on this page - I am so grateful.

Abstract

In this thesis, we examine blood flow dynamics in single vessels and the deposition of transported species to vessel walls. We develop continuum mathematical models to explore the role of fluid mechanics in two applications. First, we examine magnetic targeting applied to stem cell delivery for regenerative medicine. Second, we model the initial stages of arterial blood clot formation (thrombosis). In both applications, we use asymptotic analysis to develop reduced models. This allows us to i) design and test parameter estimation schemes which can effectively calibrate the mathematical models using *in vitro* data and ii) determine optimal therapeutic parameters by exploring regimes not tested *in vitro*. Finally, we use large scale numerical simulations to examine regimes which are not amenable to asymptotic reduction: larger vessels and high Reynolds number flows.

Firstly, to examine magnetically controlled stem cell delivery we present a 2D continuum model of the flow of blood and magnetically tagged stem cells in a single channel. Cell capture leads to the growth of a cell mass on the wall of the vessel closest to the magnet. For a safe and effective therapy, the stem cells must be delivered in large numbers under physiological flow conditions, but critically, the aggregation of cells at the target site must be controlled.

Using numerical simulations we analyse the model in the regime of *in vitro* experiments: where the size of the magnet is comparable to the channel height. The model qualitatively agrees with experimental results showing better capture with stronger magnetic fields and at lower levels of red blood cells. Using lubrication theory we explore cell delivery regimes beyond the *in vitro* setup when the channel height is much smaller than the size of the magnet. This allows us to identify parameter regimes where finite sized aggregates form and those in which potentially dangerous vessel blockage is predicted.

Secondly, we develop a 3D continuum model for thrombus formation in a diseased artery model. Blood protein Von Willebrand Factor (VWF) is critical in facilitating arterial thrombosis. At pathologically high shear rates the protein unfolds and rapidly captures platelets from the flow. Our model extends existing continuum models for thrombosis by explicitly modelling the VWF unfolding dynamics using a modified viscoelastic fluid model. Since thrombus initiation occurs over several minutes we use the initial fluid mechanics in the stenosis to predict VWF unfolding and platelet deposition.

We examine clot formation in an arterial-scale stenosis at high Reynolds numbers numerically. We demonstrate that the initial clot location and deposition rate depends on the ratio of VWF length to Reynolds number. Finally, we examine the thrombosis model in a rectangular microfluidic geometry motivated by *in vitro* data gathered by our collaborators. We exploit the small aspect ratio of the geometry to reduce the model using lubrication theory. We then explore methods of quantifying unknown model parameters using existing data for VWF dynamics and the thrombosis data obtained in this microfluidic device.

Statement of Originality

In this thesis we develop a novel model for magnetic stem cell delivery in a channel. This work extends the modelling framework developed by Grief et al. [46] for magnetic drug targeting, by considering a nonuniform magnetic field and coupling stem cell delivery to stem cell aggregation on the vessel wall. The model presented in Chapter 2 and analysis presented in Chapter 3 has been published in the Royal Society Interface [123]. One section of the analysis in Chapter 4, in which we analyse the transport of stem cells in a large reduced shear Péclet regime, extends the boundary layer analysis of Richardson et al. by considering the evolution of a stem cell aggregate and by performing exploratory numerical simulations [92].

The model developed in Chapter 5 represents, to our knowledge, the first fully mechanistic continuum model of VWF dynamics in flow. The only other continuum model for VWF dynamics by Zhussupbekov et al. in 2021 [126], follows a different modelling framework. Zhussupbekov and co-authors separate VWF into different two states, and use three empirical constitutive relations to describe its unfolding dynamics. Our model uses a configuration tensor to describe VWF and a single constitutive relation to describe its unfolding dynamics. Our thrombosis model presented in Chapter 5, adopts the structure of Sorrenson et al. and others, in splitting tracking the free species in the flow with advection-diffusion equations and the bound species on the pipe walls with ODEs at each location [105, 119].

The experimental magnetic stem cell capture data in Chapters 1 and 3 appears in papers [31, 123]. The VWF deposition data shown in Chapter 1 appears in [7].

Contents

Chapter 1

Introduction

Blood is a complex fluid composed of a multitude of highly specialised cells and proteins suspended in plasma. Developing accurate mathematical models of blood flow dynamics is a vast and evolving field. In this thesis, we theoretically study the transport and delivery of medical treatments within the blood. In particular, we consider the development of targeted therapies which aim to deliver drugs or therapeutic cells directly to the site of injury or disease in the body. These targeted therapies have the potential to reduce the dangerous side effects which arise from systemic drug delivery and also reduce the costs of treatment, as lower doses can be administered to the injury site with the same therapeutic effect. The effective development of targeted medical therapies that are delivered via the vasculature relies on a mechanistic understanding of the interplay between the complex fluid dynamics of blood flow, the drug properties, and blood vessel geometry.

The work in this thesis is motivated by the development of two targeted therapies. The first therapy involves the delivery of stem cells to damaged joints to treat osteoarthritis, where the cells then encourage cellular repair of the damage caused by this degenerative disease. Researchers at the University of Birmingham, U.K. are developing delivery methods which ensure the safe and effective delivery of the stem cells directly to the damaged joints. One method, developed by Prof. El Haj, which has demonstrated promise in initial experimental studies, implants the stem cells with magnetic nanoparticles so that external magnets can be used to guide the stem cells to the target site [31]. The second targeted therapy we consider in this thesis aims to treat pathological arterial blood clotting, which is seen in many conditions such as stroke or heart attack. Arterial blood clotting occurs at locations in the artery where pathological plaque deposition narrows the vessel, which can lead to fluid shear rates in excess of $10,000\,\mathrm{s}^{-1}$ [18]. Researchers at Technion, Israel are developing shear-sensitive coatings for existing anti-clotting drugs [65]. This allows

the drugs to respond to the high shear rate at the clot site and deliver the drug locally. This avoids the distribution of the drug to areas of the vasculature distant from the clot where it could cause excessive bleeding or haemorrhage, both of which can be potentially life-threatening complications of the treatment.

In the remainder of this introduction, we start by presenting an overview of the uses of theoretical modelling in biomedicine. We then detail the two applications we will consider and the key questions we will address with the models developed in this thesis. We then present an overview of the fluid dynamics of blood flow, and a summary of different modelling approaches for blood and and the transport of dilute species in blood.

1.1 Mathematical modelling in biomedicine

Mathematical modelling can offer guidance and possible solutions to the difficulties which novel therapies face in the translation from concept to practice. Modelling can be used during therapy development to guide future experimental work or to test medical devices or therapies across virtual patients in so-called *in silico* trials. Theoretical approaches complement the three standard processes of developing and testing therapies: *in vitro* (lab-based testing outside the body); *in vivo* (trials which are typically carried out in animals); and finally clinical trials with human participants. Models offer a rapid, low-cost exploration of parameter regimes, which can inform the optimised design of therapies and a focused selection of optimal therapeutic parameters. Reducing the required amount of *in vitro* and *in vivo* work allows potentially beneficial treatments to reach clinical testing stages faster.

The benefits and use of modelling have been recognised by the United States Food and Drug Administration and by the British Standards Institution, Sector for Healthcare [111]. However, realising the potential value of theoretical predictions relies on carefully designing the model so that it can be effectively parameterised in order to deliver accurate insight into the biological system [114]. In this thesis, we develop models in close collaboration with experimental researchers. This allows us to address questions of key concern in therapy design and to parameterise models as much as possible with existing data.

We now detail the first biomedical application which we consider in this thesis: the delivery of stem cells to injury sites using implanted magnetic nanoparticles and an external magnet.

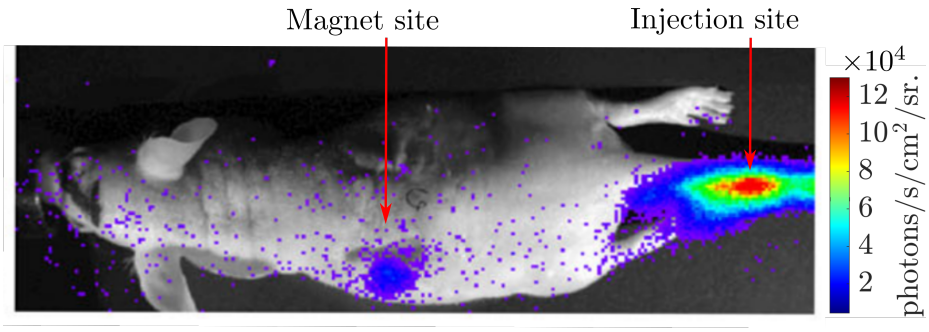

Figure 1.1: MRI scan of a mouse illustrates therapy *in vivo*; tagged cells were injected into the tail (red hot spot), and the blue region shows the deposition of tagged cells near the implanted magnet in shoulder. Reproduced from [31].

1.2 Application 1: magnetic stem cell delivery

Stem cells have the ability to repair and regenerate damaged or diseased tissue in the body [107]. They achieve this through differentiation to a number of different cell types, thereby replacing or repairing existing damaged cells at the site of disease [25]. Treatment with stem cells has been shown to improve the functionality of organs following a heart attack [100] or vessel damage [90] and are used to treat patients with leukaemia. The treatment of leukaemia is currently the largest use of stem cell therapy [37]. However, traditional intravenous injection (IV) leads to systemic distribution of the stem cells and poor localisation of the cells at the target site [57]. Magnetic targeting of stem cells aims to address this challenge.

Through the use of internalised magnetic nanoparticles (NPs), which are non-toxic to humans [72], stem cells can, in principle, be targeted to an injury site by the application of an external magnetic field. *In vitro* targeting of NP tagged cells shows their ability to withstand stresses due to the surrounding fluid flow once captured on the vessel wall [61] and that tagging does not damage the cells' ability to differentiate [117]. This potential has been further demonstrated *in vivo* by targeting magnetically tagged endothelial cells to repair damage to vessel walls [66, 83]. Figure 1.1 demonstrates the potential of the therapy *in vivo*, in a study by our collaborator Prof. Alicia El Haj. In this study, magnetised stem cells were injected into the tail of the rat and then were successfully captured at the magnet located subcutaneously in the shoulder, illustrated by the blue hot spot [31].

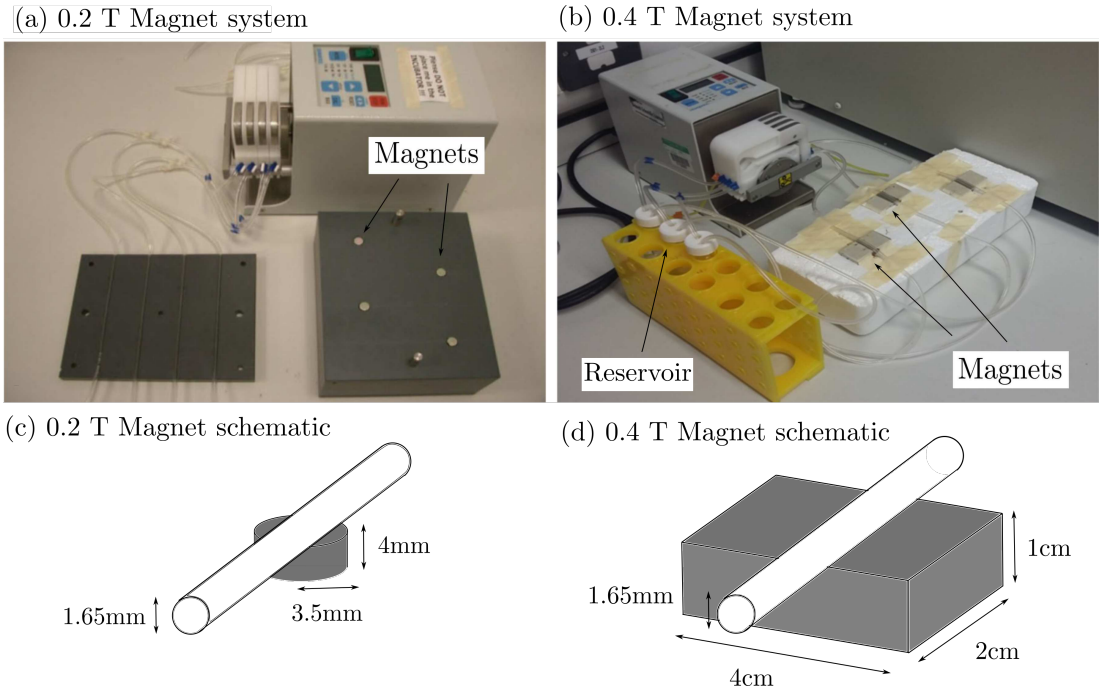

Figure 1.2: *In vitro* experimental setups in which tagged cells circulate through long tubes over magnets with flow driven by a pump, (a) shows the 0.2 T cylindrical magnet system and (b) shows the 0.4 T rectangular magnet system with pump. Close-ups of the magnet relative to the pipes are shown in (c) for the 0.2 T magnet and in (d) for the 0.4 T magnet.

1.2.1 *In vitro* data

In vitro experiments examining magnetic stem cell delivery were carried out by our collaborator Prof. El Haj, to evaluate the effect of magnet strength and red blood cell (RBC) concentration on magnetic mediated cell trapping. In brief, two systems were used to examine capture by magnets of different strengths, utilising four 0.2 T magnets and three 0.4 T magnets, respectively. The magnets are spread out and held directly underneath a loop of 30 cm PVC tubing (internal diameter 1.65mm) connected to a peristaltic pump. This setup is shown for the smaller 0.2 T magnet and the larger 0.4 T magnet in Fig. 1.2a and b respectively. For each case, we show a schematic of a single magnet relative to the pipe in Fig. 1.2c and d.

These experiments examined the capture of 1×10^6 magnetically tagged cells and a control group of unlabelled cells in the pipe when suspended in RBC concentrations of 0, 5, 10, 20 or 40 %, using sheep blood combined with anticoagulants. This suspension of stem cells and RBCs recirculated through the pipe and reservoir system for 30 minutes. Un-trapped cells remaining in the reservoir were further processed for analysis which demonstrated that cells were not damaged by either the magnetic

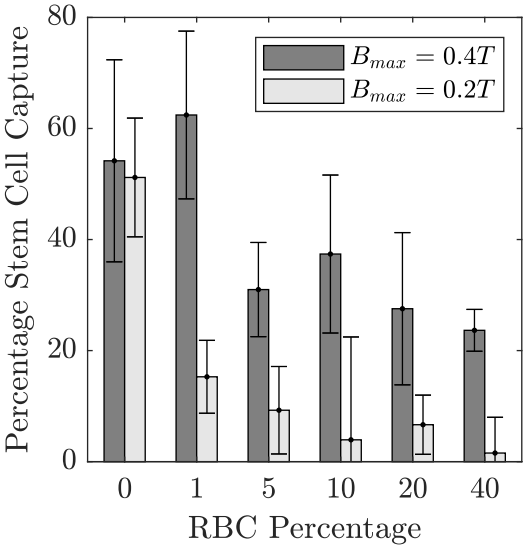

Figure 1.3: *In vitro* trapping data. Increasing RBC percentage in the system decreases trapping when the maximum magnetic field is either $B_{max} = 0.2\,\mathrm{T}$ or $0.4\,\mathrm{T}$.

tagging or the flow system.

The percentage capture of magnetically tagged stem cells achieved with both magnets is shown in Fig. 1.3. This demonstrates that both magnets are able to capture the magnetically-tagged stem cells out of the flow. Capture is most efficient when no RBCs are present, irrespective of magnet size, with approximately 50% of cells trapped at the magnet site for both the 0.2 T and the 0.4 T magnet in the absence of RBCs. The percentage of stem cell capture achieved in the system significantly drops in the presence of RBCs but to a greater extent in the smaller magnet than the larger magnet. It was noted in the experiment (not shown in Fig. 1.3) that some unlabelled cells were captured at the magnet site in the control case, with higher numbers of unlabelled cells captured with increasing RBC concentration. This is thought to be a result of RBCs sticking to the pipe walls and subsequently to the stem cells, despite the anticoagulant present.

1.2.2 Challenges to safety and efficacy

Despite the potential of magnetic stem cell targeting, there remain a number of challenges hindering its advancement to large-scale *in vivo* trials. Studies have shown that cell capture is most effective when: (i) the flow is slowest; (ii) the magnetic field strength is greatest; and (iii) no RBCs are present, as the *in vitro* results in the previous section demonstrated [31, 61]. However, successful therapy requires the

effective capture of stem cells at *in vivo* flow speeds and at physiological levels of RBCs. The efficacy of the therapy also depends on magnetic parameters such as NP size, strength, and the strength of the external magnetic field, as well as delivery parameters including the number of cells injected and the site of injection. These must all be considered alongside the physiological characteristics of the target site [73]. This illustrates the challenge of successfully designing and optimising a magnetic targeting therapy.

A final safety issue results from the agglomeration of stem cells near the magnetic source or as they travel in flow. The former is a result of the external magnet and the latter arises from magnetic interactions between the cells. It has been observed with both traditional IV injection [8, 54] and magnetic targeting that stem cells transiently enter the lungs en route to the injury site. Typically this does not pose an issue, however, if magnetic intercellular interaction leads to the aggregation of stem cells in the blood this could be potentially dangerous as it could lead to the formation of a stem cell and RBC clot.

In this thesis, we develop a mathematical model of magnetically targeted stem cell delivery with the aim of examining the interplay between RBCs, magnet strength, vascular fluid mechanics and stem cell capture. We consider the capture of stem cells as an aggregation process which occurs on the vessel wall. This allows us to determine under what conditions stem cells accumulate to potentially dangerous levels in the target vessel. Furthermore, we theoretically include and explore effects which are challenging to test *in vitro* to provide insight into *in vivo* studies. This would enable a reduction in the amount of animal experimentation required, increasing the likelihood of this therapy more rapidly reaching the clinical testing stages and ultimately the translation of the therapy from bench to bedside.

We review the physics of magnetic nanoparticles in Chapter 2 along with existing mathematical models of the transport of magnetic nanoparticles in the blood. We now detail the second application of this thesis: clotting which occurs in diseased arteries.

1.3 Application 2: targeted treatments for arterial clot formation

Coronary heart disease is characterised by the formation of plaque on the walls of arteries leading to the muscles of the heart, restricting blood flow. The plaque deposits consist of a fibrous cap over a lipid or necrotic core rich in collagen. These plaques

develop over twenty to thirty years [12]. The rupture of the fibrous cap can occur due to injury or vessel collapse and results in the exposure of the plaque core to circulating blood. A blood clot then forms rapidly to repair the damaged wall [6]. Although blood clotting (thrombosis) can occur throughout the body in healthy individuals, it only occurs within arteries as a result of disease or trauma. Arterial clots have the potential to fatally occlude the vessel within an hour or fracture and block a downstream vessel, known as an embolism [24].

Thrombosis can be treated by administering drugs that dissolve the newly formed blood clot. However, if systemically delivered, these drugs can damage areas of the vasculature away from the blood clot leading to a fatal haemorrhage [113]. Targeted administration of these drugs offers the possibility of dramatically reducing the risk of internal bleeding [52]. One method of targeted clot treatment, developed by our collaborator Prof. Netanel Korin at the University of Technion, uses shear-sensitive capsules to surround the drug [65]. Extremely high levels of shear stress occur at arterial plaque deposits since the flow is obstructed. These functionalised capsules are designed to dissolve at these high levels of shear stress so that the drug is administered locally at the clot. Understanding the location and rate at which blood clots form for a range of physiological artery geometries will enable the drug coatings to be optimised to maximise drug delivery to the clot.

Arterial thrombosis is facilitated by the shear-sensitive blood protein Von Willebrand Factor (VWF). This protein is coated in platelet binding sites and is tightly coiled at normal levels of the fluid shear rate. However, at pathologically high shear rates, this protein unfolds and facilitates the formation of a platelet-based clot in the artery. The importance of VWF in blood clotting was first noted in 1971 as patients with an inability to form blood clots were found to have a lack of this protein [95]. This blood clotting disorder is now known as Von Willebrand Disease [36, 95]. The role of VWF shape and length in relation to the fluid dynamics of vessels was first revealed in 1996 by Siediecki et al., who used atomic force microscopy to record that the protein was unfolded at shear stresses greater than 31 dyne/cm^2 [102]. With advances in imaging and experimental methods, VWF unfolding and refolding when suspended in flow was first imaged by Schneider et al. in 2007, and to date this remains the only study to successfully image the proteins when suspended [98].

However, aside from the confirmational change in VWF which facilitates platelet binding to VWF, it is not well understood how the interactions between VWF, platelets, stenosis geometry and fluid flow determine the precise location of clot formation. Fig. 1.4 shows three examples of thrombus formation *in vitro* with the

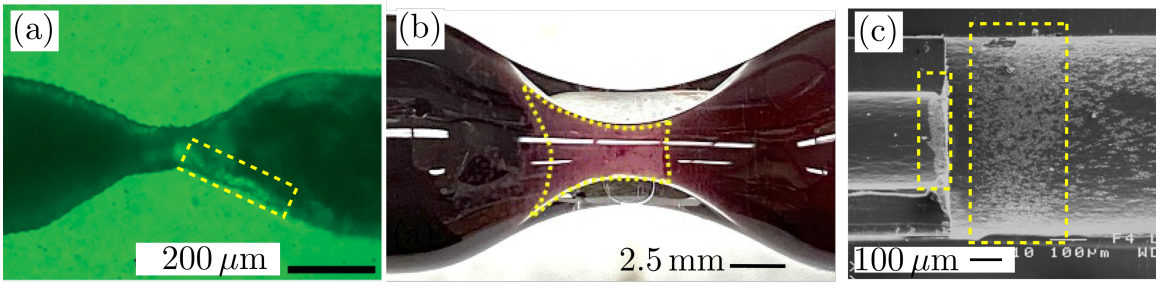

Figure 1.4: Examples of clot formation in *in vitro* experiments, clot location is highlighted with yellow box. In all cases flow is from left to right. (a) The clot forms downstream of the stenosis; (b) The clot forms at the narrowest part of the pipe and slightly upstream; (c) The clot forms both at the stenosis narrowing and downstream. Reproduced with permission from [22, 60, 45], respectively, where the yellow box was added for (a) and (c).

location of clot formation highlighted in yellow [22, 45, 60]. In Fig. 1.4a, the clot forms downstream of the pipe occlusion, in Fig. 1.4b the clot form at the occlusion, and in Fig. 1.4c the clot forms both at the occlusion and downstream. To design targeted therapies effectively, a precise knowledge of how the clot location depends on vessel geometry and flow conditions is required.

Motivated by the need to understand the role of the protein VWF and its interactions with fluid flow and platelets in Chapters 5 - 7, we develop and analyse a continuum model for VWF dynamics in flow coupled to the initial stages of clot formation. Our collaborator has gathered *in vitro* data of VWF deposition in arterial-scale stenosis [7]. However, the full clot formation was not explored in this device since a large volume of blood must be used to fill the device which can lead to excess clotting during the experiment setup. Furthermore, since so much blood is required, exploratory *in vitro* experiments are then very expensive [7]. Hence our collaborators have examined platelet and VWF deposition in a microfluidic device which can produce arterial-level shear rates due to its very small aspect ratio. The arterial-scale device and the microfluidic device are shown in Fig. 1.5a and b, respectively. An example of the data produced by these two experiments is shown in Fig. 1.5, where the red stain shows VWF deposition (in the absence of platelets) in Fig. 1.5c and the green stain shows platelet deposition in Fig. 1.5d. The geometry and scale of these two devices motivate the model geometries which use we examine thrombosis in this thesis. We detail the process of clot formation in arteries in more detail in Chapter 5, and review the mathematical modelling of clotting and the protein VWF. In this

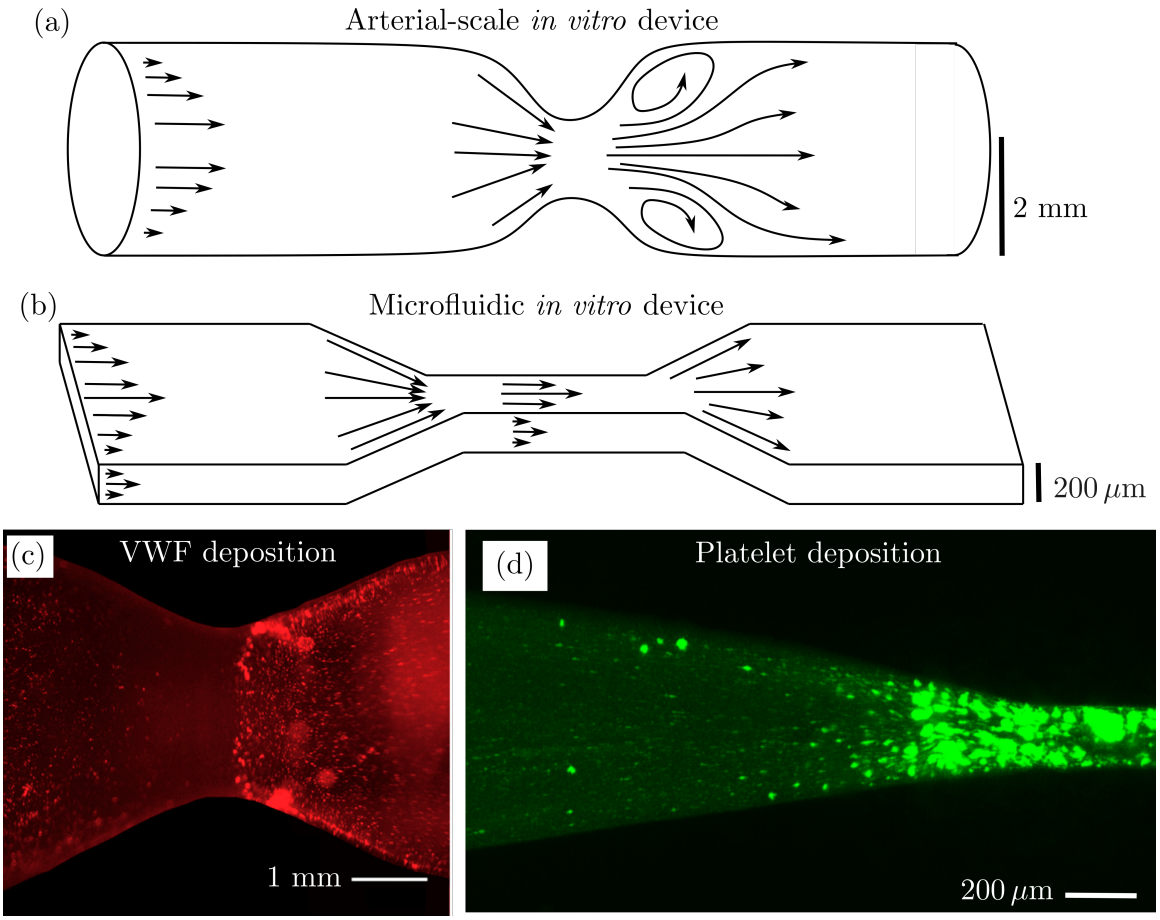

Figure 1.5: Schematics of the devices used to study elements of thrombosis *in vitro*, arrows show illustrative fluid streamlines, (a) the arterial-scale device used to examine VWF deposition [7] and (b) the microfluidic device used to examine platelet and VWF deposition. Fluorescence images of data gathered in these devices: (c) VWF deposition stained red, gathered in device shown in (a) and (d) platelet deposition, stained green, gathered in the microfluidic device shown in (b).

chapter, we now review some fundamental properties of blood flow which are relevant to both biological applications considered in this thesis.

1.4 The fluid mechanics of blood

Blood is made up of 55% plasma and 40% red blood cells (RBC) by volume, with the remaining volume being made up of white blood cells, platelets and blood proteins. RBCs have a diameter of 7 μm [110]. In capillaries, which have diameters between $3-9\,\mu$m, the RBCs travel in single-file inside the vessel and deform the vessel walls as they flow [86]. However, for vessels with diameters greater than 9 μm, the cells transition from flowing in single-file. Now collisions between cells and lift forces generated from

cell-wall interactions lead to the marginalisation of RBCs into the centre of the vessel. This generates a 'cell-free layer' which lubricates the flow through the vessel. These complex dynamics of the RBCs within blood mean that the observed or effective viscosity of blood depends nonlinearly on RBC volume fraction, the diameter of the vessel and the shear rate. We first detail the dependence of the effective viscosity on the shear rate then on RBC volume fraction and vessel diameter.

At low shear rates, in vessels larger than $9\,\mu$m, RBCs form small column clusters in the blood known as 'rouleaux'. As the shear rate of the flow increases, these clusters disperse and the effective viscosity is reduced [86]. This reduction in viscosity for increasing shear rates is known as shear thinning. In this case, the viscosity of blood at $200\,\mathrm{s}^{-1}$ is 20–30 times less than the viscosity at $0.05\,\mathrm{s}^{-1}$ [122]. An empirical fitting of the observed viscosity of blood for varying shear rates was obtained by Brookes et al. using a rheometer made up of two concentric cylinders with a gap of $44\,\mu$m [15], shown in Fig. 1.6a. For shear rates greater than $200\,\mathrm{s}^{-1}$ there is a minimal further decrease in the viscosity [15].

The haematocrit H is defined as the average volume fraction of RBC in the cross-section of the vessel. For large vessels, the cell-free layer, defined above, has a minimal effect on overall blood viscosity. However, as the vessel diameter decreases, the relative size of the cell-free layer to the vessel diameter increases and the blood viscosity nonlinearly decreases. In small vessels, with diameters less than $9\,\mu$m, the observed blood viscosity increases as the vessel diameter continues to decrease and the cell-free layer is no longer present. This viscosity increase is known as the 'Fåhræus - Lindqvist effect' [35]. An empirical fitting obtained by Pries et al. [85] for the viscosity of blood as a function of haematocrit and vessel diameter is shown in Fig. 1.6. This was obtained for shear rates greater than $50\,\mathrm{s}^{-1}$, where shear thinning effects are minimal.

Blood also shows weak viscoelastic effects. Since RBCs are deformable, they are able to store elastic energy, allowing the viscosity of blood to depend on previous deformations. This effect is most prominent when rouleaux are present in the blood for shear rates less than $0.1\,\mathrm{s}^{-1}$ [51]. We now detail the mathematical theory of non-Newtonian fluids and the most prominent models which describe these effects in blood.

A general, incompressible fluid can be modelled according to the Navier-Stokes equations as follows:

$$\rho\left(\frac{\partial \boldsymbol{u}}{\partial t} + \boldsymbol{u}\cdot\nabla\boldsymbol{u}\right) = \nabla\cdot\boldsymbol{\sigma}, \quad \nabla\cdot\boldsymbol{u} = 0, \tag{1.1}$$

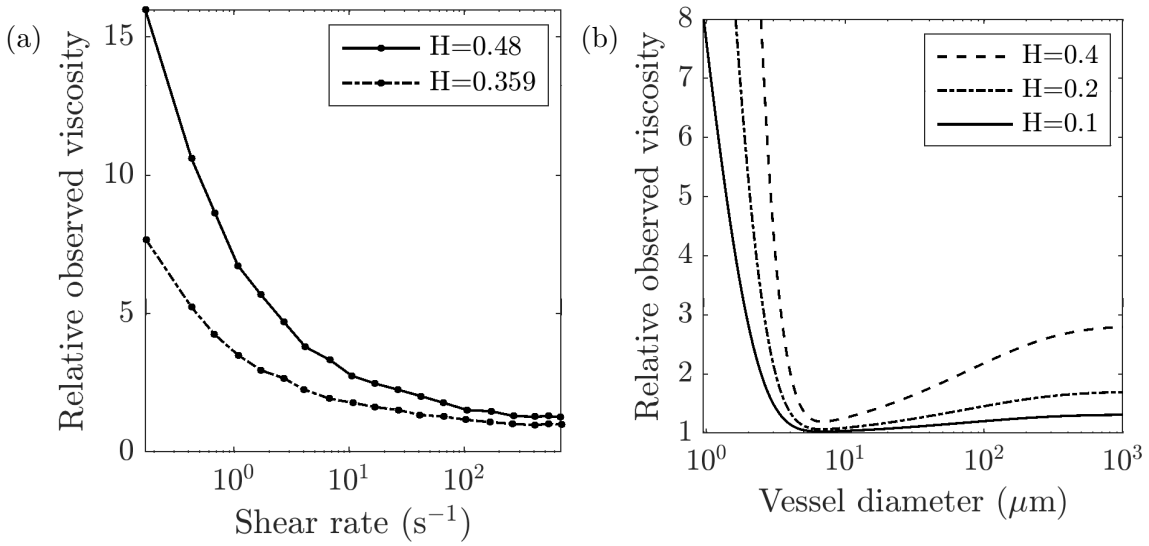

Figure 1.6: (a) Measurements for the relative viscosity of whole blood *in vitro* for varying shear rate, reproduced from [15] and normalised relative to the viscosity at $1000\,\mathrm{s}^{-1}$ for $H = 0.359$. (b) Empirical fitting for the viscosity of whole blood in a vessel of radius $825\,\mu$m for varying haematocrit and tube diameter [85].

where $\boldsymbol{u}$ is the fluid velocity and $\boldsymbol{\sigma}$ is the fluid stress tensor which is a function of the fluid velocity and the pressure p. For a Newtonian fluid, the stress tensor is modelled as

$$\boldsymbol{\sigma} = -p\boldsymbol{I} + 2\mu\boldsymbol{D}, \tag{1.2}$$

where $\boldsymbol{D} = (\nabla\boldsymbol{u} + (\nabla\boldsymbol{u})^T)/2$ is the strain rate tensor and μ is the constant viscosity of the fluid. Generalised Newtonian fluid models describe the viscosity of the fluid as a function of the shear rate $\dot{\gamma}$ such that

$$\boldsymbol{\sigma} = -p\boldsymbol{I} + 2\mu(\dot{\gamma})\boldsymbol{D}, \tag{1.3}$$

where the shear rate is defined using the 2-norm of the rate of strain tensor $\boldsymbol{D}$ as follows

$$\dot{\gamma} = \sqrt{2\boldsymbol{D} : \boldsymbol{D}} = \left(2\frac{\partial u}{\partial x}^2 + \left(\frac{\partial u}{\partial y} + \frac{\partial v}{\partial x} \right)^2 + 2\frac{\partial v}{\partial y}^2 \right)^{1/2}. \tag{1.4}$$

Generalised Newtonian models include yield-fluids such as the Bingham model, where the viscosity is zero below a critical shear rate threshold, as well as shear thinning and thickening models in which the viscosity is a decreasing or increasing function of the shear rate, respectively. Within the class of generalised non-Newtonian fluid models are the seminal works of Casson [80] and Quemada [88] in modelling the viscosity of

blood. Quemada's model allows for the fluid to have a large but finite viscosity as the fluid shear rate tends to zero, whereas Casson fluids have unbounded viscosity [84]. The Quemada viscosity outperforms the Casson viscosity in comparison to blood flow data [75].

In viscoelastic fluid models, the stress tensor is coupled to the rate of strain tensor through a time-dependent partial differential equation. For the simplest viscoelastic fluid model, the Oldroyd-B model [14], the fluid stress is coupled to the strain rate tensor through the following relation

$$\boldsymbol{\sigma} + \lambda_1 \overset{\triangledown}{\boldsymbol{\sigma}} = 2\mu(\boldsymbol{D} + \lambda_2 \overset{\triangledown}{\boldsymbol{D}}). \tag{1.5}$$

Here λ_1 is the relaxation time, which is the time the elastic fluid components take to return to their reference configuration after deformation and λ_2 is the retardation time, the time the material takes to respond to deformation. In (1.5), the over-triangles denote the upper-convected derivative, defined as follows

$$\overset{\triangledown}{\boldsymbol{\sigma}} = \frac{\partial \boldsymbol{\sigma}}{\partial t} + \boldsymbol{u} \cdot \nabla \boldsymbol{\sigma} - \boldsymbol{\sigma} \cdot \nabla \boldsymbol{u} - (\nabla \boldsymbol{u})^T \cdot \boldsymbol{\sigma}, \tag{1.6}$$

which is a material frame invariant derivative. The Oldroyd-B model allows the stress to display effects from previous deformations.

In this thesis, we model blood as a Newtonian fluid, neglecting shear-thinning and viscoelastic effects. This is justified since we adopt model geometries motivated by our collaborators' experimental setups, and in all cases, the maximum shear rates in the systems are larger than $100\,\mathrm{s}^{-1}$, so we expect shear-thinning effects to be minimal. In our model of magnetic stem cell delivery we use the observed viscosity fitting obtained by Pries et al. to describe how blood viscosity varies with haematocrit [85]. However, we assume that haematocrit is fixed and constant throughout the cross-section of the model geometry, neglecting the cell-free layer.

1.5 Transported species in blood

When a species such as a therapeutic drug or protein is transported in the blood, the cell collisions which contribute to the generation of the cell-free layer discussed above also cause an anisotropic motion of transported species known as shear-induced diffusion or shear-induced dispersion [68]. Shear-induced diffusion leads to a migration of the species across streamlines, and to a lesser degree, in the direction of the fluid flow, both of which are proportional to the fluid shear rate $\dot{\gamma}$ [23]. For low volume fractions ϕ, defined to be $\phi < 0.2$, the shear-induced diffusion across streamlines has

been determined empirically for a suspension of solid spheres to be linearly proportional to the solid volume fraction [30]. By contrast, for larger volume fractions of solid spheres, up to 0.4, the shear-induced diffusion coefficient across streamlines was determined to be $0.5\phi^2 r^2 \dot{\gamma}$ where r is the solid sphere radius [68].

The cross-streamline shear-induced diffusion experienced by a species transported in blood has been quantified to be proportional to $H^2 r_{\mathrm{RBC}}^2$ [70, 127]. This reflects the volume fraction squared dependence as was shown for solid spheres since the RBC volume fraction is high. The magnitude of this diffusion has been estimated as $0.05 r_{\mathrm{RBC}}^2$ or equivalently $0.31 H^2 r_{\mathrm{RBC}}^2$ with $H = 0.4$, by [127] (as listed in Grief et al. [46]): note that this is slightly less than the value for hard spheres at 40% volume fraction where $0.5\phi^2 r^2 = 0.08 r^2$.

The transport of a dilute species with concentration c is governed by the following equation

$$\frac{\partial c}{\partial t} + \nabla \cdot \boldsymbol{J} = 0, \tag{1.7}$$

where $\boldsymbol{J} = c\boldsymbol{u} - \boldsymbol{D}\nabla c$ is the flux of the species with diffusion tensor $\boldsymbol{D}$. Isotropic Brownian diffusion is modelled such that $\boldsymbol{J} = c\boldsymbol{u} - D\nabla c$ and D is a scalar constant. Shear-induced diffusion has been modelled as proportional to the empirical cross-streamline shear-diffusion, such that $\boldsymbol{J} = c\boldsymbol{u} - 0.31 H^2 r_{\mathrm{RBC}}^2 \dot{\gamma} \nabla c$ in for example, in Grief et al. and others [46, 92]. In this case diffusion is isotropic which will overestimate the diffusion in the direction of the velocity field.

Recent work has developed an empirical anisotropic diffusion tensor through lattice-Boltzmann simulations of a nanoparticle in blood flow [70]. This work found that the diffusion tensor of a nanoparticle in the blood is linearly proportional to the haematocrit level and nonlinearly depends on the shear rate, such that for shear rates greater than $1000\,\mathrm{s}^{-1}$, the diffusion scales sublinearly in the shear rate. This is thought to be a result of the alignment of RBCs with the direction of flow. In this thesis we follow the simpler approach, as in Grief et al., and model the effect of shear-induced diffusion as isotropic and proportional to $0.31 H^2 r_{\mathrm{RBC}}^2 \dot{\gamma}$. We now outline the structure of this thesis.

1.6 Outline of thesis

In Chapter 2 we review the electromagnetic theory of nanoparticle dynamics and a existing mathematical models of magnetic nanoparticle delivery. We then present a two-dimensional continuum model for the flow of blood and magnetically tagged stem

cells in a single channel. The geometry setup of this model is chosen to match the setup of the *in vitro* experiments presented in Section 1.2.

In Chapter 3, using numerical simulations, we analyse the magnetic cell delivery model in the regime of *in vitro* experiments presented in Section 1.2 by matching the channel flow rate, magnet size and strength as much as possible to the *in vitro* setup. We find that the model qualitatively agrees with experimental results showing better capture with stronger magnetic fields and at lower levels of red blood cells. We then describe how these results would be altered when cells leave the channel through the wall (extravasation), bridging between *in vitro* setup and the *in vivo* scenario where cells would leave the vessel to travel to the injury site.

In Chapter 4 we use lubrication theory to develop reduced models of stem cell delivery. We consider systems where the ratio of the channel radius to magnet radius, $\epsilon = d/R_{\text{mag}}$, is small. This allows us to develop reduced models which can be more simply analysed numerically. The efficiency in the numerical solution of these reduced models allows us to identify parameter regimes where finite-sized aggregates form and those in which potentially dangerous vessel blockage could occur.

In Chapter 5, we review the process of arterial thrombosis, the dynamics of the protein VWF and mathematical models for thrombosis and protein dynamics in flow. We then develop a three-dimensional mathematical model for the initiation of thrombosis at high shear rates. This model aims to determine the interaction between VWF, vessel geometry and fluid mechanics in determining the location where platelets deposit on to the vessel walls and a clot forms. Our model extends existing continuum models for thrombosis by explicitly modelling the VWF unfolding dynamics using a modified viscoelastic fluid model. This work represents the first fully mechanistic continuum model for VWF behaviour.

In Chapter 6, we examine this model for thrombus initiation in an idealised axisymmetric arterial-scale stenosis model. This geometry is chosen to match the *in vitro* setup of our collaborators which was used to examine VWF deposition [7]. Through numerical simulation, we explore model predictions for VWF dynamics and initial platelet deposition for varying Reynolds numbers and stenoses geometries.

In Chapter 7, motivated by the *in vitro* data of thrombosis obtained by Prof. Korin we examine the model in a rectangular microfluidic geometry. We exploit the small aspect ratio of the geometry to reduce the model using lubrication theory. We then explore methods of quantifying unknown model parameters determining platelet deposition and VWF unfolding mechanics using existing data for VWF dynamics and the thrombosis data obtained in the device.

Finally, in Chapter 8, we summarise our work and discuss the key results obtained. We conclude by discussing valuable extensions to the models.

Chapter 2

Aggregation model of magnetic stem cell delivery

2.1 Introduction

In this chapter, we develop a mathematical model for magnetic stem cell targeting in a single two dimensional channel. As presented in Chapter 1, the motivation for this work is the development of protocols for the magnetically-targeted delivery of stem cells to diseased regions of the body. Magnetic nanoparticles are implanted into the stem cells, which are then guided to the intended delivery site using an external magnet. In our mathematical model we model the aggregation of stem cells on the wall of the channel closest to the magnet through the growth of a solid aggregate. We include the effect of fluid erosion on the surface of the aggregated cells and cells leaving the vessel wall, a process known as extravasation. This effect cannot be easily studied *in vitro*. We then use this model to: (i) explain trends seen in *in vitro* experimental data; (ii) examine how the *in vitro* experimental trends may translate to the *in vivo* delivery through the inclusion of extravasation; (iii) explore magnetic stem cell delivery outside of the regime of the *in vitro* experiments, varying the vessel geometry, magnet setup and strengths of the additional effects such as erosion. This allows us to make predictions of the optimal parameter regimes for the safe and effective delivery of stem cells. These first two objectives (i-ii) are delivered in Chapter 3 and the final objective (iii) is delivered in Chapter 4.

First we present a review of the electromagnetism relevant to magnetic nanoparticles and their behaviour in an external magnetic field. We then review the relevant modelling literature for the delivery of magnetic nanoparticles in the blood. Finally, we present our mathematical model and outline the analysis plan for Chapters 3 and 4.

2.1.1 Magnetic nanoparticle theory

In magnetic stem cell therapy the stem cells are implanted with superparamagnetic nanoparticles. These are microscale magnetic spheres which vary their magnetism in response to the applied magnetic field. In order to describe their dynamics we will first describe the electrodynamics of magnetic media and permanently magnetised nanoparticles, which retain their magnetisation in the absence of applied fields. We then extend this to the behaviour of superparamagnetic nanoparticles.

The total magnetic field $\boldsymbol{B}$ (SI unit: T) is the combination of any applied magnetic fields $\boldsymbol{H}$ (SI unit: A/m) and the internal response of magnetic media to these applied fields which is known as the magnetisation $\boldsymbol{M}$ (SI unit: A/m). These three fields are related by the expression

$$\boldsymbol{B} = \mu_0(\boldsymbol{H} + \boldsymbol{M}), \tag{2.1}$$

where $\mu_0 \approx 1.25 \times 10^{-6}$ N/A^2 is the magnetic permeability of a vacuum. Outside of a magnetised material $\boldsymbol{M} = \boldsymbol{0}$ and we have $\boldsymbol{B} = \mu_0\boldsymbol{H}$. It is important to note that in the field of electromagnetism there is some variation in the notation used in the literature related to the two fundamental fields $\boldsymbol{B}$ and $\boldsymbol{H}$, and we choose to follow the notation of Griffiths [47].

Magnetic media are composed of microscopic electric circuits which manifest at the macroscale as magnetic dipoles [47]. When subject to a magnetic field, $\boldsymbol{B}$, a magnetic dipole experiences a torque $\boldsymbol{\tau}$ and a force, $\boldsymbol{F}$, which pulls the dipole towards the source of the field. The strength and alignment of a dipole are quantified by its magnetic dipole moment $\boldsymbol{m}$. This is defined implicitly through the torque the dipole experiences in a magnetic field via the expression $\boldsymbol{\tau} = \boldsymbol{m} \times \boldsymbol{B}$. This leads to the definition of magnetisation $\boldsymbol{M}$, as the dipole moment per unit area.

Large magnetic materials are made up of domains in which neighbouring dipoles are aligned. Sufficiently small enough materials, such as nanoparticles, consist of a single domain with uniform internal alignment of neighbouring magnetic dipoles. Hence, nanoparticles are uniformly magnetised spheres. Maxwell's equations governing the magnetic field, $\boldsymbol{B}$, can be solved exactly for a uniformly magnetised sphere and therefore the field of a nanoparticle can be calculated analytically. Outside the sphere, this field is equal to the field produced by a permanently magnetised magnetic dipole, where the strength of the dipole is multiplied by the volume of the nanoparticle [41]. This allows the force on the nanoparticles to be described using the force

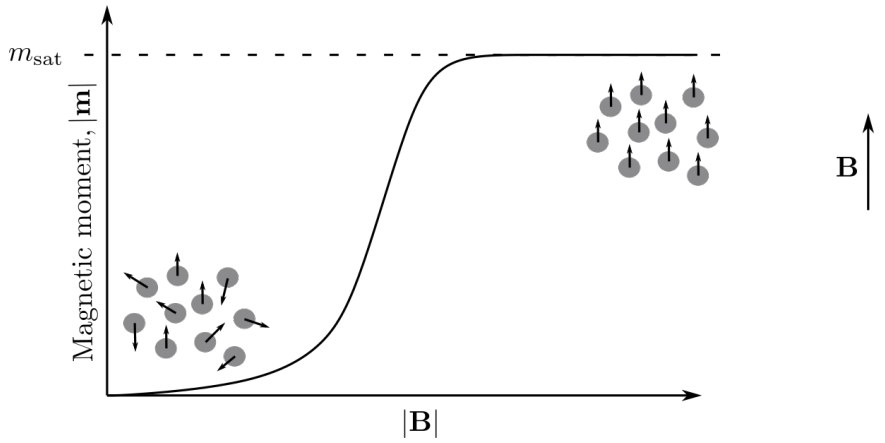

Figure 2.1: Illustration of the behaviour of superparamagnetic nanoparticles in a magnetic field of increasing strength. At low field strength, all particles are randomly aligned. At high field strength all the particles align with the field with average moment $\boldsymbol{m} = m_{\text{sat}}\hat{\boldsymbol{B}}$ where $\hat{\boldsymbol{B}} = \boldsymbol{B}/|\boldsymbol{B}|$.

$\boldsymbol{F}$ on a dipole. This is well known in classical electromagnetic theory [47], as

$$\boldsymbol{F} = \boldsymbol{m} \cdot \nabla \boldsymbol{B}. \tag{2.2}$$

We now examine how superparamagnetic nanoparticles (NPs) differ from permanently magnetised nanoparticles. The magnetic moment of the superparamagnetic nanoparticles used in stem cell therapy is a function of the magnetic field. These nanoparticles are characterised by reversible alignment which occurs parallel to the applied magnetic field and does not persist after the field is removed. This means that $\boldsymbol{B}$, $\boldsymbol{H}$ and $\boldsymbol{M}$ are all parallel. Since the particles are nanoscale, their moments are subject to random fluctuations as a result of thermal changes [11]. In the absence of an external magnetic field an individual nanoparticle within a collection of superparamagnetic nanoparticles has a random alignment direction and the collection appears to have no magnetisation. However, once the strength of the external field is large enough the entire collection will align with the direction of the magnetic field $\hat{\boldsymbol{B}} = \boldsymbol{B}/|\boldsymbol{B}|$, with an average magnetic moment of magnitude $|\boldsymbol{m}| = m_{\text{sat}}$, where m_{sat} is known as the saturation value of the magnetic nanoparticle. The magnetic moment of an individual NP is defined as the average moment observed in a collection under an applied field. This behaviour of a collection of nanoparticles and the average magnetic moment are illustrated in Fig. 2.1. In contrast to larger magnets, the response of superparamagnetic nanoparticles to an applied magnetic field is exactly reversible [11]. This is an attractive property for therapeutic applications as it avoids the NPs clustering in the absence of an external field.

An empirical relationship to describe the moment of a superparamagnetic NP was postulated and verified experimentally by Bean in 1959 [11]. Using the formulation from [46] this is given by

$$\boldsymbol{m} = m_{\text{sat}} L\left(\frac{m_{\text{sat}}|\boldsymbol{B}|}{k_B T}\right)\hat{\boldsymbol{B}} \text{ where } \hat{\boldsymbol{B}} = \boldsymbol{B}/|\boldsymbol{B}|, \quad L(x) = \coth(x) - \frac{1}{x}, \tag{2.3}$$

here k_B is the Boltzmann constant and T is the absolute temperature.

Several limits of Eq. (2.3) have been commonly used in the nanoparticle literature. As discussed in [92], when $m_{\text{sat}}|\boldsymbol{B}| \ll k_B T$ the dipole moment $\boldsymbol{m} \approx m_{\text{sat}}^2/3k_b T\hat{\boldsymbol{B}}$. In contrast, for strong magnetic fields such that $m_{\text{sat}}|\boldsymbol{B}| \gg k_B T$, the nanoparticles are at their saturation value with $\boldsymbol{m} \approx m_{\text{sat}}\hat{\boldsymbol{B}}$. Since the magnetic fields of the permanent magnets used experimentally are strong, throughout this thesis we employ the large field limit and assume that the moment of a single dipole is $\boldsymbol{m} = m_{\text{sat}}\hat{\boldsymbol{B}}$. We note that the magnetic nanoparticles will make a small contribution to the magnetic field around them which decays proportional the distance to the particle to the fourth power. However, we neglect the contribution of the dipoles to the magnetic field owing to their small strength relative to the external magnet, hence $\boldsymbol{B}$ is equal to the field of the external magnet only. This will remove any interparticle magnetic attraction. We discuss the inclusion of this effect in the future work section of Chapter 8.

2.1.2 Magnetic delivery models

Theoretical studies of magnetic nanoparticles in flow began with Driscoll et al. in 1984 who carried out a joint experimental and theoretical study [27]. The authors injected NPs into the tail of a rat and demonstrated that these NPs could be held in place by an external magnet in the portions of the tail closest to the magnet. The authors then used a discrete model to theoretically examine the forces from the flow and external magnetic field the NPs experience, both when suspended in the flow and when deposited on the vessel walls. Their theoretical work found a one-to-one relationship between the magnetic field strength which holds the nanoparticles to the vessel wall and the fluid flow speed that the NPs can resist before being swept from the wall. However, these theoretical results underestimated the fluid forces that the NPs could resist when deposited at the wall compared to an additional *in vitro* study of NP capture in a pipe. The authors attributed this to NP clumping. When clumped the magnetic nanoparticles experience additional forces from their neighbours which allows them to resist fluid flow. The authors also noted clumping is a significant potential danger with the therapy.

Since then several studies have examined the dynamics of discrete NPs and the parameter design of therapies. Furlani et al. used a discrete model of a single NP subject to flow in a 2D channel to show that for a fixed strength of the magnet, linearly increasing its size gives a superlinear increase in the size of NPs which can be captured out of the fluid flow and held on the channel wall [41]. Sharma et al. modelled the dynamics of a single NP in a 2D channel and demonstrated that the capture rate drastically reduces as the distance of the magnet to the vessel increases, since the magnetic force experienced by the NP decays proportional to the fourth power of the distance [101]. Again using a discrete NP model, Haverkort et al. showed that the most effective external magnet magnetisation direction for NP capture in a 2D channel is against the direction of the flow [49]. More extensive numerical simulations of large numbers of NPs have been used to predict NP distribution in realistic 3D blood vessel networks [58]. This study found that, while overall capture was better with larger NPs, the larger NPs could become trapped at bifurcations in the vessel network which then limits the number of NPs reaching the target of the therapy. As well as this, large-scale simulations in vessel bifurcations at high Reynolds numbers demonstrated that flow recirculation zones limit the capture of NPs at target locations near bifurcation sites since NPs are unable to easily enter the recirculation zone [67]. Although, it is worth noting that the authors demonstrate this can be overcome with increased magnetic fields.

The work of Furlani [40] modelling larger drugs tagged with NPs is of particular relevance here. A larger drug tagged with n NPs is modelled as a dipole with moment $\boldsymbol{m}_{\text{drug}} = n\boldsymbol{m}_{NP}$ where $\boldsymbol{m}_{NP}$ is the moment of an individual NP. This model is justified by the assumption that the variation of the external field inside the carrier is negligible. In this thesis we adopt this approach to model the magnetically tagged cells. Hence, the force on a tagged cell is given by

$$\boldsymbol{F} = n\boldsymbol{m}_{NP} \cdot \nabla \boldsymbol{B}, \tag{2.4}$$

where n is the number of NPs in a tagged cell.

Continuum models of dilute suspensions of magnetic particles were first developed by Grief et al. [46]. This work noted the importance of shear-induced collisions with red blood cells (RBCs) which were modelled as shear-induced diffusion, as discussed in Chapter 1. The authors used this model to examine NP capture in an idealised 2D vessel network. They found that the NP capture in each branch of the network was proportional to the strength of the magnetic velocity divided by the aspect ratio of that vessel such that, if the magnetic field is constant, longer vessels capture

more NPs. This model was extended to analyse NP transport when NPs are allowed to leave the vessel via extravasation [92]. When extravasation is large the authors found that NPs leave at the location they first land on the vessel wall. In the small extravasation regime the authors found that NPs build up in a boundary layer on the vessel wall. Cherry and Eaton included non-Newtonian descriptions of blood flow through a multiphase flow model with a discrete formulation of magnetic interactions between drug particles [20]. This formulation was then simulated over successive vessel bifurcations demonstrating the ability of the external field to steer the particles down a chosen branch. It should be noted that all of these models have focused on drug targeting where the particles are of negligible size and hence the fluid flow is unaffected by the drug transport.

In this thesis we develop a model for the transport of magnetised stem cells in a 2D channel coupled to a solid mass which represents the stem cells deposited on the vessel wall. The solid stem cell aggregate couples cell transport to the fluid mechanics in the channel which is obstructed over time. Our model follows the construction of the continuum model in Grief et al. [46], modelling cell transport with an advection-diffusion equation with an additional magnetic velocity. We extend their work by including cell aggregation on the channel wall and a spatially varying magnetic field. Since it is of key therapeutic importance to avoid vessel blockage, we focus on describing the growth of the aggregate and how this growth is affected by both fluid shear and the removal of cells from the channel via extravasation. We now detail the components of our model.

2.2 Mathematical model

We consider a two dimensional channel using a Cartesian coordinate system (x, y), with unit basis vectors $\boldsymbol{i}$ and $\boldsymbol{j}$. The channel occupies a rectangular region given by, $|x| \leq l$, $|y| \leq d$, as illustrated in Fig. 2.2. Stem cells are advected by the fluid flow and are subject to a magnetic force which pulls them towards the base of the channel. When they reach the lower wall an aggregate of cells grows. In the channel, the cells do not affect the fluid flow. Rather, the coupling between cells and fluid flow is included through the cell aggregate on the vessel wall which alters the fluid domain. The aggregate boundary grows at a rate proportional to the flux of cells arriving at the wall and represents the build-up of cells. For simplicity, we model the cell mass as a smooth, solid boundary neglecting any detailed micro-structure.

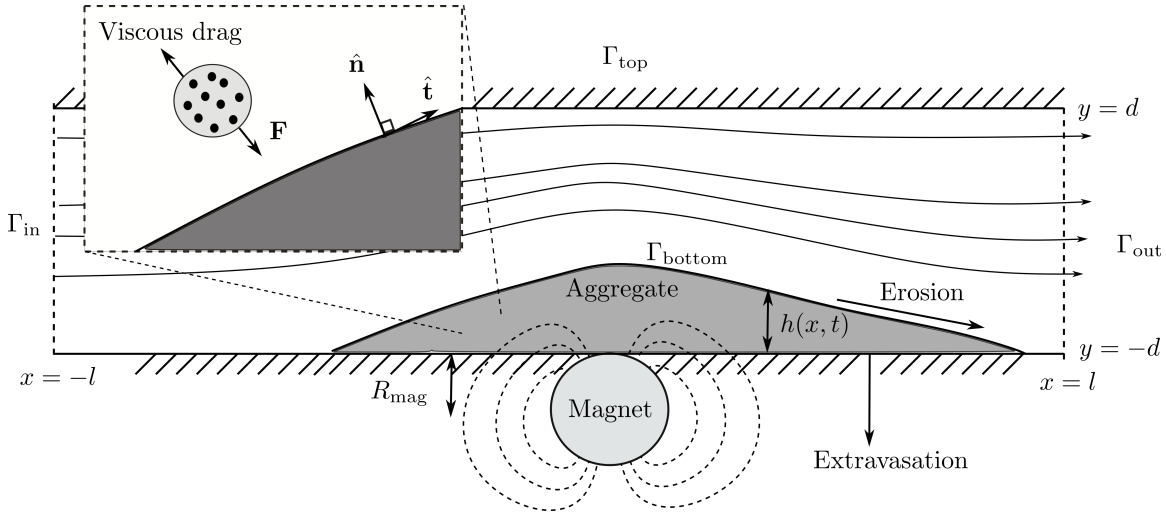

Figure 2.2: Model setup: a channel with length $2l$ and height $2d$ is located above a magnet of radius R_{mag}. The boundary of the aggregate lies at $y = -d + h(x,t)$. Illustrative fluid streamlines and magnetic field lines (dashed) are shown. Inset shows a cell tagged with NPs travelling under the action of magnetic force $\boldsymbol{F}$ and viscous drag.

The magnetic force is generated by a canonical example of a magnetic field that can be expressed analytically: the field of an infinite cylindrical magnet of radius R_{mag} located with centre at $x = 0,\ y = -d - R_{\text{mag}}$, below the channel. The length of the channel l is chosen relative to R_{mag} such that the domain captures the portion of the vessel where the magnetic field is significant. Practically, this means we require $l \gg R_{\text{mag}}$. We denote by $h(x,t)$ the thickness of the aggregate, as illustrated in Fig. 2.2, wherein the boundaries of the domain are defined as follows:

$$\Gamma_{\text{in}} = \{x = -l,\ -d + h(-l,t) \leq y \leq d\}, \tag{2.5}$$

$$\Gamma_{\text{out}} = \{x = l,\ -d + h(l,t) \leq y \leq d\}, \tag{2.6}$$

$$\Gamma_{\text{top}} = \{-l \leq x \leq l,\ y = d\}, \tag{2.7}$$

$$\Gamma_{\text{bottom}} = \{-l \leq x \leq l,\ y = -d + h(x,t)\}. \tag{2.8}$$

We note that Γ_{bottom} includes the boundary where there are aggregated stem cells ($h > 0$) and regions where there are no stem cells, defined by $h = 0$.

On the base the vectors $\hat{\boldsymbol{n}}$ and $\hat{\boldsymbol{t}}$ are the outward (relative to the aggregate) unit normal and unit tangent vectors, as illustrated in Fig. 2.2. In the following sections we detail each component of the mathematical model.

2.2.1 Fluid flow

We neglect fluid inertial effects since the therapy aims to capture stem cells in arterioles (Reynolds number 0.17, based on vessel radius and velocity in [46]) before their extravasation. Hence, we model the fluid flow with the steady Stokes and continuity equations

$$\mu_{\text{eff}}\nabla^2\boldsymbol{u} = \nabla p, \quad \nabla \cdot \boldsymbol{u} = 0, \tag{2.9}$$

where $\boldsymbol{u}$ and p are the fluid velocity and pressure respectively and μ_{eff} is a constant, effective viscosity.

We use the empirical fitting to describe the effect of haematocrit, H, on the viscosity of the fluid from Pries et al. [85, 86], as discussed in Chapter 1. We assume that viscosity is independent of the stem cell concentration and the aggregate size and that the haematocrit is fixed but can be varied in each delivery, as in the *in vitro* experiments. The viscosity of the mixture of RBCs and fluid as compared to that of water μ_{w} is given by

$$\frac{\mu_{\text{eff}}(H)}{\mu_{\text{w}}} = 1 + (a-1)\frac{(1-H)^c - 1}{(1-0.45)^c - 1}, \tag{2.10}$$

where the coefficients a and c vary with the vessel radius. Even though in the *in vitro* experiments the pipe has a diameter of 1650 μm we use this fitting since, as stated in Pries et al. [86], the viscosity does not change significantly for vessel diameters beyond 1000 μm. Throughout this model we use the values of $a = 3.19$ and $c = -0.8$ (for the pipe radius used *in vitro*). This leaves the effective viscosity as a function of H alone, which is constant for each chosen value of H. The effective viscosity is plotted in Fig. 2.3a which shows the nonlinear increase in viscosity as haematocrit increases to physiological levels, $H = 0.4$.

The boundary conditions for the flow are no-slip and no flux on the stationary, impermeable channel wall Γ_{top}. The flow is driven by a prescribed unidirectional parabolic flow at the inlet which reflects the setting of the *in vitro* experiments. We assume the channel outlet is at atmospheric pressure and impose no tangential stress at the outlet. On the base of the channel, Γ_{bottom}, the fluid moves with the velocity of the interface denoted by $v_n\hat{\boldsymbol{n}} + v_t\hat{\boldsymbol{t}}$. These boundary conditions can be expressed

as follows

$$u = u^*(1 - y^2/d^2) \quad v = 0 \quad \text{on } \Gamma_{\text{in}}, \tag{2.11}$$

$$\boldsymbol{i} \cdot \boldsymbol{\sigma} \cdot \boldsymbol{i} = -p_a, \quad \boldsymbol{i} \cdot \boldsymbol{\sigma} \cdot \boldsymbol{j} = 0 \quad \text{on } \Gamma_{\text{out}}, \tag{2.12}$$

$$u = 0, \quad v = 0 \quad \text{on } \Gamma_{\text{top}}, \tag{2.13}$$

$$\boldsymbol{u} \cdot \hat{\boldsymbol{n}} = v_n, \quad \boldsymbol{u} \cdot \hat{\boldsymbol{t}} = v_t \quad \text{on } \Gamma_{\text{bottom}}, \tag{2.14}$$

where $\boldsymbol{\sigma} = -p\boldsymbol{I} + \mu_{\text{eff}}(\nabla \boldsymbol{u} + (\nabla \boldsymbol{u})^T)/2$ is the fluid stress tensor, p_a is atmospheric pressure and u^* is the velocity scale of the imposed inlet flow. The tangential and normal velocity components of the fluid on the moving boundary, v_t and v_n, will be prescribed in Section 2.2.4. We note that to impose unidirectional flow at the inlet we must ensure that the aggregate does not grow at this point, as this would induce a vertical velocity. This is discussed in more detail in Section 2.2.4.

2.2.2 Magnetic force

We model the moment of a cell tagged with n NPs as a linear multiple of the moment for an individual NP following the approach of Furlani et al. [40]. We use the strong field limit, as discussed in Section 2.1.1, and hence express the moment of a cell as $\boldsymbol{m} = nV_p m_{\text{sat}} \hat{\boldsymbol{B}}$, where m_{sat} is the magnetic saturation of an individual nanoparticle, $\hat{\boldsymbol{B}} = \boldsymbol{B}/|\boldsymbol{B}|$ is the normalised magnetic field and V_p is the volume of a single NP. The force on a cell is then given by

$$\boldsymbol{F} = nV_p m_{\text{sat}} \nabla |\boldsymbol{B}|, \tag{2.15}$$

where $|\boldsymbol{B}|$ is the magnitude of the applied magnetic field. In the experimental model, the external field was provided by rectangular and cylindrical magnets. In our model, the magnet field is provided by an infinite cylindrical magnet of radius R_{mag} with magnetisation, M in the y-direction [41]. The magnet is located directly below the channel, as *in vitro*, such that its centre is at $x = 0$, $y = -d - R_{\text{mag}}$. The magnetic field $\boldsymbol{B}$ generated by this magnet can be found since there is no free current, by solving Maxwell's equations using the magnetic scalar potential ϕ, where $\mu_0 \nabla \phi = -\boldsymbol{B}$. The scalar potential can then found by solving $\nabla^2 \phi = \nabla \cdot \boldsymbol{M}$ where $\boldsymbol{M} = M\boldsymbol{j}$ for $|\boldsymbol{x} - (d - R_{\text{mag}})| < R_{\text{mag}}$, as in [47]. This gives the magnetic field as

$$\boldsymbol{B} = \frac{\mu_0 M R_{\text{mag}}^2}{2((y + d + R_{\text{mag}})^2 + x^2)^2} (2x(y + d + R_{\text{mag}})\boldsymbol{i} + ((y + d + R_{\text{mag}})^2 - x^2)\boldsymbol{j}), \tag{2.16}$$

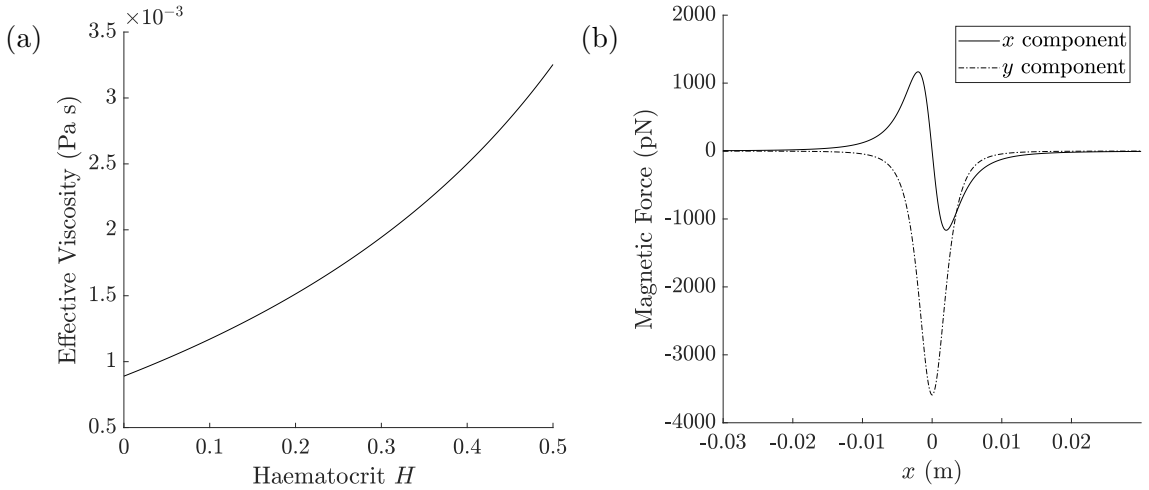

Figure 2.3: (a) Empirical model for the viscosity of whole blood in a vessel of radius 825 μm for varying haematocrit Eq. (2.10) [86]. (b) Magnetic force on a stem cell at $y = 0$ with 30 implanted NPs from a magnet with radius $R_{\text{mag}} = 0.35$ cm with $M = 0.8\mu_0$, (this corresponds to a maximum magnetic field of $B_{max} = 0.4$ T), Eq. (2.17).

The maximum value of the field is $B_{max} = M\mu_0/2$ which occurs on the surface of the cylinder. We will use this expression to calibrate (2.16) to describe a magnet of strength 0.2 T and 0.4 T, as was used in the *in vitro* experiments. Using Eqs. (2.15) and (2.16) the force on a cell can be expressed analytically [41], *viz*

$$\boldsymbol{F} = \frac{n\mu_0 m_{\text{sat}} M R_{\text{mag}}^2 V_p}{((y + d + R_{\text{mag}})^2 + x^2)^2} \left(-x\boldsymbol{i} + (y + d + R_{\text{mag}})\boldsymbol{j}\right). \tag{2.17}$$

The force on a tagged cell at the centre of the channel is shown in Fig. 2.3b. The y component shows that as the cell passes through the channel it is pulled down towards the magnet on the base. The x component of the force shows that the cell speeds up as it approaches the magnet from upstream and then slows down downstream of the magnet. This could reverse the trajectory of a cell for $x > 0$ if the fluid flow is weak.

2.2.3 Cell motion

Following Grief et al. [46], we consider the motion of a single cell to construct a continuum model for cell concentration neglecting cell inertia. Newton's second law determines the motion of a single cell under the action of a magnetic force and Stokes drag. The ratio of cell inertia to viscous drag is $\approx 10^{-5}$, justifying our neglect of cell inertia. Hence the cell velocity $\boldsymbol{V}$ can then be determined by a balance between

magnetic force $\boldsymbol{F}$ and Stokes drag, *viz*

$$0 = \boldsymbol{F} - 6\pi\mu_{\text{eff}} r(\boldsymbol{V} - \boldsymbol{u}), \tag{2.18}$$

where r is the stem cell radius. Thus, $\boldsymbol{V} = \boldsymbol{u}_m + \boldsymbol{u}$ where $\boldsymbol{u}_m = \boldsymbol{F}/6\pi\mu_{\text{eff}} r$ is the cell velocity induced by the magnet. Hence, the cells move due to advection with the flow and the magnetic velocity $\boldsymbol{u}_m$. We note that this model assumes that the cells do not alter the fluid flow.

Since the cells typically have radius $\sim 10\,\mu$m they are not subject to Brownian motion. However, collisions between stem cells and RBCs lead to diffusive motion known as shear-induced diffusion, as discussed in Chapter 1. This is modelled by taking the diffusion coefficient to be proportional to RBC radius r_{RBC}, haematocrit H and the local shear rate $\dot{\gamma}$, given by $0.31 r_{\text{RBC}}^2 H^2 \dot{\gamma} = k_{\text{sh}}\dot{\gamma}$, using the empirical value by Zydney et al. [46, 127].

We now consider a dilute collection of tagged cells which can be characterised by a continuous concentration c. Mass conservation then leads to an advection-diffusion equation for the cell concentration given by

$$\frac{\partial c}{\partial t} + \nabla \cdot \boldsymbol{q} = 0, \tag{2.19}$$

in the fluid domain, where we define the cell flux as

$$\boldsymbol{q} = (\boldsymbol{u} + \boldsymbol{u}_m)c - k_{\text{sh}}\dot{\gamma}\nabla c. \tag{2.20}$$

Equation (2.19) requires both boundary and initial conditions. We consider two inlet concentration profiles as follows

$$c_{\text{in}}^*(t) = \begin{cases} C, & \text{(2.21a)} \\ C(\tanh(t - t_1^*) - \tanh(t - t_2^*))/2, & \text{(2.21b)} \end{cases}$$

where (2.21a) defines constant inlet concentration C and (2.21b) models a bolus injection of stem cells between t_1^* and t_2^*. On the top of the channel we impose no flux of cells. At the channel outlet we impose zero diffusive flux, allowing cells to exit the channel via advection with the flow. These boundary conditions are defined as follows:

$$c = c_{\text{in}}^*(t) \quad \text{on} \quad \Gamma_{\text{in}}, \tag{2.22}$$

$$\boldsymbol{q}.\boldsymbol{j} = 0 \quad \text{on} \quad \Gamma_{\text{top}}, \tag{2.23}$$

$$\frac{\partial c}{\partial x} = 0 \quad \text{on} \quad \Gamma_{\text{out}}. \tag{2.24}$$

On the base of the channel we model how the cells enter the aggregate and the effect of shear on the aggregate through a flux boundary condition. For convenience we do not distinguish between the part of the boundary for which $h > 0$ and the part for which the aggregate height is zero (corresponding to $h = 0$). This would require tracking the moving points delineating the upstream and downstream edges of the aggregate. Additionally, we ensure that the boundary condition does not lead to negative aggregate thickness (see below for details). We impose the following flux condition on the base of the domain relative to the moving boundary

$$\boldsymbol{q} \cdot \hat{\boldsymbol{n}} - cv_n = - \underbrace{\chi^*(c - \tilde{c}^*)^+}_{\text{Absorption into aggregate}} + \underbrace{\gamma^*(\tau - \tilde{\tau}^*)^+ \mathcal{H}(h)}_{\text{Erosion reduces absorption}} = -J^*, \tag{2.25}$$

where J^* is the total flux, $\mathcal{H}(h)$ is the Heaviside function and $(\cdot)^+$ is the positive-part function defined as

$$(f)^+ = \begin{cases} f & \text{if } f > 0, \quad (2.26a) \\ 0 & \text{if } f \leq 0. \quad (2.26b) \end{cases}$$

In (2.25) the underbraces describe the effects we capture in the model. The first term on the right-hand side of (2.25) corresponds to the cells entering the aggregate at a rate $\chi^*(c - \tilde{c}^*)$ once the cell concentration on the base exceeds the growth threshold $\tilde{c}^*$. The second term in (2.25) models erosion on the aggregate surface at a rate $\gamma^*(\tau - \tilde{\tau}^*)$ for $h > 0$, where τ is the wall shear stress. This follows the approaches used in the biofilm modelling literature where erosion is taken to be proportional to the wall shear stress [94]. The wall shear stress is given by

$$\tau = \frac{\mu_{\text{eff}}}{2} \left| \hat{\boldsymbol{n}} \cdot \left(\nabla \boldsymbol{u} + (\nabla \boldsymbol{u})^T \right) \cdot \hat{\boldsymbol{t}} \right|. \tag{2.27}$$

We define a wall shear stress threshold $\tilde{\tau}^*$, so that the flux into the aggregate is reduced if $\tau > \tau^*$. We ensure that the positive part of $\tau - \tilde{\tau}^*$ is taken to ensure low shear rates do not lead to cell production from the boundary. The parameter γ^* controls the strength of shear stress erosion. Large values of γ^* indicate that cells are easily swept from the surface of the aggregate. Once the aggregate is large, the shear stress can exceed the shear erosion threshold on parts of the channel wall for which $h = 0$. Therefore, we multiply the erosion term with the Heaviside function $\mathcal{H}(h)$ to ensure that erosion only occurs on the aggregate where $h > 0$.

Recalling that the fluid boundary conditions (2.11) impose unidirectional flow at the inlet, we must ensure that the aggregate does not grow at this point as this would induce a vertical velocity. This restriction is not required at the outlet since

we impose that the tangential stress vanishes on that boundary. To ensure no growth at the inlet we first fix $\tilde{c}^* > C$, which removes the positive flux of cells into the base at the inlet. Then, since h remains equal to zero at the inlet, the second term on the right-hand side of Eq. (2.25) is zero.

We assume initially that there are no cells in the channel giving

$$c = 0 \quad \text{at} \quad t = 0. \tag{2.28}$$

2.2.4 Aggregate growth

A point on the aggregate-fluid interface has coordinates $(x, y) = (x, -d + h(x, t))$, where the aggregate height $h(x, t)$ must be determined as part of the solution. The height h is coupled to the fluid by the kinematic boundary condition, given by

$$v = \frac{\partial h}{\partial t} + u\frac{\partial h}{\partial x} \tag{2.29}$$

on Γ_{bottom}, defined in (2.8). Owing to our definition of the moving boundary this reduces to

$$\frac{\partial h}{\partial t} = v_n\sqrt{1 + \left(\frac{\partial h}{\partial x}\right)^2}. \tag{2.30}$$

The aggregate interface grows as a result of the arriving cell flux, Eq. (2.25), which can be negative if fluid shear is high enough and $h > 0$. The height is reduced by the extravasation of cells through the channel wall. We assume that the aggregate grows solely in the direction normal to its boundary with velocity v_n, such that the tangential velocity v_t is zero. The normal interface velocity is taken to be

$$v_n = \alpha^* J^* - k^*_{\text{ext}}, \tag{2.31}$$

where J^* is the flux of cells into the aggregate, and the coefficient α^* is the growth factor which determines how the concentration of cells in the flow is converted into solid aggregate. Although the mechanism and kinetics of stem cell extravasation are not fully known, experimental measurements of extravasation rates have recorded both approximately exponential decay of a fixed amount of cells [64, 74] and linear decrease in cell number over time [19, 64, 74]. Motivated by these observations we test two simple functional forms for the extravasation rate, k^*_{ext}, given by

$$k^*_{\text{ext}} = \begin{cases} \kappa^*_1 h, & \text{(2.32a)} \\ \kappa^*_2 \mathcal{H}(h), & \text{(2.32b)} \end{cases}$$

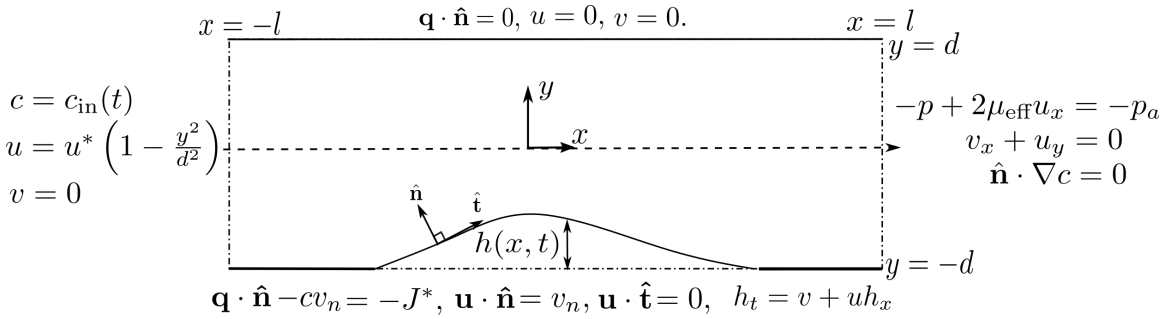

Figure 2.4: The full boundary conditions on the system are illustrated on their respective boundaries.

which describe firstly extravasation proportional to the height of cells on the base, (2.32a) and constant extravasation (2.32b). The constant κ_1^* determines the rate at which a collection of cells extravasate, whereas κ_2^* corresponds to the speed at which a single cell crosses the vessel wall. Initially, we take the aggregate height to be zero.

2.2.5 Summary

Summarising, the model consists of quasi-steady Stokes flow Eq. (2.9) with an effective viscosity Eq. (2.10); cell transport is governed by an advection-diffusion equation, Eq. (2.19), where cells travel with the fluid and an extra magnetic velocity. The growing aggregate interface, which is assumed to grow normally, is coupled to both cell transport and fluid flow through the growth condition (2.31).

The system is closed by prescribing boundary conditions for the fluid: (2.11) - (2.14), the cells: (2.22) - (2.25), and the moving boundary: (2.29) along with initial conditions of zero aggregate thickness h and zero for the cell concentration in the channel. This gives us two boundary conditions for the Stokes equations on each boundary and one for the advection-diffusion equation on each boundary, as required. These boundary conditions are summarised in Fig. 2.4.

2.3 Parameterisation

Where possible we use the physical parameters from the *in vitro* experimental system, these are listed in Table 2.1.

The nanoparticles used to obtain the *in vitro* data set are described in [76], but their magnetic saturation value is not available. We have therefore estimated the magnetic saturation using information for similar nanoparticles used in experiments [31]. The nanoparticles in [31] saturate when the applied field reaches $H_{\text{sat}} = 8 \times 10^6$ A/m.

Since m_{sat} is proportional to particle volume, we can approximate the magnetic saturation of our nanoparticles by multiplying H_{sat} by the ratio of the volumes of the two particles.

The *in vitro* experimental pipe is 30 cm long, which is much larger than the approximately 1 cm length region where cells are captured. We choose the model channel half-length to be $l = 1.65$ cm, which is sufficient to capture the region where stem cells aggregate.

There are several unknown parameters associated with aggregate growth and cell flux. In the experimental *in vitro* studies of magnetic stem cell capture discussed in Chapter 1, cells were captured over a period of 30 minutes. This is much less than the fluid speed which is in the order of seconds. This motivates choosing that both the flux of cells into the aggregate χ^* and the aggregate growth factor α^* are much less than the fluid speed. We fix $\tilde{c}^*$ and $\tilde{\tau}^*$ so that they are larger than the inlet level of cells and the initial wall shear stress values in the pipe, for model tractability and to demonstrate the full range of model solutions respectively. We then vary the parameters which control the physical effects of magnetic field strength (M), haematocrit (H), extravasation ($\kappa_1^*,\ \kappa_2^*$) and erosion (γ^*) to demonstrate the qualitatively different model behaviours in each chapter. Aggregate and cell flux parameters, which are unknown, are shown in Table 2.2.

2.4 Analysis outline

In the subsequent two chapters, we present our analysis of this model. The goal of Chapter 3 is to deliver insight into the *in vitro* experiments presented in Chapter 1 and to examine how extravasation, which was not included in these experiments, would alter the dynamics. These *in vitro* experiments provided stem cell capture efficacy for varying RBC percentages and magnet strengths shown in Fig. 1.3 in Chapter 1. To examine this data we match the channel geometry, flow rate, magnet size and strength as much as possible to the *in vitro* setup and consider the bolus type inlet condition Eq. (2.21b). This allows us to examine the stem cell capture for varying haematocrit and explain the nonlinear decrease in capture for increasing RBC percentage found in *in vitro* experiments. We then describe how these results would be altered when extravasation occurs, bridging between *in vitro* setup and the *in vivo* scenario where cells would leave the vessel to travel to the injury site.

In Chapter 3 we nondimensionalise the model, scaling both the axial and vertical directions proportional to the channel height. In the *in vitro* experiments the ratio of

the channel height to the magnet radius is $\epsilon = d/R_{\text{mag}} = 0.23$. This ratio determines the vertical distances cells travel relative to the axial distance which the magnet affects. Since this ratio is not significantly less than one we do not use lubrication theory in this chapter.

In Chapter 4 we use the model to explore magnetic stem cell delivery outside of the regime of the *in vitro* experiments. We consider systems where the ratio of the channel radius to magnet radius, $\epsilon = d/R_{\text{mag}}$, is small. We achieve this by increasing the magnet size relative to the *in vitro* system. Examining the system in the limit $\epsilon \to 0$, we gain significant tractability in the leading-order governing equations when compared to the full model. This allows us to predict parameter regimes where potentially dangerously high levels of channel occlusion will occur. This is challenging to examine in the *in vitro* regime in Chapter 3 where the numerical solution of the model is significantly more complex. In Chapter 4, we use the constant inlet condition for stem cells (2.21a) as this reduces the transport of stem cells to a quasi-steady system.

Parameter	Definition	Units	Value
C	Inlet conc. (volume conc.)	-	8.4×10^{-4}
d	Channel half height	m	8.25×10^{-4}
H	Haematocrit	-	$0 - 0.4$
n	Number of NPs in cell	-	30
μ_{w}	Viscosity of water	Pa s	8.9×10^{-3} [10]
r_{RBC}	RBC radius	m	3.6×10^{-6} [110]
r	Stem cell radius	m	1×10^{-5}
u^*	Inlet velocity scale	m/s	0.0078
μ_0	Permeability of vacuum	$\mathrm{N/A^2}$	$4\pi \times 10^{-7}$ [40]
V_p	Volume of NP	$\mathrm{m^3}$	4.18×10^{-18}
M	Magnetic saturation of external magnet	A/m	Varied
k_B	Boltzmann constant	J/K	1.38×10^{-28}
T	Temperature	K	295
l	Channel half length	m	1.65×10^{-2}
m_{sat}	Magnetic saturation of NP	A/m	1.25×10^5
R_{mag}	Magnet radius	m	3.5×10^{-3}

Table 2.1: Physical parameters and units taken directly from the *in vitro* setup in [31]. The magnetic saturation of the NP and the half length of the channel have been estimated as listed in Section 2.3. In Chapter 4, the magnet radius is increased from the *in vitro* value listed.

Parameter	Definition	Units
α^*	Aggregate growth coefficient	-
$\tilde{c}^*$	Aggregate growth threshold	-
$\tilde{\tau}^*$	Aggregate erosion threshold	Pa
χ^*	Cell uptake speed	m/s
κ_1^*	Height extravasation rate	1/s
κ_2^*	Constant extravasation rate	m/s
γ^*	Aggregate erosion coefficient	m/(s Pa)

Table 2.2: Aggregate model parameters with units. We fix χ^*, $\tilde{c}^*$, $\tilde{\tau}^*$ and χ^* to achieve physically realistic solutions and vary κ_1^*, κ_2^* and γ^* to reveal the solution behaviour. We note that α^* is dimensionless since we consider the volume concentration of stem cells.

Chapter 3

Magnetic stem cell targeting *in vitro*

In this chapter, we examine the model presented in Chapter 2 in a parameter regime as close as possible to the *in vitro* experiments conducted by our collaborators. A key challenge faced by this therapy, which was identified in these experiments, is to deliver sufficient numbers of cells to the injury site at physiological levels of RBCs: 40% by volume. Motivated by this challenge, this chapter aims to examine delivery for haematocrit levels up to 0.4 for magnetic fields up to 0.4 T as are used *in vitro*.

We begin by nondimensionalising the model, and we then present our numerical scheme for solving the resulting system. We present numerical solutions of the model exploring the effect of varying both physical parameters, such as magnetic field strength and flow speed, and the unknown aggregation parameters. We examine the model predictions for stem cell capture at varying haematocrit levels and show how these predictions qualitatively match the *in vitro* data. We then describe how these results would be altered when extravasation occurs, bridging between the *in vitro* setup and the *in vivo* scenario where cells would leave the vessel to travel to the injury site. Finally, we discuss how the analysis of the model in the *in vitro* regime is limited by the computational complexity associated with its numerical solution.

This chapter is made up of work presented in our interdisciplinary paper *Experimental and mathematical modelling of magnetically labelled mesenchymal stromal cell delivery*, Royal Society Interface, 2021 [123].

3.1 Dimensionless model

We nondimensionalise the model presented in Chapter 2, scaling lengths with the channel half width d and velocities relative to the maximum inlet velocity u^*. We

scale time relative to the timescale of fluid advection d/u^*, we scale pressure relative to atmospheric pressure using the viscous pressure scaling and we nondimensionalise the stem cell concentration relative to the maximum value of the inlet condition C. In this chapter we employ the bolus injection inlet condition, given by Eq. (2.21b). Finally, we scale the shear stress by $\mu_{\mathrm{w}}u^*/d$. We hence define dimensionless variables, denoted with hats, as follows

$$x = d\hat{x}, \quad y = d\hat{y}, \quad h = d\hat{h} \quad u = u^*\hat{u}, \quad v = u^*\hat{v},$$
$$v_n = u^*\hat{v}_n, \quad c = C\hat{c}, \quad t = \frac{d}{u^*}\hat{t}, \quad \tau = \frac{\mu_{\mathrm{w}}u^*}{d}\hat{\tau}, \quad p = p_a + \frac{\mu_{\mathrm{w}}u^*}{d}\hat{p}.$$

Under these scalings, the channel occupies the region $|\hat{x}| \leq L$ where $L = l/d$ is the dimensionless channel length and $-1 + \hat{h} \leq \hat{y} \leq 1$. Inserting these scalings into Eqs. (2.9) - (2.19), and dropping the hats, we arrive at the dimensionless system

$$\nabla^2 \boldsymbol{u} = \nabla p, \tag{3.1}$$
$$\nabla \cdot \boldsymbol{u} = 0, \tag{3.2}$$
$$\frac{\partial c}{\partial t} = -\nabla \cdot \left(\left(\boldsymbol{u} + \frac{\beta}{\mu(H)} \boldsymbol{u}_m \right) c - \frac{\dot{\gamma}}{Pe_{\mathrm{sh}}} \nabla c \right), \tag{3.3}$$

where $\beta = n\mu_0 m_{\mathrm{sat}} M R_{\mathrm{mag}}^2 V_p/(6\pi\mu_{\mathrm{w}} r d^3 u^*)$ is the ratio of the magnetic advection to fluid advection and $\mu(H) = \mu_{\mathrm{eff}}(H)/\mu_{\mathrm{w}}$ is the ratio of the effective viscosity to the viscosity of water which is a function of haematocrit levels. We note that we have left $\mu(H)$ explicitly in the model so that we can easily vary both the magnetic field strength and the haematocrit levels. Finally, $Pe_{\mathrm{sh}} = d^2/k_{\mathrm{sh}}$ is the shear Péclet number which is the ratio of pipe diameter squared to the distance pushed by collisions with RBCs squared. We recall $k_{\mathrm{sh}} = 0.31 H^2 r_{\mathrm{RBC}}^2$ is the strength of shear-induced diffusion. The dimensionless shear rate in (3.3) is

$$\dot{\gamma} = \left(\left(\frac{\partial u}{\partial y} + \frac{\partial v}{\partial x} \right)^2 + 2\left(\frac{\partial u}{\partial x} \right)^2 + 2\left(\frac{\partial v}{\partial y} \right)^2 \right)^{1/2}. \tag{3.4}$$

The dimensionless magnetic velocity in (3.3) is $\boldsymbol{u}_m = (u_m, v_m)$ where

$$u_m = \frac{-x}{((y+1+R)^2 + x^2)^2}, \quad v_m = \frac{-(y+1+R)}{((y+1+R)^2 + x^2)^2}, \tag{3.5}$$

where $R = R_{\text{mag}}/d$ is the dimensionless magnet radius. The dimensionless boundary conditions are

$$-p + 2\frac{\partial u}{\partial x} = 0, \quad \frac{\partial v}{\partial x} + \frac{\partial u}{\partial y} = 0, \quad \frac{\partial c}{\partial x} = 0 \qquad \text{on } x = L, \tag{3.6}$$

$$u = 0, \quad v = 0, \quad \boldsymbol{q} \cdot \boldsymbol{j} = 0 \qquad \text{on } y = 1, \tag{3.7}$$

$$\boldsymbol{u} \cdot \hat{\boldsymbol{n}} = v_n, \quad \boldsymbol{u} \cdot \hat{\boldsymbol{t}} = 0, \quad \boldsymbol{q} \cdot \hat{\boldsymbol{n}} - cv_n = -J \qquad \text{on } y = -1 + h, \tag{3.8}$$

$$u = (1 - y^2), \quad v = 0, \quad c = c_{\text{in}}(t) \qquad \text{on } x = -L, \tag{3.9}$$

where the dimensionless inlet concentration is $c_{\text{in}}(t) = (\tanh(t - t_1) - \tanh(t - t_2))/2$, with $t_1 = t_1^* u^*/d$ and $t_2 = t_2^* u^*/d$ being the dimensionless start and end times of the injection. The dimensionless cell flux J is given by

$$J = \chi(c - \tilde{c})^+ - \gamma\mu \left(\tau - \frac{\tilde{\tau}}{\mu}\right)^+ \mathcal{H}(h), \tag{3.10}$$

where $\chi = \chi^*/u^*$ is the dimensionless uptake rate, $\gamma = \gamma^* \mu_{\text{w}}/dC$ is the dimensionless erosion factor, $\tilde{c} = \tilde{c}^*/C$ is the dimensionless growth threshold and $\tilde{\tau} = \tilde{\tau}^* d/u^* \mu_{\text{w}}$ is the dimensionless erosion threshold.

The dimensionless aggregate growth velocity is defined by

$$v_n = -\alpha(\boldsymbol{q} \cdot \hat{\boldsymbol{n}} - cv_n) - k_{\text{ext}}, \tag{3.11}$$

where

$$k_{\text{ext}} = \begin{cases} \kappa_1 h, & \text{(3.12a)} \\ \kappa_2 \mathcal{H}(h). & \text{(3.12b)} \end{cases}$$

Here $\kappa_1 = \kappa_1^* d/u^*$ is the dimensionless height-dependent extravasation rate and $\kappa_2 = \kappa_2^*/u^*$ is the dimensionless constant dependent extravasation rate. Finally, the dimensionless PDE for the aggregate height, is given by (3.8) but we restate it here for clarity:

$$\frac{\partial h}{\partial t} = v_n \sqrt{1 + \left(\frac{\partial h}{\partial x}\right)^2}. \tag{3.13}$$

To summarise, the dimensionless model consists of the quasi-steady Stokes equations (3.1) and (3.2), and an advection diffusion equation for cell concentration (3.3), where the contribution of the magnetic velocity is determined by $\beta/\mu(H)$ and the strength of fluid advection to shear-induced diffusion is determined by Pe_{sh}. At the inlet we prescribe a unidirectional parabolic velocity field and a temporal inlet concentration of cells where cells arrive between $t = t_1$ and $t = t_2$. At the outlet, we

impose zero normal and tangential stress, and we have zero diffusive flux of cells. On the top of the channel we prescribe no-slip and no flux of fluid and no flux of cells. On the base we have no tangential flow and the normal fluid velocity is v_n. This normal velocity is prescribed by the balance of cell flux and cell extravasation given by Eq. (3.11), and corresponds to the growth of the aggregate defined by Eq. (3.13).

3.2 Parameter selection

The model is determined by geometry and flow parameters, which are matched where possible to the setup of the *in vitro* experiments, and aggregation and cell parameters, which are not known and are qualitatively chosen as we will now detail. All parameters are listed in Table 2.1

In the experiments the magnetic field was provided by two magnets: a cylindrical magnet (radius 0.35 cm and length 4 mm) and a rectangular magnet (dimensions 1 cm by 2 cm by 4 cm). In this chapter we use the magnetic field of an infinite cylinder with radius $R_{\text{mag}} = 0.35$ cm to match the radius of the cylindrical magnet used *in vitro*. The cylinder is oriented perpendicular to the channel. We choose values of the magnetic saturation of the external magnet so that the maximum field strength is 0.1–0.4 T. We consider haematocrit values from 0–0.4. The model setup compared to the *in vitro* magnets is shown in Fig. 3.1

As stated in Section 2.3, the values of aggregation and cell parameters cannot be determined via literature. We choose values of $\tilde{c}$ and $\tilde{\tau}$ at values 10% higher than the inlet concentration and the initial levels of wall shear stress respectively. We fix $\chi = 0.1$, so that deposition occurs on a longer timescale than the fluid transport. Then having fixed these parameters, we explore how varying the parameters which control extravasation and erosion influence stem cell capture. We choose the bolus injection start and end times to be $t_1 = 3$ and $t_2 = 35$ respectively. This represents a period of 4.7 s, which is significantly shorter than the 30 minute duration of the *in vitro* experiments. However aggregate growth parameters for this model have not yet been determined hence we are limited to a qualitative understanding of the system. We choose this shorter period of the bolus injection to gain insight into bolus delivery while reducing computational time.

The shear Péclet number for the *in vitro* experimental system ranges from $Pe_{\text{sh}} = d^2/k_{\text{sh}} = 8.5 \times 10^6$ to 1.35×10^{10} when H varies from 0.4 to 0.01, since $k_{\text{sh}} = 0.05H^2 r_{\text{RBC}}^2$. In this chapter, we use the finite element method to numerically solve our model, as detailed in Section 3.3. Since this is adapted to solve elliptic PDEs we

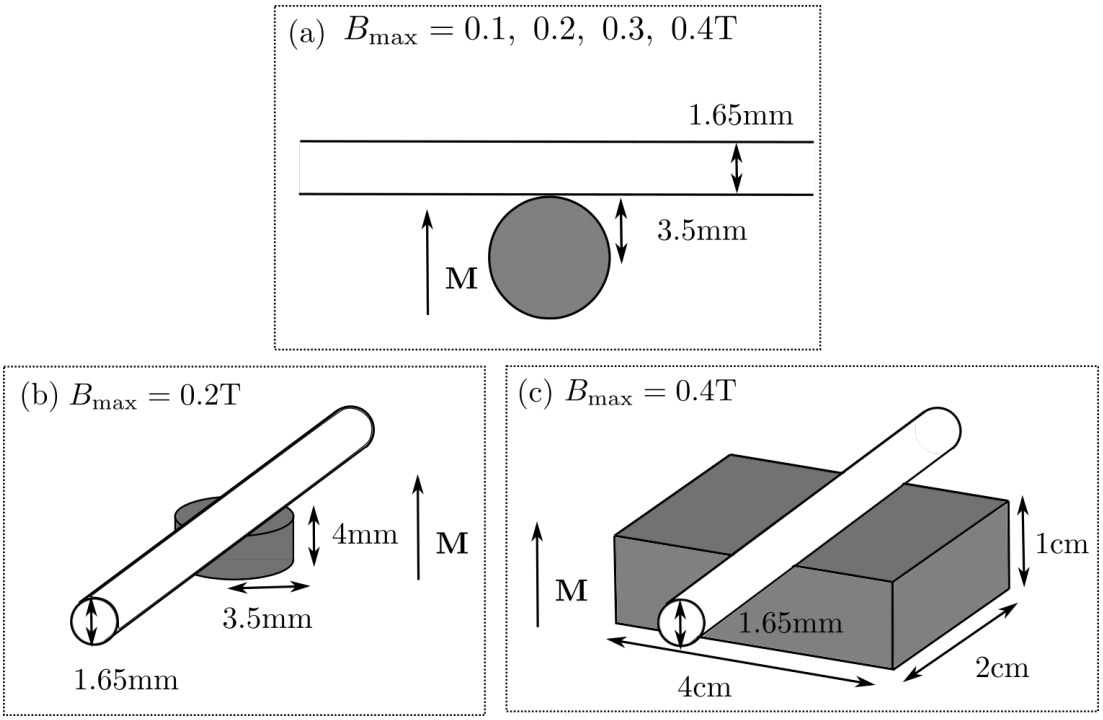

Figure 3.1: Dimensions and strengths of magnets used in model compared to *in vitro* experiments, magnets shown in grey and pipe or channel where stem cells are transported shown by white cylinder or box. (a) Shows the setup of the mathematical model, (b) 0.2 T cylindrical magnet and (c) 0.4 T rectangular magnet.

are unable to solve this system with this method at these very large Péclet numbers as the system is close to hyperbolic. Hence we opt to consider the system for a smaller Péclet number, choosing $Pe_{\text{sh}} = 10$. Although this is much smaller than the Péclet number for the *in vitro* experiments we are still be able to gain qualitative insight into the system.

The values of all dimensionless parameters appearing in the model are listed in Table 3.1. We now detail our numerical solution method for the model.

3.3 Numerical solution

To solve the governing equations we use a finite element formulation of the PDEs coupled to the moving lower boundary through the use of the Arbitrary Lagrangian-Eulerian Method (ALE) [53]. All simulations use the commercial software COMSOL [21]. Taylor-Hood elements (quadratic and linear Lagrange) are used for the fluid velocity and pressure owing to their established stability properties [109]. The advection-diffusion equation was solved with quadratic elements. We use the an in-

Parameter	Definition	Value
μ	$\mu_{\text{eff}}/\mu_{\text{w}}$	Defined in Eq (2.10)
Pe_{sh}	$d^2/0.31H^2r_{\text{RBC}}^2$	10^*
β	$n\mu_0 m_{\text{sat}} M R_{\text{mag}}^2 V_p/(6\pi\mu_{\text{w}} r d^3 u^*)$	52, 105, 157, 210
α	$\alpha^* C$	0.1
κ_1	$\kappa_1^* d/u^*$	0.001,0.01,0.1
κ_2	κ_2^*/u^*	0.1
χ	χ^*/u^*	0.1
γ	$\gamma^*\mu_{\text{w}}/dC$	0-0.1
$\tilde{c}$	$\tilde{c}^*/C$	1.1
$\tilde{\tau}$	$\tilde{\tau}^* d/\mu_{\text{w}} u^*$	4
R	R_{mag}/d	4.24
L	l/d	20
t_1	$t_1^* u^*/d$	3
t_2	$t_2^* u^*/d$	35

Table 3.1: Dimensionless parameter definitions and values used in our simulations. The Péclet number, marked with a star, had to be decreased from 10^6 to ensure numerical stability.

built adaptive time-stepping method: IDA. This uses implicit backwards differentiation formula of order 1 or 2 depending on the local error. We set the relative tolerance to 0.001 and the absolute tolerance to 0.05. Full details of the time-dependent solver are listed in the COMSOL documentation [21].

The inclusion of shear-induced diffusion is a significant challenge numerically as the shear rate vanishes in the centre of the channel. This renders the cell transport equation hyperbolic. In this case the finite element method is unstable and leads to spurious oscillations in the numerical solution. To ensure the simulations are tractable, the shear-induced diffusion is approximated by isotropic diffusion, removing the dependence of the diffusion coefficient on fluid shear and haematocrit.

To implement the Heaviside functions in Eq. (3.10), we use an inbuilt function $flc1hs(x-\delta)$ which is zero for $x < 0$ and equal to one for $x > \delta$. This has a continuous first derivative which improves the stability properties of the numerical method. We take $\delta = 0.1$ which leads to 0.22% relative error in the cell concentration when compared to $\delta = 10^{-4}$. This is shown in the Appendix, Section B.1.1.

We solve the system on an evolving domain using an unstructured quadrilateral mesh. We allow free movement of mesh points throughout the entire domain and remeshing is not required. We compare the relative maximum error (defined as the maximum error divided by the maximum value of the variable) on a range of meshes with 1000 – 8000 elements using variables values calculated on a mesh with 12758

elements as a reference. We select the mesh with 4202 elements, which returns solutions with less than 1.59% relative error in each independent variable compared to the fine reference mesh. This is shown in the Appendix, Section B.1.2. We carried out this error analysis using $\beta = 210$, γ up to 0.1, $H = 0.2$ and κ_1 up to 0.1. We limit ourselves to values of $\gamma \leq 0.1$ as for larger values of γ we are unable to achieve sufficient error convergence as the number of elements increases. The parameter γ determines the impact of the wall shear stress on the moving boundary. Coupling the boundary to the wall shear stress means that any oscillations in the wall shear stress lead to oscillations in the aggregate surface as the boundary grows. We expect that to solve the system for high values of γ would require a finer mesh.

3.4 Numerical Results

We first examine a prediction of stem cell delivery arising from the mathematical model using $\beta = 210$, $H = 0.2$ with erosion and extravasation present. We use the height-dependent extravasation condition (3.12a); we will explore the effect of constant extravasation in Section 3.4.3. The transport of stem cells, and the evolution of the cell aggregate on the wall, are shown in Fig. 3.2. First, shown in Fig. 3.2a, the cells are advected with the flow. Then, once the cells are within range of the magnet, some of the cells are captured on the base of the channel. As more cells arrive the stem cells form an aggregate, seen in Fig. 3.2b. Note that since the normalised magnetic field strength is large, the aggregate forms upstream of the centre of the magnet located at $x = 0$. As more cells arrive the aggregate significantly obstructs the channel, as shown in Fig. 3.2c. To preserve the flux through the channel the flow speeds up over the peak and the shear stress experienced by the aggregate increases. As a result, cells are eroded from the surface by shear stress. Eventually, shown in Fig. 3.2d, as the source of cells at the inlet ends, the aggregate stops growing. Once the aggregate is smaller it translates upstream to the centre of the magnet. Since extravasation is present, the remaining cells leave the channel through the wall.

The stages are illustrated clearly in Fig. 3.3 illustrating the velocity of the aggregate boundary at $x = -2$ (the location of the aggregate peak when it is at its maximum height). Here a negative velocity indicates that the aggregate is shrinking. The relative size of the growth rate compared to erosion and extravasation rates determines the capture efficacy of stem cells and whether the channel will potentially block.

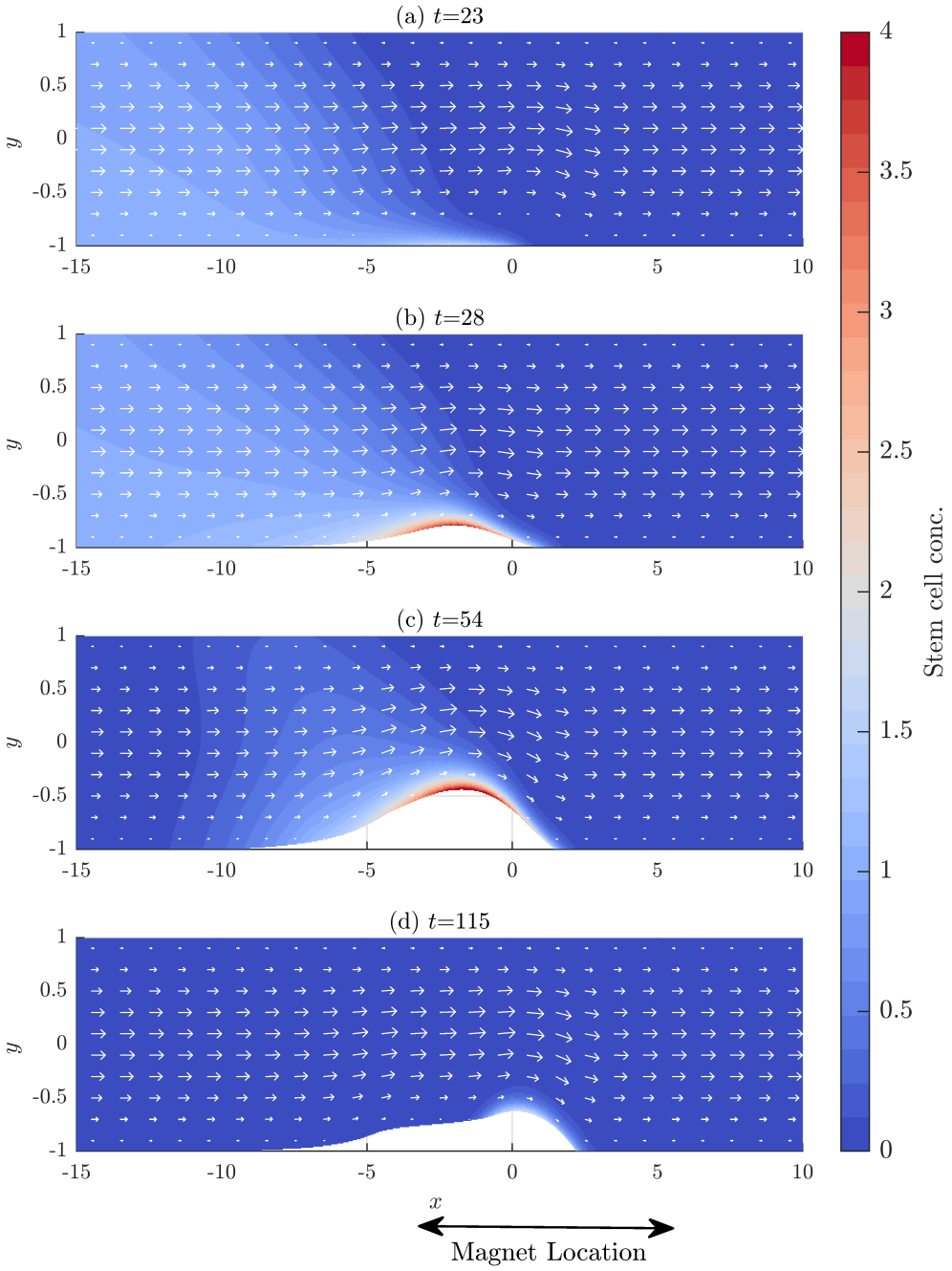

Figure 3.2: Transport of stem cells and cell aggregation at the channel wall is shown in snapshots of cell concentration relative to the inlet concentration together with the fluid velocity field. We show the section of channel $-15 < x < 10$. (a) Stem cells arrive via fluid advection and then begin to build up on the base close to the magnet, $t = 23$. (b) Stem cell level increases (shown by the colour bar) and the solid aggregate begins to form at $t = 28$. (c) The aggregate extent grows and the channel is obstructed significantly at $t = 54$. (d) Once the inlet source of stem cells ends, the captured stem cells are eroded by fluid shear and cells extravasate (via height-dependent extravasation) out of the channel (both shown by decreasing aggregate size) by $t = 115$. Parameter values: $H = 0.2$, $\beta = 210$, $\kappa_1 = 0.01$, $\gamma = 0.1$, all other parameters as in Table 3.1.

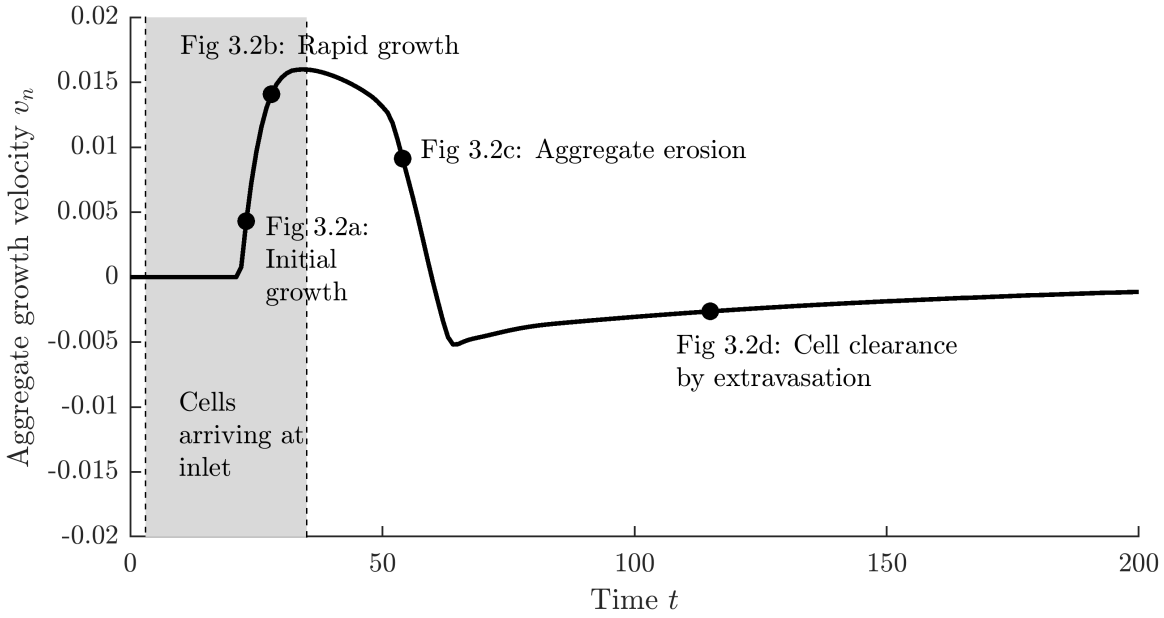

Figure 3.3: Aggregate interface velocity at $x = -2$ as stem cells are captured. Negative velocity indicates when the aggregate is shrinking. The points correspond to snapshots of the system in Fig. 3.2. The shaded region illustrates when stem cells are arriving at the channel inlet. Parameter values as in Fig. 3.2.

3.4.1 Cell capture for varying magnetic field strength

We now vary the normalised magnetic field strength β and examine how this alters cell capture and aggregation at a fixed time. We do not include erosion or extravasation for simplicity. Increasing the normalised magnetic field strength β increases cell capture, as shown in Figure 3.4 by an increase in both the height and the extent of the aggregate. For lower β, cells enter the aggregate upstream while other cells flow over the aggregate and are captured downstream, thus ensuring approximately symmetric capture of cells around the magnet. However, as β increases the cells no longer flow over the aggregate, all entering upstream of the peak, the aggregate peak occurs further upstream and the downstream slope becomes steeper. This results in similar aggregate heights for both $\beta = 210$ and $\beta = 157$. However, the larger normalised magnetic field strength ($\beta = 210$) produces an aggregate with a 10% larger area and a 3% larger contact set on the boundary than the smaller normalised magnetic field strength ($\beta = 157$).

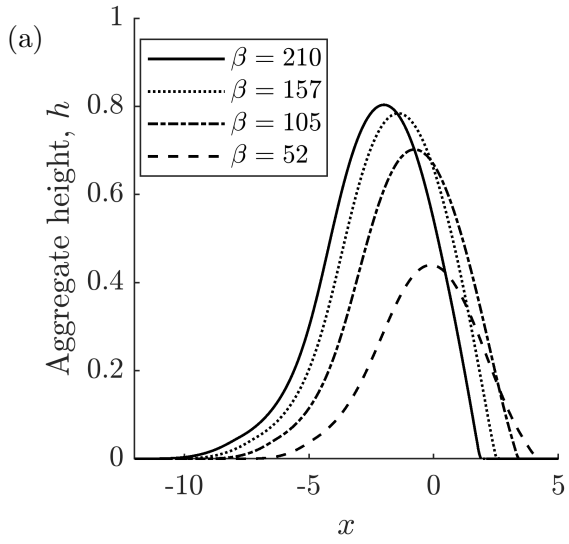

Figure 3.4: Aggregate interface profiles increase for increasing normalised magnetic field strength. Parameter values: $H = 0.2$, $\kappa_1 = 0$ (no extravasation), $\gamma = 0$ (no erosion) at $t = 80$, all others in Table 3.1.

3.4.2 Cell capture for varying haematocrit: comparison to *in vitro* data

We now compare the maximum channel blockage produced for varying haematocrit levels at the magnetic field strengths and haematocrit values used in the *in vitro* experiments: $B_{\max} = 0.2$ T and 0.4 T for $H = 0 - 0.4$. We have an erosion strength of $\gamma = 0.1$ and no extravasation as this was not present in the *in vitro* setup. We compare the maximum height achieved during the time of our simulations to the percentage capture which was recorded in the experiments. The stem cell capture which was obtained in the *in vitro* experiments is shown in Fig. 3.5a. In these experiments stem cell capture reduced as the RBC percentage increased for both magnet strengths. The stronger magnet $B_{\max} = 0.4$ T, achieved a higher level of capture at all RBC percentages.

The maximum aggregate height obtained in model solutions for varying haematocrit is shown in Fig. 3.5b. For both strengths of magnetic fields, increasing haematocrit decreases the maximum aggregate height captured, reflecting the results obtained *in vitro*. We find that the stronger magnet (solid line Fig. 3.5b) is better able to capture stem cells at higher levels of RBCs than the weaker magnet. This was also shown in the *in vitro* results in Fig. 3.5a.

Increasing haematocrit levels increases the viscosity of the fluid which in turn decreases the relative effect of the magnetic force, as the drag on the cells increases. It

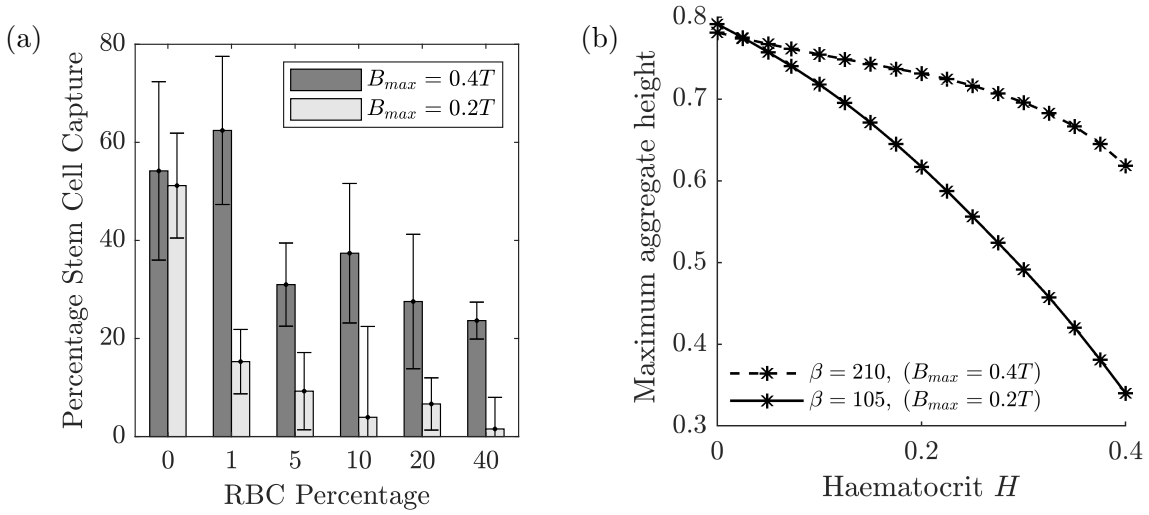

Figure 3.5: (a) Mean stem cell percentage capture obtained for varying RBC% *in vitro* show that increasing RBC% decreases stem cell capture, but the stronger magnet can retain capture at larger values of haematocrit. 95% confidence intervals of three experimental repeats are indicated by the bars around the mean at each RBC% [123]. (b) Maximum aggregate height decreases as haematocrit increases, although the stronger magnet can capture more cells at larger haematocrit values. Parameters: $\gamma = 0.1$ and no extravasation, all other parameters in Table 3.1.

additionally increases the strength of erosion on the aggregate. As shown in Fig. 3.5b, for both magnetic field strengths, $B_{\max} = 0.2$ T and 0.4 T, the maximum aggregate height obtained at $H = 0$ is approximately $h = 0.8$. As discussed in Section 3.4.1, increasing the magnetic field strength initially increases aggregate height, then aggregation occurs further upstream and covers a more significant portion of the channel. This allows two different magnetic field strengths to obtain a similar maximum aggregate height in the channel. However, we note that the stronger magnet does capture marginally more cells, achieving a 2% larger maximum area aggregate than the weaker magnet.

3.4.3 Exploring aggregate erosion and extravasation

Aggregate profiles for increasing erosion susceptibility parameter γ are shown in Figure 3.6a. For larger values of the susceptibility parameter γ the aggregate peak, where the fluid shear is greatest, is reduced. The threshold of erosion that cells are assumed to withstand is set at 10% higher than the fluid shear on the walls in the absence of an aggregate. Once the aggregate exceeds 20% of the channel height ($h = 0.4$) erosion begins to remove the cells arriving on the upstream slope. These cells are then

captured on the downstream slope of the aggregate, which moves further downstream as γ increases.

Including extravasation through the vessel wall reduces the height of the aggregate at all axial positions, as illustrated for height-dependent extravasation in Figure 3.6b. To compare the effect of the two extravasation kinetics, constant and height-dependent (defined in Eq. (3.11)), we plot the height of the aggregate across the channel over time, Fig. 3.7. To quantitatively compare we choose an extravasation rate such that $\kappa_1 h$ is comparable to κ_2 when $h = 0.1$ by setting $\kappa_1 = 0.1$ and $\kappa_2 = 0.01$. Constant extravasation leads to greater obstruction of the channel and the cells persist in the channel for a longer time and over a larger area. Height-dependent extravasation leads to an aggregate which clears from the vessel more rapidly. This is because when $h = 0.6$ height-dependent extravasation is greater than constant extravasation, $\kappa_1 h > \kappa_2$, so the aggregate decreases from its maximum height more rapidly in Fig. 3.7a.

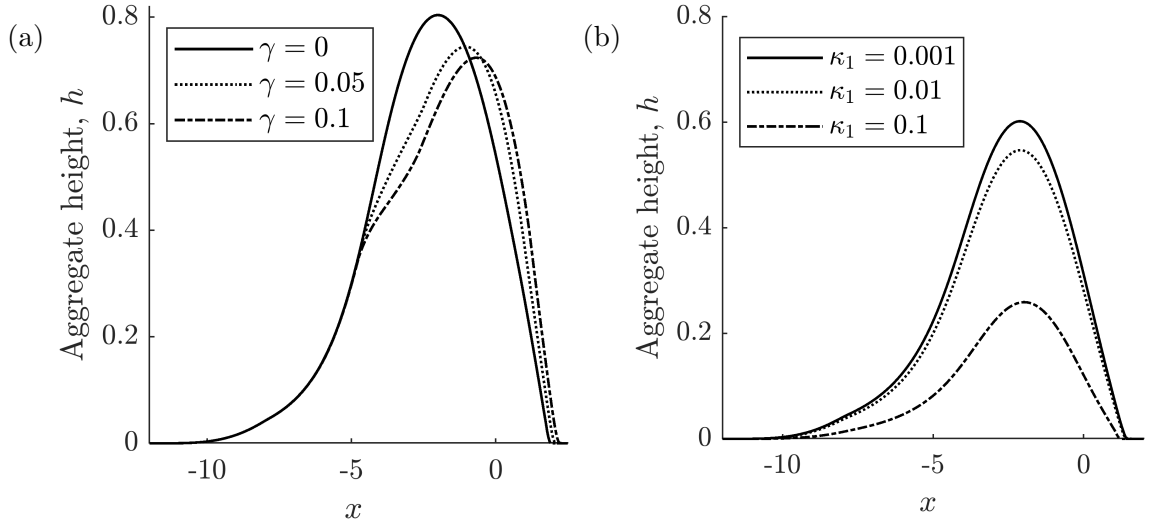

Figure 3.6: (a) Aggregate peak decreases for increasing erosion parameter $\gamma = 0$–0.1 at $t = 80$. Parameter values: $H = 0.2$, $\beta = 210$, $\kappa_1 = 0$ (no extravasation), all others as in Table 2.2. (b) Aggregate interface profiles decrease for increasing height-dependent extravasation parameter $\kappa_1 = 0.001$–0.1 at $t = 50$. Parameter values: $H = 0.2$, $\beta = 210$, $\gamma = 0$ (no erosion), all others as in Table 3.1.

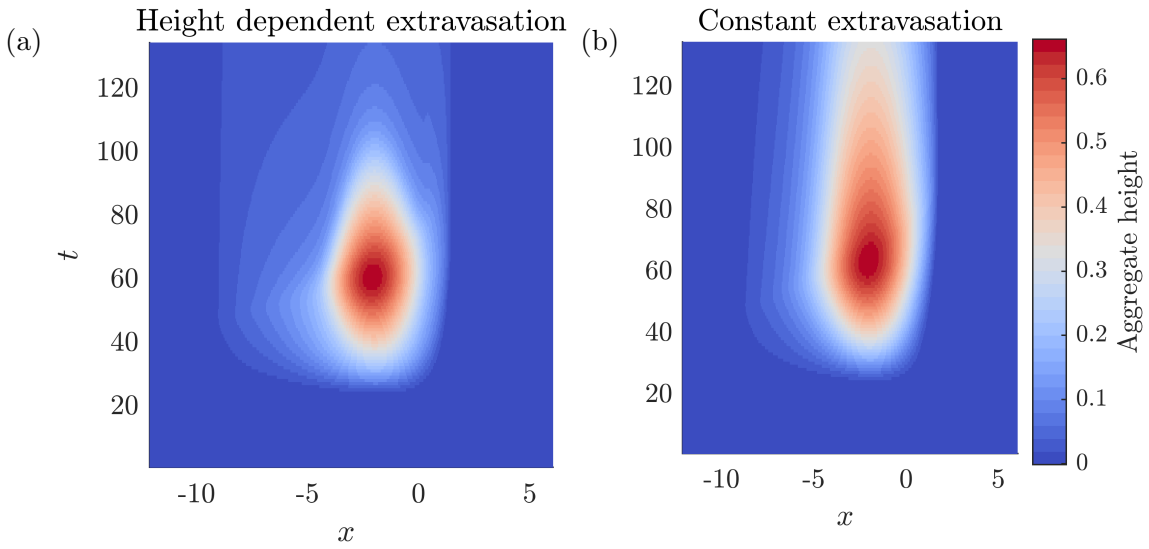

Figure 3.7: Aggregate evolution across the centre of the channel over time. (a) Height-dependent extravasation with $\kappa_1 = 0.1$, (b) constant extravasation with $\kappa_2 = 0.01$. Constant extravasation leads to a much larger aggregate which persists in the channel for a longer time. Parameter values: $H = 0.2$, $\beta = 210$, $\gamma = 0$ and all others as in Table 3.1. Note that we chose the values of κ_1 and κ_2 such that $\kappa_2 h$ is comparable to κ_1 (assuming an approximate size of $h = 0.1$).

3.5 Discussion

In this chapter, we have numerically solved the aggregation model for magnetic stem cell delivery presented in Chapter 2 in the parameter regime of the *in vitro* experiments. We solved the full model numerically for a bolus injection of stem cells. We demonstrated that the dynamics of delivery has three stages: i) rapid cell capture and aggregate growth, ii) erosion as the aggregate obstructs the channel, and iii) clearance of cells via extravasation. We noted that the balance between growth, erosion and extravasation is key in determining if the aggregate remains within safe levels.

A key goal of this chapter was to examine how delivery varies if the magnetic field strength or RBC percentage is changed. We first showed that if the magnetic field increases more stem cells are captured and the aggregate centre of mass occurs further upstream as the magnetic field strength is increased further. This leads to a nonlinear relationship between the magnetic field strength and aggregate height. In our model, β is the ratio of magnetic field strength to fluid advection. In this chapter, we demonstrated that increasing β, via an increase in the magnetic field strength, increases the number of stem cells which are captured. However, an increase in β could also be achieved by decreasing the flux through the channel. This demonstrates that it is vitally important to characterise the fluid mechanics of the target vasculature

in vivo to ensure that aggregation can be minimised by controlling the magnetic field strength.

Second, we examined how varying haematocrit affects stem cell capture. Increasing haematocrit increases the viscosity of the suspension which decreases the relative effect of the magnetic field on the stem cells as Stokes drag on each cell is greater. Our model results also showed that stronger magnets lead to larger aggregate formation at a higher levels of haematocrit compared to weak magnets. This reflects the *in vitro* experimental data where the 0.4 T magnet captured 25% of the stem cells, compared to 2% stem cell capture achieved with the 0.2 T magnet. Furthermore, we showed that it is possible to achieve approximately the same aggregate height with a 0.2 T and a 0.4 T magnet at 0% RBC. This is because as the magnetic field increases the cells are captured further upstream, hence can obtain the same aggregate height at different magnetic field strengths.

However, the model did not produce the same qualitative form of the decrease in capture which was convex for 0.2 T *in vitro*. There are several factors which could explain the difference between the *in vitro* data compared to the mathematical model. For instance, stem cells can bind to the pipe walls without magnets, as was observed by our collaborators during the experiments. Furthermore, a large variation was found between experimental repeats which leads to the large confidence intervals in Fig. 3.5a. A key point to note is that the *in vitro* data is in terms of the percentage of stem cells which are captured whereas we have compared the relative aggregate height for varying haematocrit. This comparison could be improved by calculating the total flux at the inlet in the model and comparing this to the total flux at the channel outlet, thus estimating the capture.

For the remainder of this chapter, we explored the effect on stem cell aggregation of varying erosion strength, extravasation strength and the functional form of extravasation. We demonstrated that increasing erosion limits the aggregate height. This is because once the aggregate is large enough for wall shear stress threshold $\tilde{\tau}$, additional captured cells above this height on the upstream edge are eroded. Extravasation however reduces aggregation across the whole channel. We showed that height-dependent and constant extravasation had different time-dependent dynamics with constant extravasation leading to more aggregation across the channel which takes longer to clear. Further experiments would allow the unknown model parameters to be quantified, which would enable us to select the appropriate extravasation mechanism and put a bound on magnetic field strengths which achieve an acceptable level of aggregation.

The analysis in this chapter demonstrated the rich dynamics that this model can produce. However, this analysis was limited to a small selection of parameter values since the numerical solution of the model is very computationally demanding. We were unable to examine regimes which lead to large aggregation, since the moving mesh implementation in this chapter is not stable to extreme deformations, or regimes with very large erosion, which did not adequately converge on the numerical meshes we tested. Furthermore, in this chapter, it was not possible to solve the model at the physiological Péclet numbers of 10^6 in the numerical simulations. This motivates the reduced framework we develop and analyse in the subsequent chapter. We consider delivery outside the regime of the *in vitro* experiments, considering geometry and magnet setups where the magnet radius is much larger than the pipe diameter. We will then explore delivery regimes as a function of the Péclet number and relative magnetic velocity strength β.

Chapter 4

Asymptotic analysis of magnetic stem cell delivery

4.1 Introduction

In this chapter we develop reduced models for magnetic stem cell delivery, returning to the aggregation model presented in Chapter 2. We exploit a disparity in both timescales and lengthscales by considering regimes where firstly, the timescale of aggregate growth is much slower than the timescale of fluid advection and secondly, the channel thickness is much smaller than the magnet radius. In the previous chapter, our analysis of the model in the regime of the *in vitro* experiments was limited due to the complexity associated with its numerical solution. This meant that the shear-induced diffusion was neglected and a limited range of model parameters was explored. Using the reduced models in this chapter, which retain shear-induced diffusion, we explore delivery regimes as a function of the magnetic field strength and flow speed, and carry out a more extensive parameter analysis.

The model system is characterised by: the channel half height d, the channel half length l, and the magnet radius R_{mag}. The channel half height and length impact the fluid mechanics in the channel. The magnet radius determines the region of the channel which is affected by the magnetic field, since the magnetic force on the cells decays $\sim x^{-4}$ as $|x| \to \infty$, where $|x|$ is the distance from the magnet centre. Across all human vessels the aspect ratio, d/l, is small [46]. In the absence of significant vessel curvature, this results in axial fluid velocities that are an order of magnitude larger than the radial velocities. In this chapter, we consider magnetic cell delivery in systems where the ratio of the channel half height to the magnet radius is small, such that $\epsilon = d/R_{\text{mag}} \ll 1$. This allows us to use the thin-film approximation to examine the stem cell transport equation and the fluid flow. We additionally assume that the

ratio of the magnet radius to channel length is small, such that $R_{\text{mag}}/l \ll 1$. This means that the strength of the magnetic field is minimal at the inlet of the channel. In the *in vitro* system examined in Chapter 3, $\epsilon = 0.24$, which is at the edge of the validity of this lubrication assumption.

Since the model aggregation parameters are not known, the timescale of aggregate growth is unknown. The *in vitro* experiments examined in Chapter 3 lasted thirty minutes, however it is not clear precisely how long the stem cells took to be captured at the magnet as we only have data from the end of the experiment. In this thesis we assume that the fluid advection timescale, approximately 0.1 seconds in the *in vitro* system, is much shorter than the aggregate growth timescale. In Chapter 3, we used the low Reynolds number to remove fluid inertia but we did not carry out any further model reduction. Furthermore, we considered a bolus injection inlet condition for the stem cells over a timescale of 5 seconds, and since we did not consider longer bolus time periods, we could not examine any dynamics of aggregation which occur over a longer time period, such as the erosion of the entire aggregate or slow channel obstruction. In this chapter we employ the constant inlet condition for stem cell concentration, defined in (2.21a), and we use the height-dependent extravasation form, defined in (2.32a). We also consider the system on the aggregate growth timescale, which is assumed to be much longer than the timescale of fluid advection, which leads to quasi-steady fluid flow and cell transport at leading-order.

We characterise delivery into regimes according to the relative size of the normalised magnetic field strength $\hat{\beta}$ and reduced Péclet number, defined by $\epsilon^3 \hat{Pe}_{\text{sh}}$. In this chapter the normalised magnetic field strength $\hat{\beta}$ is defined as $\hat{\beta} = \epsilon^3 \beta$ where β is the parameter used in Chapter 2. The Péclet number is defined by $\hat{Pe}_{\text{sh}} = R_{\text{mag}}^2/k_{\text{sh}}$ which represents the ratio of the magnet radius squared to the strength of shear-induced diffusion. We analyse two tractable asymptotic limits: small reduced Péclet number and large reduced Péclet number delivery. To have a small reduced Péclet number, $\epsilon^3 \hat{Pe}_{\text{sh}}$, the magnet radius must be much larger than the pipe radius so that $\epsilon \ll 1$ and the Péclet number $R_{\text{mag}}^2/k_{\text{sh}}$, cannot be too large. Since $k_{\text{sh}} = 0.31 H^2 r_{\text{RBC}}$, the Péclet number is largest at physiological RBC percentages, $H = 0.4$.

The large reduced Péclet number delivery regime corresponds to the regime considered by Richardson et al. [92]. In this work, the authors present the asymptotic structure for the capture of a magnetic drug under a constant magnetic force in a straight, circular pipe without the growth of an aggregate. They consider the delivery in which the magnetic velocity balances the fluid velocity with a uniform inlet concentration of the drug. They demonstrate that the pipe is divided into two regions by

the trajectories of the drug particles originating from the top half of the inlet, with a constant drug concentration in the region below these dividing trajectories and a concentration of zero in the region above them. The drug concentration then builds up in a boundary layer on the base. The magnitude of the drug concentration in the boundary layer is determined by the size of the flux into the wall. Their work examines both small and large nanoparticle flux out of the walls of the vessel. The authors show that for a large flux coefficient, the magnetic drug exits the vessel at the location it lands on the pipe wall, whereas for small flux coefficients there is an axial flux of the drug in the boundary layer. We extend their analysis by coupling the boundary layer structure to the moving aggregate boundary and carrying out exploratory numerical simulations of the model.

We now proceed by nondimensionalising the model using lubrication theory scalings, then examining the leading-order fluid system and the leading-order cell transport dynamics in both small and large reduced Péclet regimes. In each regime, we solve the reduced model numerically, determine when steady state aggregate heights are possible and when aggregation becomes dangerously large. We then conclude by discussing other delivery regimes and comparing the insight we have gained in this chapter to that gained in Chapter 3.

4.2 Lubrication limit

We nondimensionalise the model from Chapter 2, making the following assumptions.

1. The lubrication approximation that the channel height is much less than both the channel length and magnet radius, with $R_{\text{mag}} < l$, so that the magnetic field is minimal at the inlet. This defines the key small parameter $\epsilon = d/R_{\text{mag}}$.

2. The timescale of the fluid advection is much less than the timescale of aggregate growth.

Following these assumptions we consider two cases where i) the reduced Péclet number, $\epsilon^3 Pe_{\text{sh}}$, is large and ii) the reduced Péclet number, is small. We then select the normalised magnetic field strength, $\hat{\beta}$, and all aggregation parameters so that we retain all physical effects in the leading-order reduced models. The scalings of all dimensionless model parameters which we select to achieve this for both the large and small Péclet number cases are shown in Table 4.1.

Name	Param.	Definition	Assumed size
Relative magnetic field strength	$\hat{\beta}$	$\dfrac{n\mu_0 m_{\text{sat}} M V_p}{6\pi\mu_{\text{eff}} R_{\text{mag}} r u^*}$	S. 4.6: $O(1)$ S. 4.7: $O(\epsilon)$
Reduced Péclet number	$\epsilon^3 \hat{Pe}_{\text{sh}}$	$\epsilon^3 R_{\text{mag}}^2 / k_{\text{sh}}$	S. 4.6: $O(\epsilon^2)$ S. 4.7: $O(\epsilon^{-1})$
Aggregate growth rate	α	α^*/C	$O(\epsilon)$
Extravasation speed	$\hat{\kappa}$	$\kappa_1^* R_{\text{mag}}/u^*$	$O(\epsilon)$
Cell flux rate	χ	χ^*/u^*	$O(\epsilon)$
Aggregate erosion susceptibility	$\hat{\gamma}$	$\gamma^* \mu_{\text{eff}}/R_{\text{mag}} C$	$O(\epsilon^2)$
Aggregation threshold	$\hat{c}$	$\tilde{c}^*/C$	$O(1)$
Erosion threshold	$\hat{\tau}$	$\tilde{\tau}^* R_{\text{mag}}/u^* \mu_{\text{eff}}$	$O(\epsilon^{-1})$
Channel half length	$\hat{L}$	l/R_{mag}	$O(1)$

Table 4.1: Definitions of dimensionless model parameters in this chapter and assumptions of their size. Starred parameters are dimensional. The order of normalised magnetic field strength and reduced Péclet number are listed for the small reduced Péclet number regime we analyse in Section 4.6 and the large reduced Péclet number regime in Section 4.7. The assumptions on the size of aggregate growth and cell capture parameters arise since we choose to analyse the fullest balance in the leading-order system for each regime.

We choose the characteristic axial lengthscale to be the magnet radius, R_{mag}, as this determines the size of the region where stem cells deposit. We choose the characteristic axial velocity scale to be the maximum inlet velocity u^*. Using the lubrication scaling we scale vertical distances and velocities with ϵR_{mag} and ϵu^* respectively. We scale the aggregate thickness with ϵR_{mag}, which assumes that it is the same order as the width of the channel. Since we use the constant inlet condition for stem cell concentration, we nondimensionalise the cell concentration relative to the inlet concentration C. In Chapter 3, we used the channel width as the reference lengthscale in both the x- and y- directions. In this chapter, we employ a lubrication scaling and we use hats to denote when the arising nondimensional parameters differ from their counterparts in Chapter 3.

We consider the system on the timescale of aggregate growth, which we now determine. The aggregate grows with a normal velocity v_n, which is determined by the cell flux J^*. These are defined in Chapter 2, Eqs. (2.25), (2.30) and (2.31), which

we restate here:

$$\frac{\partial h}{\partial t} = v_n \sqrt{1 + \left(\frac{\partial h}{\partial x}\right)^2}, \tag{4.1}$$

where

$$v_n = \alpha^* J^* - \kappa_1^* h, \tag{4.2}$$

and the flux into the aggregate is defined as follows

$$J^* = \chi^*(c - \tilde{c}^*)^+ - \gamma^*(\tau - \tilde{\tau}^*)^+ \mathcal{H}(h). \tag{4.3}$$

Examining (4.1) we can define the timescale of aggregate growth $[t_g]$, as $[t_g] = [h]/[v_n]$. From (4.2) and (4.3), the size of the normal velocity is $[v_n] = \alpha^* \chi^* [c]$. Since h is scaled relative to ϵR_{mag} and the cell concentration is scaled relative to C, we obtain $[t_g] = \epsilon R_{\text{mag}}/\alpha^* \chi^* C$.

The timescale of fluid advection is $[t_f] = R_{\text{mag}}/u^*$. We recall that χ^* determines the speed which cells bind to the aggregate and α^* determines how the concentration of cells is converted into the solid aggregate. Hence to ensure that the timescale of aggregate growth is less than the timescale of fluid advection, $[t_g] \ll [t_f]$, we fix $\alpha^* \chi^* C \ll \epsilon u^*$. To have that $\alpha^* \chi^* C \ll \epsilon u^*$, we prescribe that i) that the ratio of the aggregate flux coefficient to fluid velocity is small, such that $\chi^*/u^* = O(\epsilon)$ and ii) the aggregate growth coefficient is small relative to the inlet concentration of stem cells, such that $\alpha^*/C = O(\epsilon)$. We then define $\alpha^* = \epsilon \alpha_0 C$ and $\chi^* = \epsilon \chi_0 u^*$ where the χ_0 and α_0 are $O(1)$ and dimensionless. With these definitions, the timescale of aggregate growth is $R_{\text{mag}}/\epsilon C u^*$. We note that under these assumptions the aggregate growth velocity will be $O(\epsilon^2)$, and this is reflected in the nondimensionalisation of v_n.

Using these assumptions, we define rescaled variables, shown with hats, as follows

$$x = R_{\text{mag}} \hat{x}, \quad y = \epsilon R_{\text{mag}} \hat{y}, \quad h = \epsilon R_{\text{mag}} \hat{h}, \quad t = \frac{R_{\text{mag}}}{\epsilon C u^*} \hat{t}, \tag{4.4}$$

$$u = u^* \hat{u}, \quad v = \epsilon u^* \hat{v}, \quad p = p_a + \frac{u^* \mu_{\text{eff}}}{R_{\text{mag}} \epsilon^2} \hat{p}, \tag{4.5}$$

$$v_n = \epsilon^2 u^* \hat{v}_n, \quad \dot{\gamma} = \frac{u^*}{R_{\text{mag}}} \frac{\hat{\dot{\gamma}}}{\epsilon}, \quad \tau = \frac{u^* \mu_{\text{eff}}}{R_{\text{mag}}} \frac{\hat{\tau}}{\epsilon}, \quad c = C \hat{c}, \tag{4.6}$$

where we have used the standard lubrication pressure scaling to balance the axial pressure gradient with the transverse viscous forces in (2.9). The domain is now defined by $(\hat{x}, \hat{y}) \in [-\hat{L}, \hat{L}] \times [-1 + \hat{h}, 1]$, where $\hat{L} = l/R_{\text{mag}}$. The shear stress τ and shear rate $\dot{\gamma}$ are scaled by $1/\epsilon$ as a result of the velocity scalings.

Inserting scalings (4.4) - (4.6) into the Stokes equations, (2.9), and dropping hats on rescaled variables, we have the following dimensionless lubrication equations

$$\frac{\partial u}{\partial x} + \frac{\partial v}{\partial y} = 0, \tag{4.7}$$

$$\epsilon^2 \frac{\partial^2 u}{\partial x^2} + \frac{\partial^2 u}{\partial y^2} = \frac{\partial p}{\partial x}, \tag{4.8}$$

$$\epsilon^4 \frac{\partial^2 v}{\partial x^2} + \epsilon^2 \frac{\partial^2 v}{\partial y^2} = \frac{\partial p}{\partial y}, \tag{4.9}$$

for $|x| < \hat{L}$ and $-1 + h < y < 1$. On the aggregate surface, $y = -1 + h(x,t)$, the unit normal and tangential vectors depend on the aggregate height as follows

$$\hat{\boldsymbol{n}} = \frac{1}{M}\left(\boldsymbol{j} - \epsilon \frac{\partial h}{\partial x}\boldsymbol{i}\right), \quad \hat{\boldsymbol{t}} = \frac{1}{M}\left(\boldsymbol{i} + \epsilon \frac{\partial h}{\partial x}\boldsymbol{j}\right), \tag{4.10}$$

where

$$M = \sqrt{1 + \epsilon^2 \left(\frac{\partial h}{\partial x}\right)^2}. \tag{4.11}$$

Hence, by (4.7) - (4.9) in Chapter 2, the dimensionless boundary conditions for the thin-film fluid equations are given by

$$u = (1 - y^2), \quad v = 0 \quad \text{at } x = -\hat{L}, \tag{4.12}$$

$$2\epsilon^2 \frac{\partial u}{\partial x} - p = 0 \quad \epsilon^2 \frac{\partial v}{\partial x} + \frac{\partial u}{\partial y} = 0, \quad \text{at } x = \hat{L}, \tag{4.13}$$

$$u = 0, \quad v = 0 \quad \text{at } y = 1, \tag{4.14}$$

$$M\left(v - \frac{\partial h}{\partial x}u\right) = \epsilon v_n, \quad u = -\epsilon^2 \frac{\partial h}{\partial x} v \quad \text{at } y = -1 + h. \tag{4.15}$$

The dimensionless stem cell transport equation, derived from Eq. (2.19), is

$$\epsilon \frac{\partial c}{\partial t} + \frac{\partial q_x}{\partial x} + \frac{\partial q_y}{\partial y} = 0, \tag{4.16}$$

where the dimensionless cell flux is defined $\boldsymbol{q} = q_x \boldsymbol{i} + q_y \boldsymbol{j}$, with components given by

$$q_x = \left(u + \hat{\beta} u_m\right) c - \frac{\dot{\gamma}}{\epsilon \hat{P}e_{\text{sh}}} \frac{\partial c}{\partial x}, \quad q_y = \left(v + \frac{\hat{\beta}}{\epsilon} v_m\right) c - \frac{\dot{\gamma}}{\epsilon^3 \hat{P}e_{\text{sh}}} \frac{\partial c}{\partial y}, \tag{4.17}$$

here the shear Péclet number is defined $\hat{P}e_{\text{sh}} = R_{\text{mag}}^2 / k_{\text{sh}}$, which is the ratio of the magnet radius squared to cross-streamline diffusion; and the normalised magnetic

field strength is $\hat{\beta} = n\mu_0 m_{\text{sat}} M V_p / 6\pi\mu_{\text{eff}} R_{\text{mag}} r u^*$, which is the ratio of the magnetic force to Stokes drag on the cell. The dimensionless shear rate in (4.17) is defined by

$$\dot{\gamma} = \left(\left(\frac{\partial u}{\partial y} + \epsilon^2 \frac{\partial v}{\partial x} \right)^2 + 2\epsilon^2 \left(\frac{\partial u}{\partial x} \right)^2 + 2\epsilon^2 \left(\frac{\partial v}{\partial y} \right)^2 \right)^{1/2}, \tag{4.18}$$

and the dimensionless magnetic velocity components are

$$u_m = \frac{-x}{((\epsilon y + \epsilon + 1)^2 + x^2)^2}, \quad v_m = \frac{-(\epsilon y + \epsilon + 1)}{((\epsilon y + \epsilon + 1)^2 + x^2)^2}. \tag{4.19}$$

The dimensionless boundary conditions for (4.16) are as follows

$$c = 1 \quad \text{at } x = -\hat{L}, \tag{4.20}$$

$$\frac{\partial c}{\partial x} = 0 \quad \text{at } x = \hat{L}, \tag{4.21}$$

$$q_y = 0 \quad \text{at } y = 1, \tag{4.22}$$

$$M \left(q_y - \frac{\partial h}{\partial x} q_x \right) - \epsilon c v_n = -J_0 \text{ at } y = -1 + h, \tag{4.23}$$

In (4.23) the dimensionless flux into the aggregate is scaled by ϵ, so that $J = \epsilon J_0$, where J_0 is given by

$$J_0 = \chi_0 (c - \hat{c})^+ - \hat{\gamma}_0 (\tau - \hat{\tau}_0)^+ \mathcal{H}(h); \tag{4.24}$$

here χ_0 is the dimensionless flux coefficient, defined such that $\chi = \epsilon\chi_0$ where $\chi = \chi^*/u^*$; $\hat{c} = \tilde{c}^*/C$ is the dimensionless growth threshold; $\hat{\gamma}_0$ is the dimensionless erosion susceptibility defined such that $\hat{\gamma} = \epsilon^2\hat{\gamma}_0$ with $\hat{\gamma} = \gamma^*\mu_{\text{eff}}/R_{\text{mag}}C$; finally, $\hat{\tau}_0$ is the dimensionless erosion threshold defined such that $\hat{\tau} = \epsilon^{-1}\hat{\tau}_0$ with $\hat{\tau} = \tilde{\tau}^* R_{\text{mag}}/u^*\mu_{\text{eff}}$. The dimensionless aggregate growth velocity, derived from (2.31), is given by

$$v_n = \alpha_0 J_0 - \hat{\kappa}_0 h \text{ at } y = -1 + h, \tag{4.25}$$

where the dimensionless extravasation speed $\hat{\kappa}_0$ is defined such that $\hat{\kappa} = \epsilon\hat{\kappa}_0$ with $\hat{\kappa} = \kappa_1^* R_{\text{mag}}/u^*$. Similarly α_0 is the dimensionless aggregate conversion factor defined such that $\alpha = \epsilon\alpha_0$ with $\alpha = \alpha^*/C$.

The aggregate growth condition, derived from (2.30), is

$$\frac{\partial h}{\partial t} = M v_n. \tag{4.26}$$

Initially we have $c = 0$ in the channel and no aggregate, such that $h = 0$ at $t = 0$. All the dimensionless parameters together with their assumed orders are shown in Table 4.1.

We anticipate that in the small reduced Péclet number regime the leading-order cell concentration will be a function of x only. Hence before we analyse the system using asymptotics as $\epsilon \to 0$, we construct an integrated conservation equation for the stem cell concentration. We first integrate Eq. (4.16) between $y = -1 + h$ and $y = 1$, giving

$$\epsilon \int_{-1+h}^{1} \frac{\partial c}{\partial t} dy + \int_{-1+h}^{1} \frac{\partial q_x}{\partial x} dy + [q_y]_{y=-1+h}^{y=1} = 0. \tag{4.27}$$

Using the Leibnitz integral rule and the no-flux condition on the top of the channel, (4.22), we have the following

$$\epsilon \frac{\partial}{\partial t} \left(\int_{-1+h}^{1} c \, dy \right) + \frac{\partial}{\partial x} \left(\int_{-1+h}^{1} q_x \, dy \right) = \left[q_y - q_x \frac{\partial h}{\partial x} - \epsilon c \frac{\partial h}{\partial t} \right]_{y=-1+h}. \tag{4.28}$$

Using the definition of $\partial h/\partial t$ in (4.26), the boundary term on the right of (4.28) is equal to the flux into the moving aggregate, defined by (4.23). Inserting (4.23) into (4.28) therefore gives the final form of the integrated conservation equation, namely

$$\epsilon \frac{\partial}{\partial t} \left(\int_{-1+h}^{1} c \, dy \right) + \frac{\partial}{\partial x} \left(\int_{-1+h}^{1} \left(\left(u + \hat{\beta} u_m \right) c - \frac{\dot{\gamma}}{\epsilon \hat{P}e_{\mathrm{sh}}} \frac{\partial c}{\partial x} \right) dy \right) = -J_0, \tag{4.29}$$

where we have inserted the expression for the axial cell flux from (4.17) into (4.29). We now discuss the regimes of this model that we analyse in this chapter.

4.3 Delivery regimes

The delivery regimes can be characterised by considering dominant balances of the cell transport equation, (4.16), as the normalised magnetic field strength $\hat{\beta}$ and the reduced Péclet number, $\epsilon^3 \hat{P}e_{\mathrm{sh}}$, vary relative to ϵ.

We consider two asymptotic limits of the cell delivery problem: cell delivery when the reduced Péclet number is small and large. In both of these regimes, we assume that the magnetic velocity balances the fluid advection close to the magnet. In the small reduced Péclet number regime, the stem cell concentration is a function of the axial coordinate only, so that the richest dominant balance is most readily identified from the integrated conservation equation (4.29). To retain the effect of the magnetic force in the leading-order system, we balance the axial magnetic velocity with the axial fluid flow which requires $\hat{\beta} = O(1)$. In the large Péclet number regime we balance the vertical magnetic velocity with fluid advection, which is the same order in both axial and vertical directions in the cell transport equation, defined in (4.16)

Name	Reduced Param.	Definition	Value
Extravasation speed	$\hat{\kappa}_0$	$\hat{\kappa}/\epsilon$	0 - 1
Aggregate erosion susceptibility	$\hat{\gamma}_0$	$\hat{\gamma}/\epsilon$	0 - 1
Cell flux rate	χ_0	χ/ϵ	1
Aggregation threshold	$\hat{c}$	-	1.1
Erosion threshold	$\hat{\tau}_0$	$\epsilon\hat{\tau}$	2.2
Dimensionless channel half length	$\hat{L}$	-	5
Aggregate growth factor	α_0	$\epsilon\alpha^*/C$	1

Table 4.2: Model parameter values. Values of the normalised magnetic field strength and reduced Péclet number are listed in Section 4.6 and Section 4.7.

and (4.17). This balance requires $\hat{\beta} = O(\epsilon)$. The small Péclet number regime results in a one-dimensional advection-diffusion equation for cell concentration as a function of x and t, whereas the large Péclet number regime is a singular perturbation problem of the cell transport equation and results in a hyperbolic problem in the centre of the channel coupled to a boundary layer on the moving aggregate. The large reduced Péclet number case corresponds to the regime in Chapter 3, where the equivalent reduced Péclet number is $\epsilon^3\hat{P}e_{\text{sh}} \approx 10^7$ for 1% RBCs and $\epsilon^3\hat{P}e_{\text{sh}} \approx 10^4$ for 40% RBCs.

4.4 Parameter selection

In this chapter we use values of the reduced parameters listed with their definitions in Table 4.2. Values of the relative magnetic field and reduced Péclet number are listed in Section 4.6 and Section 4.7 respectively. Following our approach in Chapter 3 we set the erosion threshold to be 10% higher than the shear stress when there is no aggregate in the channel. Similarly we set the aggregation threshold to be 10% higher than the inlet level of stem cells. We choose the reduced cell flux coefficient χ_0 and α_0 to both equal one. We then vary the erosion strength and extravasation speed in both Section 4.6 and Section 4.7. We take the dimensionless length of the channel to be $\hat{L} = 5$, and using this length the magnetic field at the inlet is less than 1% of the strength it is at the centre of the channel.

We now consider the fluid mechanics in the channel which only depend on the stem cell concentration through the aggregate height h.

4.5 Fluid motion

We now expand fluid variables as follows

$$(u,\ v,\ p,\ v_n,\ h) \sim (u_0,\ v_0,\ p_0,\ v_{n0},\ h_0) + O(\epsilon) \text{ as } \epsilon \to 0. \tag{4.30}$$

Then Eqs. (4.7) - (4.9) give us the following system of equations to leading-order

$$\frac{\partial u_0}{\partial x} + \frac{\partial v_0}{\partial y} = 0, \tag{4.31}$$

$$\frac{\partial^2 u_0}{\partial y^2} = \frac{\partial p_0}{\partial x}, \tag{4.32}$$

$$\frac{\partial p_0}{\partial y} = 0, \tag{4.33}$$

for $|x| < \hat{L}$ and $-1 + h_0 < y < 1$. The leading-order boundary conditions, derived from (4.12) - (4.15), are

$$u_0 = (1 - y^2),\ v_0 = 0 \quad \text{at } x = -\hat{L}, \tag{4.34}$$

$$p_0 = 0,\ v_0 = 0 \quad \text{at } x = \hat{L}, \tag{4.35}$$

$$u_0 = 0,\ v_0 = 0 \quad \text{at } y = 1, \tag{4.36}$$

$$u_0 = 0,\ v_0 = 0 \quad \text{at } y = -1 + h_0, \tag{4.37}$$

In the long, thin regime the normal vector to the aggregate, defined in (4.10), is equal to $\boldsymbol{j}$ at leading-order. Hence the normal growth of the aggregate drives a vertical fluid velocity, hence $v_0 = 0$ on the aggregate in (4.37) because $v_n = O(\epsilon^2)$.

By (4.33), the leading-order pressure is a function of axial position only. Hence we can solve (4.32) to determine that the axial flow is parabolic between the moving aggregate boundary and the top of the channel, given by

$$u_0 = \frac{1}{2}\frac{\partial p_0}{\partial x}(y - h_0 + 1)(y - 1). \tag{4.38}$$

The leading-order pressure can be determined by integrating the continuity equation, (4.31), between $y = -1 + h_0$ and $y = 1$ and applying the no-flux boundary conditions (4.36) and (4.37) to arrive at Reynolds equation,

$$\frac{\partial}{\partial x}\left((2 - h_0)^3 \frac{\partial p_0}{\partial x}\right) = 0. \tag{4.39}$$

The inlet velocity condition, (4.34), supplies the boundary condition for the pressure gradient at the inlet, requiring

$$\frac{\partial p_0}{\partial x} = -2 \text{ at } x = -\hat{L}. \tag{4.40}$$

This gives us the following leading-order solution for the axial pressure gradient

$$\frac{\partial p_0}{\partial x} = -\frac{16}{(2-h_0)^3}. \tag{4.41}$$

Only the axial pressure gradient is required to determine the leading-order axial velocity in (4.38), so we do not need to solve for p_0. The vertical velocity can then be found by integrating Eq. (4.31) with respect to y, giving

$$v_0 = \frac{1}{2}\frac{\partial p_0}{\partial x}\frac{\partial h_0}{\partial x}y(y-2) - \frac{\partial^2 p_0}{\partial x^2}\left(-2y^2 - 3h_0 y + 6 + 6h_0\right) - \frac{16(h_0-1)}{(2-h_0)^4}\frac{\partial h_0}{\partial x}, \tag{4.42}$$

where the final term is the 'constant of integration' which is found by prescribing boundary conditions $v_0 = 0$ on $y = 1$ or $y = -1 + h_0$. We note that, since $v_0 = O(1)$ we require the axial gradient of the aggregate surface to be at most of $O(1)$.

4.6 Small reduced Péclet number delivery

We now consider cell transport when the reduced Péclet number is small, so that vertical diffusive forces dominate cell transport in (4.16). We consider the fullest balance where the magnetic and fluid velocities balance in the axial direction and axial shear-induced diffusion is present in the leading-order integrated conservation equation (4.29). Hence we define $\epsilon^3 \hat{Pe}_{\mathrm{sh}} = \epsilon^2 Pe_0$ where Pe_0 is $O(1)$ and we fix $\hat{\beta} = O(1)$.

We now determine the leading-order cell concentration in this regime by considering an asymptotic expansion for the cell concentration as follows

$$c = c_0 + O(\epsilon). \tag{4.43}$$

The asymptotic expansion of the shear rate $\dot{\gamma}$, can be determined by inserting our known velocity solutions, (4.38) and (4.42), into (4.18). Hence, the leading-order component of the shear rate, $\dot{\gamma}_0$, is

$$\dot{\gamma}_0 = \left|\frac{\partial u_0}{\partial y}\right| = \left|\frac{\partial p_0}{\partial x}\left(y - \frac{h_0}{2}\right)\right|. \tag{4.44}$$

Considering the cell transport equation, Eq. (4.16), diffusion in the vertical direction would appear to dominate. However, the leading-order shear rate is a linear function of y and in the region close to the centre of the channel, where $|y - h_0/2| = O(\epsilon)$, the shear rate is $O(\epsilon)$. Hence we should consider this region, separately. Considering first the region $|y - h_0/2| = O(1)$, at leading-order (4.16) gives

$$\frac{\partial}{\partial y}\left(\dot{\gamma}_0 \frac{\partial c_0}{\partial y}\right) = 0, \tag{4.45}$$

with boundary conditions, derived from (4.22) and (4.23), given by

$$\frac{\partial c_0}{\partial y} = 0 \text{ at } y = 1 \text{ and } y = -1 + h_0. \tag{4.46}$$

It follows that leading-order the cell concentration is independent of y, i.e. $c_0 = c_0(x,t)$ in this region, perhaps with different values for $y > 0$ and $y < 0$.

We now consider the central region, $|y - h_0/2| < \epsilon$, defining the boundary layer variable

$$\tilde{y} = \frac{y - h_0/2}{\epsilon} \tag{4.47}$$

such that $\tilde{y} = O(1)$ in the centre of the channel. In this region, the shear rate is of $O(\epsilon)$, so we write $\dot{\gamma} = \epsilon\tilde{\gamma}$ with $\tilde{\gamma} = O(1)$. Defining the cell concentration in this region as $\tilde{c}$, the stem cell transport equation (4.16) is then

$$\epsilon\frac{\partial \tilde{c}}{\partial t} + \frac{\partial}{\partial x}\left(\left(u + \hat{\beta}u_m\right)\tilde{c} - \frac{\epsilon\tilde{\gamma}}{Pe_0}\frac{\partial \tilde{c}}{\partial x}\right) + \frac{\partial}{\partial \tilde{y}}\left(\left(\frac{v}{\epsilon} + \frac{\hat{\beta}}{\epsilon}v_m\right)\tilde{c} - \frac{\tilde{\gamma}}{\epsilon^3 Pe_0}\frac{\partial \tilde{c}}{\partial \tilde{y}}\right) = 0. \tag{4.48}$$

We see that the vertical diffusive forces still dominate in this region: the leading-order version of (4.48) is

$$\frac{\partial}{\partial \tilde{y}}\left(\tilde{\gamma}_0\frac{\partial \tilde{c}_0}{\partial \tilde{y}}\right) = 0, \tag{4.49}$$

where $\tilde{\gamma}_0$ is the leading-order shear rate in this region. Matching with the outer regions of the channel, we require $\partial\tilde{c}_0/\partial\tilde{y} \to 0$ as $\tilde{y} \to \pm\infty$. This is satisfied by $\partial\tilde{c}_0/\partial\tilde{y} = 0$ in this central region. We conclude that the leading-order stem cell concentration is independent of y throughout the channel.

We now use the conservation equation determined in Section 4.2, Eq. (4.29), to determine the governing equation for $c_0(x,t)$. We substitute our known leading-order components for the fluid and magnetic velocities, namely (4.38) and (4.19), and since the cell concentration is independent of y at leading-order, it can be removed from all integrals. This gives the following quasi-steady advection-diffusion equation for c_0

$$\frac{\partial}{\partial x}\left(c_0\eta_0\left(\overline{u_0} + \hat{\beta}\overline{u_{m0}}\right) - \frac{\eta_0\overline{\dot{\gamma}_0}}{Pe_0}\frac{\partial c_0}{\partial x}\right) = -J_0, \tag{4.50}$$

where $\eta_0 = 2 - h_0$ is the channel thickness, and the width-averaged quantities, defined by variables with bars, are as follows

$$\overline{u_{m0}} = \frac{1}{\eta_0}\int_{-1+h_0}^{1} u_{m0}\, dy \quad = \frac{-x}{(1+x^2)^2}, \tag{4.51}$$

$$\overline{u_0} = \frac{1}{\eta_0}\int_{-1+h_0}^{1} u_0\, dy \quad = \frac{4}{3\eta_0} \tag{4.52}$$

$$\overline{\dot{\gamma}_0} = \frac{1}{\eta_0}\int_{-1+h_0}^{1} \left|\frac{\partial u_0}{\partial y}\right| dy = \frac{4}{\eta_0^2}. \tag{4.53}$$

In Eq. (4.50), J_0 is given by

$$J_0 = \chi_0(c_0 - \hat{c})^+ - \hat{\gamma}_0\,(\tau_0 - \hat{\tau}_0)^+\,\mathcal{H}(2-\eta_0), \tag{4.54}$$

and the wall shear stress on the aggregate is

$$\tau_0 = \frac{8}{\eta_0^2}, \tag{4.55}$$

which follows from the leading order axial flow, (4.38). The advection-diffusion equation for c_0, Eq. (4.50), is subject to boundary conditions which are derived from (4.20) and (4.21), as follows

$$c_0 = 1 \text{ at } x = -\hat{L}, \tag{4.56}$$

$$\frac{\partial c_0}{\partial x} = 0 \text{ at } x = \hat{L}. \tag{4.57}$$

The system for c_0 and the channel width η_0 is then defined by Eq. (4.50), fluid solutions (4.38) and (4.41) and the growth condition, (4.26), which determines the change in channel width as a function of cell concentration, and given by

$$\frac{\partial \eta_0}{\partial t} = -\alpha_0\left(\chi_0(c_0-\hat{c})^+ - \hat{\gamma}_0\left(\frac{8}{\eta_0^2} - \hat{\tau}_0\right)^+\mathcal{H}(2-\eta_0)\right) + \hat{\kappa}_0(2-\eta_0), \tag{4.58}$$

with $\eta_0 = 2$ at $t = 0$.

We now detail our numerical method for solving (4.50) and (4.58), and then explore the stem cell delivery in this regime for varying the normalised magnetic field strength $\hat{\beta}$, erosion strength γ_0 and extravasation speed κ_0.

4.6.1 Numerical solution

To numerically solve the quasi-steady cell transport equation Eq. (4.50) coupled to the PDE for channel width at each point, Eq. (4.58), we first use a first-order spatial

finite difference scheme to approximate Eq. (4.50) at each spatial point, but leave the time coordinate as continuous. We use $N = 400$ grid points in the spatial dimension. We solve (4.50) and (4.58) using MATLAB's ODE solver *ode15s*. We use the inbuilt "Events" functionality within MATLAB's ODE toolbox to terminate the integration when either i) the maximum aggregate height reaches 40% of the channel width, ii) the maximum rate of change of the aggregate is less than 10^{-9} so that we consider the solution to have reached steady state or iii) when we reach the final time point $t = 1000$. We validate the convergence of this scheme spatially and temporally in Appendix B.2.1.

In this section we use $Pe_0 = 1$ and consider a range of normalised magnetic field strengths $\hat{\beta} = 0 - 3$. All other parameters are listed in Table 4.2.

4.6.2 Stem cell delivery dynamics

We now examine two examples of stem cell delivery. Firstly, when there is no erosion or extravasation, then when aggregate erosion is present. These examples illustrate the two key behaviours of the model: when aggregation leads to a highly occluded channel in the absence of erosion or extravasation, and the potential for aggregate growth to be limited by erosion and (or) extravasation, which can result in a steady state aggregate.

Fig. 4.1a shows the leading-order stem cell concentration (top) and the aggregate height (bottom). The leading-order stem cell concentration builds up over the magnet and the aggregate of cells grows until the maximum height reaches 40% of the channel width (corresponding to $h_0 = 0.8$), which is a termination condition of the numerical solver. This occurs at $t = 9.3$. Fig. 4.1b shows stem cell capture when erosion is present, which significantly alters the aggregate shape. Initially, the aggregate grows and obstructs the channel above the centre of the magnet at $x = 0$. At later times, newly arriving cells join on the downstream face of the aggregate, avoiding the larger flow rates on the peak of the aggregate. This leads to a broad, flat aggregate. This simulation reaches a steady state at $t = 590$ at which point the aggregate occupies the whole region where the magnetic field strength is large enough for the stem cell concentration to exceed $\hat{c}$.

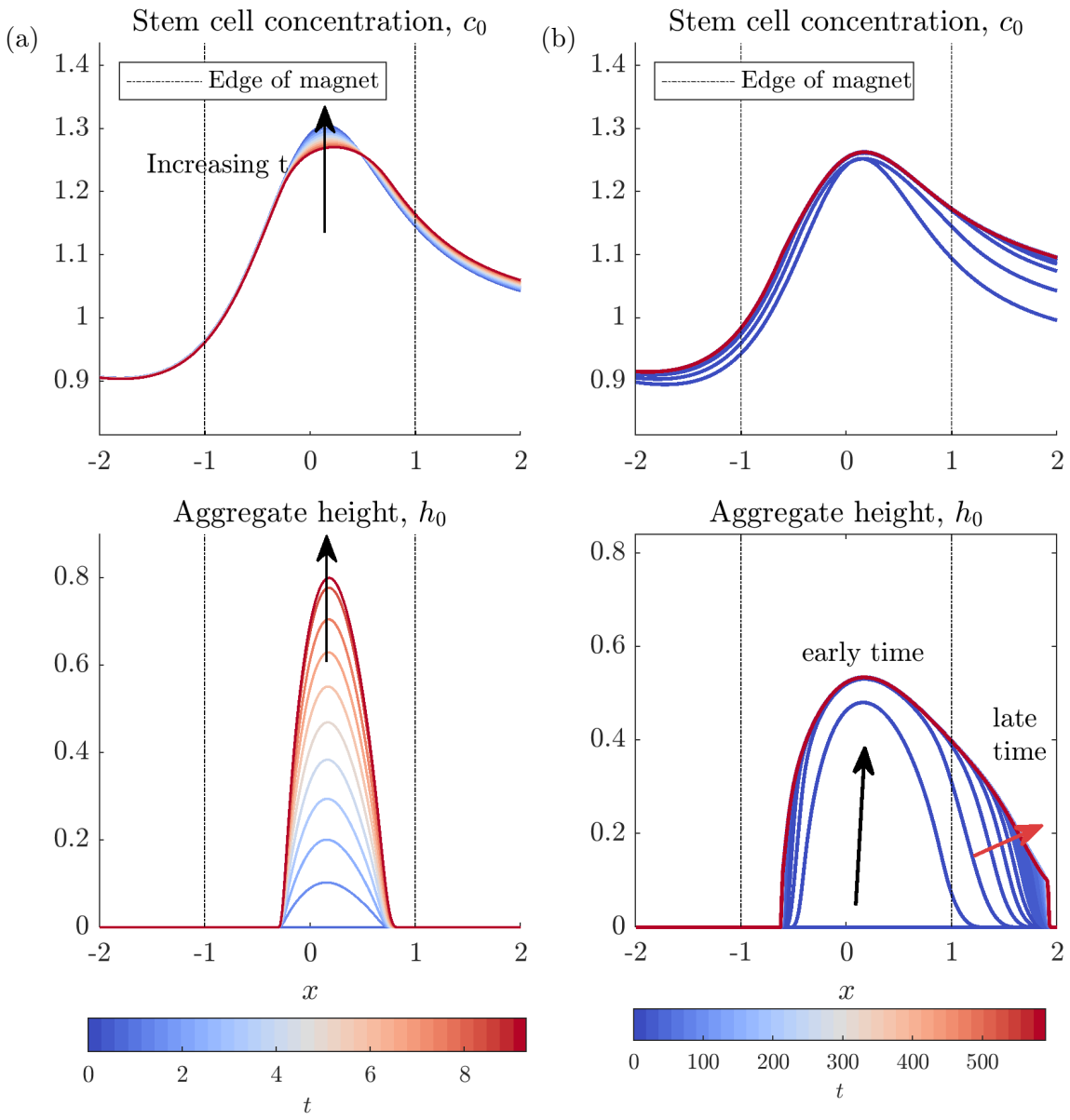

Figure 4.1: a) Stem cell capture with no erosion and no extravasation. The leading-order stem cell concentration builds up over the magnet and the aggregate of cells grows until the maximum aggregate height reaches 40% of the channel width, $h_0 = 0.8$, at which the simulation terminates. Parameter values: $\hat{\beta} = 1$, $\hat{\gamma}_0 = 0$, $\hat{\kappa}_0 = 0$ and all others as in Table 4.2. b) Stem cell capture when erosion is present. Initially the aggregate grows and obstructs the channel closest to the magnet, and at later times the aggregated cells spread out, avoiding the larger flow rates in the centre of the channel. Parameter values: $\hat{\beta} = 1$, $\hat{\gamma}_0 = 0.1$, $\hat{\kappa}_0 = 0$ and all others as in Table 4.2. The line colour indicates the time, shown for each case by the colour bars, arrows indicate the direction of increasing time.

4.6.3 Exploring safe parameter regimes

Motivated by the two different behaviours presented in the previous section, we now explore the interplay between the two aggregation limiting mechanisms, erosion and extravasation, and the normalised magnetic field strength. Therapeutically, regimes where the aggregate significantly occludes the channel are potentially dangerous, as blood flow will be restricted to downstream areas of the vasculature and there is a risk of the fracture of the stem cell aggregate. There are a number of interesting mathematical problems involved in determining which parameter regimes could lead to a steady state aggregate height using our mathematical model. However, we note that since our model neglects to include the internal structure of the clot, our model cannot predict fracture. As a result, despite the fact that the lubrication model we have developed is valid for very large values of aggregate height, its relevance to the physical system will diminish as the channel approaches occlusion. Hence in this analysis we take a pragmatic approach and fix a threshold of occlusion at 40% and then determine which parameter regimes the maximum aggregate height exceeds this threshold.

The maximum cell concentration and aggregate height are shown in Fig. 4.2a and b, respectively, for a range of normalised magnetic field strengths and extravasation strengths. The shaded grey region illustrates regimes where the aggregate reaches 40% of the channel width. As illustrated in Fig. 4.2b, for $\hat{\beta} < 0.1$ no aggregation occurs as the magnetic field strength is not sufficiently large that the stem cell concentration exceeds the aggregation threshold $\hat{c} = 1.1$. It is clear that increasing extravasation speed reduces the maximum aggregate height, as was noted in the previous chapter.

Fig. 4.3 shows the maximum cell concentration (4.3a) and aggregate height (4.3b) for a range of normalised magnetic field strengths and erosion strengths. Again, the grey region shows where the aggregate reaches 40% of the channel width, demonstrating that erosion is also able to limit aggregation. Comparing Figs. 4.2 and 4.3, extravasation requires a larger extravasation speed $\hat{\kappa}_0$ to have the same effect as erosion in reducing aggregation. This is because extravasation is proportional to $2 - h_0$ and erosion is proportional to $8/(2 - h_0)$. Hence when $h_0 = 0.8$ erosion is five times larger than extravasation.

For both effects, we can determine a line of best fit between the normalised magnetic field strength $\hat{\beta}$ and the erosion or extravasation strengths that defines the boundary of the unsafe regions in Figs. 4.2 and 4.3. We find that the boundary of the region with high occlusion is defined by $\hat{\beta} \sim \hat{\kappa}_0^{0.63}$ in Fig. 4.2, such that if the extravasation speed is doubled, we are able to increase the magnetic field strength

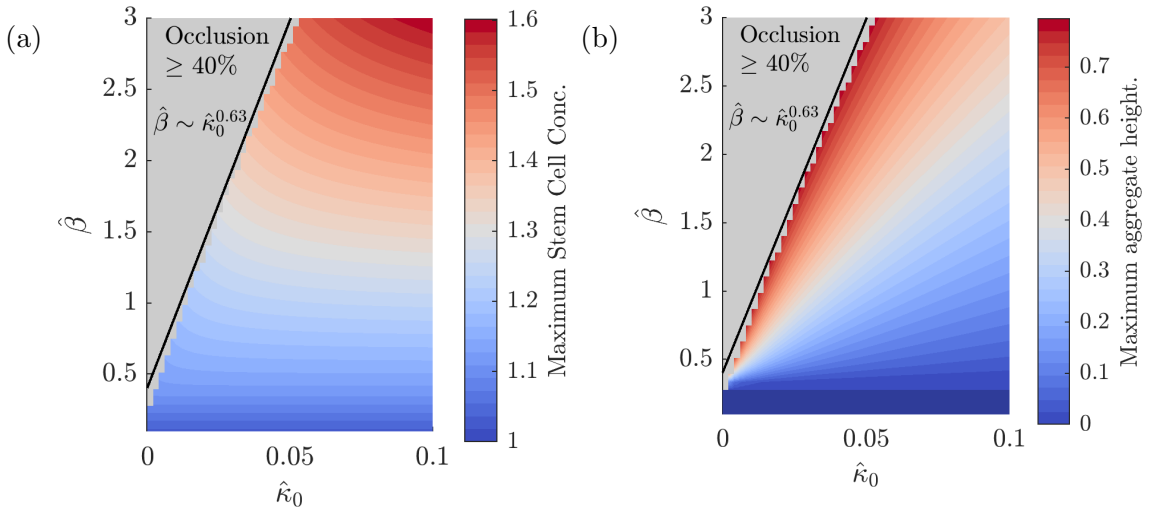

Figure 4.2: Evaluation of (a) maximum stem cell concentration in the channel and (b) aggregate height for varying normalised magnetic field strength $\hat{\beta}$ and extravasation speed $\hat{\kappa}_0$. The grey region is where the aggregate reaches 40% of the channel width when simulations are terminated. The edge of the occluded region is shown by the black line of best fit with fitting exponent shown as $\hat{\beta} = \hat{\kappa}_0^{0.64}$.

by a factor of 1.5. Similarly we find that the high occlusion region in the Fig. 4.3 is defined by $\hat{\beta} \sim \hat{\gamma}_0^{0.65}$. These fittings are specific to an occlusion level of 40%, it would be interesting to understand the exponent in these fittings and determine how it depends on system parameters and if the value of the exponent varies at other levels of occlusion (future work). Overall, this demonstrates how the model could be used to identify safe values of the magnetic field strength to keep aggregation under a desired threshold if the extravasation speed or erosion strength are known.

4.7 Large reduced Péclet number delivery

We now consider large reduced Péclet number delivery, with $\epsilon^3 \hat{Pe}_{\text{sh}} \gg 1$ so that diffusion is subdominant to the fluid and magnetic advection. We choose $\hat{\beta} = O(\epsilon)$ to balance the vertical magnetic velocity with the fluid flow in the cell transport equation, given by (4.16) and (4.17). We choose to consider the case in which the reduced Péclet number is of $O(\epsilon^{-1})$ to simplify the scalings. For clarity we define $\hat{\beta} = \epsilon\hat{\beta}_0$ and $\epsilon^3 \hat{Pe}_{\text{sh}} = \epsilon^{-1} Pe_0$, where $\hat{\beta}_0$ and Pe_0 are of $O(1)$. Using these parameter definitions, Eq. (4.16) becomes

$$\epsilon\frac{\partial c}{\partial t} + \frac{\partial}{\partial x}\left(\left(u + \epsilon\hat{\beta}_0 u_m\right)c - \frac{\epsilon^3\dot{\gamma}}{Pe_0}\frac{\partial c}{\partial x}\right) + \frac{\partial}{\partial y}\left(\left(v + \hat{\beta}_0 v_m\right)c - \frac{\epsilon\dot{\gamma}}{Pe_0}\frac{\partial c}{\partial y}\right) = 0. \quad (4.59)$$

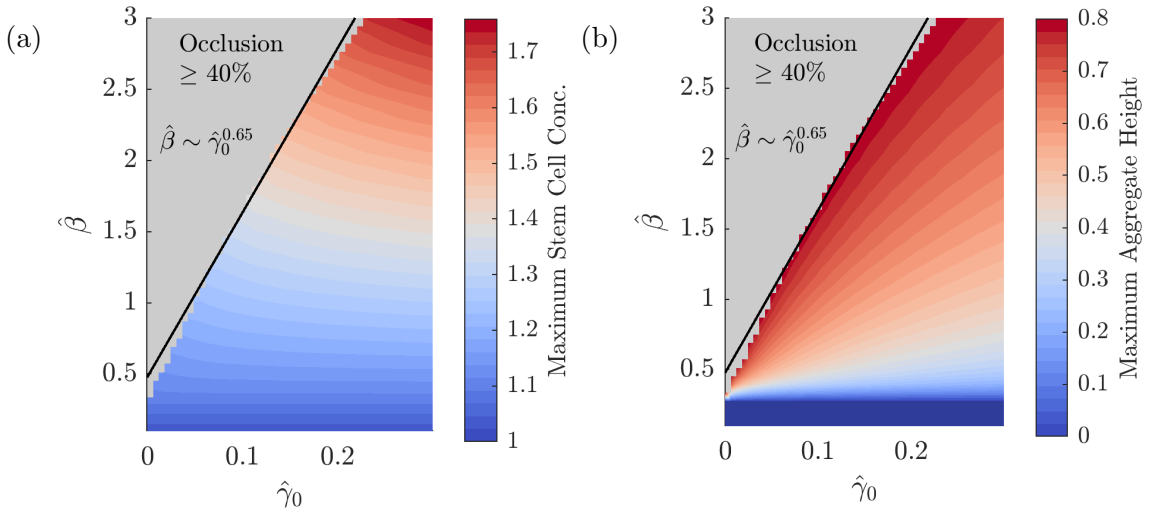

Figure 4.3: Evaluation of (a) maximum stem cell concentration in the channel and (b) aggregate height for varying normalised magnetic field strength $\hat{\beta}$ and erosion strength $\hat{\gamma}_0$. The grey region is where the aggregate reaches 40% of the channel width when simulations are terminated. The edge of the occluded region is shown by the black line of best fit with fitting exponent shown as $\hat{\beta} = \hat{\gamma}_0^{0.65}$

Since diffusion is subdominant in this regime, this leads to a singular perturbation problem for the cell concentration. We have a region in the channel away from the walls where cells are transported by advection alone, which we refer to as the outer region. This is coupled to a boundary layer on the growing aggregate. As in Richardson et al. [92], the outer region is split by the trajectory of cells from the top of the inlet. This trajectory divides the boundary layer as it joins the base of the channel, as illustrated in Figure 4.4. We note that there will be an interior boundary layer around the dividing trajectory in which diffusion acts to smooth the discontinuity in the leading-order equations. However, we do not analyse this boundary layer in this chapter as we can analyse the aggregate growth without it. We proceed by examining the outer region and then the boundary layer. Boundary layer variables are denoted with capital letters.

4.7.1 Outer region: main channel

The outer region makes up the majority of the channel, where $y = O(1)$ and $x = O(1)$. In this region, we asymptotically expand the cell concentration as follows $c = c_0 + O(\epsilon)$ as $\epsilon \to 0$ so that Eq. (4.59) yields the following leading-order equation

$$\frac{\partial}{\partial x}(u_0 c_0) + \frac{\partial}{\partial y}\left(\left(v_0 + \hat{\beta}_0 v_{m0}\right) c_0\right) = 0, \tag{4.60}$$

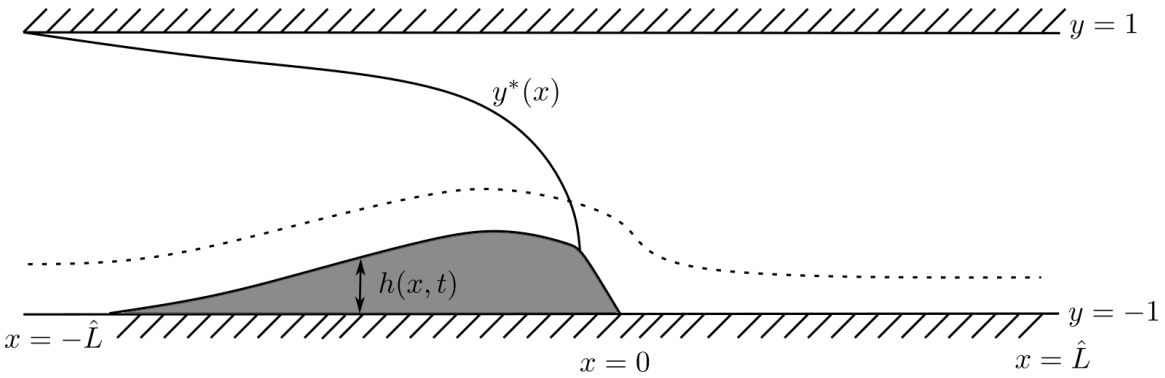

Figure 4.4: Asymptotic regions for the large reduced Péclet delivery regime. The outer region of the channel is split by the dividing characteristic $y = y^*(x)$ and we have a boundary layer on the growing aggregate, illustrated by the dashed line.

where the leading-order vertical magnetic velocity, derived from (4.19), is given by

$$v_{m0} = \frac{-1}{(x^2+1)^2}. \tag{4.61}$$

Since the leading-order vertical magnetic velocity is independent of y, and the leading-order flow is incompressible according to (4.31), we can reformulate (4.60) into the non-conservative form

$$u_0 \frac{\partial c_0}{\partial x} + \left(v_0 + \hat{\beta}_0 v_{m0}\right) \frac{\partial c_0}{\partial y} = 0. \tag{4.62}$$

We note that $(u_0, v_0 + \hat{\beta}_0 v_{m0})$ points into the domain on $x = -\hat{L}$ and $y = 1$ and out of the domain on $x = -\hat{L}$ and $y = -1 + h_0$ (as shown in Fig. 4.5 for $h_0 = 0$). The boundary condition (4.20), implies that

$$c_0 = 1 \text{ at } x = -\hat{L}, \text{ for } -1 + h_0 < y < 1. \tag{4.63}$$

The top wall at $y = 1$ yields the other boundary condition for (4.62), namely that $c_0 = 0$ at $y = 1$, for $|x| < \hat{L}$. This is shown in Appendix C. Using our leading-order fluid solutions, we can determine the characteristics of (4.62). These are equivalent to the trajectories followed by the cells. The equations of these characteristics $y(x)$ are given by

$$\frac{dy}{dx} = \frac{v_0 + \hat{\beta}_0 v_{m0}}{u_0}. \tag{4.64}$$

The value of c_0 is preserved along each characteristic, so that the region spanned by the characteristics from the inlet have $c_0 = 1$, while all regions spanned by the the

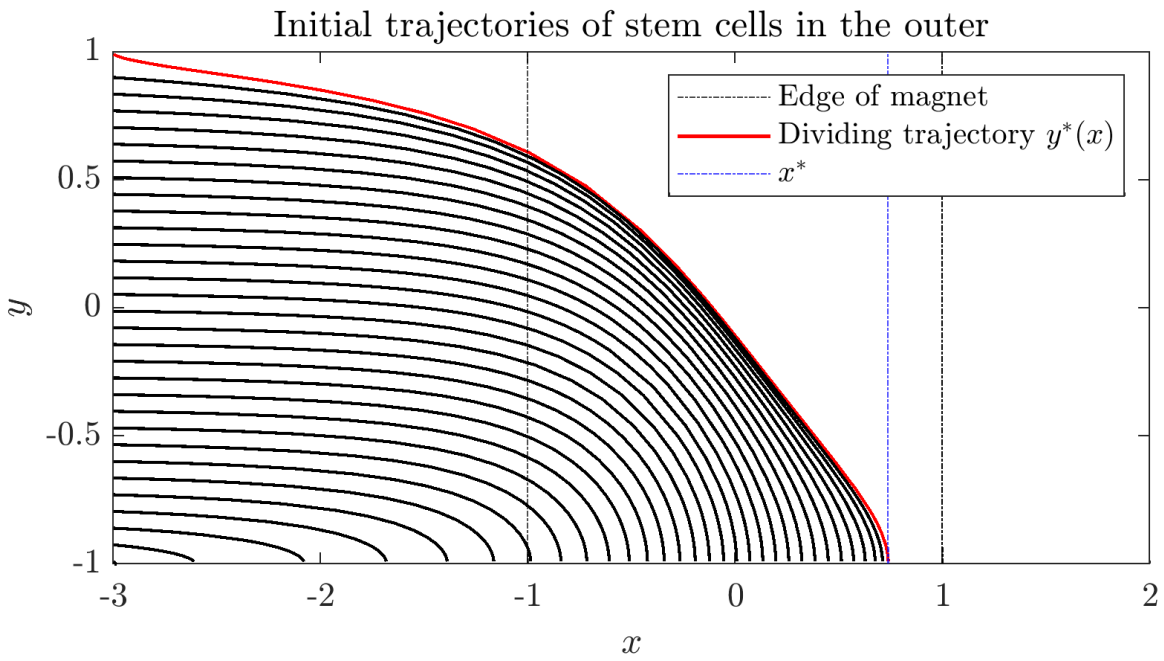

Figure 4.5: Trajectories of the stem cells from the inlet. Example trajectories are shown in black, the dividing trajectory is shown in red. The point where the dividing characteristic meets the boundary layer, x^*, is marked in blue. Parameters: $\hat{\beta}_0 = 1$.

characteristics from the top of the channel have $c_0 = 0$. We note that the characteristics will vary over time as the aggregate grows and the fluid velocity components are altered.

We can define the region reached by the cells from the inlet by defining a dividing characteristic $y^*(x)$ as the characteristic which propagates from $y = 1$, $x = -\hat{L}$. Hence for all (y, x) above $y^*(x)$, $c_0 = 0$ and below $y^*(x)$, we have $c_0 = 1$. The dividing characteristic defines the region where the cells are entering the boundary layer on the aggregate interface. We define x^* as the point where this dividing trajectory meets the start of the boundary layer, defined by

$$y^*(x^*) = -1 + h_0(x^*). \tag{4.65}$$

Hence points on the boundary layer with $x > x^*$ will have no flux of cells from the outer. To demonstrate an example of the dynamics we solve the ODE (4.64) numerically using MATLAB's *ode15s* solver for the initial trajectories when $h_0 = 0$, are shown in Fig. 4.5. The dividing trajectory is shown in red. All cells have landed by $x^* = 0.78$, which is just past the centre of the magnet at $x = 0$.

4.7.2 Boundary layer

In this section we examine the boundary layer on the growing aggregate. We consider a change of variables into boundary layer coordinates (X, Y, T) defined as follows

$$X = x, \quad Y = \frac{y + 1 - h(x,t)}{\delta}, \quad T = t. \tag{4.66}$$

Here δ is the thickness of the boundary layer, which we will determine to be ϵ in this section. We can define the aggregate height in the boundary layer as $h(x,t) = H(X,T)$. Then using (4.66), partial derivatives transform as follows

$$\frac{\partial}{\partial x} = \frac{\partial}{\partial X} - \frac{1}{\delta}\frac{\partial H}{\partial X}\frac{\partial}{\partial Y}, \tag{4.67}$$

$$\frac{\partial}{\partial t} = \frac{\partial}{\partial T} - \frac{1}{\delta}\frac{\partial H}{\partial T}\frac{\partial}{\partial Y}, \tag{4.68}$$

$$\frac{\partial}{\partial y} = \frac{1}{\delta}\frac{\partial}{\partial Y}. \tag{4.69}$$

Here we note that the derivatives with respect to Y in (4.67) and (4.68) are promoted proportional to δ^{-1}. This is because we have assumed that the aggregate height is the same order as the channel width.

Since we do not have a boundary layer in the fluid solutions, we can use the known leading-order fluid solutions to determine the order of the fluid velocities in the boundary layer, U_0 and V_0. Substituting (4.66) into Eqs. (4.38) and (4.42) and Taylor expanding about $Y = 0$, gives $u_0 \sim \delta U_0$ and $v_0 \sim \delta V_0$ where

$$U_0 = \frac{Y}{2}\frac{\partial P_0}{\partial X}, \tag{4.70}$$

$$V_0 = \frac{Y}{2}\frac{\partial H_0}{\partial X}\frac{\partial P_0}{\partial X}. \tag{4.71}$$

Hence in the boundary layer, both the axial and vertical fluid velocities are $O(\delta)$. This differs from boundary layer analysis on flat boundaries (i.e. $H_0 = 0$) where the vertical velocity is of $O(\delta^2)$. However we note that the normal velocity to the boundary is of $O(\delta\epsilon)$, with the power of ϵ arising from our lubrication scaling, which reflects the flat boundary case.

We now consider the cell transport dynamics. We define the cell concentration and shear rate in the boundary layer as $c(x,y,t) = C(X,Y,T)$ and $\dot{\gamma}(x,y,t) = \dot{\Gamma}(X,Y,T)$. Since the fluid components are both $O(\delta)$ in the boundary layer we use $\delta\boldsymbol{U}$ to denote the velocity in the boundary layer where $\boldsymbol{U} = (U_0, V_0) + O(\delta)$. Hence the cell transport equation (4.59) in this region is

$$\epsilon\frac{\partial C}{\partial T}-\frac{\epsilon}{\delta}\frac{\partial H}{\partial T}\frac{\partial C}{\partial Y}+\left(\frac{\partial}{\partial X}-\frac{1}{\delta}\frac{\partial H}{\partial X}\frac{\partial}{\partial Y}\right)Q_X+\frac{\partial Q_Y}{\partial Y}=0, \tag{4.72}$$

where the cell flux components are defined by

$$Q_X=\left(\delta U+\epsilon\hat{\beta}_0U_m\right)C-\frac{\epsilon^3\dot{\Gamma}}{Pe_0}\left(\frac{\partial C}{\partial X}-\frac{1}{\delta}\frac{\partial H}{\partial X}\frac{\partial C}{\partial Y}\right) \tag{4.73}$$

$$Q_Y=\left(V+\frac{\hat{\beta}_0}{\delta}V_m\right)C-\frac{\epsilon\dot{\Gamma}}{\delta^2Pe_0}\frac{\partial C}{\partial Y}. \tag{4.74}$$

The shear rate in the boundary layer $\dot{\Gamma}$ is defined by

$$\dot{\Gamma}=\left(\left(\frac{\partial U}{\partial Y}+\epsilon^2\delta\frac{\partial V}{\partial X}-\epsilon^2\frac{\partial H}{\partial X}\frac{\partial V}{\partial Y}\right)^2+2\epsilon^2\left(\delta\frac{\partial U}{\partial X}-\frac{\partial H}{\partial X}\frac{\partial U}{\partial Y}\right)^2+2\epsilon^2\left(\frac{\partial V}{\partial Y}\right)^2\right)^{1/2}, \tag{4.75}$$

which remains the same order as in the outer region. The boundary layer magnetic velocity components are

$$U_m=\frac{-X}{((\epsilon\left(\delta Y+1-H\right)+\epsilon+1)^2+X^2)^2}, \tag{4.76}$$

$$V_m=\frac{-(\epsilon\left(\delta Y+1-H\right)+\epsilon+1)}{((\epsilon\left(\delta Y+1-H\right)+\epsilon+1)^2+X^2)^2}. \tag{4.77}$$

The boundary condition on the aggregate, (4.23) becomes

$$M\left(Q_Y-\frac{\partial H}{\partial X}Q_x\right)-\epsilon CV_n=-J_0 \text{ at } Y=0. \tag{4.78}$$

To balance vertical diffusion with the vertical magnetic advection in (4.72) we require $\delta=\epsilon$. Since we have an $O(1)$ flux J_0 we have a balance of flux in (4.78) at leading-order. Hence the stem cell concentration will remain $O(1)$ in the boundary layer and we can expand the cell concentration as $C=C_0+O(\epsilon)$ as $\epsilon\to 0$. The leading-order problem for C_0 then is given by

$$\frac{\partial}{\partial Y}\left(\hat{\beta}_0V_{m0}C_0-\frac{\dot{\Gamma}_0}{Pe_0}\frac{\partial C_0}{\partial Y}\right)=0, \tag{4.79}$$

for $Y\geq 0$, where the leading-order magnetic velocity and shear rate are given by

$$V_{m0}=\frac{-1}{(X^2+1)^2},\quad \dot{\Gamma}_0=\frac{1}{2}\frac{\partial P_0}{\partial X}. \tag{4.80}$$

We solve (4.79) subject to the boundary conditions and matching conditions given by

$$\left(\hat{\beta}_0 V_{m0} C_0 - \frac{\dot{\Gamma}_0}{Pe_0}\frac{\partial C_0}{\partial Y}\right) = \chi_0 (C_0 - \hat{c})^+ - \hat{\gamma}_0 \left(\tau_0 - \hat{\tau}_0\right)^+ \mathcal{H}(h_0), \text{ at } Y = 0, \tag{4.81}$$

$$C_0 \to c_0(X,T) \text{ as } Y \to \infty, \tag{4.82}$$

where we match with the leading-order outer solution $c_0(X,T)$ in (4.82), since the stem cell concentration is of $O(1)$ in the boundary layer. The outer solution $c_0(X,T)$ is given by

$$c_0(X,T) = \begin{cases} 1 \text{ for } X < x^*(T), \\ 0 \text{ for } X > x^*(T). \end{cases} \tag{4.83}$$

The solution to Eq. (4.79) is then

$$C_0(X,Y,T) = c_0(X,T) + A(X,T)\exp\left(-\frac{\hat{\beta}_0 Pe_0 |V_{m0}|}{\dot{\Gamma}_0} Y\right), \tag{4.84}$$

where $A(X,T)$ can, in principle, be found from the flux boundary condition (4.81), which gives

$$\hat{\beta}_0 V_{m0} c_0 = \chi_0 (c_0 + A - \hat{c})^+ - \hat{\gamma}_0 \left(\tau_0 - \hat{\tau}_0\right)^+ \mathcal{H}(h_0) = J_0. \tag{4.85}$$

We note that our constitutive relation for cell flux into the aggregate requires that we only have growth if $c_0 + A > \hat{c}$. If $c_0 + A \leq \hat{c}$ then we cannot satisfy (4.85), in this case we would have no flux into the boundary layer. This would ensure that the solution accumulates in the boundary layer and the leading order system would differ from (4.79). In this section we set $\hat{c} = 0$ so that we are always in the regime where we have a solution defined by (4.85).

In the case that $\hat{c} = 0$, we have the following solution for the leading-order cell concentration in the boundary layer

$$C_0(X,Y) = c_0 + \left(\frac{\hat{\beta}_0 c_0 V_{m0}}{\chi_0} + c_0 + \hat{\gamma}_0 \left(\tau_0 - \hat{\tau}\right)^+ \mathcal{H}(h)\right)\exp\left(-\frac{\hat{\beta}_0 Pe_0 |V_{m0}|}{\dot{\Gamma}_0} Y\right), \tag{4.86}$$

where c_0 is the outer solution, defined in (4.83). Examining (4.85), we can see that the flux into the aggregate is equal to the flux from the outer $J_0 = c_0 \hat{\beta}_0 V_{m0}$. This yields the growth condition from (4.25), with

$$\frac{\partial \eta_0}{\partial t} = -\alpha_0 c_0 \hat{\beta}_0 V_{m0} + \hat{\kappa}_0 (2 - \eta_0). \tag{4.87}$$

It is useful to note that since the flux from the outer region is equal to the flux into the aggregate, erosion does not alter aggregate growth, it only alters the stem cell concentration in the boundary layer according to (4.86). Hence the only mechanism which is able to limit aggregate growth in this regime is extravasation, which is present in (4.87). We now present our numerical scheme for solving the leading-order system given by (4.64) and (4.87).

4.7.3 Numerical solution

At the top of the inlet, there will be a boundary layer of thickness ϵ, which is required to satisfy the no flux condition on the cell concentration on the top of the channel. We do not analyse this boundary layer, instead we approximate the region where the cells from the top of the inlet reach by defining a dividing characteristic $y^*(x)$ as the characteristic which propagates from $y = 1,\ x = -\hat{L}$. Hence for all (y, x) above $y^*(x)$, $c_0 = 0$ and below $y^*(x)$, we have $c_0 = 1$.

It remains to numerically solve for the dividing characteristic y^*, defined by Eq. (4.64) with initial condition $y^*(-\hat{L}) = 1$ and determine the point at which y^* meets the aggregate which defines, x^*. This is then coupled to the aggregate height as it evolves over time according to Eq. (4.87). We start by discretising time, defining $t_i = i\delta t$, for $i = 0, 1, ...$ where δt is a fixed timestep. We then discretise in the axial space $-\hat{L} < x < \hat{L}$, defining $x_j = -\hat{L} + j\delta x$, for $j = 0, 1...N$ where $\delta x = 2\hat{L}/N$. We first solve Eq. (4.64) for the point $y^*(t_i)$, using the MATLAB ODE solver *ode15s* to solve for the trajectory

$$\frac{dy^*(t_i, x)}{dx} = \frac{v_0(x, y, t_i) + \hat{\beta}_0 v_{m0}(x)}{u_0(x, y, t_i)}. \tag{4.88}$$

We define the initial and end points of the trajectory using a small numerical tolerance to avoid solving (4.88) when $u_0 = 0$. Hence we have initial condition $y^*(t_i, -\hat{L}) = 1 - tol$, where $tol = 0.018$ is our selected numerical tolerance. We terminate the solution when $y^*(t_i, x) = 1 + \eta_0 + tol$, which determines $x^*(t_i)$, using MATLAB's event functionality. We use the default relative and absolute tolerances for *ode15s* of 10^{-3} and 10^{-6} respectively. The leading-order fluid velocity components u_0 and v_0 are given by (4.38) and (4.42). The x value at which we terminate the simulation defines $x^*(t_i)$. We use this to define the source of cells from the outer region $c_0(x_j, t_i)$ to be

$$c_0(x_j, t_i) = \begin{cases} 1 \text{ for } x_j < x^*(t_i), \\ 0 \text{ for } x_j > x^*(t_i). \end{cases} \tag{4.89}$$

We then use an explicit Euler scheme to calculate the channel width at the next timestep $\eta_0(x_j, t_{i+1})$, using a fixed timestep of $\delta t = 0.01$, as follows

$$\eta_0(x_j, t_{i+1}) = \eta_0(x_j, t_i) + \delta t \left(-\hat{\beta}_0 \alpha_0 c_0(x_i, t_j) u_{mn0}(x_j) + \hat{\kappa}_0 (2 - \eta_0(x_j, t_i)) \right). \quad (4.90)$$

This timestep achieves less than 1% error compared to using $\delta t = 10^{-4}$ (see Appendix B Section B.2.2). We repeat this time-stepping scheme until either the aggregate reaches 40% of the channel width (with the motivation as discussed in Section 4.6.3), the aggregate peak reaches a steady state height (which we define as a rate of change of less than 10^{-9}) or until we reach the prescribed end time $t = 1000$.

We use $N = 1000$ grid points in the axial direction. This obtains an error of 10^{-3} compared to a solution using $N = 5 \times 10^5$, as shown in Appendix B Section B.2.2.

4.7.4 Delivery examples and parametric analysis

We now examine stem cell delivery and aggregate growth in the large Péclet number regime. Fig. 4.6 shows an example of stem cells delivery and aggregate growth where we have extravasation present with relative strength $\hat{\kappa}_0 = 2$. We have plotted the composite expansion using the boundary layer solution (4.86) and the discontinuous outer solution. We have used $\epsilon = 0.2$ so that the solution in the boundary layer can be seen on the plots. The main channel shows the outer solution of $c_0 = 1$ below the dividing characteristic and $c_0 = 0$ above it. In the boundary layer we can see that the cell concentration builds up over the magnet, which occupies the region $|x| < 1$. Over time the cell aggregate grows, which alters the profile of the dividing trajectory. Since the growth is proportional to the flux from the outer region, the aggregate surface follows the same qualitative shape as the vertical magnetic velocity, defined in (4.80).

We can summarise these dynamics by examining the time evolution of the aggregate interface and the dividing characteristic. In Fig. 4.7 we plot the dynamics to compare the effect of extravasation. Fig. 4.7a shows cell capture in the absence of extravasation, whereas Fig. 4.7b shows the case when $\hat{\kappa}_0 = 2$, which was the case for Figure 4.6. When no extravasation is present, the aggregate reaches 40% of the channel width at $t = 1.68$. However, when extravasation is present the aggregate reaches a steady state height, up to our defined numerical tolerance, at $t = 8$ with a maximum channel occlusion of ≈25%.

Finally, we now carry out a parametric analysis varying both the relative extravasation strength and the normalised magnetic field strength. This is shown in Fig. 4.8. We can see that extravasation limits aggregate height as in the small Péclet number regime. Similarly, we obtain a line of best fit for the occluded region which is defined

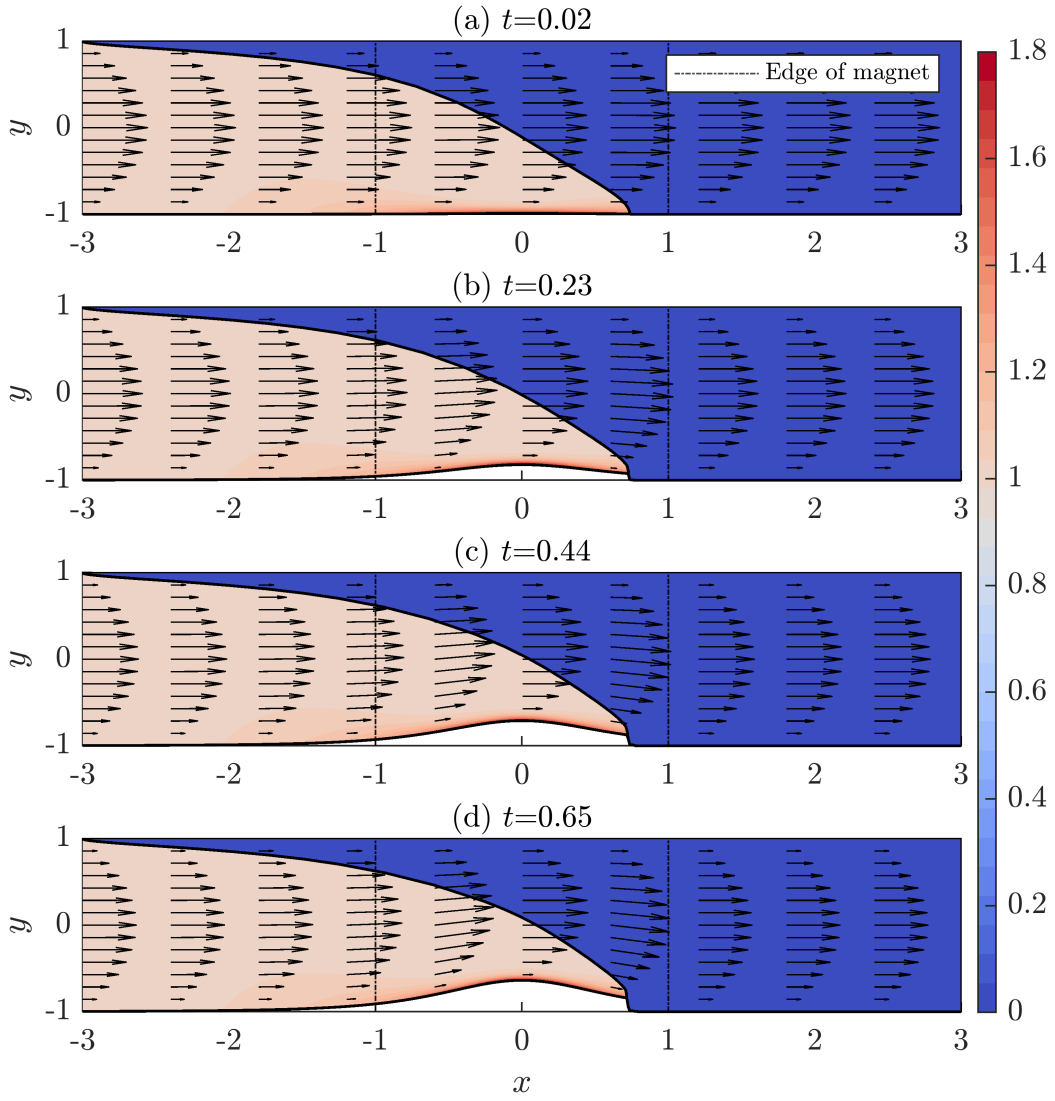

Figure 4.6: An example of the large Péclet number delivery. The solution over time is shown from top to bottom. The discontinuous outer solution is shown with the dividing characteristic marked in black. The boundary layer solution is plotted using $\epsilon = 0.2$ for visual clarity. Arrows indicate the fluid velocity field. Colour bar illustrates the stem cell concentration. Parameter values: $\hat{\beta}_0 = 1$, $Pe_0 = 1$, $\hat{\kappa}_0 = 2$.

by $\beta_0 \sim \hat{\kappa}_0^{1.05}$ which demonstrates that the linear relationship between β_0 and $\hat{\kappa}_0$ in (4.87) is preserved despite the complexity of the system arising from the dividing trajectory.

4.8 Discussion

In this chapter, we have analysed the magnetic stem cell aggregation model presented in Chapter 2, in regimes where the magnet radius is much larger than the channel

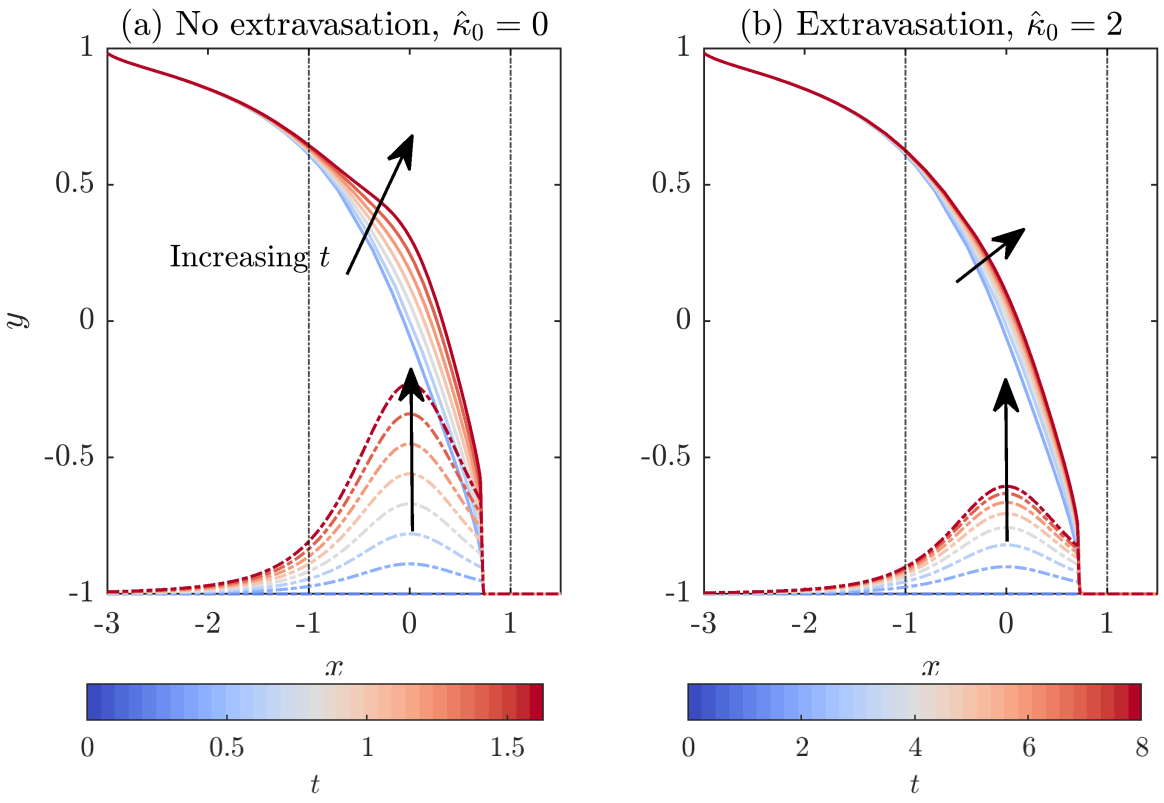

Figure 4.7: Aggregate growth for no extravasation (a) and extravasation (b). Dashed lines are the aggregate interface and the solid lines are the dividing characteristic. Colour indicates the time of the solution, shown by colourbars below. Black dashed lines show the extent of the magnet $|x| < 1$. Parameter values: $\hat{\beta}_0 = 1$, $Pe_0 = 1$, $\hat{\kappa}_0 = 0$ (a), $\hat{\kappa}_0 = 2$ (b).

width and the timescale of aggregate growth is much longer than the timescale of fluid advection. This allowed us to develop reduced models for stem cell delivery and the evolution of the aggregate boundary near the magnet. Through lubrication theory we were able to reduce the dimensionality of the system and our assumption of the slow timescale of aggregate growth reduces the complexity of the transport dynamics as the stem cell transport is quasi-steady on this timescale.

We analysed stem cell delivery in two regimes, when the reduced Péclet number is small and secondly when the reduced Péclet number is large. In the small Péclet number regime, vertical diffusive forces dominate and the leading-order cell concentration is independent of the vertical coordinate, so that its transport is determined by a one-dimensional quasi-steady advection-diffusion equation in the axial coordinate x. This is coupled to a time-dependent PDE for the aggregate height at each location on the channel wall. Through numerical simulations of this reduced model, we examined typical delivery and aggregation behaviour. In this regime stem cells

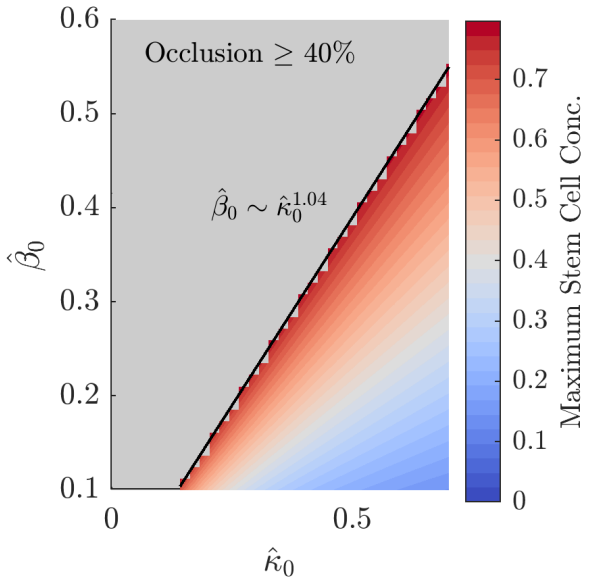

Figure 4.8: Maximum aggregate height for varying normalised magnetic field strength $\hat{\beta}_0$ and varying relative extravasation strength $\hat{\kappa}_0$; the grey region is where the aggregate reaches 40% of the channel width when simulations are terminated.

are present throughout the entire channel, but their concentration is greatest in the region surrounding the magnet. As soon as the concentration in this region exceeds the threshold for aggregation, the aggregate of stem cells then grows on the wall. The leading-order model includes both extravasation and erosion as in Chapter 3. We show that extravasation decreases the aggregate height along its entire axial extent whereas erosion has a dramatic effect on the aggregate shape. Erosion limits the flux of cells into the aggregate in regions where the shear stress is greatest. This leads to a flatter, broader aggregate as cells accumulate downstream of the aggregate to avoid the regions of high shear.

The large Péclet number regime is a singular perturbation problem of the cell transport equation where diffusive effects are limited to a boundary layer. In this regime, the solution consists of an outer region which is divided into two regions separated by the dividing trajectory of stem cells from the top of the channel; there is a constant concentration of cells below this and no cells above it. On the base of the channel, a boundary layer forms where vertical diffusion balances vertical magnetic velocity. Following our assumption that the flux into the aggregate is of $O(\epsilon)$, the flux into the base balances flux from the outer region. In this case, the boundary layer solution does not alter aggregate growth, the normal velocity of the aggregate being proportional to the flux from the outer region. As a result, erosion does not alter the aggregate height, only the cell concentration in the boundary layer. Hence the only

aggregation limiting effect is extravasation.

In both regimes, we were most interested in determining which parameter combinations lead to large aggregates. In Chapter 3 we determined that the interplay between erosion, extravasation and growth is key in the ultimate occlusion of the channel. Hence, using the two reduced models we carried out broad parameter sweeps varying the normalised magnetic field strength against erosion and extravasation. In the small Péclet number regime, we showed that both erosion and extravasation are able to limit aggregation. In the large Péclet number regime, erosion does not alter the flux into the aggregate hence we explore the effect of the extravasation speed on maximum aggregate height. Using these broad parameter sweeps we numerically determined the region where the stem cell aggregate exceeds a prescribed threshold, which we set to be 40% of the channel width. We then used these parameter sweeps to determine relationships between the between normalised magnetic field strength and extravasation or erosion strength, defined by the lines of best fit of the edge of the occluded region. This method can be used to determine bounds on safe magnetic field strengths which can be used to keep aggregation below a desired threshold.

In this chapter, we selected two asymptotic limits to analyse which were tractable and physiologically relevant. The small reduced Péclet number regime occurs at high levels of haematocrit when the magnet radius is much larger than the vessel radius. The large reduced Péclet number regime occurs for a larger range of magnet to vessel radius ratios, due to the size of the shear-induced diffusion coefficient. As a result, this regime is of the most relevance to *in vivo* delivery.

There are a number of alternative regimes which could be explored in future work. Regimes with weak relative magnetic fields $\hat{\beta} \ll 1$ will lead to the growth of an aggregate which has $h \ll 1$, and analysis of these regimes could be of interest if the therapy aims to deliver low levels of cells over a period of days, for instance. Within the small reduced Péclet number regime, subcases include when the axial diffusion is not present at leading-order in the conservation equation, which would yield a hyperbolic conservation equation, but we would expect the aggregate growth to be qualitatively similar.

In the large reduced Péclet number regime, we considered the case where the flux from the outer region balances the flux into the aggregate. However, if the flux into the aggregate is smaller, then the concentration will build up in the boundary layer. This corresponds to the small nanoparticle flux case considered by Richardson et al. for a flat boundary [92]. Furthermore, in the large reduced Péclet number regime, if the normalised magnetic field strength, $\hat{\beta}$, is larger than $O(\epsilon)$ then the vertical

magnetic field will balance with axial advection in an upstream region, rather than over the magnet. This will lead to accumulation and aggregate growth upstream.

4.9 Conclusion

This chapter concludes the section of this thesis which focuses on magnetic stem cell delivery. In the subsequent chapters we develop and analyse a model for high shear thrombosis. This builds on the model development and asymptotic analysis in Chapters 2 - 4. However, we focus more heavily on model parameterisation which is crucial in ensuring our mathematical models can offer quantitative predictions.

Chapter 5

Mathematical modelling of the role of Von Willebrand Factor in arterial blood clotting

In Chapter 1, we presented an introduction to arterial blood clotting (thrombosis). This occurs as a result of coronary heart disease, which causes plaque deposition in arteries and narrows the vessel; this is referred to as a stenosis. The key blood protein which facilitates the deposition of platelets and the formation of a clot is Von Willebrand Factor (VWF). VWF is shear-sensitive so that at low shear rates it is tightly coiled, and then at high shear rates, $\dot{\gamma} > 5,000\ \text{s}^{-1}$, it unfolds into a long chain [18, 98]. This facilitates rapid platelet deposition from the blood onto the vessel wall. The exact unfolding of VWF and its interaction with the flow is not fully characterised in the current literature. Furthermore, a mechanistic, continuum model of VWF's role in thrombosis has, to date, not been developed.

In this chapter, we develop a mathematical model for the initiation of blood clot formation under high shear rates. This model aims to determine the interaction between the key blood protein, VWF, vessel geometry, and fluid mechanics in determining the location where platelets deposit and a clot forms. This represents the first continuum model for VWF which mechanistically describes its behaviour in varying flow structures. In Chapter 6, we present work which outlines the mechanistic insight this model can provide in complex flow regimes. Since the model contains five unknown parameters controlling VWF binding, an unknown platelet-VWF binding rate and an unknown initial concentration of VWF, in Chapter 7 we design methods for determining these unknown values using experimental data.

This chapter is structured as follows: we first summarise the relevant parts of the thrombosis cascade in Section 5.1. In Section 5.2, we review VWF dynamics

when the protein is in suspension and when it is tethered to walls, including existing models and experimental work on the protein. In Section 5.3, we review models for the thrombosis cascade focusing on their modelling of VWF dynamics. In Section 5.4, we outline the derivation of the FENE-P model for protein suspensions which we use to develop a model for VWF in Section 5.5. We then pick illustrative VWF-unfolding parameters to explore the model's behaviour for some simple flows in Section 5.5.1. We then present the full mathematical model in Section 5.6. Finally, in Section 5.7, we outline the analysis which we will carry out on this model in Chapters 6 and 7.

5.1 Arterial clotting & VWF

We start by summarising the process of thrombosis within arteries and the role of VWF. Blood clots form on artery walls when an existing plaque deposit ruptures, exposing internal collagen to the flowing blood. These clots are composed predominantly of platelets which are present in the flowing blood. The platelets are required to bind rapidly to overcome the high flow rates within arteries. Rapid binding is facilitated by the shear-sensitive blood protein VWF [106]. In diseased arteries, the shear rate can be up to $10,000\,\mathrm{s}^{-1}$ as the flow travels through the stenosis. These pathological shear rates cause a conformational change in VWF as the protein unfolds from a ball-like globular state to a chain configuration [18]. VWF binds to both collagen and platelets.

Arterial thrombosis has several distinct stages which are illustrated in Fig. 5.1 and detailed in the review article [18], which we summarise here. Firstly initiation: in which VWF binds to collagen on the damaged plaque forming a net over its surface [18, 38, 98]. The bound VWF is unfolded which exposes many binding sites, enabling the protein to rapidly capture platelets from the flow [59]. Clot initiation typically lasts up to five minutes and ends when there is a $10\,\mu$m thick layer of platelets deposited [18]. After initiation, the second phase is characterised by rapid thrombus growth. Shear forces activate the bound platelets. Once activated, the platelets solidify their attachment to the plaque through further bonds with another blood protein, fibrinogen. The platelets then begin to produce VWF. This results in an auto-catalytic cascade inducing fast clot formation as more platelets are bound from the flow. Deposition rates during this phase are an order of magnitude larger than during the initiation phase [18].

After rapid thrombus growth, the clot either totally occludes the vessel or the fractures — the latter being an embolism — producing smaller blood clots that travel

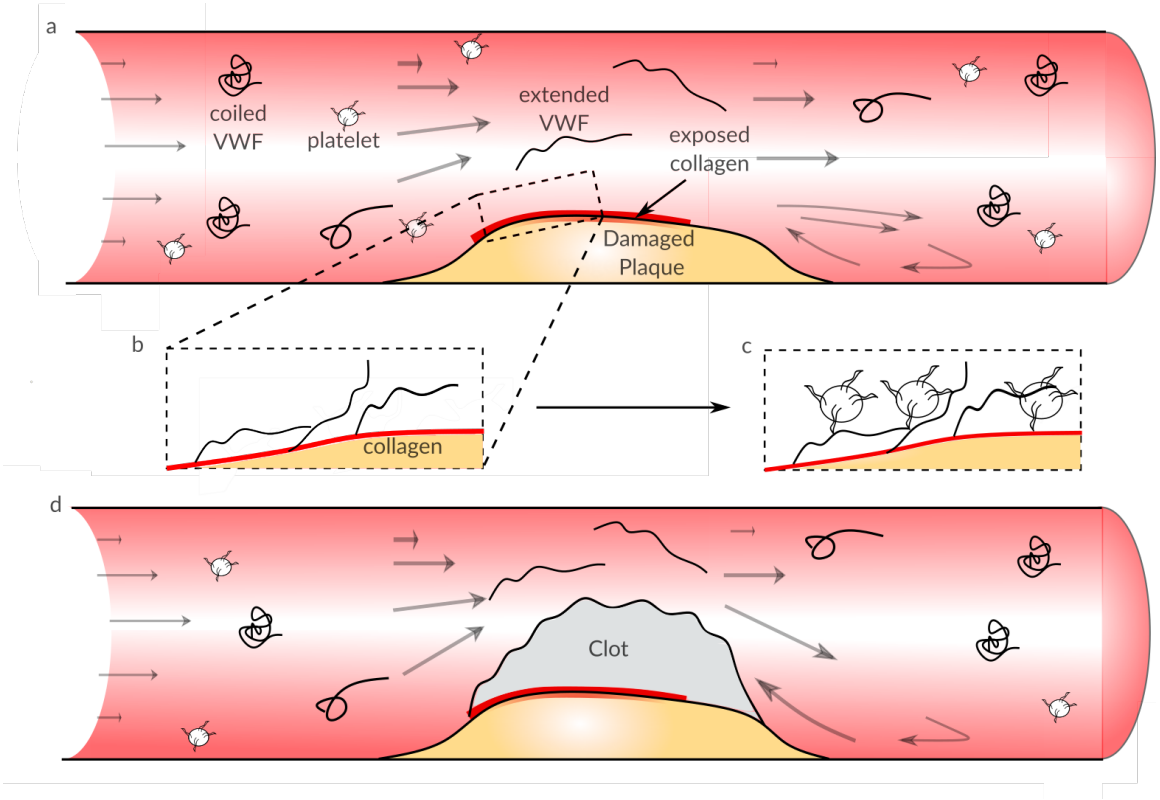

Figure 5.1: Diagram illustrating the stages of arterial thrombosis: (a) plaque rupture exposes collagen to blood flow, (b) extended VWF binds to exposed collagen forming a net, (c) platelets bind to deposited VWF, (d) following activation and the release of VWF by platelets, a rapid clot forms occluding the vessel. The modelling in this thesis focuses on steps (a) - (c).

with the flow. Both of these outcomes have the potentially fatal consequences of a heart attack or a stroke, respectively, depending on whether the clots block an artery or a vessel in the brain.

In this thesis, we model the early stages of clot formation before platelet activation. Since the timescale of initiation is much longer than that of thrombus growth, and platelet deposition is restricted to a thin layer, we assume that, in this first stage, the thrombus does not grow. This allows us to focus on the extension of VWF in flow and examine the complex interplay of stenosis geometry, protein mechanics and fluid flow on initial platelet deposition.

5.2 VWF dynamics in flow

We now review the kinematics of velocity fields, following Segel [99], as this allows us to classify flow patterns and their effects on VWF later on in this section.

5.2.1 Kinematics of flow fields

For a general fluid velocity $\boldsymbol{u}$, the action of the flow locally can be described by examining the motion of two nearby points $\boldsymbol{x}$ and $\boldsymbol{x} + \delta\boldsymbol{x}$. The rate of change of the line segment $\delta\boldsymbol{x}$ can be determined by Taylor-expanding the velocity field to first order to obtain

$$\frac{d}{dt}\delta\boldsymbol{x} = \delta\boldsymbol{x} \cdot \nabla\boldsymbol{u}(\boldsymbol{x}), \tag{5.1}$$

where $\nabla\boldsymbol{u}$ is the deformation gradient. The deformation gradient can be split into symmetric and antisymmetric components:

$$\nabla\boldsymbol{u} = \frac{1}{2}\left(\nabla\boldsymbol{u} + \nabla\boldsymbol{u}^T\right) + \frac{1}{2}\left(\nabla\boldsymbol{u} - \nabla\boldsymbol{u}^T\right) = \boldsymbol{D} + \boldsymbol{W}, \tag{5.2}$$

where $\boldsymbol{D}$ and $\boldsymbol{W}$ are known as the rate of strain tensor and the rotation tensor, respectively. The eigenvalues of $\boldsymbol{D}$ and λ_D, represent the magnitude of elongation caused to the line element along the three principal directions defined by the eigenvectors of $\boldsymbol{D}$. In incompressible flow, $\sum \lambda_D = 0$, but the magnitude of the elongation can be defined by the largest eigenvalue. Since $\boldsymbol{W}$ is antisymmetric, its eigenvalues λ_W are complex, hence the absolute value of the eigenvalues $|\lambda_W|$ represents the magnitude of rotation in each principal direction. Purely elongational flow is defined by $\boldsymbol{W} = \boldsymbol{0}$ and purely rotational flows have $\boldsymbol{D} = \boldsymbol{0}$, while shear flow is defined by equal parts elongation and rotation so that $\max|\lambda_W| = \max\lambda_D$.

We now summarise the behaviour of free and bound VWF along with existing experimental and mathematical models of its dynamics.

5.2.2 Free VWF dynamics

Von Willebrand Factor is a large protein which naturally exists in the blood as multimers composed of between two and eighty dimers, where the largest multimers play the most dominant role in haemodynamics [39, 96]. When subjected to increased shear rates, as occurs in arterial stenoses, the protein unfolds from a typical globular width of $1\,\mu$m and can reach lengths of up to $250\,\mu$m [89, 98]. *In vitro* models have established that the length of a VWF molecule has a linear relationship with available platelet binding sites as the protein unfolds [38].

In shear flow with a constant shear rate above the unfolding threshold of $5000\,\mathrm{s}^{-1}$, the protein unfolds, tumbles and then refolds. The period between this unfolding and refolding and the magnitude of unfolding both increase as the shear rate increases [98, 104]. This is attributed to the equal rotational and elongational components of

shear flow [125]. If the flow is removed, the protein relaxes back to its globular form over approximately 0.32 s [98]. This demonstrates hysteresis, since the time taken to relax back to its natural length is much longer than the time taken to unfold when the flow is turned on which is < 0.01 s [38]. In purely elongational flow, similar proteins to VWF, such as DNA, extend without tumbling, reaching their maximum length at lower values of shear rate than in shear flow [104], this is thought to also occur for VWF but has not been captured *in vitro* [103].

The relaxation time of 0.32 s is less than the time required to travel the length of the coronary artery which we estimate to be 1 s ($\approx$ 10 cm length, velocity 0.1 m/s [46]). However, 0.32 s is three times longer than the time required to pass a typical stenosis of 0.1 s ($\approx$ 1.7 cm stenosis and 0.16 m/s pathological velocity [33, 124]). This means that the proteins could remain partially unfolded in the downstream region behind the stenosis.

Since tracking and imaging proteins in suspension at high shear rates is challenging, there are few experimental studies of VWF in flow in which the protein is not tethered to a boundary. To date, there are only two studies which have presented experimental data for VWF unfolding in suspension. In 2007, Schneider et al. tracked VWF molecules as they circulated a microfluidic loop, measuring the length of the proteins at increasing shear rates [98]. In these experiments, VWF unfolded at all shear rates greater than $5,000$ s^{-1} and reached a length of approximately 15 μm. In 2016, Lippok et al. [69] measured the cleavage of VWF multimers at increasing shear rates. The proteins were sheared in combination with an enzyme which cleaves VWF at an internal bond, usually hidden when the protein is globular. Hence the authors used cleavage as a proxy for VWF length. Combining this data with a discrete mathematical model, where the protein is described using beads and springs, the authors were able to determine an empirical fitting of VWF unfolding, quantifying that in shear flow VWF first begins to unfold at $2,000$ s^{-1} and reaches its maximum length at $10,000$ s^{-1}. The protein reaches half of its maximum length at a shear rate 5522 s^{-1} which is quantitatively similar to the value found by Schneider et al.

VWF dynamics have been modelled using discrete bead and spring models very effectively. These mathematical models of VWF aim to capture either its unfolding in flow, its adhesion to vessel walls or its behaviour when tethered to walls. We first summarise the works which model VWF in flow and then those which examine VWF behaviour when tethered to walls. Rack et al. [89] modelled VWF dynamics and its interactions with discrete RBCs suspended in a straight fluid channel. The model couples the dynamics of RBCs and fluid molecules with stochastic ODEs for

the position of each cell or fluid particle in time. The model included internal attraction between the subunits of VWF which was shown to be essential to reproduce VWF unfolding once the shear rate exceeds a certain threshold. The authors demonstrated that VWF remains globular in the centre of the channel and elongates close to the channel wall where the shear rate is greater. They highlighted that remaining globular in the centre of the channel enabled the protein to travel to the edge of the vessel more easily since collisions with RBCs displace globular proteins more than the extended proteins. Furthermore, the authors demonstrated that the combination of physiological levels of RBCs and high shear rates ensures that VWF is extended and in sufficient concentration levels close to the wall to facilitate significant adhesion.

Sing et al. [103] carried out Brownian Dynamics simulations of discrete VWF multimers in a Newtonian fluid, including hydrodynamic interactions and attractive forces between VWF dimers. The authors showed that elongational flow has a key role in VWF unfolding. Their model predicts that in elongational flow, VWF can begin to unfold at shear rates of $500\,\mathrm{s}^{-1}$, an order of magnitude lower than in shear flow which they predict to occur at $5{,}000\,\mathrm{s}^{-1}$. However, this lower threshold remains to be reproduced quantitatively in experiments.

Discrete models of VWF can characterise *in vitro* data and offer insights into protein mechanics. However, these models are only able to include a limited number of proteins or platelets before their numerical solution becomes demanding. An alternative approach is to employ continuum models that can examine the dynamics of a large number of VWF molecules and their interactions with platelets and flow.

VWF dynamics were modelled using a continuum framework by Zhussupbekov et al. in 2021 [126]. The authors used a two-species model where VWF exists in one of two states: either fully unfolded or completely globular. Each species was tracked using an advection-diffusion equation. The transition rates from globular to unfolded were modelled by first classifying the local flow as either shear, elongational or rotational using the 2-norm of the rate of strain and the rate of rotation tensors described in Section 5.2.1. The authors then prescribed transition rates in each case. The unfolding of VWF in shear flow, which moves proteins from the globular to the unfolded state, used the empirically determined unfolding rate of Lippok et al. discussed above [69]. The transition from globular to unfolded was modelled as constant in elongational flow and zero in rotational flow. This model approximated hysteresis as the rate of transition between unfolded and globular was constant in all flow types and was smaller than the maximum rate of transition to unfolded from globular. In other words, the proteins remain in the unfolded state after the flow is removed.

5.2.3 Tethered VWF dynamics

When tethered to a surface, the dynamics of bound VWF differ greatly from the free dynamics reviewed in the previous section. Proteins tethered artificially to an inert wall do not exhibit tumbling when subjected to flow as their motion is restricted by the wall. Furthermore, tethered proteins do not exhibit a threshold for extension. Instead, they unfold even at low shear rates [38].

The dynamics of wall-tethered proteins have been examined using Brownian Dynamics simulations by Wang et al. [112] where VWF was modelled using a bead and spring approach with a finitely extensible, nonlinear, elastic spring (FENE). The model was validated with *in vitro* experiments and demonstrates that proteins unfold gradually as the shear rate increases to 20,000 s^{-1}. Furthermore, the authors demonstrated that extension results are heavily dependent on the location of the tethering point along the VWF molecule and the initial length of VWF [112].

During clotting, VWF tethers to the exposed collagen of the damaged plaque with multiple anchors along the protein [18, 38, 98]. This leads to the formation of 'carpets' of flattened VWF, as has been observed *in vitro* [98]. In this chapter, we assume that the bound VWF is completely immobilised along its length so that the proteins do not continue to change length once they have bound.

5.3 Thrombosis modelling

We proceed by reviewing models of arterial thrombosis, with a focus on models that capture VWF dynamics. The existing mathematical models of high-shear thrombosis can be partitioned into either phenomenological or mechanistic models. Phenomenological models, such as [9, 77], model thrombus growth rates as empirically derived functions of the shear rate, neglecting the sub-constituents of clotting. Simple growth laws allow these models to be effectively parameterised and they can therefore achieve quantitative agreement with experimental data. The models can be solved numerically more readily than models which include all clotting constituents and can therefore be used to make predictions of clotting in patient-specific geometries [77] or to examine the effect of varying geometry on clot formation rate [9].

Mechanistic models examine the complex interplay of the different species during thrombosis. Wu et al. [118] developed a continuum model for thrombus growth in a three-dimensional, microfluidic stenosis model. Their model builds on previous work of Sorensen et al. [105] by using their detailed model of reactions between the constituents of the blood. The effect of VWF on platelet deposition is included in the

binding rates of platelets to the vessel walls. The binding rate increases as the shear rate increases through an the Lippok et al. unfolding expression [69]. Yet the model does not account for flow kinematics or variation in the distribution of VWF. The authors predicted thrombus growth downstream of the stenosis and demonstrated that, for higher degrees of stenosis, platelets are deposited more rapidly.

Du et al. [29] modelled a growing clot as a porous viscoelastic scaffold and examined clot formation in a straight channel. This model examines the risk of clot embolism which was found to be greater for more porous clots. The model includes VWF binding to platelets above when the elongation rate is greater than $1,000\ \mathrm{s}^{-1}$ (through a step function), defining the elongational rate to be the square root of the shear rate squared minus the rotation rate squared. The authors demonstrate that VWF increases the rate of clot formation as more platelets accumulate in the regions of high shear rate.

In this chapter, we develop a continuum model for the dynamics of VWF coupled to a model for platelet transport and blood flow. This allows us to examine the effects of protein mechanics, fluid mechanics and geometry on platelet deposition. Our model is based on the finitely extensible nonlinear elastic dumbbell model with the Peterlin closure (FENE-P). The continuum model in this thesis does not split the local flow into discrete categories as in the work of Zhussupbekov et al. [126]. Our model can describe VWF dynamics in shear, elongation and rotational flows and combinations of these in three dimensions using a single unfolding rate, thereby allowing us to accurately quantify the protein unfolding throughout the full range of flow types. Furthermore, we allow for partially unfolded states, allowing more detailed modelling of platelet binding dynamics. This allows our model to capture the role of both flow structure and shear rate on thrombosis initiation.

We begin by outlining the derivation of the viscoelastic fluid model FENE-P as this offers insight into its underlying mechanistic assumptions. In Section 5.5, we describe how we adapt the FENE-P model to describe VWF in blood.

5.4 Derivation of the FENE-P model

In this section, we outline the derivation of the FENE-P model from microscopic dynamics of a single protein which forms the basis of our description of VWF in this thesis. The FENE-P model describes dilute suspensions of proteins or polymers under large strains with the Peterlin closure for the spring rule [17]. We note that the FENE-P model is an adaptation of the Oldroyd-B model discussed in Chapter

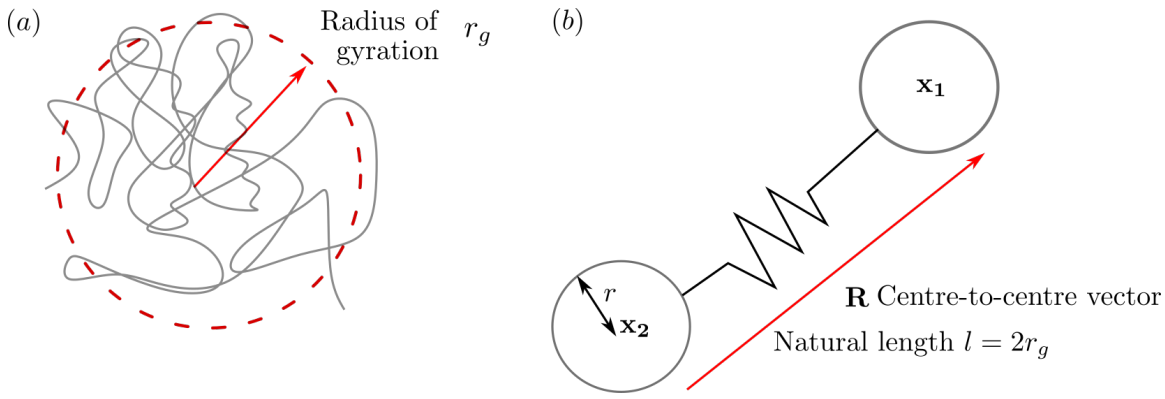

Figure 5.2: (a) Schematic of VWF molecule with radius of gyration r_g. (b) Microscopic model of VWF as a dumbbell made up of two beads with radius r, the centre of the beads is connected by vector $\boldsymbol{R}$. The dumbbell has natural length $2r_g$.

1, which restricts the length of the elastic components of the flow. We follow the derivation of Bird [17] with the nonlinear spring force averaging from [87]. The derivation begins with a microscopic description of the protein as a stochastic, elastic dumbbell. We then present a Fokker-Planck equation of the probability distribution function for the length of the dumbbell in configuration space. Finally, we present the average behaviour of the dumbbell described by a deterministic PDE for the protein length for a given flow.

We begin by modelling a single protein molecule as two identical beads with radius r connected by a finitely extensible spring with natural length l. To approximate the size of the protein, the natural length l is set to equal twice the radius of gyration which is the approximate size of the protein. The radius of gyration of the polymer and the dumbbell model are illustrated in Figure 5.2a and b. Neglecting inertia due to the size of the beads, the dynamics of the dumbbell in a viscous fluid can be determined by a force balance. Each bead experiences viscous drag, the spring force from the opposite bead and Brownian motion. If the two beads are located at $\boldsymbol{x}_1$ and $\boldsymbol{x}_2$, their respective force balances are as follows

$$\xi(\dot{\boldsymbol{x}}_1 - \boldsymbol{u}(\boldsymbol{x}_1)) + \boldsymbol{f}(\boldsymbol{x}_1 - \boldsymbol{x}_2) + \sqrt{4k_BT\xi}\boldsymbol{n}(t) = \boldsymbol{0}, \tag{5.3}$$

$$\xi(\dot{\boldsymbol{x}}_2 - \boldsymbol{u}(\boldsymbol{x}_2)) - \boldsymbol{f}(\boldsymbol{x}_1 - \boldsymbol{x}_2) + \sqrt{4k_BT\xi}\boldsymbol{m}(t) = \boldsymbol{0}, \tag{5.4}$$

where $\xi = 6\pi\mu r$ is the drag coefficient of the fluid, μ is the viscosity of the fluid, $\boldsymbol{u}$ is the fluid velocity, k_B is Boltzmann's constant, T is the temperature in Kelvin, $\boldsymbol{f}(\boldsymbol{x}_1 - \boldsymbol{x}_2)$ is the nonlinear spring force exerted on the first bead by the second bead and $\boldsymbol{n}(t)$ and $\boldsymbol{m}(t)$ are independent Wiener processes with zero mean and a variance

of t. The Warner spring force is used to model springs which have a maximum length of R_0, and is given by

$$\boldsymbol{f}(\boldsymbol{x}_1 - \boldsymbol{x}_2) = \frac{k(\boldsymbol{x}_1 - \boldsymbol{x}_2)}{1 - |\boldsymbol{x}_1 - \boldsymbol{x}_2|^2/R_0^2}, \tag{5.5}$$

where k is the spring constant. When the dumbbell is extended slightly, $|\boldsymbol{x}_1 - \boldsymbol{x}_2| \ll 1$, Eq. (5.5) reduces to the Hookean spring law in which $\boldsymbol{f}(\boldsymbol{x}_1 - \boldsymbol{x}_2) = k(\boldsymbol{x}_1 - \boldsymbol{x}_2)$. The spring constant k can be approximated in terms of the natural length of the protein, l [81]. It is given by

$$k = \frac{3k_BT}{l^2}. \tag{5.6}$$

We define the centre-to-centre vector of the dumbbell $\boldsymbol{R}$, and its centre of mass, $\boldsymbol{R}_c$ as follows

$$\boldsymbol{R} = \boldsymbol{x}_1 - \boldsymbol{x}_2, \quad \boldsymbol{R}_c = \frac{\boldsymbol{x}_1 + \boldsymbol{x}_2}{2}. \tag{5.7}$$

Using these definitions we can rearrange Eqs. (5.3) and (5.4) giving

$$\dot{\boldsymbol{R}} = \boldsymbol{u}\left(\boldsymbol{R}_c + \frac{\boldsymbol{R}}{2}\right) - \boldsymbol{u}\left(\boldsymbol{R}_c - \frac{\boldsymbol{R}}{2}\right) - \frac{2}{\xi}\boldsymbol{f}(\boldsymbol{R}) + \frac{\sqrt{4k_BT\xi}}{\xi}(\boldsymbol{n}(t) - \boldsymbol{m}(t)), \tag{5.8}$$

$$\dot{\boldsymbol{R}}_c = \frac{1}{2}\left(\boldsymbol{u}\left(\boldsymbol{R}_c + \frac{\boldsymbol{R}}{2}\right) - \boldsymbol{u}\left(\boldsymbol{R}_c - \frac{\boldsymbol{R}}{2}\right)\right) + \frac{\sqrt{4k_BT\xi}}{2\xi}(\boldsymbol{n}(t) + \boldsymbol{m}(t)). \tag{5.9}$$

We proceed by assuming that the lengthscale of the protein, $|\boldsymbol{R}|$, is much less than the lengthscale of the flow, thus allowing us to Taylor expand the velocities around the centre of mass, $\boldsymbol{R}_c$. Retaining only the leading-order terms in $\boldsymbol{R}$, this leads to a system of SDEs for the length of the dumbbell and its position given by

$$\dot{\boldsymbol{R}} = \boldsymbol{R} \cdot \nabla \boldsymbol{u}(\boldsymbol{R}_c) - \frac{2}{\xi}\boldsymbol{f}(\boldsymbol{R}) + \frac{\sqrt{4k_BT\xi}}{\xi}(\boldsymbol{n}(t) - \boldsymbol{m}(t)), \tag{5.10}$$

$$\dot{\boldsymbol{R}}_c = \boldsymbol{u}(\boldsymbol{R}_c) + \frac{\sqrt{4k_BT\xi}}{2\xi}(\boldsymbol{n}(t) + \boldsymbol{m}(t)), \tag{5.11}$$

Here ∇ denotes the gradient operator with respect to $\boldsymbol{R}_c$. The deterministic components of this system can be interpreted physically: the centre-to-centre vector of the protein is defined by the gradient of the flow along its length and the spring force relative to the viscous drag. The position of the centre of mass is defined naturally so that it moves with the velocity of the fluid at its centre.

The Fokker-Planck equation for the probability density function $\psi(\boldsymbol{R}, t)$ which describes the distribution of dumbbell lengths, given in [17], is

$$\frac{\partial \psi}{\partial t} = -\nabla_{\boldsymbol{R}} \cdot \left(\nabla \boldsymbol{u} \cdot \boldsymbol{R}\psi - \frac{2}{\xi}\boldsymbol{f}(\boldsymbol{R})\psi\right) + \frac{2k_BT}{\xi}\nabla^2_{\boldsymbol{R}}\psi. \tag{5.12}$$

Here $\nabla_{\boldsymbol{R}}$ denotes the gradient operator with respect to $\boldsymbol{R}$. Finally, to determine the average length of the protein for a given velocity field, we take the second moment of the centre-to-centre vector of the dumbbell. In configuration space this is defined by integrating $\boldsymbol{RR}\psi$ over $\boldsymbol{R}$, for which we write

$$\langle \boldsymbol{RR} \rangle = \int \boldsymbol{RR}\psi \; d\boldsymbol{R}. \tag{5.13}$$

Multiplying (5.12) by $\boldsymbol{RR}$ and integrating over $\boldsymbol{R}$, again by Bird [17], gives

$$\frac{\partial \langle \boldsymbol{RR} \rangle}{\partial t} = \langle \boldsymbol{RR} \rangle \cdot \nabla \boldsymbol{u} + (\nabla \boldsymbol{u})^T \cdot \langle \boldsymbol{RR} \rangle - \boldsymbol{u}(\boldsymbol{R}_c) \cdot \nabla \langle \boldsymbol{RR} \rangle + \int \frac{2}{\xi} \nabla_{\boldsymbol{R}} \boldsymbol{f} \boldsymbol{RR}\psi \; d\boldsymbol{R} + \frac{4k_B T}{\xi} \boldsymbol{I}. \tag{5.14}$$

There is no closed form expression for the integral of the nonlinear spring force and an approximation must be used to close the model. In this thesis we consider the Peterlin closure of the spring rule [14]. Other common spring force closures, such as the Chilcott and Rallison closure [91], result in a minimal difference in the behaviour of the protein, although these models have different behaviours when combined with the fluid stress in the Navier-Stokes equations [50]. The Peterlin closure is defined by replacing the denominator of the integrand in Eq. (5.14) with its pre-averaged quantity as follows

$$\begin{aligned} \int \frac{2k}{\xi} \nabla_{\boldsymbol{R}} \left(\frac{\boldsymbol{R}\psi}{1 - |\boldsymbol{R}|^2/R_0^2} \right) \boldsymbol{RR} \; d\boldsymbol{R} &\approx \left(\frac{2k}{\xi(1 - \langle |\boldsymbol{R}| \rangle^2/R_0^2)} \right) \int \nabla_{\boldsymbol{R}} (\boldsymbol{R}\psi) \boldsymbol{RR} \; d\boldsymbol{R}, \\ &= -\frac{4k}{\xi} \frac{\langle \boldsymbol{RR} \rangle}{1 - \langle |\boldsymbol{R}| \rangle^2/R_0^2}, \end{aligned} \tag{5.15}$$

where the final line is obtained by integrating by parts. Equation (5.14) can then be written

$$\frac{\partial \langle \boldsymbol{RR} \rangle}{\partial t} = \langle \boldsymbol{RR} \rangle \cdot \nabla \boldsymbol{u} + (\nabla \boldsymbol{u})^T \cdot \langle \boldsymbol{RR} \rangle - \boldsymbol{u}(\boldsymbol{R}_c) \cdot \nabla \langle \boldsymbol{RR} \rangle - \frac{4k}{\xi} \frac{\langle \boldsymbol{RR} \rangle}{1 - \langle |\boldsymbol{R}| \rangle^2/R_0^2} + \frac{4k_B T}{\xi} \boldsymbol{I}, \tag{5.16}$$

Finally, we define the symmetric configuration tensor $\boldsymbol{A}$ proportional to the second moment of $\boldsymbol{R}$, $\langle \boldsymbol{RR} \rangle$ as follows

$$\boldsymbol{A} = \frac{Tr(\boldsymbol{I})}{l^2} \langle \boldsymbol{RR} \rangle, \tag{5.17}$$

where $Tr(\boldsymbol{I})/l^2$ is the trace of the identity tensor, i.e. 2 or 3, and the scaling $Tr(\boldsymbol{I})/l^2$ in (5.17) is defined so that when the configuration tensor is equal to the identity tensor

then we have $|\boldsymbol{R}| = l$, meaning the dumbbell is at its natural length l. Using (5.17), if we define the natural length to balance between spring forces and diffusion such that $l^2 = 3k_bT/f(l^2)$, then we can then rewrite (5.16) as

$$\frac{\partial \boldsymbol{A}}{\partial t} + \boldsymbol{u}\cdot\nabla\boldsymbol{A} - \boldsymbol{A}\cdot\nabla\boldsymbol{u} - (\nabla\boldsymbol{u})^T\cdot\boldsymbol{A} = -\frac{1}{\tau}\left(\frac{\boldsymbol{A}}{1 - Tr(\boldsymbol{A})/L^2} - a\boldsymbol{I}\right). \tag{5.18}$$

Here we define $1/\tau = 4k/\xi$ as the relaxation time, $L^2 = Tr(\boldsymbol{I})R_0^2/l^2$ is referred to as the extensibility parameter which restricts the size of $Tr(\boldsymbol{A})$ and $a = 1/(1 - Tr(\boldsymbol{I})/L^2)$. The terms in Eq. (5.18) from left to right are: the transport of the proteins with the fluid; the effect of fluid shear increasing protein length and the nonlinear spring force between the two ends of the dumbbell.

In the FENE-P model the configuration tensor is used to model the extra stress in the fluid arising from the proteins [16], as we shall now describe. The Navier-Stokes equations are as follows

$$\nabla\cdot\boldsymbol{u} = 0, \tag{5.19}$$

$$\rho\left(\frac{\partial \boldsymbol{u}}{\partial t} + \boldsymbol{u}\cdot\nabla\boldsymbol{u}\right) = \nabla\cdot\boldsymbol{\sigma}. \tag{5.20}$$

The fluid stress tensor, $\boldsymbol{\sigma}$, is then split into the stress contribution from the suspension fluid, often referred to as the solvent stress, and a contribution from the proteins:

$$\boldsymbol{\sigma} = \underbrace{-p\boldsymbol{I} + \mu(\nabla\boldsymbol{u} + (\nabla\boldsymbol{u})^T)}_{\text{Solvent stress}} + \underbrace{G(f(\boldsymbol{A})\boldsymbol{A} - a\boldsymbol{I})}_{\text{Protein stress}}, \tag{5.21}$$

where the constant G is defined as $G = \phi_p k_b T$ and determines the magnitude of protein contribution to the fluid stress [87]. Here ϕ_p is the number of proteins per unit volume, which has units m^{-3}.

5.4.1 Interpretation of the configuration tensor

We now explore how to infer physical information about the proteins from the configuration tensor $\boldsymbol{A}$. This section was developed using the framework established by Advani et al. where the authors examined how the configuration tensor which arises from the Oldroyd-B model in simple flows can be used to describe filament orientation [1].

We first define our dumbbell as oriented in three-dimensional, Cartesian space. The centre-to-centre vector can then be defined as

$$\boldsymbol{R} = R_x\boldsymbol{i} + R_y\boldsymbol{j} + R_z\boldsymbol{k}, \tag{5.22}$$

where $\boldsymbol{i}$, $\boldsymbol{j}$ and $\boldsymbol{k}$ are the standard Cartesian basis vectors. Using this definition, we have

$$\boldsymbol{RR} = \begin{pmatrix} R_x^2 & R_xR_y & R_xR_z \\ R_xR_y & R_y^2 & R_yR_z \\ R_xR_z & R_yR_z & R_z^2 \end{pmatrix}. \tag{5.23}$$

Hence, returning to the definition of the configuration tensor, Eq. (5.17), we have

$$\begin{pmatrix} A_{xx} & A_{xy} & A_{xz} \\ A_{xy} & A_{yy} & A_{yz} \\ A_{xz} & A_{yz} & A_{zz} \end{pmatrix} = \frac{3}{l^2} \begin{pmatrix} \langle R_x^2 \rangle & \langle R_xR_y \rangle & \langle R_xR_z \rangle \\ \langle R_xR_y \rangle & \langle R_y^2 \rangle & \langle R_yR_z \rangle \\ \langle R_xR_z \rangle & \langle R_yR_z \rangle & \langle R_z^2 \rangle \end{pmatrix}. \tag{5.24}$$

So the diagonal components of $\boldsymbol{A}$ represent the average length in each Cartesian direction squared, scaled by $3/l^2$.

The interpretation of the off-diagonal components is best understood through an example. We consider Eq. (5.18) when there is no flow. In this case, a steady-state value of the configuration tensor satisfies

$$\frac{\boldsymbol{A}}{1 - Tr(\boldsymbol{A})/L^2} = \frac{\boldsymbol{I}}{1 - 3/L^2}. \tag{5.25}$$

It is clear that the three-dimensional identity tensor is a solution of this equation. In this case, our definition of $\boldsymbol{A}$, Eq. (5.17), yields

$$\langle \boldsymbol{RR} \rangle = \frac{l^2}{3}\boldsymbol{I}, \tag{5.26}$$

so that the off-diagonal entries of $\boldsymbol{A}$ are equal to zero when there is no flow, in which case the dumbbells will be randomly oriented.

In this thesis, we will use the configuration tensor to describe the length of VWF proteins. We recall that we have

$$Tr(\boldsymbol{A}) = \langle R_x^2 \rangle + \langle R_y^2 \rangle + \langle R_z^2 \rangle = \langle |\boldsymbol{R}|^2 \rangle. \tag{5.27}$$

This is the average length of the protein squared [91]. We then approximate the average length of the proteins as $\sqrt{Tr(\boldsymbol{A})}$, and we define a normalised length $\mathcal{L}$ as

$$\mathcal{L} = \frac{\sqrt{Tr(\boldsymbol{A})}}{\sqrt{Tr(\boldsymbol{I})}}, \tag{5.28}$$

which is defined so that when the protein is at its natural length, defined by $\boldsymbol{A} = \boldsymbol{I}$, then $\mathcal{L} = 1$. We can similarly define the extension of the proteins, $\mathcal{E}$, as

$$\mathcal{E} = \frac{\sqrt{Tr(\boldsymbol{A})}}{\sqrt{Tr(\boldsymbol{I})}} - 1. \tag{5.29}$$

We now describe how we adapt the FENE-P model (5.19) - (5.21) to describe the protein VWF in blood.

5.5 Adaptation of the FENE-P model

The magnitude of the protein contribution to fluid stress will be less than viscous stress if $G/\mu\dot{\gamma} \ll 1$ for a typical fluid shear rate γ. To calculate G, we first calculate the number density of VWF in the blood. This can be calculated using the concentration of VWF in the blood which is 0.055 g/m^3, Avogadro's constant, and VWF's molecular weight which is between 500 and 20,000 KDa depending on the number of dimers combined [82, 39]. Hence the value of G can be estimated as between 0.027 and 6.7×10^{-4} Pa. In arteries the value of $\mu\dot{\gamma}$ ranges between 1 and 10^3 Pa. The ratio $G/\mu\dot{\gamma}$ is then small for all but the largest values of shear stress, and hence we neglect any contribution to the fluid stress from VWF.

Under this assumption, the flow is not coupled to protein extension and remains Newtonian. This implies that the Navier-Stokes equations reduce to the standard form for a Newtonian incompressible viscous fluid and we retain Eq. (5.18) to model VWF length as follows

$$\frac{\partial \boldsymbol{A}}{\partial t} + \boldsymbol{u}\cdot\nabla\boldsymbol{A} - \boldsymbol{A}\cdot\nabla\boldsymbol{u} - (\nabla\boldsymbol{u})^T\cdot\boldsymbol{A} = -\frac{1}{\tau}\left(\frac{\boldsymbol{A}}{1-Tr(\boldsymbol{A})/L^2} - a\boldsymbol{I}\right). \tag{5.30}$$

As presented in our review of VWF behaviour in Section 5.2, the proteins remain globular at all shear rates below approximately $5,000\ \mathrm{s}^{-1}$ in shear flow. The spring law included in the microscopic model of the VWF depends nonlinearly on protein length such that the protein cannot extend infinitely. However, the model does not include any threshold for extension. We demonstrated that when the deformation of the protein is small, which occurs at small shear rates, the spring force is approximately linear.

To include this threshold of unfolding, we propose a modification to the FENE-P equation so that the relaxation time is a saturating function of the fluid shear rate as follows

$$\tau(\dot{\gamma}) = \alpha\left(\frac{1}{2}(\tanh(\beta(\dot{\gamma}-\gamma^*))+1)+\delta\right), \tag{5.31}$$

where β, γ^*, α and δ are parameters whose role we shall now describe. The relaxation time, (5.31), is constructed so that it is small if $\dot{\gamma} \ll \gamma^*$, which is obtained by enforcing $\delta \ll 1$. Hence, in Eq. (5.30), elastic forces dominate and the protein remains globular. Once $\dot{\gamma} \gg \gamma^*$, the relaxation time increases to $\approx \alpha$ and in Eq. (5.30), extension balances elastic forces and the protein unfolds. This nonlinear relaxation time is shown in Fig. 5.3a. We note that this model cannot predict hysteresis because once the shear rate decreases below γ^*, the proteins will relax back to their natural length

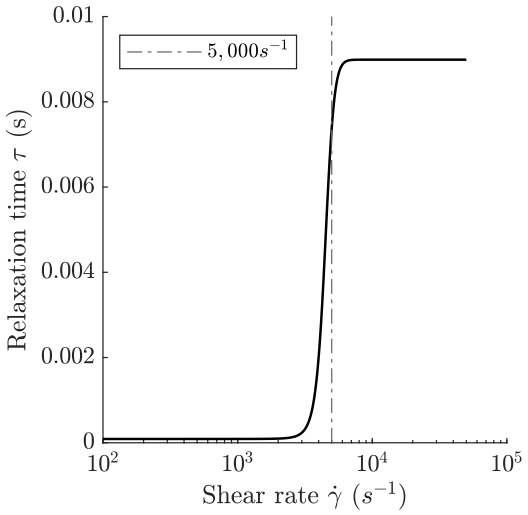

Figure 5.3: Modified relaxation time of VWF, Eq. (5.31). At low shear rates, the relaxation time is small and the proteins do not extend; at high shear rates, the relaxation time is larger which allows the proteins to extend.

over the same timescale as they unfolded over. We discuss the limitations of this assumption in the following chapters.

We note that the FENE-P equation model was derived in the absence of walls. The effect of walls has been examined in the context of confined flows of proteins [13] and for a similar system of confined flow of bacteria [97]. This results in Neumann boundary conditions for the PDF in the Fokker-Planck equation (5.12). However, this ensures that the governing equation for the configuration tensor does not have a closed form [13]. To maintain tractability, we use the solution of the FENE-P equation on the boundary to describe the length of VWF at the boundary. Finally, we note that the unfolding of a multimeric protein differs biomechanically to the extension of a dumbbell. VWF unfolds through the successive unfolding of each dimer leading to period of sudden increases in length for increasing force [78]. However, we adopt the dumbbell description as this simple model has been shown to effectively describe suspensions of polymers and proteins in flow [56, 87].

We will now discuss the behaviour of Eq. (5.30) in simple flows.

5.5.1 Behaviour in flow

To demonstrate the behaviour of the model, we now examine the FENE-P equation Eq. (5.30) in simple flow types: simple 2D shear flow, 2D elongational flow and 2D rotational flow. We first examine the behaviour of the model using our modified relaxation time and then compare it to a constant relaxation time set to equal the

maximum value of $\tau(\dot{\gamma})$. We select α γ^*, β, L and δ so that the proteins remain globular for $\gamma < 1000\,\mathrm{s}^{-1}$ which then has a maximum length of $\mathcal{L} = 16$, approximately matching the maximum extension recorded in the data of Schneider et al. [98].

For all flows, we will examine solutions of the model which are independent of time and position. To quantitatively compare the solutions, for elongational flow and shear flow we set the flows to have the same scalar shear rate, $\dot{\gamma}$. For a two-dimensional flow (u, v) in the (x, y) plane this is defined by

$$\dot{\gamma} = \sqrt{2\boldsymbol{D} : \boldsymbol{D}} = \left(2\frac{\partial u}{\partial x}^2 + \left(\frac{\partial u}{\partial y} + \frac{\partial v}{\partial x} \right)^2 + 2\frac{\partial v}{\partial y}^2 \right)^{1/2}, \tag{5.32}$$

where $\boldsymbol{D} = (\nabla \boldsymbol{u} + (\nabla \boldsymbol{u})^T)/2$ is the rate of strain tensor.

The velocity field and deformation gradient of shear flow, with shear rate $\dot{\gamma}$, are defined by

$$\boldsymbol{u} = \dot{\gamma} y \boldsymbol{i}, \quad \nabla \boldsymbol{u} = \begin{pmatrix} 0 & 0 \\ \dot{\gamma} & 0 \end{pmatrix}. \tag{5.33}$$

In two-dimensions the configuration tensor is

$$\boldsymbol{A} = \begin{pmatrix} A_{xx} & A_{xy} \\ A_{xy} & A_{yy} \end{pmatrix}. \tag{5.34}$$

This has three unique components as a result of symmetry, where A_{xx} and A_{yy} are the average length squared in x and y directions, respectively. The 2D assumption is made by comparing $\boldsymbol{A}$ to the two-dimensional identity matrix when determining the VWF length $\mathcal{L}$ according to (5.28). This is equivalent to assuming that protein length in the third dimension is zero, i.e. $A_{zz} = 0$.

Seeking a configuration tensor independent of time and space, we find that Eq. (5.30) reduces to the following algebraic system:

$$2\dot{\gamma} A_{xy} = \frac{1}{\tau(\dot{\gamma})} \left(\frac{L^2 A_{xx}}{L^2 - A_{xx} - A_{yy}} - a \right), \tag{5.35}$$

$$\dot{\gamma} A_{yy} = \frac{1}{\tau(\dot{\gamma})} \left(\frac{L^2 A_{xy}}{L^2 - A_{xx} - A_{yy}} \right), \tag{5.36}$$

$$0 = \frac{1}{\tau(\dot{\gamma})} \left(\frac{L^2 A_{yy}}{L^2 - A_{xx} - A_{yy}} - a \right). \tag{5.37}$$

Due to the nonlinear spring rule we solve the system numerically, reformulating it as a cubic equation for A_{xx}; then A_{xy} and A_{yy} can be determined using (5.36) and (5.37). We next express the system for elongational and rotational flows before comparing the numerical solutions for $\boldsymbol{A}$.

Elongational flow, with shear rate $\dot{\gamma}$, has velocity field and deformation gradient as follows:

$$\boldsymbol{u} = \frac{\dot{\gamma}}{\sqrt{2}}\left(x\boldsymbol{i} - y\boldsymbol{j}\right), \quad \nabla\boldsymbol{u} = \frac{\dot{\gamma}}{\sqrt{2}}\begin{pmatrix} -1 & 0 \\ 0 & 1 \end{pmatrix}. \tag{5.38}$$

Again we seek spatially and temporally constant, two-dimensional solutions of (5.30). This gives the following system of equations:

$$-\sqrt{2}\dot{\gamma}A_{xx} = \frac{1}{\tau(\dot{\gamma})}\left(\frac{L^2 A_{xx}}{L^2 - A_{xx} - A_{yy}} - a\right), \tag{5.39}$$

$$\sqrt{2}\dot{\gamma}A_{yy} = \frac{1}{\tau(\dot{\gamma})}\left(\frac{L^2 A_{yy}}{L^2 - A_{xx} - A_{yy}} - a\right), \tag{5.40}$$

$$A_{xy} = 0, \tag{5.41}$$

so that the configuration tensor is diagonal, reflecting that the directions of principal stretch are the $x-$ and $y-$ axes.

Finally, we consider rotational flow. Since rotational flow has $\boldsymbol{D} = \boldsymbol{0}$, the scalar shear rate is zero. It is nevertheless insightful to consider the behaviour of the proteins in this flow. Defining rotational flow with rotation rate ω

$$\boldsymbol{u} = \frac{\omega}{2}\left(y\boldsymbol{i} - x\boldsymbol{j}\right), \tag{5.42}$$

this has deformation tensor

$$\nabla\boldsymbol{u} = \frac{\omega}{2}\begin{pmatrix} 0 & -1 \\ 1 & 0 \end{pmatrix}, \tag{5.43}$$

such that Eq. (5.30) gives

$$\omega A_{xy} = \frac{1}{\tau(\dot{\gamma})}\left(f(\boldsymbol{A})A_{xx} - a\right), \tag{5.44}$$

$$-\omega A_{xy} = \frac{1}{\tau(\dot{\gamma})}\left(f(\boldsymbol{A})A_{yy} - a\right), \tag{5.45}$$

$$\frac{\omega}{2}(A_{yy} - A_{xx}) = \frac{f(\boldsymbol{A})}{\tau(\dot{\gamma})}A_{xy}. \tag{5.46}$$

Adding (5.44) and (5.45) we can see that $A_{xx} = A_{yy}$. Which, using (5.46), yields $A_{xy} = 0$. Thus, we have $A_{xx} = A_{yy} = 1$. This implies that the proteins remain at their natural length. Since $A_{xy} = 0$, the proteins are randomly oriented. Hence, as expected, rotational flow only rotates the proteins but does not extend them.

We now return to the shear and elongational flow systems (5.35) - (5.37) and (5.39) - (5.41). We solve these systems numerically, using first the nonlinear relaxation time

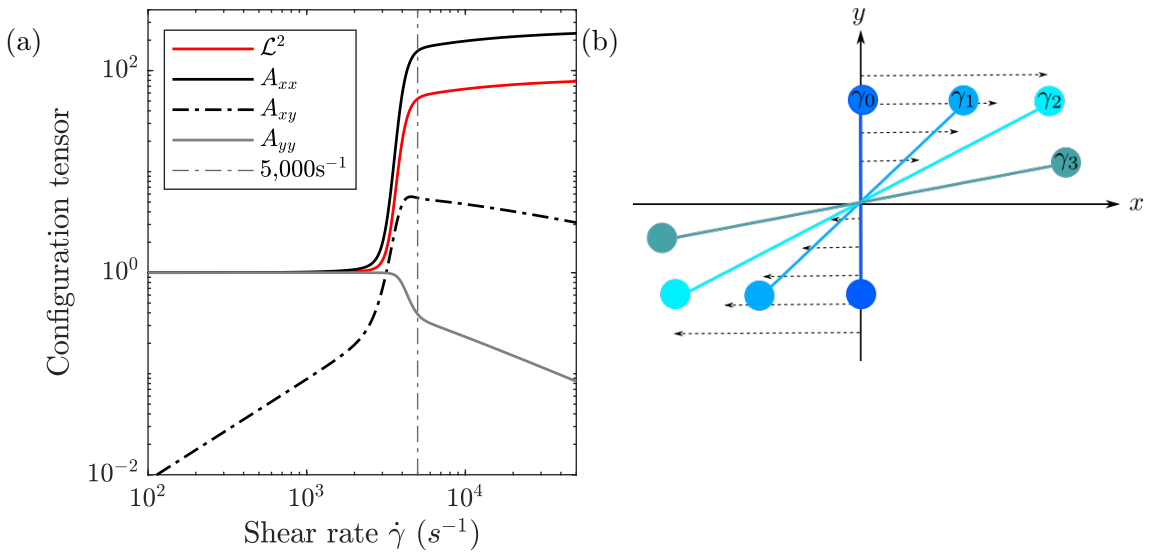

Figure 5.4: For shear flow we show: (a) the numerical solution of the (5.30) with nonlinear relaxation time (5.31) where unfolding begins at approximately $1000\,\mathrm{s}^{-1}$, reaching maximum length at 5000 s^{-1}; (b) an illustration of a FENE dumbbell for increasing shear rates γ_0 to γ_3 where dashed lines illustrate velocity field. The dumbbell extends in the $x-$ direction only, as illustrated by increasing A_{xx}. At high shear rates, since the finite length must be retained, A_{yy} decreases so the dumbbell contracts in y and A_{xx} stops increasing so the dumbbell stops extending in x. We have $\mathcal{L} = 16$ so the maximum value of A_{xx} is $\mathcal{L}^2$.

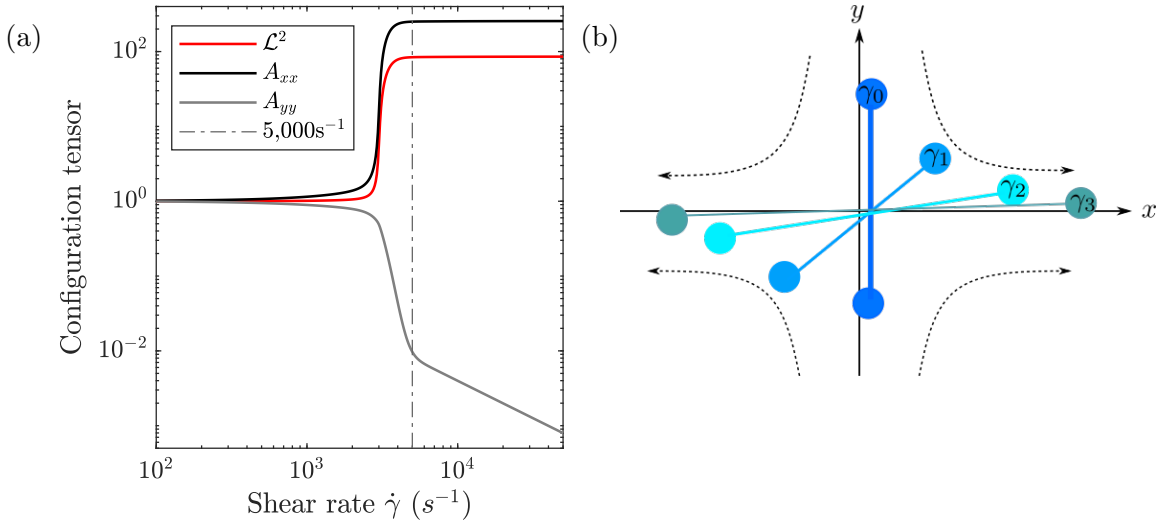

Figure 5.5: For elongational flow we show: (a) the numerical solution of (5.30) with nonlinear relaxation time (5.31). Unfolding begins at approximately $1000\,\mathrm{s}^{-1}$, reaching maximum length at 2500 s^{-1}; (b) an illustration of a FENE dumbbell for increasing shear rates γ_0 to γ_3 where dashed lines illustrate the velocity field. The dumbbell contracts in y-direction, shown by decreasing A_{yy}, and extends in the x-direction, shown by increasing A_{xx}. The finite-length requirement stops A_{xx} from further increasing and the dumbbell becomes parallel to the $x-$ axis as $A_{yy} \to 0$. We have $\mathcal{L} = 16$ so the maximum value of A_{xx} is $\mathcal{L}^2$.

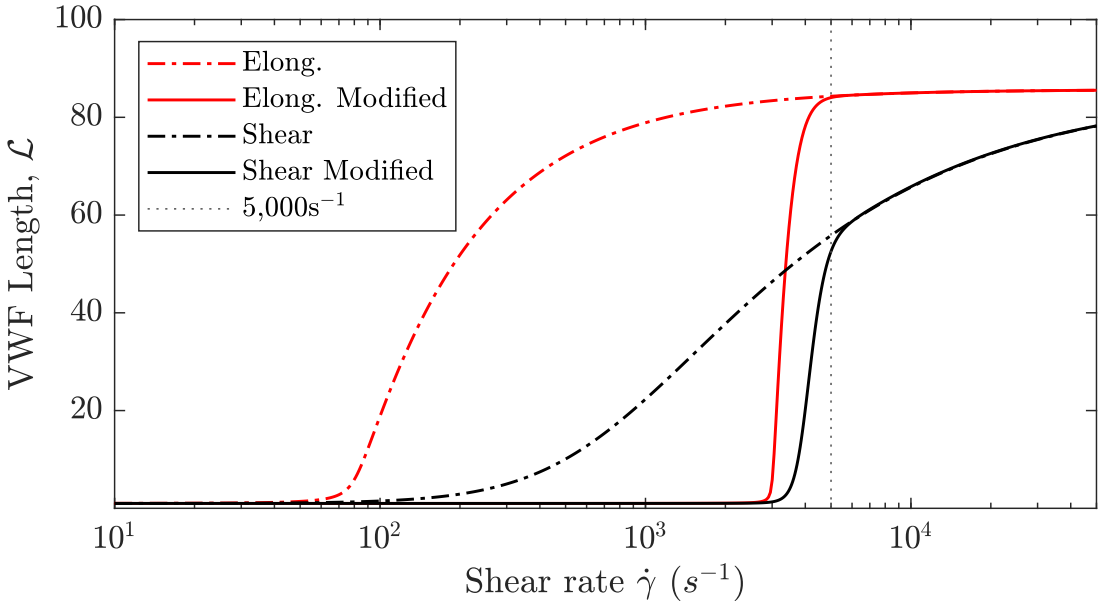

Figure 5.6: VWF length for (5.30) with nonlinear relaxation time (5.31) (solid) and constant relaxation time (dashed). In elongational flow (red), regardless of the relaxation time, the protein unfolds at a lower shear rate than in shear flow (black).

before comparing the numerical predictions to those under constant relaxation time. The solution in shear flow is shown in Fig. 5.4a along with an illustration of an example dumbbell's behaviour in Fig. 5.4b. At low shear, we have $\boldsymbol{A} \approx \boldsymbol{I}$ since the shear rate does not exceed the unfolding threshold. As the shear rate increases, A_{xx} increases and the dumbbell unfolds in the x direction. At large shear rates, $\dot{\gamma} > 5000\,\mathrm{s}^{-1}$, to maintain a finite length, A_{yy} decreases and A_{xx} stops increasing.

The numerical solution in elongation flow is shown in Fig. 5.5a with illustration in Fig. 5.5b. Similarly, at low shear, $\boldsymbol{A} \approx \boldsymbol{I}$, and the protein is globular. As the shear rate increases, A_{xx} increases, and the protein extends in the x direction. As soon as the shear rate is larger than $1000\,\mathrm{s}^{-1}$, A_{yy} decreases independently of the finite length requirement as the flow field causes the protein to shrink in the y direction. For $\dot{\gamma} > 2500\,\mathrm{s}^{-1}$, A_{xx} stops increasing as the maximum length has been reached.

Since shear flow is defined by an elongation and a rotation, whereas elongation flow is pure elongation, the proteins extend to their maximum length at a much lower shear rate in elongation flow. This demonstrates that the model reflects well-established properties of polymers and proteins in flow [14, 103].

We now examine the effect of the modified relaxation time. VWF length $\mathcal{L}$ in shear and elongational flow are shown in Figure 5.6 where the constant relaxation time solution is shown with dashed lines and the modified relaxation time Eq. (5.31)

is shown with solid lines. For both versions of the relaxation time, elongational flow produces greater VWF extension for a given shear rate. In shear flow, the proteins extend although they require larger shear rates to reach maximum length, agreeing with VWF behaviour reviewed in Section 5.2. This also demonstrates that for both elongation flow and shear flow, our modified relaxation time ensures that the proteins remain globular at low shear rates, reflecting the true VWF behaviour, whereas the constant relaxation time solution predicts the protein extends at shear rates $\approx 100\,\mathrm{s}^{-1}$.

We now proceed by detailing the setup of the mathematical model and its remaining components.

5.6 Model setup

In Chapters 6 and 7, we consider thrombosis in two idealised stenosis geometries: an arterial-scale axisymmetric stenosis (Chapter 6), and a microfluidic stenosis model with a rectangular cross section (Chapter 7). These two geometries are shown in Fig. 5.7. For both geometries, the inlet is denoted as Γ_i, the walls of the channel are denoted Γ_w and the outlet is denoted Γ_o. In the axisymmetric geometry in Chapter 6, we also have Γ_c which is the centre of the channel. We proceed by detailing the model components and boundary conditions using these boundary definitions.

We model blood as a Newtonian, viscous fluid transporting platelets and the protein VWF. The flow is driven by a unidirectional inlet flow. We track the concentration of platelets and VWF, splitting them into free and bound populations (adopting the structure of models such as [105, 118]). The bound populations are attached to the stenosis walls and are governed by time-dependent equations at each point on the walls Γ_w. The free populations are advected with the fluid and experience both Brownian motion and shear-induced diffusion which models collisions with RBCs. We assume that platelets and VWF do not influence the blood flow. We do not explicitly model other components of the blood such as RBCs but use an empirical viscosity which has been measured for whole blood [85]. We use (5.30) with nonlinear relaxation time (5.31) to describe the length of VWF at each location which we assume to be independent of its concentration.

We assume that platelet deposition is much slower than the timescale of the flow, and we only consider the initial stages of thrombosis before rapid thrombus growth. Hence, we assume that the pipe remains unchanged and the fluid flow and VWF configuration tensor are both steady. The transport of free VWF and platelets and the equations for bound species are then the only time-dependent equations in the

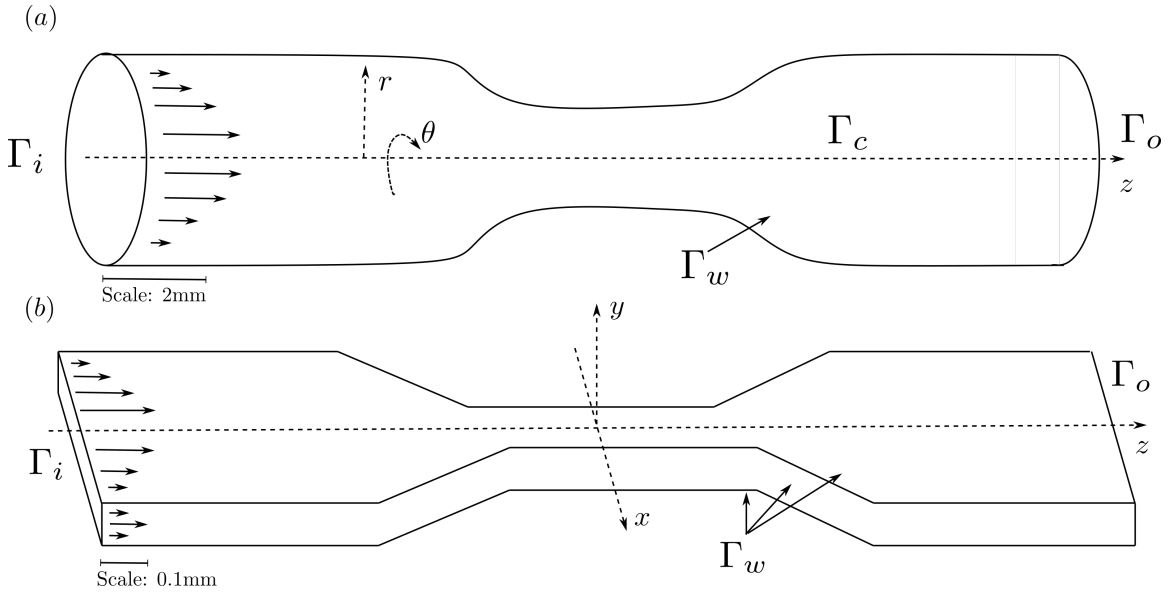

Figure 5.7: (a) In Chapter 6, the geometry is an axisymmetric arterial-scale pipe. Cylindrical polar coordinates are marked. (b) In Chapter 7, the geometry is a 3D microfluidic pipe with a rectangular cross-section. Cartesian coordinates are marked. On each domain, the inlet is marked Γ_i, the outlet is Γ_o, the walls are Γ_w and for the axisymmetric geometry, the pipe centre is marked Γ_c.

model. Since collagen-VWF binding rates are far greater than VWF-platelet bind rates, a VWF layer will form on available collagen much faster than platelets can bind [48]. Hence, we initialise the model with a constant layer of VWF on all walls. We discuss approaches to model VWF-collagen binding in Chapter 8.

We now detail the governing equations for blood, free species and bound species.

5.6.1 Blood flow

We model blood as an incompressible, Newtonian, viscous fluid with velocity $\boldsymbol{u}$ and pressure p. The flow is governed by the steady and incompressible Navier-Stokes equations. We retain inertia as the Reynolds number can reach 800 in the coronary artery [116]. We neglect the effect of gravity. Under these assumptions, the governing equations are

$$\nabla \cdot \boldsymbol{u} = 0, \tag{5.47}$$

$$\rho \boldsymbol{u} \cdot \nabla \boldsymbol{u} = -\nabla p + \mu \nabla^2 \boldsymbol{u}, \tag{5.48}$$

where ρ is the density of the fluid and μ is the viscosity of the fluid.

The flow is driven by a unidirectional, parabolic inlet flow on Γ_i with maximum velocity $w_{\max}$. At the outlet, Γ_o, we prescribe the conditions of no normal stress and

unidirectional flow. In Chapter 6, the latter condition creates a requirement for the pipe to be longer than any recirculation zone behind the stenosis. We prescribe no slip on the walls of the domain Γ_w. In Chapter 6, on the centre of the domain, Γ_c, we prescribe no normal flow and a symmetry condition that the normal derivative of the axial flow vanishes.

5.6.2 Extension of VWF in flow

VWF extension in the flow is governed by the steady version of the modified FENE-P model introduced in Section 5.5. The governing equation is

$$\boldsymbol{u} \cdot \nabla \boldsymbol{A} - \boldsymbol{A} \cdot \nabla \boldsymbol{u} - \nabla \boldsymbol{u}^T \cdot \boldsymbol{A} = -\frac{1}{\tau(\dot{\gamma})}(f(\boldsymbol{A})\boldsymbol{A} - a\boldsymbol{I}). \tag{5.49}$$

We recall that $\boldsymbol{A}$ is the configuration tensor which describes the protein's orientation and length. The relaxation time is a function of the shear rate, defined in Eq. (5.31), which we restate here:

$$\tau(\dot{\gamma}) = \alpha \left(\frac{1}{2}(\tanh(\beta(\dot{\gamma} - \gamma^*)) + 1) + \delta \right). \tag{5.50}$$

In Eq. (5.6), $a = L^2/(L^2 - Tr(\boldsymbol{I}))$ and $f(\boldsymbol{A}) = L^2/(L^2 - Tr(\boldsymbol{A}))$. At the inlet, Γ_i, we prescribe an inlet configuration of VWF $\boldsymbol{A}_{\text{in}}$ which is the numerical solution of Eq. (5.49) under the imposed parabolic flow. Throughout Chapters 6 and 7 we model the relative length and extension of VWF using

$$\mathcal{L} = \frac{\sqrt{Tr(\boldsymbol{A})}}{\sqrt{Tr(\boldsymbol{I})}}, \tag{5.51}$$

$$\mathcal{E} = \frac{\sqrt{Tr(\boldsymbol{A})}}{\sqrt{Tr(\boldsymbol{I})}} - 1, \tag{5.52}$$

as discussed in Section 5.4.1. We use the solution of the Eq. (5.49) on the boundary to describe the length of VWF at the boundary. We now detail the VWF and platelet dynamics.

5.6.3 Transport of VWF and platelets in flow

Free VWF and platelets in the pipe experience both Brownian motion and shear-induced diffusion due to collisions with red blood cells. Hence their concentrations ϕ_v, and ϕ_p, are traced by the following advection-diffusion equations:

$$\frac{\partial \phi_v}{\partial t} + \nabla \cdot (\boldsymbol{u}\phi_v - (D_v + k_{\text{sh}}\dot{\gamma})\nabla \phi_v) = 0, \tag{5.53}$$

$$\frac{\partial \phi_p}{\partial t} + \nabla \cdot (\boldsymbol{u}\phi_p - (D_p + k_{\text{sh}}\dot{\gamma})\nabla \phi_p) = 0, \tag{5.54}$$

where D_v and D_p are the Brownian motion diffusion coefficients. As in Chapters 2 - 4, the shear-induced diffusion is $k_{\text{sh}} = 0.31 r_{\text{RBC}}^2 H^2$ where r_{RBC} is the RBC radius, H is the RBC percentage and 0.31 is an empirically determined constant [46]. This diffusive effect is proportional to the scalar shear rate $\dot{\gamma}$.

At the inlet Γ_i, we prescribe the concentration of VWF and platelets to be ϕ_{vi} and ϕ_{pi}, respectively, the natural concentrations in the blood. Concentrations are measured in kg/m^3. At the outlet Γ_o, the species exit with the flow and we impose no normal diffusive flux. On the pipe walls Γ_w, we prescribe fluxes of the VWF and platelets to model deposition, detailed in Section 5.6.4. The initial concentrations of platelets and VWF in the geometry are constant and equal to ϕ_{vi} and ϕ_{pi}, respectively.

5.6.4 Deposition and bound species

On the stenosis boundary, we track the wall concentration of deposited VWF ϕ_{vb} and platelets ϕ_{pb}. These are surface concentrations with units $[\phi_{pb}] = [\phi_{vb}] =$kg/m^2. We model the deposition of free platelets and VWF on the walls by flux boundary conditions for equations (5.53) and (5.54). We assume that the bound VWF retains the length it had immediately before binding. Hence, the length of the initial bound layer of VWF is determined by the solution of the modified FENE-P equation in the steady flow in the domain, evaluated at the wall.

We assume that free platelets can bind only to bound VWF on the wall and that free VWF can only bind to bound platelets. We neglect any binding in the flow between free platelets and free VWF. A linear relation between VWF length and its binding rate was established in [38]. Hence, we model the binding rate of free platelets to bound VWF on the stenosis surface with the rate $\kappa\mathcal{E}$ where κ is the binding rate of one platelet to a VWF binding site. This means that if the protein is more extended, it binds more rapidly to platelets. These dynamics are summarised in Fig. 5.8.

These modelling assumptions lead to the following flux boundary conditions for Eq. (5.53) and (5.54) on the geometry walls Γ_w:

$$(\phi_v \boldsymbol{u} - (D_v + \dot{\gamma} k_{\text{sh}}) \nabla \phi_v) \cdot \hat{\boldsymbol{n}} = \kappa \mathcal{E} \phi_v \phi_{pb}, \tag{5.55}$$

$$(\phi_p \boldsymbol{u} - (D_p + \dot{\gamma} k_{\text{sh}}) \nabla \phi_p) \cdot \hat{\boldsymbol{n}} = \kappa \mathcal{E} \phi_{vb} \phi_p, \tag{5.56}$$

where $\hat{\boldsymbol{n}}$ is the outward unit normal to the fluid domain. The right-hand-sides of (5.55) and (5.56) model free VWF binding to bound platelets and free platelets binding to bound VWF, respectively.

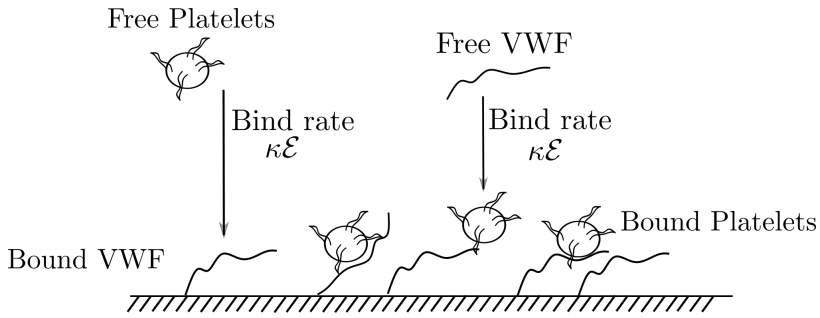

Figure 5.8: Illustration of binding dynamics included in the model. Free species bind to bound species with a binding rate $\kappa\mathcal{E}$.

The concentration of bound platelets and VWF at a fixed location of the stenosis wall are modelled by PDEs, defined by mass conservation, given by

$$\frac{\partial \phi_{vb}}{\partial t} = \kappa\mathcal{E}\phi_v\phi_{pb}, \tag{5.57}$$

$$\frac{\partial \phi_{pb}}{\partial t} = \kappa\mathcal{E}\phi_p\phi_{vb}, \tag{5.58}$$

so that the concentration of bound VWF and bound platelets increase at a rate $\kappa\mathcal{E}$. Initially, we have no bound platelets and a uniform concentration of VWF with $\phi_{vb} = \phi_{vbi}$.

5.6.5 Parameterisation

Model parameters are shown in Table 5.1. Geometric parameters in each of the subsequent chapters are chosen to match the experimental devices of our collaborators shown in Fig. 5.7. Blood, VWF and platelet properties such as concentration and diffusion coefficients are determined from the existing literature [46, 105, 115]. We have estimated the VWF Brownian motion coefficient using the Stokes-Einstein diffusion coefficient $D_v = k_B T/(6\pi\mu r)$ where k_B is Boltzmann's constant, $T = 295K$ is the room temperature in Kelvin. We use a radius of $0.5\,\mu$m as the globular diameter of VWF which is approximately 1 μm [98].

In our model, there are seven unknown parameters: the VWF-platelet binding rate κ, the initial concentration of bound VWF ϕ_{vbi} and the VWF unfolding parameters α, γ^*, β, L, and δ. The qualitatively chosen parameters which we used in Section 5.2 are shown in Table 5.1.

Name	Param.	Value(s)	Units	Source
Viscosity of blood	μ	0.0025	Pa s	[85]
Density of water	ρ	997	kg m^{-3}	
Diffusion coeff. of VWF	D_v	4.9×10^{-13}	m^2 s^{-1}	Estimated
Diffusion coeff. of platelets	D_p	1.58×10^{-13}	m^2 s^{-1}	[105]
Haematocrit	H	0.4	-	[31]
Red blood cell radius	r_{RBC}	3.6×10^{-6}	m	[110]
Shear diffusion coeff.	k_{sh}	6.4×10^{-13}	m^2	[46]
Inlet conc. of VWF	ϕ_{vi}	0.01	kg m^{-3}	[121, 43]
Inlet conc. of platelets	ϕ_{pi}	4.7	kg m^{-3}	[115]
Initial conc. of bound VWF	ϕ_{vbi}	unknown	kg m^{-2}	
Rapid relaxation time	α	9.3×10^{-2}	s	Estimated
Extension parameter	β	6.9×10^{-4}	s	Estimated
Extension parameter	δ	1.59×10^{-4}	-	Estimated
Extension threshold	γ^*	3.8×10^{3}	s^{-1}	Estimated
VWF extensibility	L	16	-	Estimated
Bind rate VWF to platelets	κ	unknown	$m^3(\mathrm{kg\ s})^{-1}$	

Table 5.1: Dimensional model parameters. The VWF parameters listed are the heuristically determined parameters which we use in this chapter. Parameters α - L are estimated in Section 5.5 and κ and ϕ_{vbi} are unknown.

5.7 Analysis outline

We now detail the analysis in the subsequent two chapters. In Chapter 6, we examine this model in the idealised arterial-scale stenosis shown in Fig. 5.7. We reach the shear rates required to unfold VWF by considering flow in this geometry with Reynolds numbers up to 500, which corresponds to shear rates of up to $6,000$ s^{-1}. In this chapter, the stenosis is twice as long as it is tall so that at high Reynolds numbers, the flow recirculates downstream of the stenosis. In Chapter 6, we use the illustrative VWF unfolding parameters which were used in Section 5.5. We then vary the platelet binding parameter rate κ and the initial concentration of bound VWF ϕ_{vbi} to explore the model's behaviour in this regime where the flow is complex.

In Chapter 7, we present a framework for parameterising the model that is motivated by *in vitro* data obtained in the rectangular microfluidic device, shown in Fig. 5.7b. The ratio of the device's height to its length is small, hence it can reproduce arterial-level shear rates albeit with a much simpler flow structure than an arterial-scale device. This simple flow structure and small aspect ratio make the system amenable to model reduction through lubrication theory. The reduced model can then be solved efficiently which makes the large number of simulations needed

for model parameterisation significantly more tractable. Using this reduced model, we then examine how platelet deposition varies if we impose alternative binding conditions. In particular, we consider binding proportional to VWF length and binding which accounts for the available space on the wall.

Our collaborators have shared a data set of thrombosis in the microfluidic device in which the maximum shear rate is $10,000$ s^{-1}. Experimental work is ongoing to obtain more data on thrombosis in these microfluidic devices for varying flow rates and exploring alternative geometries. However, our reduced model allows us to determine which *in vitro* geometries and flow rates would provide the optimal setup to carry out model parameterisation in the future.

Chapter 6

Thrombosis in arterial geometries

In this chapter we examine the model for high-shear thrombosis initiation, presented in Chapter 5, in an idealised, axisymmetric, arterial-scale stenosis geometry. This geometry is chosen to match the *in vitro* setup used by our collaborators to examine VWF deposition [7]. Experiments examining platelet deposition using this arterial scale device are expensive due to the large volume of blood required to fill the system. Furthermore, it is challenging to avoid excess clotting during the experiment setup when compared to smaller volume blood experiments. This motivates this use of our model in this regime as it allows us to offer mechanistic insight into the clotting initiation in this arterial-scale device. In this chapter, we examine our model predictions of VWF unfolding and platelet transport dynamics in the complex flow fields, which occur in large pipes. We then predict the key parameters and geometric features that control platelet deposition location. Accurately predicting the location of clot formation in this device will help guide the design of shear sensitive coatings for thrombosis treatment, as discussed in Chapter 1.

In Section 6.1 we first present our model geometry, which is an axisymmetric reduction of the three-dimensional device used *in vitro*. In Section 6.2 we detail: the model parameters used to describe this geometry; the flow parameters; and our choice of the unknown model parameters that control platelet deposition and VWF unfolding. In Section 6.3 we nondimensionalise the thrombosis model presented in Chapter 5. We discuss the flow and transport regimes of the model and the approximations that are required to solve the model numerically in Section 6.4. Using numerical solutions of the model, we explore the interaction between the Reynolds number, the geometry of the device, and initial platelet deposition. We find that the ratio of VWF length to Reynolds number controls both the rate and location of platelet deposition.

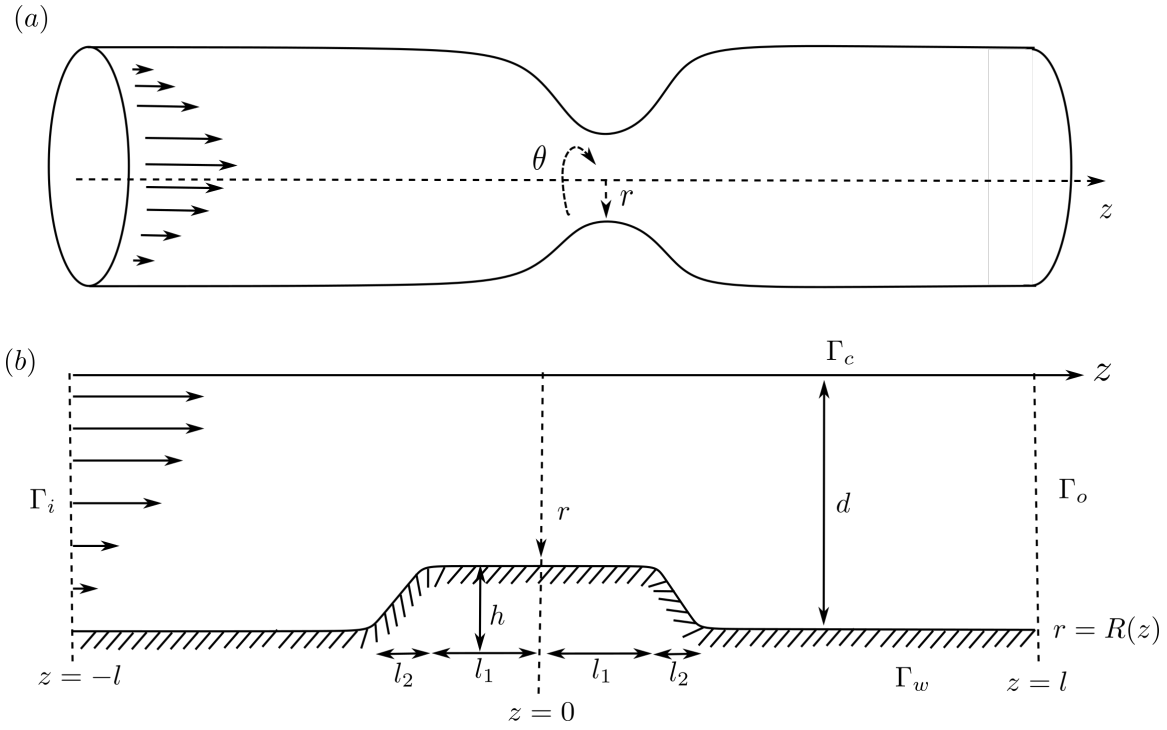

Figure 6.1: (a) Experimental *in vitro* arterial-scale device used by our collaborators Prof. Korin et al. [7]. Cylindrical polar coordinate system which we use in our model is shown. (b) Three-dimensional axisymmetric stenosis geometry. The stenosis is symmetric around $z = 0$ and is defined by parameters l_1, l_2 and h which define the length, steepness and height. Axisymmetric cylindrical polar coordinate axis are marked.

6.1 Geometry description

In this chapter we use an axisymmetric cylindrical polar coordinate system (r, z) with unit vectors $\hat{\boldsymbol{r}}$ and $\hat{\boldsymbol{z}}$ respectively. We consider the geometry of a stenosed pipe, where the pipe has radius $R(z)$, length $2l$ and a constriction centred at $z = 0$, based on our collaborators' *in vitro* model shown in Fig. 6.1a. The stenosis is defined by its height h, length l_1 and steepness h/l_2 as shown in the axisymmetric diagram in Fig. 6.1b. The pipe radius $R(z)$, which is symmetric around $z = 0$, is given by the following equation

$$R(z) = \begin{cases} d & \text{for } -l < z < -l_1 - l_2, \\ s(z) & \text{for } |z| < l_1 + l_2, \\ d & \text{for } l_1 + l_2 < z < l, \end{cases} \tag{6.1}$$

where d is the radius of the unobstructed region of the pipe. Here $s(z)$ describes the stenosis of the pipe, which is made up of a cubic spline in the region $-l_1 - l_2 < z < -l_1$ that smoothly increases from d to $d - h$, then for $-l_1 < z < l_1$, $s(z) = d - h$ and

similarly in the region $l_1 < z < l_1 + l_2$ a spline decreases from $d - h$ to d. This is illustrated in Figure 6.1b. The boundaries of the domain are denoted by

$$\Gamma_i = \{z = -l,\ 0 \leq r \leq d\}, \tag{6.2}$$

$$\Gamma_o = \{z = l,\ 0 \leq r \leq d\}, \tag{6.3}$$

$$\Gamma_w = \{-l \leq z \leq l,\ r = R(z)\}, \tag{6.4}$$

$$\Gamma_c = \{-l \leq z \leq l,\ r = 0\}, \tag{6.5}$$

corresponding to the inlet, outlet, pipe wall and pipe centre, respectively. In the *in vitro* experiments, the stenosis has $l_1 = 0$. However, we retain this parameter so that we can explore pipe geometries outside of the *in vitro* system.

6.2 Parameterisation

Model parameters that are specific to this chapter are shown in Table 6.1 and all other parameters are listed in Table 5.1. The vessel radius is chosen to match the *in vitro* device and the half length (8cm) is chosen so that the fluid recirculation zone can be fully contained in the model domain. This threshold is determined in Appendix B.3. In this chapter we use the qualitatively chosen VWF extension parameters employed to examine the FENE-P model in Chapter 5. This leaves the binding rate κ and the initial concentration of bound VWF ϕ_{vbi} as unknowns. We vary these parameters along with the inlet flow velocity, stenosis height, width and steepness in the ranges shown in Table 6.1. This allows us to consider the system for a range of Reynolds numbers and geometries, as well as performing a systematic parameter study to examine how the predictions depend on unknown parameters.

6.3 Dimensionless model

We now nondimensionalise the model defined in Section 5.6 in Chapter 5. We nondimensionalise by scaling lengths with the maximum pipe radius d. The fluid velocity components are scaled with the maximum inlet velocity w_{max}. We consider the system on the timescale of platelet deposition $1/\kappa\phi_{pi}$. We scale the free VWF and platelet concentrations relative to their inlet concentrations ϕ_{pi} and ϕ_{vi} respectively. The two bound species are both scaled relative to the initial concentration of bound VWF ϕ_{vbi}. The configuration tensor is dimensionless so does not require scaling. Hence we

Name	Param.	Value(s)	Units	Source
Pipe half length	l	0.08	m	Appendix B.3
Radius of system	d	0.002	m	[7]
Stenosis height	h	$[0.6-1]\times10^{-4}$	m	Describes 30 - 50% occlusion
Stenosis length	l_1	0 - 0.006	m	Varied from 0 - $3d$
Stenosis para.	l_2	0.002 - 0.006	m	Varied from d - $3d$
Maximum inlet velocity	w_{max}	0.089 - 0.22	m s^{-1}	Varied around value used in [7]
Bind rate VWF to platelets	κ	0.047-0.47	$m^3(s\,kg)^{-1}$	Unknown, example values chosen
Initial conc. of bound VWF	ϕ_{vbi}	$[0.094-9.4]\times10^{-4}$	kg m^{-2}	Unknown, example values chosen

Table 6.1: Model parameters with values used in this chapter. All other parameters are shown in Table 5.1.

define dimensionless variables with hats as follows

$$z = d\hat{z}, \qquad r = d\hat{r}, \qquad t = \frac{1}{\kappa\phi_{pi}}\hat{t}, \qquad p = \frac{w_{max}\mu}{d}\hat{p}, \qquad u = w_{max}\hat{u}, \tag{6.6}$$

$$w = w_{max}\hat{w}, \quad \phi_v = \phi_{vi}\hat{\phi}_v, \quad \phi_p = \phi_{pi}\hat{\phi}_p, \quad \phi_{pb} = \phi_{vbi}\hat{\phi}_{pb}, \quad \phi_{vb} = \phi_{vbi}\hat{\phi}_{vb}. \tag{6.7}$$

Under these scalings the pipe half-length is $\hat{l} = l/d$ and the pipe wall is defined as $\hat{R}(\hat{z}) = R(z)/d$. Inserting scalings (6.6) and (6.7) into Eqs. (5.47) - (5.48) and dropping hats on dimensionless variables, the dimensionless Navier-Stokes equations are

$$\nabla \cdot \boldsymbol{u} = 0, \tag{6.8}$$

$$Re\,\boldsymbol{u}\cdot\nabla\boldsymbol{u} = -\nabla p + \nabla^2\boldsymbol{u}, \tag{6.9}$$

where the Reynolds number is defined $Re = \rho w_{max} d/\mu$. The dimensionless steady FENE-P equation, (5.49), is

$$\boldsymbol{u}\cdot\nabla\boldsymbol{A} - \boldsymbol{A}\cdot\nabla\boldsymbol{u} - \nabla\boldsymbol{u}^T\cdot\boldsymbol{A} = -\frac{1}{\xi Re\hat{\tau}(\dot{\gamma})}(f(\boldsymbol{A})\boldsymbol{A} - a\boldsymbol{I}), \tag{6.10}$$

where $\xi = \alpha\mu/d^2\rho$ is defined so that the product ξRe is the Deborah number, which represents the ratio of the timescales of protein relaxation to fluid advection. However, we choose to work with ξ rather than the Deborah number so that we are able to examine the system for varying Re. The FENE-P function $f(\boldsymbol{A}) = L^2/(L^2 - Tr(\boldsymbol{A}))$

and $a = L^2/(L^2-2)$ remain unchanged as L is dimensionless. The dimensionless VWF relaxation time is

$$\hat{\tau}(\dot{\gamma}) = \frac{1}{2}\left(\tanh\left(\hat{\beta}Re\left(\dot{\gamma} - \frac{\hat{\gamma}^*}{Re}\right)\right) + 1\right) + \delta, \tag{6.11}$$

where $\hat{\beta} = \beta\mu/d^2\rho$ and $\hat{\gamma}^* = \gamma^*\rho d^2/\mu$ are the dimensionless relaxation time parameters. VWF extension is then defined, from (5.52), as

$$\mathcal{E} = \frac{\sqrt{Tr(\boldsymbol{A})}}{\sqrt{2}} - 1. \tag{6.12}$$

The dimensionless free VWF and platelet transport equations, derived from (5.53) and (5.54), are given by

$$\frac{\hat{\kappa}}{Re}\frac{\partial\phi_v}{\partial t} + \nabla\cdot\left(\boldsymbol{u}\phi_v - \hat{D}_v\nabla\phi_v\right) = 0, \tag{6.13}$$

$$\frac{\hat{\kappa}}{Re}\frac{\partial\phi_p}{\partial t} + \nabla\cdot\left(\boldsymbol{u}\phi_p - \hat{D}_p\nabla\phi_p\right) = 0. \tag{6.14}$$

Here the dimensionless VWF-platelet binding rate is $\hat{\kappa} = d^2\kappa\phi_{pi}\rho/\mu$. The ratio $\hat{\kappa}/Re$ is equal to inverse of the Damköhler number, $Da = w_{max}/\kappa\phi_{pi}d$, which is the ratio of the timescale of platelet deposition to the timescale of fluid advection. If the deposition is slower than the fluid timescale, then $Da > 1$ or equivalently $\hat{\kappa} < Re$. (This appears with the time derivatives in (6.13) and (6.14) since we have nondimensionalised on the timescale of platelet deposition.) The dimensionless diffusion coefficients for VWF and platelets are

$$\hat{D}_v = \left(\frac{1}{Pe_v} + \frac{\dot{\gamma}}{Pe_{sh}}\right), \quad \hat{D}_p = \left(\frac{1}{Pe_p} + \frac{\dot{\gamma}}{Pe_{sh}}\right). \tag{6.15}$$

Here we define the Brownian Péclet numbers for VWF and platelets as $Pe_v = w_{max}l/D_v$ and $Pe_p = w_{max}l/D_p$ respectively, which define the ratio of advection to the diffusion for each species. The final dimensionless parameter is shear Péclet number $Pe_{sh} = d^2/k_{sh}$, which is the squared ratio of the pipe width to the length scale over which cells are pushed by collisions with RBCs.

The dimensionless bound species equations, derived from (5.58) and (5.57), are

$$\frac{\partial\phi_{vb}}{\partial t} = \sigma_v\phi_v\phi_{pb}\mathcal{E}, \tag{6.16}$$

$$\frac{\partial\phi_{pb}}{\partial t} = \phi_p\phi_{vb}\mathcal{E}. \tag{6.17}$$

Here $\sigma_v = \phi_{vi}/\phi_{pi}$ is the ratio of the inlet concentrations of VWF and platelets.

The dimensionless boundary conditions for the system, derived from their dimensional equivalents described in Chapter 5, Sections 5.6, are

$$w = \left(1 - r^2\right), \quad u = 0, \quad \boldsymbol{A} = \boldsymbol{A}_{in}(r), \quad \phi_v = 1, \quad \phi_p = 1 \quad \text{on} \quad \Gamma_i, \tag{6.18}$$

$$\hat{\boldsymbol{n}} \cdot \boldsymbol{\sigma} \cdot \hat{\boldsymbol{n}} = 0, \quad u = 0, \quad \nabla\phi_p \cdot \hat{\boldsymbol{n}} = 0, \quad \nabla\phi_v \cdot \hat{\boldsymbol{n}} = 0 \quad \text{on} \quad \Gamma_0, \tag{6.19}$$

$$u = 0, \quad \frac{\partial w}{\partial r} = 0, \quad \nabla\phi_v \cdot \hat{\boldsymbol{n}} = 0, \quad \nabla\phi_p \cdot \hat{\boldsymbol{n}} = 0 \quad \text{on} \quad \Gamma_c, \tag{6.20}$$

$$\boldsymbol{u} = \boldsymbol{0}, \quad (\phi_p \boldsymbol{u} - \hat{D}_p \nabla\phi_p) \cdot \hat{\boldsymbol{n}} = \sigma_b \frac{\hat{\kappa}}{Re} \phi_p \phi_{vb} \mathcal{E} \quad \text{on} \quad \Gamma_w, \tag{6.21}$$

$$(\phi_v \boldsymbol{u} - \hat{D}_v \nabla\phi_v) \cdot \hat{\boldsymbol{n}} = \sigma_b \frac{\hat{\kappa}}{Re} \phi_v \phi_{pb} \mathcal{E} \quad \text{on} \quad \Gamma_w. \tag{6.22}$$

In (6.21) and (6.22) $\sigma_b = \phi_{vbi}/d\phi_{pi}$ is the ratio of the initial concentration of bound VWF to the inlet concentration of platelets. The inlet value of the configuration tensor $\boldsymbol{A}_{in}$ can be found by solving Eq. (6.10) using the parabolic inlet flow. This is detailed in Section 6.4. The initial conditions for the free and bound concentrations are

$$\phi_v = 1, \ \phi_p = 1, \ \phi_{vb} = 1, \ \phi_{pb} = 0 \text{ at } t = 0. \tag{6.23}$$

Dimensionless parameters and their values are shown in Table 6.2. To summarise: the model consists of the steady Navier-Stokes equations, (6.8) and (6.9), with Reynolds numbers from $200 - 500$. We have a steady, FENE-P equation, (6.10) with a modified relaxation time, (6.11), which describe the extension of VWF in the fluid. We note that we have assumed VWF extension is independent of VWF and platelet concentration. The nonlinear relaxation time multiplied by the Deborah number, $\xi Re\tau$, ranges from 0.002 to 666 when $Re = 200$ and $Re = 600$ respectively, demonstrating that at lower Reynolds numbers the protein elasticity dominates in (6.10), whereas, at higher Re the elastic forces are subdominant to fluid shear forces. VWF and platelet concentrations are determined by (6.13) and (6.14) which are only one-way coupled to the fluid flow and VWF extension. The range of Péclet numbers in Table 6.2 illustrates their values at the maximum and minimum flow rates we consider in this chapter. The Brownian and shear Péclet number are large for both VWF and platelets at all flow rates. As we detail in the following section, we decrease the size of these Péclet numbers and neglect shear-induced diffusion when performing numerical simulations. The bound species are coupled to the free species through (6.16) and (6.17) on the wall of the pipe. The bound VWF equation (6.16) has growth rate $\sigma_v = 0.0021$ which is small since the concentration of VWF is much less than the concentration of platelets in the blood.

We now detail the numerical scheme which we use to solve this model.

Name	Param.	Definition	Value(s)
Dimensionless pipe length	$\hat{l}$	l/d	$30 + \hat{l}_1 + \hat{l}_2$
Dimensionless stenosis height	$\hat{h}$	h/d	0.3–0.5
Dimensionless stenosis length	$\hat{l}_1$	l_1/d	0–3
Dimensionless stenosis parameter	$\hat{l}_2$	l_2/d	1–3
Reynolds number	Re	$w_{max}d\rho/\mu$	200–500
VWF Péclet number	Pe_v	$w_{max}d/D_v$	$[3.6\text{–}8.9]\times10^8*$
Platelet Péclet number	Pe_p	$w_{max}d/D_p$	$[1.1\text{–}2.7]\times10^8*$
Shear Péclet number	Pe_{sh}	d^2/k_{sh}	$1.6 \times 10^7*$
VWF extension parameter	$\hat{\beta}$	$\beta\mu/d^2\rho$	3.12×10^{-4}
VWF globular relaxation time	δ	-	1×10^{-4}
VWF extension parameter	ξ	$\alpha\mu/d^2\rho$	4/3
VWF extension threshold	$\hat{\gamma}^*$	$\gamma^* d^2\rho/\mu$	2×10^4
VWF binding rate to platelets	$\hat{\kappa}$	$\kappa\phi_{pi}d^2\rho/\mu$	1–10
Ratio of VWF-platelet inlet concs.	σ_v	ϕ_{vi}/ϕ_{pi}	0.0021
Ratio of bound VWF to inlet platelet concs.	σ_b	$\phi_{vbi}/d\phi_{pi}$	0.001–0.1

Table 6.2: Dimensionless model parameters. Péclet numbers are listed at their *in vitro* values, however we decrease these values in our simulations, as detailed in Section 6.4.

6.4 Numerical solution of the model

In this chapter we examine the system for Reynolds number ranges from 200 to 500 for an illustrative range of stenosis geometries. The Péclet numbers are extremely large for both platelets and VWF, so we can expect that the transport dynamics of both species to be dominated by advection. We will use the finite element method to solve this system. This is designed for elliptic PDEs and is unable to solve PDEs with large Péclet numbers. As a result, in this chapter, we include artificially large diffusion in VWF and platelet transport equations to avoid oscillations in the solution. As well as this, we neglect the effect of shear-induced diffusion. In all equations we use a Péclet numbers of 10^3 to avoid instability. Despite this being several orders of magnitude smaller than the true Péclet number, we expect these results to give insight into the physiological regime.

Furthermore, we add artificial diffusion to the FENE-P equation (6.10) so that the equation is elliptic, with Péclet number 1000. Hence, we must prescribe boundary conditions for the configuration tensor on all boundaries. We prescribe the symmetry

condition $\nabla \boldsymbol{A} \cdot \hat{\boldsymbol{n}} = \boldsymbol{0}$ on the centre of the pipe and no normal diffusive flux on the walls as this avoids excessive increases in the configuration tensor in boundary layers on the walls, following the approach by [93, 108]. We note that, as discussed in Chapter 5, the FENE-P equation was derived in the absence of walls. Hence the choice of boundary conditions when artificial diffusion is added is an open question for both the FENE-P model and other viscoelastic fluid models [32].

6.4.1 Numerical method

We solve the model using the finite element method implemented using the Python Package FEniCS [2, 71] which allows implementation of the weak form in the language UFL [3, 4]. This problem is then compiled by FIAT [62, 63] and assembled into finite element form by UFC [3, 5]. We use GMSH to construct a mesh of the stenosis geometry [42]. Since the PDEs for flow are uncoupled, and the FENE-P equations and transport equations are only one-way coupled to the flow, we solve the problems separately. We first solve the steady PDEs, for the flow and configuration tensor, and then solve the time-dependent equations for free and bound concentrations. We now summarise the scheme. The weak form of all governing equations is shown in Appendix A for brevity.

We first solve numerically the steady Navier-Stokes equations. We use Taylor Hood elements of first- and second-order for the pressure and velocity vector respectively. The steady nonlinear system is solved using the inbuilt Newton Solver *solve* as part of the FEniCS package. The velocity gradients in each direction, along with the wall shear rate on the pipe wall, are determined using first-order elements as functions of the velocity solution. The velocity gradients, velocity field and the shear rate can then be used to solve all subsequent PDEs.

The FENE-P equation consists of four coupled advection-diffusion equations with the velocity field coming from the solution of the Navier-Stokes equations. As discussed above, we include diffusion in these equations to maintain numerical tractability. We use first-order Lagrange elements to solve for each component of the configuration tensor. To solve the system we employ continuation in the Reynolds number. Our initial guess for the solver for $Re = 0$ is that $\boldsymbol{A} = \boldsymbol{I}$. We then continue in the Reynolds number, by increasing Re in steps of 12, using the solution at each iteration as the initial condition for the Newton solver at the current Re. We regularise the square root in the definition of VWF extension (6.12) to avoid numerical error as

follows

$$\mathcal{E} = \frac{\sqrt{A_{rr} + A_{zz} + 0.01}}{\sqrt{2}} - 1. \tag{6.24}$$

Here 0.01 is added to avoid the production of complex numbers when the trace of the configuration tensor $Tr(\boldsymbol{A})$ is small but negative due to numerical error. The value 0.01 represents 0.004% of the maximum value of the trace of the configuration tensor L^2, so this regularisation will not significantly affect the value of $\mathcal{E}$ we use in the solution of the transport equations.

The inlet value of the configuration tensor is found by solving Eq. (6.10) under the imposed inlet flow $\boldsymbol{u} = (1 - r^2)\hat{\boldsymbol{z}}$. Eq. (6.10) then reduces to the following algebraic system

$$\frac{A_{rr}}{L^2 - A_{rr} - A_{zz}} = \frac{1}{L^2 - 2}, \tag{6.25}$$

$$-2r\tau A_{rr} = \left(\frac{L^2 A_{rz}}{L^2 - A_{rr} - A_{zz}}\right), \tag{6.26}$$

$$-4r\tau A_{rz} = \left(\frac{L^2 A_{zz}}{L^2 - A_{rr} - A_{zz}} - \frac{L^2}{L^2 - 2}\right). \tag{6.27}$$

We solve the nonlinear system numerically, using the *NumPy* Newton solver *fsolve*, with an initial guess of $\boldsymbol{A} = \boldsymbol{I}$.

We then solve the time-dependent system for the free and bound VWF and platelet concentrations. We use first-order Lagrange elements for the free species. The bound species are modelled by a vector of their values at each node of the mesh on the boundary Γ_w. We use explicit first-order time-stepping to solve for the free species ϕ_p and ϕ_v, which are governed by (6.13) and (6.14), coupled to the bound species ϕ_{pb} and ϕ_{vb}, which are governed by (6.16) and (6.17). We define the discrete time points as $t_i = i\delta t$ where $\delta t = 0.005$ is the fixed timestep. We solve for free species ϕ_p and ϕ_v at time $t_i = i$ using the bound solution from t_{i-1}. We then solve for the bound species ϕ_{pb} and ϕ_{vb} at time t_i using the solution $\phi_p(t_i)$ and $\phi_v(t_i)$. We choose to solve this system until deposited platelets have built up to a fixed value which we chose as twice the level at the inlet, given by $\max \phi_{pb} = 2$. This allows comparison between different geometries and binding dynamics.

The mesh convergence, time-stepping analysis, numerical continuation verification, and confirmation of geometry length required to contain the entire fluid recirculation zone are all shown in Appendix B.3.

6.5 Numerical results

We first examine an example of the model solution for $Re = 400$. In Section 6.5.1, we then examine how the platelet deposition varies for a fixed geometry as the Reynolds number varies. In Section 6.5.2, we fix the Reynolds number and vary the stenosis geometry. Finally, in Section 6.5.3, we examine how deposition depends on the platelet-VWF binding rate and the initial concentration of VWF on the wall.

Figure 6.2 shows the numerical solution of the model obtained for $Re = 400$. All subfigures illustrate solutions overlaid by the fluid streamlines. In these simulations we set $\hat{\kappa} = 10$ and $\sigma_b = 0.1$ so that the binding is approximately forty times slower than fluid advection and there is a low initial concentration of VWF on the boundary. At this Reynolds number, a recirculation zone forms downstream of the stenosis as illustrated by the streamlines. The magnitude of the fluid velocity is shown in Fig. 6.2a. The flow is almost three times faster as it crosses the stenosis compared to upstream. VWF extension $\mathcal{E}$ is shown Fig. 6.2b. VWF reaches $\mathcal{E} \approx 11$ which is the maximum extension achievable with the extensibility parameter $L = 16$. The maximum extension is obtained at the boundary, slightly upstream of the stenosis centre. Free VWF and free platelets are shown in Fig. 6.2c and d, respectively $t = 0.06$, when bound platelets reach $\phi_{pb} = 2$. Free VWF and platelets are absorbed in a boundary layer, with the maximum absorption located where VWF is most extended.

We now examine the interaction between the stenosis shape, the wall shear rate and the extension on the base, which are shown in Fig. 6.3a,b and c, respectively. The wall shear rate is greatest at $z \approx -1.33$, at the upstream edge of the stenosis, this is marked by the red line on all the plots. The recirculation zone begins at the point where the shear rate is zero at $z \approx 1.7$. We can see that the VWF extension, shown in Fig. 6.3c, has a similar qualitative shape to the shear rate, and attains its maximum value of $\mathcal{E} = 10.8$ at the same location as the maximum wall shear rate. We note that the wall shear rate only exceeds the unfolding threshold $\gamma^*/Re = 50$ for a very small region $z \in [-1.38, -1.31]$ but VWF is able to extend to significant levels across the entire stenosis. We recall that for $\dot{\gamma} \ll \gamma^*/Re$ we have a relaxation time of $\tau = \delta = 0.01$ and for $\dot{\gamma} \gg \gamma^*/Re$ the relaxation time is $\tau = 1 + \delta$. Hence the amount VWF can extend at low shear rates is determined by the parameter δ, which has been qualitatively selected. It is possible that for other values of δ, VWF may not extend at all at low shear rates.

We now examine the bound platelets and VWF on the base, which are shown over increasing time intervals of $\delta t = 0.005$ in Fig. 6.4a and b. We have marked the

location where the wall shear rate, and VWF extension are greatest by the black vertical line. The bound platelets, shown in Fig. 6.4b, build up slightly upstream of the point of maximum VWF extension. VWF then binds to the bound platelets with a peak at the same location shown in Fig. 6.4a. Since $\sigma_v = 0.0021$ the bound VWF concentration does not significantly increase on the timescale of platelet deposition and stays close to its initial value of $\phi_{vb} = 1$. Since σ_v has been estimated using well established values of the concentrations of VWF and platelets in the blood, VWF deposition will always be slower than platelet deposition in the current model framework. This demonstrates the importance of the choice of the initial bound VWF concentration and that, in future analysis of this model, additional VWF deposition can be neglected.

At this Reynolds number platelet deposition occurs predominantly close to the upstream edge of the stenosis. This is, therefore, the likely location for thrombus location. We proceed by examining the dependence of this location on Reynolds number and geometry.

6.5.1 Platelet deposition for varying Reynolds number

We now examine how platelet deposition changes as the Reynolds number varies for a fixed stenosis geometry. We solve the model for Re between 200 and 500 in intervals of $Re = 25$. The wall shear rate, VWF extension, VWF relaxation time and bound platelet concentration for increasing Reynolds number are shown in Figure 6.5 , where we plot each variable along the stenosis wall against the Reynolds number. For the bound platelet concentration we show the solution at the final time, when the solution first exceeds $\phi_{pb} = 2$.

The shear rate on the stenosis wall is shown in Fig. 6.5a, illustrating that as the Reynolds number increases, the shear rate increases. The maximum shear rate occurs upstream of the stenosis centre for all Re with the location of the maximum moving further upstream for increasing Re. We use the point where $\dot{\gamma} = 0$, which is shown dashed, to show the start of the recirculation zone on all plots. VWF extension on the base of the stenosis is shown in Fig. 6.5c. The protein first begins to significantly unfold at $Re = 325$ and reaches a maximum extension of $\mathcal{E} = 10.8$ at $Re = 400$. As Re increases beyond this, VWF unfolds further upstream and remains unfolded as it travels downstream. This reflects the increasing shear rate which occurs as Re increases. The relaxation time of VWF is shown in Fig. 6.5b which increases in the regions where the shear rate exceeds γ^*/Re, allowing VWF to unfold more easily. As we noted in the previous section, at our choice of δ VWF is able to extend for lower

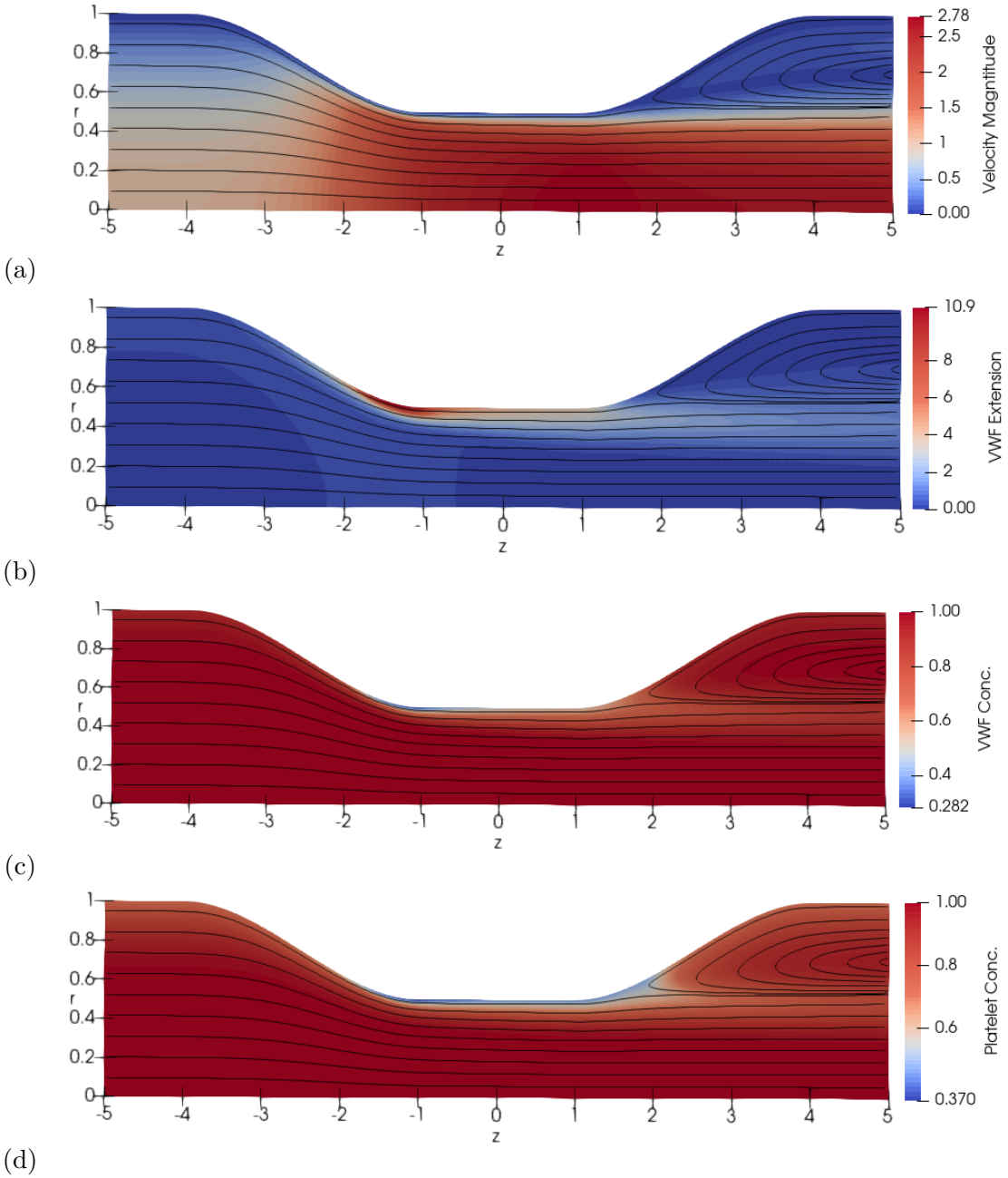

Figure 6.2: Numerical solutions for $Re = 400$. (a) A recirculation zone forms downstream of the stenosis, indicated by circular streamlines. (b) VWF is fully extended at the upstream peak of the stenosis. (c) Free VWF is used up in a boundary layer at the upstream stenosis peak. (d) Free platelets are absorbed in the boundary layer across the stenosis. Plots (c) and (d) are shown at $t = 0.06$. Parameter values: $\hat{l}_1 = 1,\ \hat{l}_2 = 2,\ \hat{h} = 0.5,\ \hat{\kappa} = 10,\ \sigma_b = 0.1$.

values of the wall shear rate, as shown by comparison between Fig. 6.5b and c, e.g. the protein is able to obtain extensions of $\mathcal{E} = 5$ at $Re = 300$ when $\hat{\tau}$ remains equal

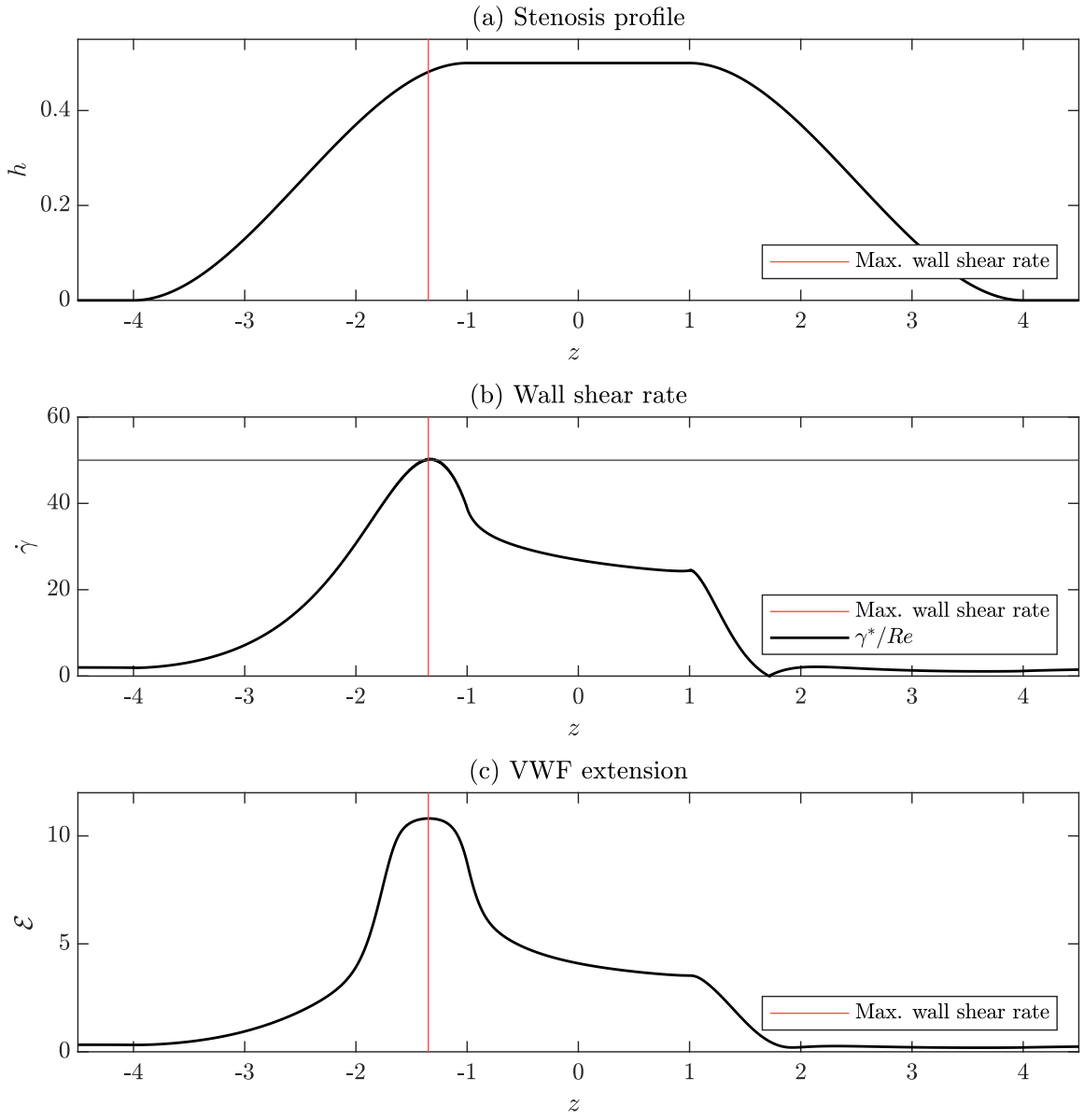

Figure 6.3: Variables on the pipe wall for the solution shown in Fig. 6.2. The maximum wall shear rate is marked with a red line and $\dot{\gamma} = \gamma^*/Re$ is shown by horizontal line in (b). (a) The stenosis profile. (b) Wall shear rate has a peak at the upstream edge of the stenosis $z \approx -1.33$, the recirculation zone begins when $\dot{\gamma} = 0$. (c) VWF extension, the protein reaches its maximum extension of $\mathcal{E} \approx 11$ where the wall shear rate is greatest. Parameter values: $\hat{l}_1 = 1,\ \hat{l}_2 = 2,\ \hat{h} = 0.5,\ \hat{\kappa} = 10,\ \sigma_b = 0.1,\ Re = 400$.

to 0.01.

The distribution of bound platelets is shown in Fig. 6.5d at the time when the maximum bound platelet concentration is $\phi_{pb} = 2$. For $Re \leq 300$, the platelet deposition occurs across the entire stenosis, with a higher deposition on the upstream

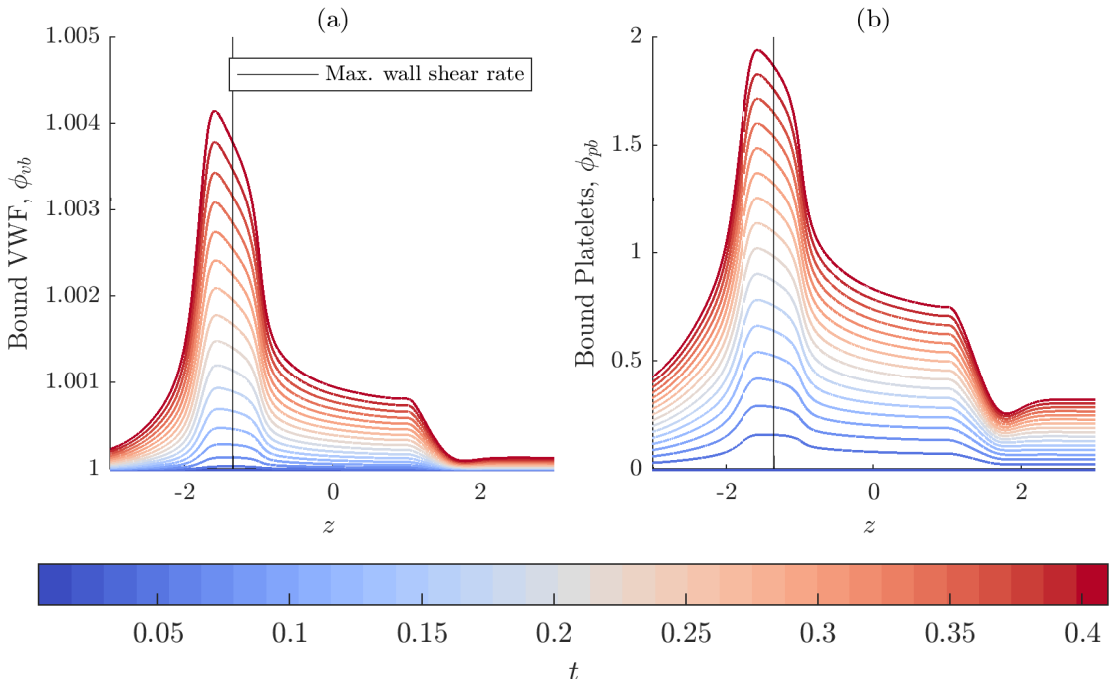

Figure 6.4: Variables on the pipe wall for the solution shown in Fig. 6.2. The location of maximum wall shear rate is shown by black line. (a) Bound VWF, and (b) bound platelets are shown at increasing timesteps of $t = 0.025$ until $t = 0.41$ when ϕ_{pb} reaches 2. The time of the solution is indicated by the colour bar below. Platelets are deposited slightly downstream of the point of maximum extension close to the stenosis apex. Bound VWF are deposited in lower levels to the bound platelets. Parameter values: $\hat{l}_1 = 1,\ \hat{l}_2 = 2,\ \hat{h} = 0.5,\ \hat{\kappa} = 10,\ \sigma_b = 0.1,\ Re = 400$.

edge. At approximately $Re = 350$, when the protein is unfolded, platelet deposition occurs predominantly on the upstream edge of the stenosis. Then for $Re \geq 400$, platelets are deposited again across the entire stenosis.

The time taken to reach $\phi_{pb} = 2$ is plotted in Fig. 6.6. For $Re < 350$ when VWF is globular, deposition is relatively slow. Then at $Re = 350$, VWF extends and the deposition rate increases.

6.5.2 Platelet deposition for varying stenosis geometry

We now examine VWF extension as we vary the stenosis geometry for a fixed Reynolds number of $Re = 400$. We compare varying the overall length of the stenosis, $\hat{l}_1$ while maintaining a constant height, $\hat{h} = 0.5$ and steepness, $\hat{l}_2 = 1.5$. As illustrated in Fig. 6.7a, increasing the length of the stenosis leads to VWF unfolding further upstream and remaining unfolded further downstream. This reflects that the maximum shear rate, which triggers VWF unfolding, occurs at the upstream edge of the steno-

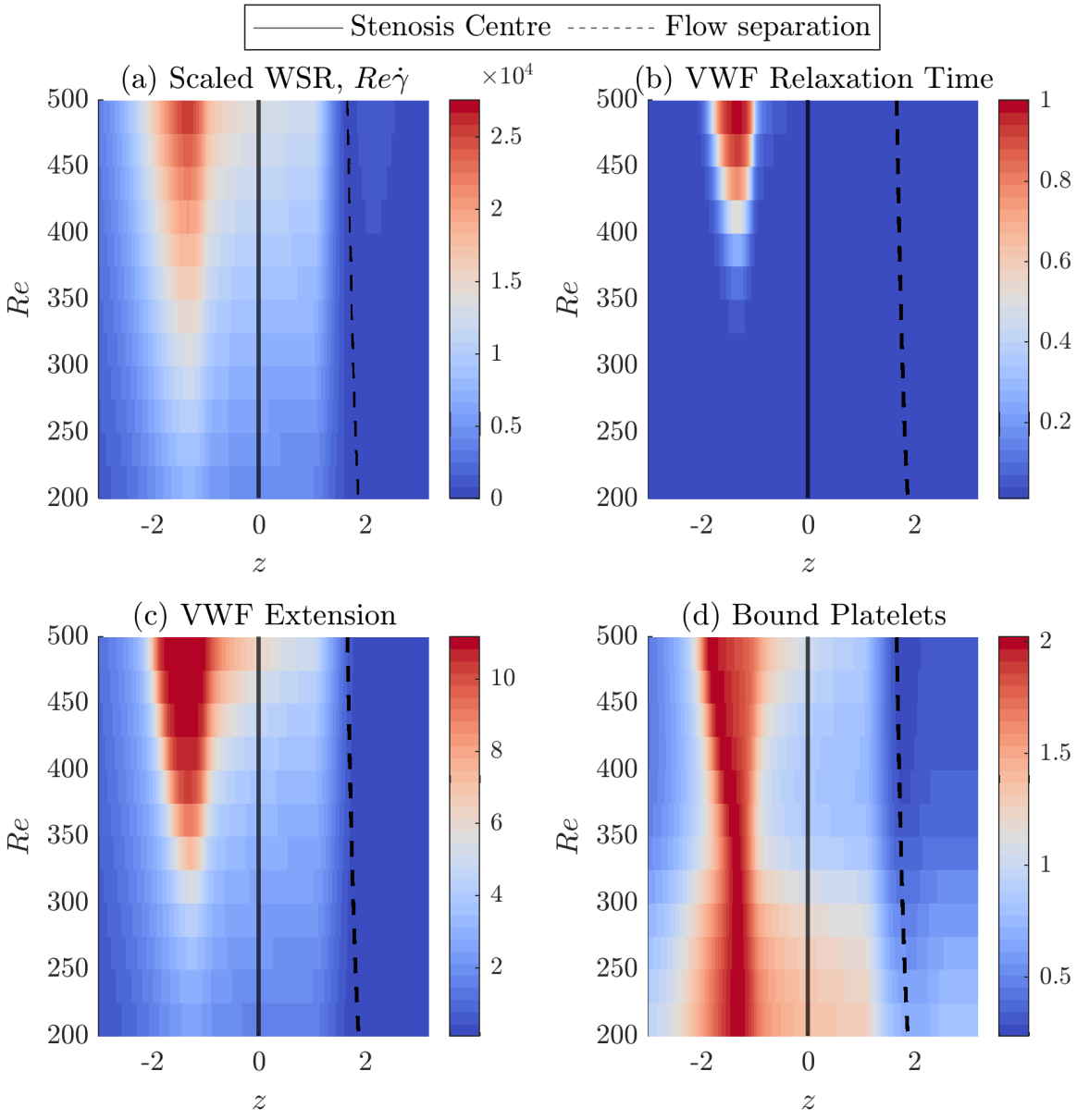

Figure 6.5: Solution of the model for increasing Re for a stenosis which obstructs flow from $z = -2.5$ to $z = 2.5$. (a) Wall shear rate for increasing Re; flow separation occurs at all Re shown, as indicated by zero wall shear rate (dashed line) (b) VWF relaxation time illustrates where the shear exceeds the unfolding threshold. (b) VWF extension at the wall shows that the maximum extension occurs upstream of the stenosis centre with the proteins remaining extended over a greater region as Re increases. (d) Platelet deposition is shown: for low Re deposition occurs all over the stenosis, at mid Re it occurs predominantly upstream and at high Re it is deposited across more of the stenosis. Parameter values: $\hat{l}_1 = 1,\ \hat{l}_2 = 2,\ \hat{h} = 0.5,\ \hat{\kappa} = 10,\ \sigma_b = 0.1$.

sis. Furthermore, increasing the stenosis length leads to an overall larger region of the pipe where the shear rate is high and, therefore, where VWF can unfold, which

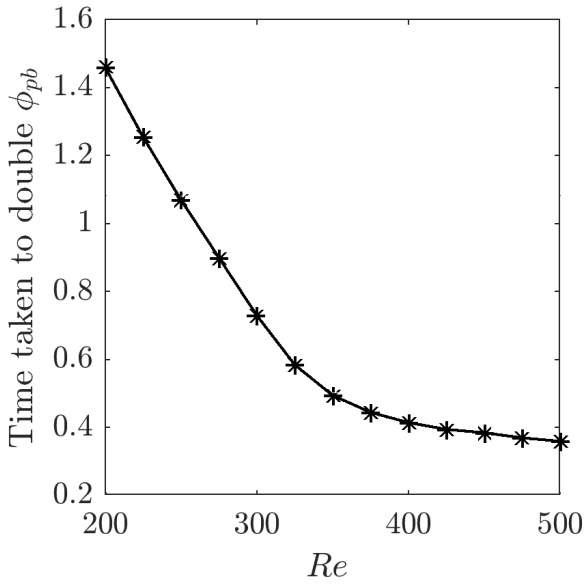

Figure 6.6: Time taken to double ϕ_{pb} for each Reynolds number.

will result in platelet deposition over a larger region.

VWF extension for increasing stenosis steepness is shown in Fig. 6.7b. This corresponds to decreasing the parameter $\hat{l}_2$. Increasing the steepness of the stenosis increases the maximum shear rate in the pipe and causes VWF to unfold more. For all cases we fixed $\hat{h} = 0.5$, and then reduced $\hat{l}_2$ to examine steeper stenoses. As a result, shallower stenoses that have larger values of $\hat{l}_2$ obstruct more of the length of the pipe. This results in VWF extension over a larger region.

Finally, VWF extension for increasing stenosis height with $\hat{l}_1$ and $\hat{l}_2$ fixed is shown in Fig. 6.7b. Similarly to the steepness, increasing the stenosis height increases the maximum shear rate in the pipe and causes greater VWF unfolding. However, the qualitative extent of the protein elongation remains the same for all stenosis heights as this is set by gradient of the stenosis.

6.5.3 Examining model parameters

For all numerical solutions in this chapter we have held the platelet binding rate fixed, with $\hat{\kappa} = 10$, and the relative initial concentration of bound VWF fixed, with $\sigma_b = 0.1$. We now explore how varying these parameters alters the initial thrombosis dynamics for a fixed Reynolds number of $Re = 400$.

It is valuable to recall the effects which $\hat{\kappa}$ and σ_b determine. Firstly the flux of free platelets onto the wall is proportional to $\hat{\kappa}\sigma_b/Re$, as defined in (6.22). For clarity we

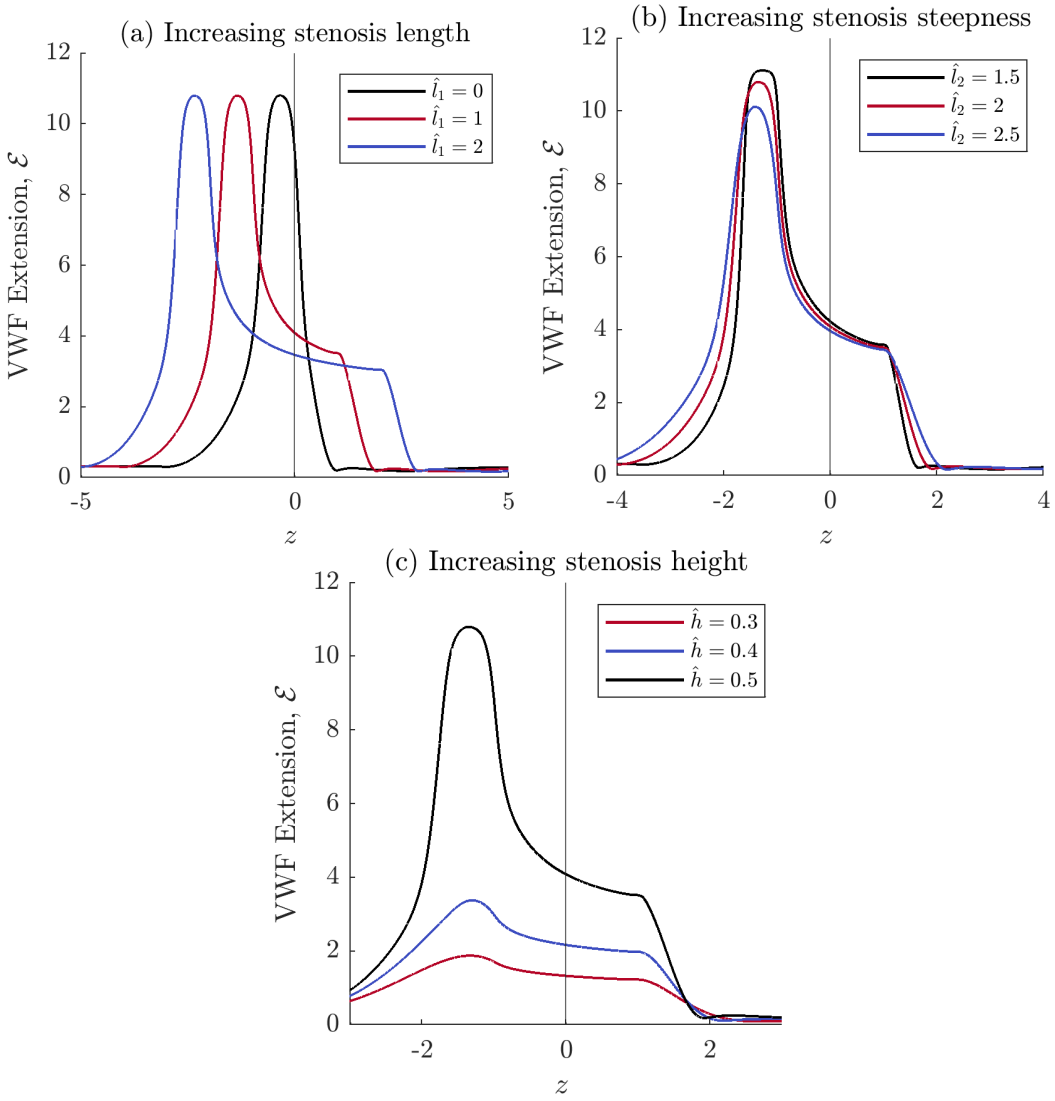

Figure 6.7: VWF extension for varying stenosis geometry at $Re = 400$. When not stated in the legend, all other geometry parameters are: $\hat{l}_1 = 1$, $\hat{l}_2 = 1.5$ and $\hat{h} = 0.5$. (a) Increasing stenosis length $\hat{l}_1$ causes VWF to unfold further upstream. (b) Increasing stenosis steepness by decreasing $\hat{l}_2$ causes VWF to unfold more as the shear rate increases. (c) Increasing stenosis height $\hat{h}$ increases VWF extension.

define $\hat{\kappa}\sigma_b/Re$ as k_{flux}. This means that if k_{flux} is large, we expect more free platelet absorption in boundary layers on the stenosis.

We consider three cases (a) $k_{flux} = 1/Re$ and $\hat{\kappa} = 10$, (b) $k_{flux} = 0.1/Re$ and $\hat{\kappa} = 1$ and (c) $k_{flux} = 0.01/Re$ and $\hat{\kappa} = 1$ all for $Re = 400$. These are shown in In Fig. 6.8a, b and c, respectively. We can see that when k_{flux} is larger, there is more absorption of free platelets in a boundary layer on the stenosis. We divide the nondimensional time taken to reach $\phi_{pb} = 2$ by $\hat{\kappa}$ so that all three cases can be compared (recalling we

included $\hat{\kappa}$ in our nondimensionalisation of time). The time taken to reach $\phi_{pb} = 2$ is then determined by $k_{flux}\hat{\kappa}$, so that if there are more free platelets absorbed in the boundary layer on the stenosis then bound platelets accumulate quicker and they are able to bind faster if $\hat{\kappa}$ is larger.

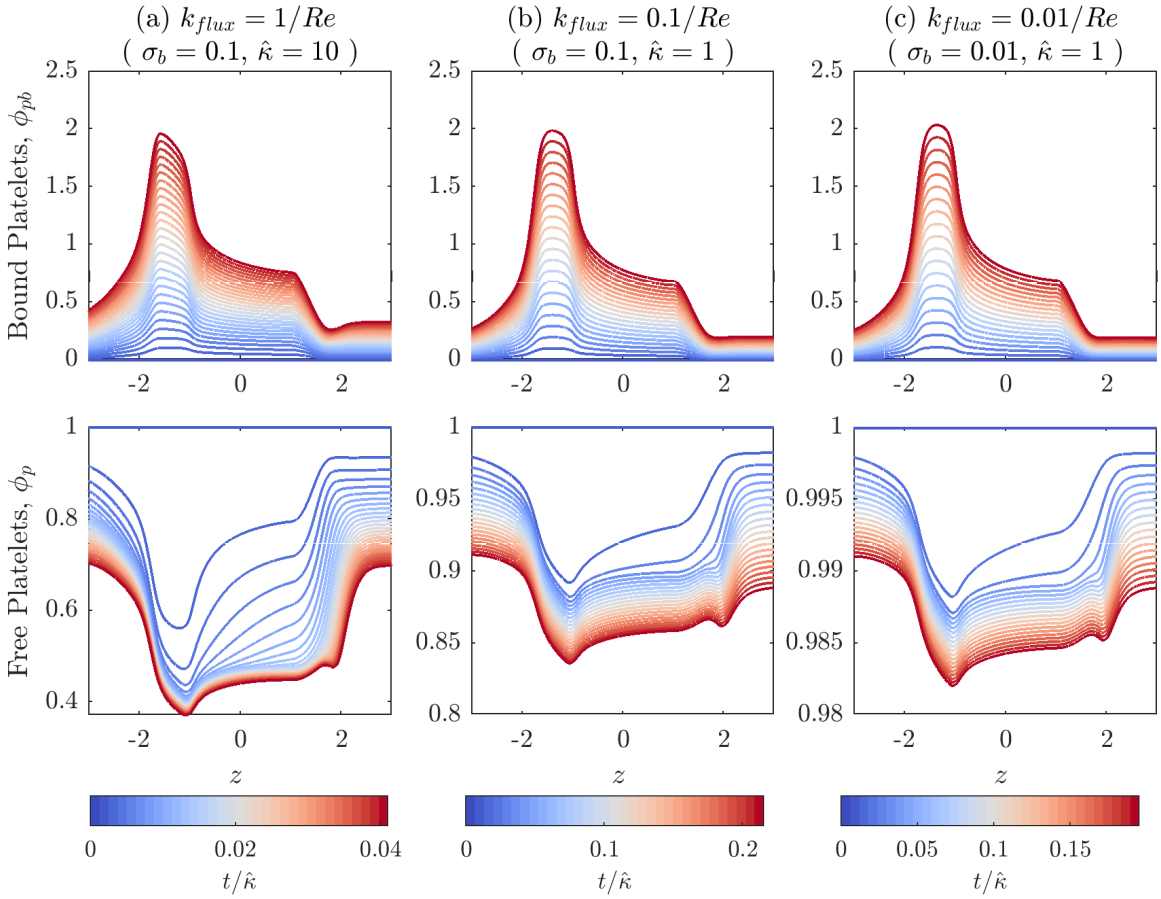

Figure 6.8: Exploration of varying the VWF-platelet binding rate $\hat{\kappa}$ and the relative initial concentration of bound VWF σ_b. For all cases we have $\hat{h} = 0.5$, $\hat{l}_1 = 1$, $\hat{l}_2 = 2$ and $Re = 400$. We have scaled nondimensional time by $\hat{\kappa}^{-1}$ to compare between different binding rates. Parameter values: (a): $k_{flux} = 1/Re$ and $\hat{\kappa} = 10$, (b): $k_{flux} = 0.1/Re$ and $\hat{\kappa} = 1$, (c): $k_{flux} = 0.01/Re$ and $\hat{\kappa} = 1$. The size of k_{flux} determines the absorption of platelets in the boundary layer on the stenosis and $\hat{\kappa}$ determines the relative time to deposit platelets.

6.6 Discussion

In this chapter we have examined our continuum model for the early stages of high-shear thrombosis in an arterial-scale stenosed pipe. Through the numerical solution

of the model, we explored VWF behaviour and platelet deposition for a range of Reynolds numbers and arterial geometries.

Numerical solutions of the model demonstrated that there are three distinct regimes of platelet deposition as a function of the Reynolds number. At low Re, VWF does not fully extend. This results in slow platelet deposition which occurs across the full stenosis length. As Re increases the shear rate increases, which unfolds VWF. Once unfolded, the platelet deposition rate increases and platelets are deposited further upstream, at the start of the stenosis. As Re increases further, VWF extends over a larger region and as a result, platelets are deposited further downstream.

The scale and aspect ratio of the geometry investigated in this chapter necessitated that numerical simulations must be used to analyse the model. The Péclet numbers associated with the transport of platelets and VWF are very large at the flow rates considered in this chapter. In order to maintain tractability, we artificially decreased the Péclet numbers associated with transport and neglected shear-induced diffusion. This will lead to an overestimation of the thickness of boundary layers of free VWF and platelets on the base of the stenosis. Accurately capturing the boundary layer dynamics is crucial to accurately describe binding; we discuss methods of examining this model for large Péclet numbers in Chapter 8.

Examining the time-dependent dynamics of deposition, we found that VWF deposition rates were significantly smaller than platelet deposition rates. This is because the inlet concentration of VWF is much less than the concentration of platelets. As a result, bound VWF remained close to its initial levels as platelets were deposited. Since the time taken to deposit platelets is proportional to the initial concentration of VWF multiplied by the platelet-VWF binding rate $\hat{\kappa}\sigma_b$. This highlights the importance of estimating model parameters which is the key objective of Chapter 7.

In this chapter we model the VWF extension using the metric $\mathcal{E}$ which is proportional to the squareroot of the length of the protein squared minus its mean length squared. We model platelet binding as proportional to $\mathcal{E}$. Since $\mathcal{E} = 0$ when the protein is not extended, this neglects the binding which could occur when the protein is completely globular. Our model predicts VWF to be globular in the recirculation zone behind the stenosis, where shear rates are low. Including binding when VWF is globular would allow us to examine if clots can form in this location. Further examination of the alternative constitutive relations for the binding dynamics forms part of Chapter 7. Finally, a comparison of wall shear rate on the stenosis and our nonlinear relaxation time demonstrated that for our choice of unfolding parameters, VWF was

able to extend significantly when the shear rate was below the unfolding threshold. This motivates the focus of Chapter 7 where we develop a framework to estimate the unknown model parameters which control VWF unfolding and platelet binding.

Chapter 7

Thrombosis in a microfluidic geometry

In the previous chapter, we examined the thrombosis model in an arterial-scale stenosis geometry using qualitatively chosen parameters for VWF unfolding and binding. This allowed us to examine the interplay between VWF and platelet dynamics with the complex fluid mechanics which occur at high Reynolds numbers in arteries. In this chapter, we focus on improving the capacity of the model to predict thrombosis by (i) exploring binding constitutive relations beyond those used in Chapter 6, and (ii) parameterising the model using experimental data of VWF dynamics and microfluidic thrombosis data.

The work in this chapter is motivated by microfluidic experiments examining thrombosis carried out by our collaborators at Technion, as presented in Chapter 1. The microfluidic device has a rectangular cross-section, a constant height and a piecewise linearly varying width which narrows in the centre. The *in vitro* microfluidic device geometry is shown in Fig 7.1. As a result of the small height and width of the device relative to its length, it is possible to achieve arterial shear rates of $10,000\ \mathrm{s}^{-1}$ in the narrow region. Our collaborators have provided an initial dataset of thrombosis in this device at a single flow rate. This dataset allows us to set up a framework for parameterising the model using microfluidic imaging data.

To compare the model to spatial and temporal experimental thrombosis data, we exploit the small aspect ratio of the device, $\epsilon = h/l = 0.003$, where h is the device half height and l is its half length, to reduce the model presented in Chapter 5 using the lubrication approximation. We then analyse the model in the case that the reduced Péclet number, $\epsilon^3 Pe_{\mathrm{sh}}$, is of $O(\epsilon)$, where the Péclet number, the ratio of the channel half height squared to the strength of shear-induced diffusion, is defined as $Pe_{\mathrm{sh}} = h^2/k_{\mathrm{sh}}$. This offers a significant analytical reduction of the model and an

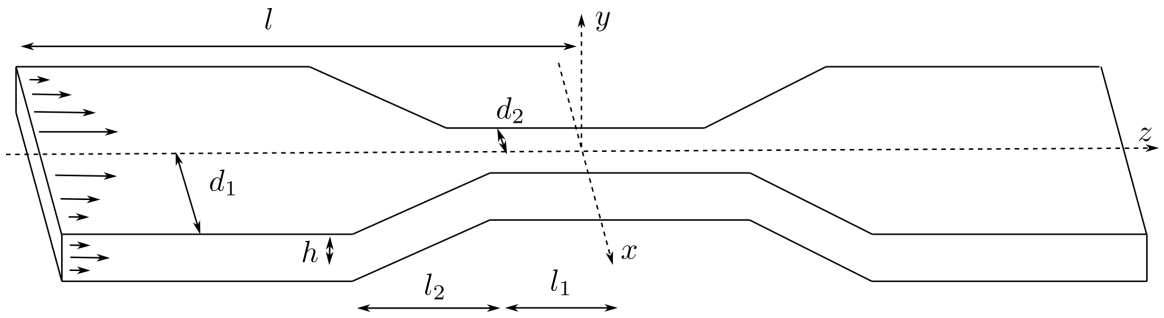

Figure 7.1: Diagram of stenosis device used *in vitro*, with Cartesian axes marked. The device has a constant height as well as narrowing width and length which is much longer than the height. Inlet parabolic flow is marked.

equivalent reduction in computational time compared to the full model. The regime we analyse considers the reduced Péclet number to be smaller than in the regime of the *in vitro* experiments where the reduced Péclet number is ≈11. The regime where $\epsilon^3 Pe_{\text{sh}} = O(\epsilon)$ could be reached if the aspect ratio of the device was slightly decreased. Despite being slightly outside the regime of the current microfluidic dataset, we use this regime to develop a framework for determining the unknown model parameters using numerical optimisation. Since experimental work is ongoing, this framework can be used in the future when more experimental data is available in devices with smaller aspect ratios.

We first present the existing experimental data for VWF which we will use to parameterise the model in this chapter. Then, in Section 7.2, we present the *in vitro* experimental setup and an example of the available thrombosis data. In Section 7.3, we discuss alternative VWF-platelet binding models motivated by our observations of the thrombosis data. In Section 7.4, we present the model domain and lubrication scaling. In Section 7.6, we determine the leading-order system for flow, VWF extension and platelet deposition for the case when the reduced Péclet number is of $O(\epsilon)$. In Sections 7.7 - 7.9, we use these reduced equations to explore the effect of varying the geometry and flow conditions as well as varying binding models within the lubrication regime.

In Section 7.10, we conclude the chapter by examining methods for determining the unknown model parameters. We first use the existing VWF literature to determine the VWF unfolding parameters. We then examine how the microfluidic data could be used to determine the VWF-platelet binding rate and the initial concentration of VWF. We conclude by discussing the experimental data and analysis which would be required in the future to fully apply this calibration.

7.1 *In vitro* VWF data

We now discuss the existing experimental data for VWF behaviour in flow. This was summarised in Chapter 5, but we now examine the datasets in more detail. The aim of this section is to determine how these datasets could be used to parameterise our model for VWF behaviour.

There are two studies which quantify VWF behaviour for a range of shear rates as the protein unfolds. The first study, conducted by Schneider et al. in 2007, examined VWF unfolding by measuring the protein length as it circulated around a microfluidic channel loop where no binding occurred with the channel walls [98]. The authors increased the flow rate in the channel and recorded the extension of the proteins shown in Figure 7.2a. In this figure, $\dot{\gamma} = 5 \times 10^3$ s^{-1} is marked by the vertical dash-dot line. Their experiment recorded that VWF remains globular for $\dot{\gamma} < 5 \times 10^3$ s^{-1} and is extended at $\dot{\gamma} = 5 \times 10^3$ s^{-1} and with an extension of 15 μm at $\dot{\gamma} = 7.9 \times 10^3$ s^{-1}. However, there are a number of challenges when interpreting this data. The authors refer to extension and length interchangeably. Furthermore, their data has error bars, but no information is present in their article or online regarding whether these refer to measurement errors from an individual experiment or confidence intervals obtained from multiple experiments to yield statistical inference

The second study by Lippok et al. used *in vitro* experiments and a discrete theoretical model where VWF is modelled as a chain of beads and springs to examine the cleavage between VWF dimers at varying shear rates [69]. *In vitro*, they measured the cleavage of VWF when subjected to shear flow combined with an enzyme which separates an internal bond between VWF dimers. The authors suggested that VWF can only cleave into small chains when the protein is unfolded, that is, when its internal bonds are exposed to the external enzyme. The authors obtained a fitting of the *in vitro* data and the model data giving the following cleavage rate:

$$\kappa_{cleave}(\dot{\gamma}) = \frac{3.5 \times 10^{-3}}{1 - \exp((\dot{\gamma} - 5522\,\mathrm{s}^{-1})/1271\,\mathrm{s})}\mathrm{nM/s}. \tag{7.1}$$

This is shown in Figure 7.2b. We now present and analyse the microfluidic thrombosis data gathered by our collaborators.

7.2 *In vitro* thrombosis data

This chapter is motivated by *in vitro* thrombosis data provided by Prof. Netanel Korin's Cardiovascular NanoMed Engineering Laboratory (Technion). These exper-

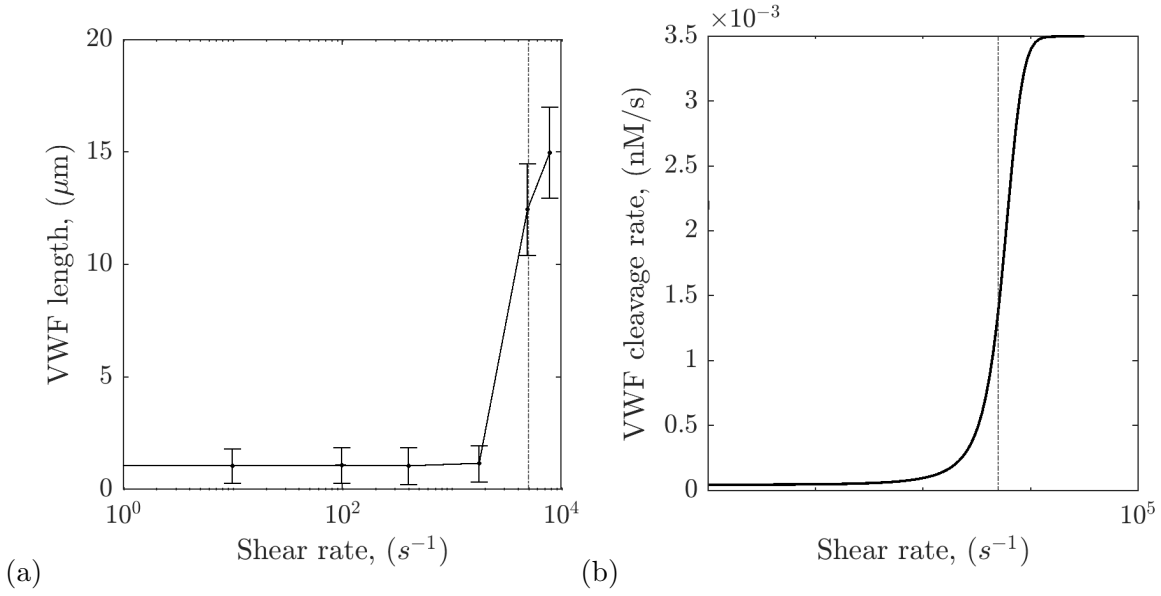

Figure 7.2: Experimental data of VWF behaviour in shear flow. In both plots, $\dot{\gamma} = 5,000\ \mathrm{s}^{-1}$ is marked by the dashed vertical line. (a) Schneider et al.data of VWF length [98]. Data points are *in vitro* data and the connecting line is linear between each point (b) Lippok et al. empirical fitting, Eq. (7.1) [69].

Name	Param.	Value(s)	Units
Model half length	l	0.0325	m
Inlet width	d_1	0.001	m
Minimum width	d_2	0.0001	m
Height	h	0.0001	m
Stenosis length	l_1	0.0065	m
Tapering section length	l_2	0.0065	m
Inlet flux	Q_{in}	9.5×10^{-9}	m^3/s

Table 7.1: *In vitro* device dimensions and flow parameters.

iments examined the entire process of thrombosis within the microfluidic device discussed above. We recall, as discussed in Chapter 5, thrombosis consists of an initial slower stage where a thin layer of VWF and platelets accumulate on the vessel wall and a late stage where a significant clot forms rapidly. In the late stage, the flow will be significantly obstructed by the growing clot. The model we have developed does not include clot growth and is limited to consider the slower, initial stage of thrombosis. As a result, our model can only be compared to experimental data from the early stages of thrombosis. We determine an upper bound on this in Section 7.2.1. We now summarise these thrombosis experiments.

The stenosis geometry is pictured in Fig. 7.1 with dimensions listed in Table 7.1.

The device is fabricated using the rigid polymer polydimethylsiloxane (PDMS). The device is then perfused at a low flow rate with a collagen suspension of 0.31 mg/ml. This leaves a coating of bound collagen on the internal PDMS walls. The low flow rate ensures that the coating is approximately uniform throughout the device. The collagen coating allows VWF and subsequently platelets to bind to the entire surface of the device.

Freshly collected sheep blood (containing platelets, RBCs and VWF) is treated with an anticoagulant to avoid clotting in transit. Then, the platelets are labelled using a fluorescent stain. A syringe pump perfuses the blood through the device at a constant flow rate of 57 μl/min which leads to a maximum shear rate of $10,000\ \mathrm{s}^{-1}$ in the narrowest portion of the device and $1,000\ \mathrm{s}^{-1}$ in the upstream region. To obtain the spatial and temporal distribution of platelet capture, a microscope photographs the device every five seconds. The experiments are repeated five times and are run for twenty minutes, including a short period required to focus the microscope in each repeat.

An example of thrombus formation over two minutes is shown in Fig. 7.3. The image times are shown relative to t^* which is the longest time taken to focus the microscope over all repeats (2 min 54 s). Green illustrates the platelets with the intensity corresponding to the number of platelets at that location. Platelets deposit in the narrow region with the accumulation increasing over time. As platelets deposit, they form clots which obstruct the fluid flow in the device. Since the flux is imposed through the device, the shear force increases as the device becomes obstructed. Eventually, this overcomes the clot's internal bonds and it fractures, known as an embolism. This can be seen between $t^* + 100$ s and $t^* + 125$ s by the reduced platelet fluorescence at the later time.

We now detail the image analysis protocol for this data so that it can be compared to our modelling predictions.

7.2.1 Image analysis

The *in vitro* images contain spatial and temporal information about platelet deposition. In Fig. 7.3, the deposition in the cross-sectional direction has a considerable amount of spatial variation due to the clumping of the platelets into small clots. There is still significant variation in the axial direction, but the trend is clearer: platelets predominantly deposit in the narrowest portion of the device. We cannot capture stochastic variation in either direction using our deterministic continuum

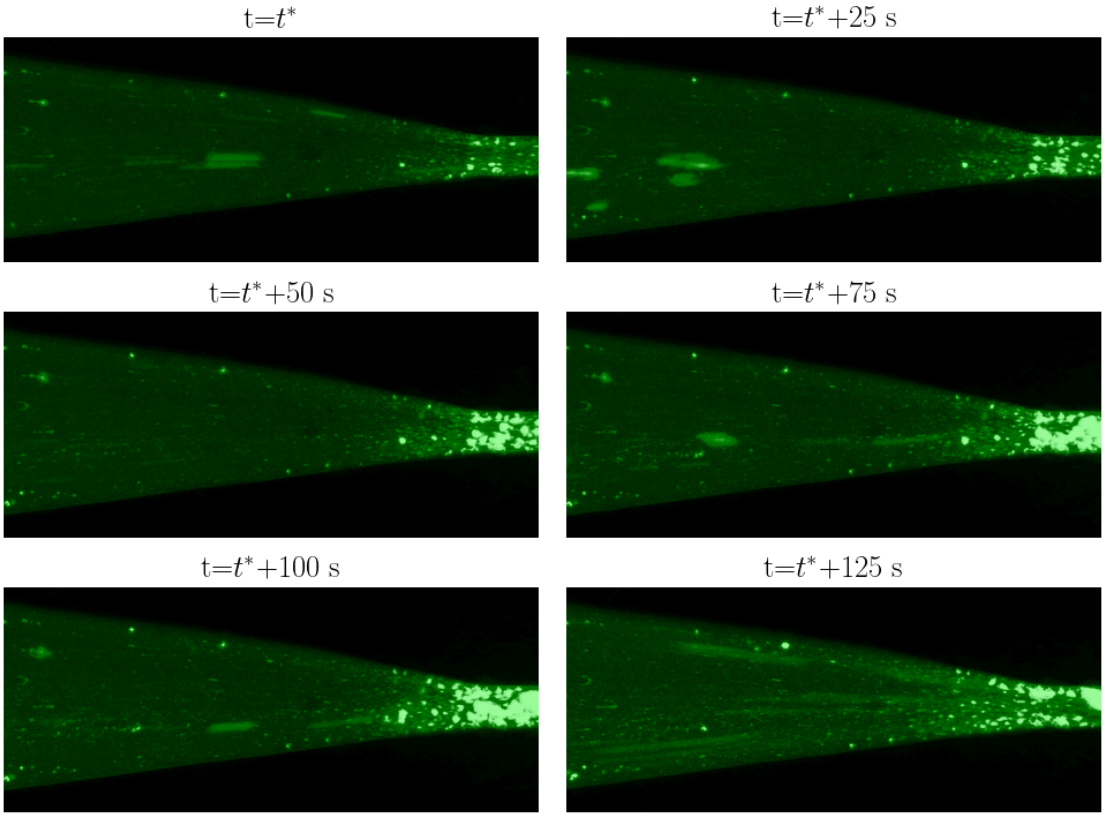

Figure 7.3: *In vitro* images of platelet deposition over 125 s from t^*, the time when the microscope was focused. Fluorescent platelets can be seen building up in the stenosis. Between $t^* + 100$ s and $t^* + 125$ s the thrombus embolises.

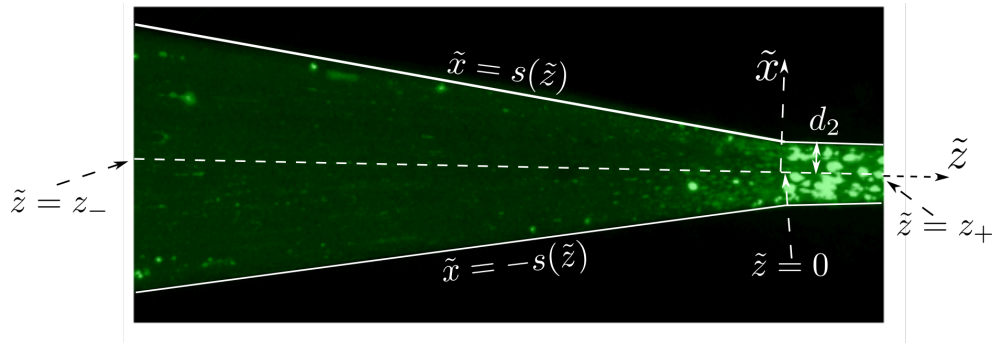

Figure 7.4: Schematic of integration method for an example *in vitro* image of platelet deposition. We define the axial coordinate $\tilde{z}$ with $\tilde{z} = 0$ at the start of the straight section of the stenosis. The cross-sectional coordinate $\tilde{x}$ is marked. Using image analysis, we can measure the stenosis half width d_2.

model, hence this chapter aims to quantitatively capture the overall trend of platelet deposition in the axial dimension.

To compare the theoretical prediction of the bound platelet concentration to the *in vitro* data, we average the *in vitro* image for each repeat in the cross-sectional direction. To do this, we use image analysis to determine the edges of the microfluidic device in each image, identifying the centre of the device which we use to define the axial coordinate $\tilde{z}$ and the cross-sectional coordinate $\tilde{x}$. We can determine the lengthscale of each image by measuring the width of the stenosis which corresponds to the known length d_2. We define the maximum and minimum axial coordinates as z_- and z_+ respectively, with $\tilde{z} = 0$ set at the start of the narrowest section of the stenosis. We then define the width of the device at point $\tilde{z}$ using the function $s(\tilde{z})$. This is shown in Fig. 7.4.

We discretise the cross-sectional coordinate $\tilde{x}$ at each axial position using $N+1$ points such that $\tilde{x}_k = -s(\tilde{z}) + k\delta x$, where $\delta x = 2s(\tilde{z})/N$ for $k = 0, 1, 2, ..., N$. We can then define the average platelet fluorescence at each axial position in the pipe for each experimental repeat $i = 1, 2, .., 5$ as follows:

$$\bar{\phi}^i_{pb}(t, \tilde{z}) = \frac{1}{N+1} \sum_{k=0}^{N} \phi^i_{pb}(t, \tilde{x}_k, \tilde{z}). \tag{7.2}$$

We then discretise the axial coordinate into $M+1$ points such that $\tilde{z}_j = z_- + j\delta z$, where $\delta z = (z_+ - z_-)/M$ for $j = 0, 1, 2, ..., M$. This allows us to define the total platelet fluorescence for each repeat at time t as

$$\bar{\Phi}^i_{pb}(t) = \frac{1}{(N+1)(M+1)} \sum_{j=0}^{M} \sum_{k=0}^{N} \phi^i_{pb}(t, \tilde{x}_k, \tilde{z}_j). \tag{7.3}$$

We use 1200 points in both axial and cross-sectional directions so $M = N = 1199$.

Recall from Section 7.2 that the image data for each of the repeats begins after an initial period required to focus the microscope. We standardise the images from each repeat by considering images from each repeat from $t^* = 2$ min 54 s after the flow was turned on, which is the longest time taken to focus the microscope amongst the five repeats.

Our theoretical model captures only the initial stages of platelet deposition. Therefore, we must determine a bound on the experimental data after which the flow will be disturbed and our model will be a poor description of the dynamics. We can use the first time that an embolism occurs as an upper bound on the model validity, although by this point there will be a significant clot. Further experimental data on

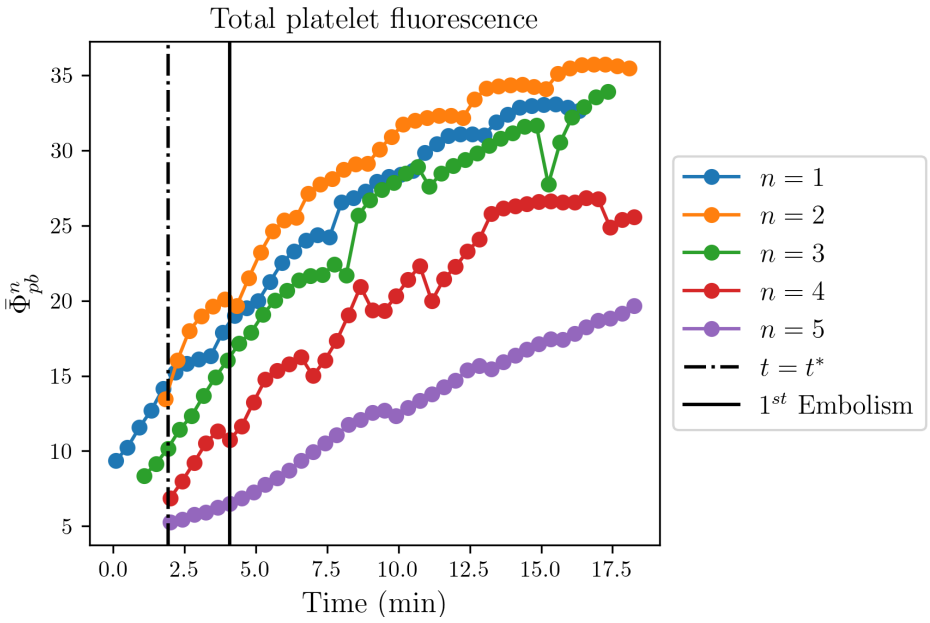

Figure 7.5: Total platelet deposition over time for each repeat. A decrease in the total platelet fluorescence for any given repeat illustrates an embolism.

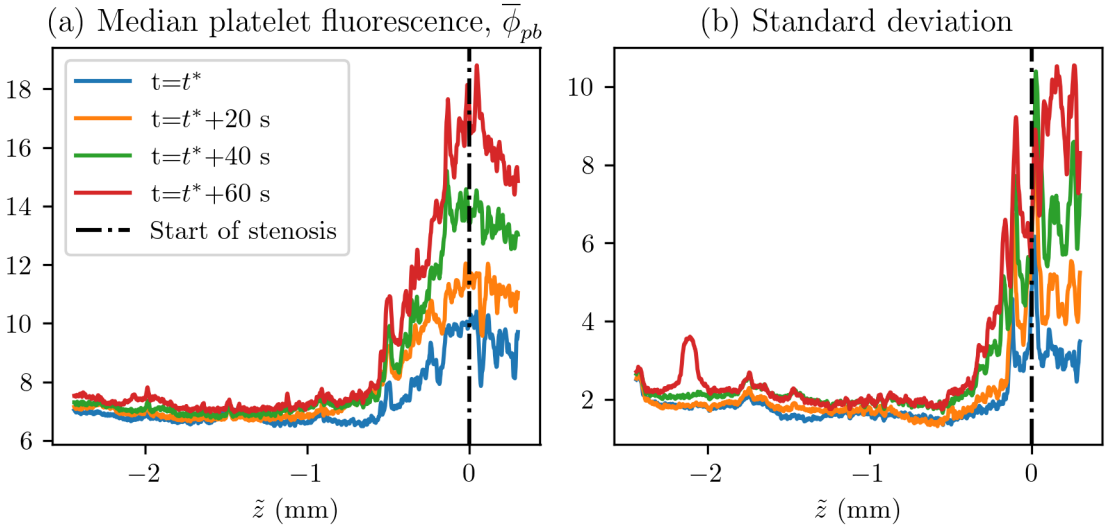

Figure 7.6: (a) Median platelet fluorescence and (b) the standard deviation of the five experimental repeats over time. The standard deviation increases over time and is greater in the stenosis region close to $\tilde{z} = 0$.

the size of the clot for a given fluorescence would allow us to determine a stricter bound in the future. By calculating $\bar{\Phi}^i_{pb}$ for each repeat, we can examine when the total platelet concentration in the pipe decreases, which represents an embolism. We determine the time of the first embolism to be $t = t^* + 75$ s. Hence, we use data from

$t = t^*$ until $t^* + 60$ s. This is shown in Fig. 7.5.

We can now define the mean and median platelet fluorescence at location $\tilde{z}$ at time t over all of the five experimental repeats as follows:

$$\mu(t,\tilde{z}) = \frac{\sum_{n=1}^{5} \bar{\phi}_{pb}^{n}(t,\tilde{z})}{5} \quad \text{and} \quad \bar{\phi}_{pb}(t,\tilde{z}) = \text{med}\{\bar{\phi}_{pb}^{n}(t,\tilde{z})\}, \text{ for } n = 1,2,..,5. \quad (7.4)$$

We can also define the standard deviation $\sigma(t,z)$, using

$$\sigma^2(t,\tilde{z}) = \frac{\sum_n (\bar{\phi}_{pb}^{n}(t,\tilde{z}) - \mu(t,\tilde{z}))^2}{5}. \quad (7.5)$$

The median and standard deviation of the five repeats are shown in Fig. 7.6. The large standard deviation demonstrates that there is significant variation between the fluorescence obtained in each repeat. This variation is greatest in the narrowest section of the device and increases over time. This demonstrates the need to gather more data in order to accurately estimate model parameters.

Finally, to quantitatively compare our theoretical values of the bound platelet concentration to the experimental data, we must convert the measured platelet fluorescence to bound platelet concentration in kg/m^2. In our model, the number of platelets which can accumulate on the walls of the domain is proportional to the initial concentration of bound VWF plus any further accumulation of VWF. We can estimate the maximum number of platelets that could be captured by the concentration of bound VWF initially, ϕ_{vbi}, multiplied by the number of platelets a single VWF molecule can bind to. Since the longest multimer of VWF in the blood has 80 monomers, we can assume that each VWF molecule can accommodate 80 platelets so that the maximum bound platelet concentration is $80\phi_{vbi}$. The initial concentration of bound VWF is not known experimentally, but this estimate allows us to determine the prediction of platelet fluorescence once we estimate a value of ϕ_{vbi}. To accurately determine the conversation factor between platelet fluorescence in the imaging data and bound platelet concentration, we could carry out experiments where fluorescence images are taken and platelets are counted.

Motivated by the distribution of platelet deposition in the microfluidic device, we now discuss extensions to the platelet - VWF binding dynamics considered in Chapters 5 and 6.

7.3 Binding dynamics

In Fig. 7.6a, the *in vitro* thrombosis data shows that platelets deposit everywhere in the pipe, although predominantly in the stenosis. In Chapter 6, we modelled platelet

binding to VWF to be linearly proportional to VWF extension $\mathcal{E}$. This meant that platelets do not bind upstream of the stenosis when shear rates were low, and $\mathcal{E} \approx 0$, as was seen in our numerical results. Using binding proportional to VWF extension we will not be able to predict platelet binding upstream of the stenosis, as is shown in Fig. 7.6a. Hence, we consider several modifications to the binding dynamics which allow for upstream binding so that we can more closely match the *in vitro* data.

Upstream of the stenosis, the proteins are not extended so the dimensionless VWF length $\mathcal{L}$ is equal to unity and the extension is zero. We consider two alternative binding models. Firstly, we consider binding proportional to VWF length $\mathcal{L}$ which will allow platelets to bind upstream. Secondly, we consider binding which is limited by the available binding sites on bound species, which we refer to as saturating binding. We model the available binding sites on bound VWF as the product of VWF length $\mathcal{L}$ and the concentration of bound VWF ϕ_{vb}. Hence, we model free platelets binding to bound VWF to be proportional to $\kappa\mathcal{L}(1-\phi_{pb}/\mathcal{L}\phi_{vb})$. This means that as $\phi_{pb} \to \mathcal{L}\phi_{vb}$, binding decreases as the available binding sites on bound VWF are used up. Similarly, we model the available binding sites for free VWF on the bound platelets as ϕ_{pb}, assuming each bound platelet can bind to one VWF molecule. Thus, as $\phi_{vb} \to \phi_{pb}$, binding decreases as the available space on bound platelets fills. Hence, free VWF binding to bound platelets is taken to be $\kappa\mathcal{L}(1 - \phi_{vb}/\phi_{pb})$.

Accordingly, the three models of binding dynamics are as follows for free VWF:

$$(\phi_v \boldsymbol{u} - (D_v + \dot{\gamma} k_{\text{sh}})\nabla\phi_v)) \cdot \hat{\boldsymbol{n}} = \begin{cases} \kappa\mathcal{E}\phi_v\phi_{pb}, & \text{(7.6a)} \\ \kappa\mathcal{L}\phi_v\phi_{pb}, & \text{(7.6b)} \\ \kappa\mathcal{L}\phi_v\phi_{pb}\left(1 - \dfrac{\phi_{vb}}{\phi_{pb}}\right), & \text{(7.6c)} \end{cases}$$

where (7.6a), (7.6b) and (7.6c) refer to binding proportional to VWF extension, VWF length and saturating binding, respectively. These three conditions lead to the following flux conditions for free platelets:

$$(\phi_p \boldsymbol{u} - (D_p + \dot{\gamma} k_{\text{sh}})\nabla\phi_p)) \cdot \hat{\boldsymbol{n}} = \begin{cases} \kappa\mathcal{E}\phi_p\phi_{vb}, & \text{(7.7a)} \\ \kappa\mathcal{L}\phi_p\phi_{vb}, & \text{(7.7b)} \\ \kappa\mathcal{L}\phi_p\phi_{vb}\left(1 - \dfrac{\phi_{pb}}{\mathcal{L}\phi_{vb}}\right), & \text{(7.7c)} \end{cases}$$

where similarly (7.7a) (7.7b) and (7.7c) refer to binding proportional to VWF extension, VWF length and saturating binding, respectively.

We now return to the model presented in Chapter 5 and nondimensionalise it in the microfluidic geometry, incorporating these variations in boundary conditions.

7.4 Thin-film model formulation

We now formulate the model presented in Chapter 5 in the microfluidic geometry. In subsection 7.4.1, we nondimensionalise the model incorporating the lubrication assumption, and note the restrictions this assumption places on the pipe geometry. In Section 7.4.2, we derive integrated conservation equations for the free VWF and platelet concentrations in the pipe. In Section 7.5, we discuss the parameters which arise in the dimensionless model and the values of these parameters in the microfluidic *in vitro* experiments. We then present our assumptions on the sizes of these parameters in the model, we match the parameter orders as much as possible to the *in vitro* setup, aside from the reduced shear Péclet number which we decrease. In Section 7.6, we use these assumptions about the model parameters to derive the leading-order model.

We recall that the thrombosis model consists of (i) the steady Navier-Stokes equations, (5.47) and (5.48), which are driven by a prescribed flux at the inlet, (ii) the steady FENE-P equation, (5.49), with a modified nonlinear relaxation time (5.50), which determines the VWF extension, (iii) advection-diffusion equations, (5.53) and (5.54), which determine the free platelet and VWF concentrations in the pipe and (iv) PDEs which determine the concentration of bound VWF and platelets on the wall of the pipe, (5.57) and (5.58). The bound species are coupled to the free species through flux boundary conditions (7.6a) - (7.6c) and (7.7a) - (7.7c) which incorporates the three different binding models we discussed in Section 7.3. We restate the dimensional model parameters from Chapter 5 in Table 7.2 for clarity.

In this chapter, we use Cartesian coordinates with z as the axial coordinate as marked in Fig. 7.1. The inlet is located at $z = -l$ and the outlet at $z = l$. The pipe walls are defined by $y = \pm h$ and $x = \pm s(z)$ which defines the piecewise linear width as follows:

$$s(z) = \begin{cases} d_1 & \text{for } z < -l_1 - l_2, \\ -(d_1 - d_2)(z + l_1)/l_2 + d_2 & \text{for } -l_1 - l_2 < z < -l_1, \\ d_2 & \text{for } -l_1 < z < l_1, \\ (d_1 - d_2)(z - l_1)/l_2 + d_2 & \text{for } l_1 < z < l_1 + l_2, \\ d_1 & \text{for } z > l_1 + l_2. \end{cases} \tag{7.8}$$

Here, d_2 is the minimum pipe half width and d_1 is the maximum pipe half width. We define the fluid velocity components in the (x, y, z) directions are denoted using the standard notation (u, v, w). We define the fluid domain as V, cross-section of the pipe at position z as $V_\perp(z)$, and the boundary of this cross-section is denoted as $S_\perp(z)$.

Name	Param.	Value(s)	Units
Viscosity of blood	μ	0.0025	Pa s
Density of blood	ρ	997	kg m^{-3}
Diffusion coeff. of VWF	D_v	4.9×10^{-13}	m^2 s^{-1}
Diffusion coeff. of platelets	D_p	1.58×10^{-13}	m^2 s^{-1}
Haematocrit	H	0.4	-
Red blood cell radius	r_{rbc}	3.6×10^{-6}	m
Shear diffusion coeff.	k_{sh}	1.03×10^{-12}	m^2
Inlet conc. of VWF	ϕ_{vi}	0.01	kg m^{-3}
Inlet conc. of platelets	ϕ_{pi}	4.7	kg m^{-3}
Initial conc. of bound VWF	ϕ_{vbi}	unknown	kg m^{-2}
Rapid relaxation time	α	9.3×10^{-2}	s
Extension parameter	β	6.9×10^{-4}	s
Extension parameter	δ	1.59×10^{-4}	-
Extension threshold	γ^*	3.8×10^{3}	s^{-1}
VWF extensibility	L	16	-
Bind rate VWF to platelets	κ	unknown	$m^3(\text{kg s})^{-1}$

Table 7.2: Dimensional model parameters restated from Chapter 5. The VWF parameters listed are the heuristically determined parameters from Chapter 5.

It is convenient to denote vector operators and variables in the (x, y) cross-sectional plane with the subscript $\perp$. For instance,

$$\boldsymbol{u}_\perp = (u, v)^T \text{ and } \nabla_\perp = \left(\frac{\partial}{\partial x}, \frac{\partial}{\partial y}\right)^T. \tag{7.9}$$

7.4.1 Nondimensionalisation

We now nondimensionalise the model by exploiting the disparity in lengthscales between the pipe half length l and the height h to define the small parameter $\epsilon = h/l$. In the experimental setup, $\epsilon = 0.003$. In this analysis, since the minimum pipe width is the same order of magnitude as the pipe height, we scale both cross-sectional variables x and y and their corresponding fluid components, u and v with ϵ. In the upstream region, the pipe is wider than in the stenosis region; by scaling both directions with ϵ, we are assuming that d_1/d_2 is of $O(1)$. In the experimental setup, d_1/d_2 is 10 which is slightly outside of the $O(1)$ regime. Furthermore, as a result of assuming x is small, this analysis is then restricted to pipes where the gradient of the wall in the axial direction ds/dz is at most of $O(1)$. If the larger axial wall gradient was large, the velocity component in the x direction would be $O(1)$, violating the lubrication approximation.

We consider this system on the timescale of platelet deposition $1/\kappa\phi_{pi}$ as we did in Chapter 6. The velocity scale is determined by the inlet flux Q_{in} relative to the cross-sectional area scaling h^2, giving $U = Q_{in}/h^2$. We use the lubrication pressure scaling in order to balance the axial pressure gradient with cross-sectional viscous dissipation. The shear rate in the pipe is scaled by $U/\epsilon l$ to account for the large shear rate caused by the small pipe height. We scale the free platelet and VWF concentrations with their inlet levels ϕ_{pi} and ϕ_{vi}, respectively. Both the bound species are scaled relative to the initial concentration of bound VWF ϕ_{vbi}.

Under these scalings, we define dimensionless variables, denoted with hats, as follows:

$$x = \epsilon l\hat{x},\ y = \epsilon l\hat{y},\ z = l\hat{z},\ t = \frac{1}{\kappa\phi_{pi}}\hat{t}, \tag{7.10}$$

$$u = \epsilon U\hat{u},\ v = \epsilon U\hat{v},\ w = U\hat{w},\ p = p_a + \frac{U\mu}{\epsilon^2 l}\hat{p},\ \dot{\gamma} = \frac{U}{\epsilon l}\hat{\dot{\gamma}}, \tag{7.11}$$

$$\phi_v = \phi_{vi}\hat{\phi}_v,\ \phi_p = \phi_{pi}\hat{\phi}_p,\ \phi_{pb} = \phi_{vbi}\hat{\phi}_{pb},\ \phi_{vb} = \phi_{vbi}\hat{\phi}_{vb}, \tag{7.12}$$

where, in (7.11), p_a is the atmospheric pressure at the outlet. Under scalings (7.10), the pipe is now defined by $z \in [-1, 1]$, $x \in [-\hat{s}(z), \hat{s}(z)]$ and $y \in [-1, 1]$, where $\hat{s} = s/(\epsilon l)$. We now drop the hats on dimensionless variables and insert these scalings (7.10) - (7.12) into Eqs. (5.47) - (5.49) and (5.57) - (5.58). This gives the dimensionless steady Navier-Stokes equations in the pipe volume V as follows:

$$\frac{\partial u}{\partial x} + \frac{\partial v}{\partial y} + \frac{\partial w}{\partial z} = 0, \tag{7.13}$$

$$\epsilon^2 Re\left(u\frac{\partial u}{\partial x} + v\frac{\partial u}{\partial y} + w\frac{\partial u}{\partial z}\right) = \frac{\partial^2 u}{\partial x^2} + \frac{\partial^2 u}{\partial y^2} + \epsilon^2\frac{\partial^2 u}{\partial z^2} - \frac{1}{\epsilon^2}\frac{\partial p}{\partial x}, \tag{7.14}$$

$$\epsilon^2 Re\left(u\frac{\partial v}{\partial x} + v\frac{\partial v}{\partial y} + w\frac{\partial v}{\partial z}\right) = \frac{\partial^2 v}{\partial x^2} + \frac{\partial^2 v}{\partial y^2} + \epsilon^2\frac{\partial^2 v}{\partial z^2} - \frac{1}{\epsilon^2}\frac{\partial p}{\partial y}, \tag{7.15}$$

$$\epsilon^2 Re\left(u\frac{\partial w}{\partial x} + v\frac{\partial w}{\partial y} + w\frac{\partial w}{\partial z}\right) = \frac{\partial^2 w}{\partial x^2} + \frac{\partial^2 w}{\partial y^2} + \epsilon^2\frac{\partial^2 w}{\partial z^2} - \frac{\partial p}{\partial z}. \tag{7.16}$$

Here, the reduced Reynolds number is $\epsilon^2 Re = \rho U h^2/\mu l$ which is the ratio of fluid inertia to viscous dissipation in the cross-sectional direction. The corresponding dimensionless shear rate is

$$\dot{\gamma} = \sqrt{2\epsilon^2 u_x^2 + 2\epsilon^2 v_y^2 + 2\epsilon^2 w_z^2 + \epsilon^2(u_y + v_x)^2 + (\epsilon^2 u_z + w_x)^2 + (\epsilon^2 v_z + w_y)^2}. \tag{7.17}$$

The dimensionless free VWF and platelet advection-diffusion equations in the pipe

volume V are

$$\frac{\hat{\kappa}}{Re}\frac{\partial \phi_v}{\partial t} + \nabla_\perp \cdot \left(\boldsymbol{u}_\perp \phi_v - \frac{\hat{D}_v}{\epsilon^2}\nabla_\perp \phi_v \right) + \frac{\partial}{\partial z}\left(w\phi_v - \hat{D}_v \frac{\partial \phi_v}{\partial z} \right) = 0, \tag{7.18}$$

$$\frac{\hat{\kappa}}{Re}\frac{\partial \phi_p}{\partial t} + \nabla_\perp \cdot \left(\boldsymbol{u}_\perp \phi_p - \frac{\hat{D}_p}{\epsilon^2}\nabla_\perp \phi_p \right) + \frac{\partial}{\partial z}\left(w\phi_p - \hat{D}_p \frac{\partial \phi_p}{\partial z} \right) = 0. \tag{7.19}$$

Here, the dimensionless VWF platelet binding rate is $\hat{\kappa} = l^2 \kappa \phi_{pi} \rho / \mu$. The ratio $\hat{\kappa}/Re$ is equal to the inverse Damköhler number where $Da = U/\kappa \phi_{pi} l$ is the ratio of the timescale of platelet deposition to the timescale of fluid advection as in Chapter 6. This appears with the time derivatives in (7.18) and (7.19) since we have nondimensionalised on the timescale of platelet deposition. The dimensionless diffusion coefficients in Eq. (7.18) and (7.19), denoted with hats to highlight their difference from the dimensional Brownian coefficients, are defined as follows:

$$\hat{D}_v = \left(\frac{1}{Pe_v} + \frac{\dot{\gamma}}{\epsilon Pe_{\mathrm{sh}}} \right) \text{ and } \hat{D}_p = \left(\frac{1}{Pe_p} + \frac{\dot{\gamma}}{\epsilon Pe_{\mathrm{sh}}} \right). \tag{7.20}$$

Here we define the Brownian Péclet numbers for VWF and platelets as $Pe_v = Ul/D_v$ and $Pe_p = Ul/D_p$, respectively. The Péclet numbers are the ratio of fluid advection to the Brownian diffusion of the species. The shear Péclet number, which is equal for both species, is defined as $Pe_{\mathrm{sh}} = l^2/k_{\mathrm{sh}}$ and represents the squared ratio of the pipe width to the lengthscale over which cells are pushed by collisions with RBCs.

Finally, in three dimensions, the configuration tensor has six unique components and is defined as follows:

$$\boldsymbol{A} = \begin{pmatrix} A_{xx} & A_{xy} & A_{xz} \\ A_{xy} & A_{yy} & A_{yz} \\ A_{xz} & A_{yz} & A_{zz} \end{pmatrix}. \tag{7.21}$$

Using this definition of $\boldsymbol{A}$, the dimensionless steady FENE-P equations in V are

$$\boldsymbol{u}\cdot\nabla A_{xx} - 2A_{xx}\frac{\partial u}{\partial x} - 2A_{xy}\frac{\partial u}{\partial y} - 2\epsilon A_{xz}\frac{\partial u}{\partial z} = -\frac{(fA_{xx}-a)}{\xi Re\hat{\tau}(\dot{\gamma})}, \tag{7.22}$$

$$\boldsymbol{u}\cdot\nabla A_{yy} - 2A_{xy}\frac{\partial v}{\partial x} - 2A_{yy}\frac{\partial v}{\partial y} - \epsilon A_{yz}\frac{\partial v}{\partial z} = -\frac{(fA_{yy}-a)}{\xi Re\hat{\tau}(\dot{\gamma})}, \tag{7.23}$$

$$\boldsymbol{u}\cdot\nabla A_{zz} - \frac{2A_{xz}}{\epsilon}\frac{\partial w}{\partial x} - \frac{2A_{yz}}{\epsilon}\frac{\partial w}{\partial y} - 2A_{zz}\frac{\partial w}{\partial z} = -\frac{(fA_{zz}-a)}{\xi Re\hat{\tau}(\dot{\gamma})}, \tag{7.24}$$

$$\boldsymbol{u}\cdot\nabla A_{xy} - A_{xx}\frac{\partial v}{\partial x} - A_{xy}\frac{\partial v}{\partial y} - \epsilon A_{xz}\frac{\partial v}{\partial z} - A_{xy}\frac{\partial u}{\partial x} - A_{yy}\frac{\partial u}{\partial y} - \epsilon A_{yz}\frac{\partial u}{\partial z} = -\frac{fA_{xy}}{\xi Re\hat{\tau}(\dot{\gamma})}, \tag{7.25}$$

$$\boldsymbol{u}\cdot\nabla A_{yz} - \frac{A_{xy}}{\epsilon}\frac{\partial w}{\partial x} - \frac{A_{yy}}{\epsilon}\frac{\partial w}{\partial y} - A_{yz}\frac{\partial w}{\partial z} - A_{xz}\frac{\partial v}{\partial x} - A_{yz}\frac{\partial v}{\partial y} - \epsilon A_{zz}\frac{\partial v}{\partial z} = -\frac{fA_{yz}}{\xi Re\hat{\tau}(\dot{\gamma})}, \tag{7.26}$$

$$\boldsymbol{u}\cdot\nabla A_{xz} - \frac{A_{xx}}{\epsilon}\frac{\partial w}{\partial x} - \frac{A_{xy}}{\epsilon}\frac{\partial w}{\partial y} - A_{xz}\frac{\partial w}{\partial z} - A_{xz}\frac{\partial u}{\partial x} - A_{yz}\frac{\partial u}{\partial y} - \epsilon A_{zz}\frac{\partial u}{\partial z} = -\frac{fA_{xz}}{\xi Re\hat{\tau}(\dot{\gamma})}. \tag{7.27}$$

Here, $\xi = \alpha\mu/l^2\rho$ is the ratio of protein properties to fluid properties. When multiplied by the Reynolds number, ξRe is known as the Deborah number $De = U\alpha/l$ and represents the ratio of the timescales of protein relaxation to fluid advection. The FENE-P function is $f(A) = L^2/(L^2 - Tr(\boldsymbol{A}))$ and $a = L^2/(L^2-3)$. The dimensionless relaxation time is defined by

$$\hat{\tau}(\dot{\gamma}) = \frac{1}{2}\left(\tanh\left(\hat{\beta}Re\left(\frac{\dot{\gamma}}{\epsilon} - \frac{\hat{\gamma}^*}{Re}\right)\right) + 1\right) + \delta, \tag{7.28}$$

where $\hat{\beta} = \beta\mu/l^2\rho$ and $\hat{\gamma}^* = \gamma^*\rho l^2/\mu$ are the dimensionless relaxation time parameters and δ remains unchanged as it is dimensionless in our original definition of the relaxation time (5.50).

The dimensionless bound VWF equation, which holds on $S_\perp$ for all z, is one of

$$\frac{\partial\phi_{vb}}{\partial t} = \begin{cases} \sigma_v\mathcal{E}\phi_v\phi_{pb}, & \text{(7.29a)} \\ \sigma_v\mathcal{L}\phi_v\phi_{pb}, & \text{(7.29b)} \\ \sigma_v\mathcal{L}\phi_v\phi_{pb}\left(1 - \dfrac{\phi_{vb}}{\phi_{pb}}\right), & \text{(7.29c)} \end{cases}$$

for the three cases of binding dynamics we consider in this chapter. Here, $\sigma_v = \phi_{vi}/\phi_{pi}$ is the ratio of the VWF inlet concentration to the platelet inlet concentration. Likewise, the bound platelet equation on, $S_\perp$ for all z, is one of

$$\frac{\partial\phi_{pb}}{\partial t} = \begin{cases} \mathcal{E}\phi_p\phi_{vb}, & \text{(7.30a)} \\ \mathcal{L}\phi_p\phi_{vb}, & \text{(7.30b)} \\ \mathcal{L}\phi_p\phi_{vb}\left(1 - \dfrac{\phi_{pb}}{\mathcal{L}\phi_{vb}}\right). & \text{(7.30c)} \end{cases}$$

The dimensionless boundary and initial conditions are

$$p = 0,\ u = 0,\ v = 0,\ \frac{\partial \phi_p}{\partial z} = 0,\ \frac{\partial \phi_v}{\partial z} = 0 \qquad \text{at} \quad z = 1, \tag{7.31}$$

$$u = 0,\ v = 0,\ w = 0 \qquad \text{on} \quad S_\perp \ \forall\ z, \tag{7.32}$$

$$\phi_v = 1,\ \phi_p = 1,\ u = 0,\ v = 0,\ w = w^*(x, y) \quad \text{at} \quad z = -1, \tag{7.33}$$

where in (7.33) w^* is defined so that we have unit flux at the inlet:

$$\iint_{V_\perp} w^*(x, y)\ dxdy = 1. \tag{7.34}$$

The dimensionless flux of free VWF onto the pipe walls $S_\perp$ for all z is given by

$$D_v \nabla \phi_v \cdot \hat{\boldsymbol{n}} = \begin{cases} -\sigma_b \dfrac{\hat{\kappa}}{Re} \mathcal{E} \phi_v \phi_{pb}, & \text{(7.35a)} \\ -\sigma_b \dfrac{\hat{\kappa}}{Re} \mathcal{L} \phi_v \phi_{pb}, & \text{(7.35b)} \\ -\sigma_b \dfrac{\hat{\kappa}}{Re} \mathcal{L} \phi_v \phi_{pb} \left(1 - \dfrac{\phi_{vb}}{\phi_{pb}}\right). & \text{(7.35c)} \end{cases}$$

Here, $\sigma_b = \phi_{vbi}/\phi_{pi} l$ is the ratio of the initial bound VWF concentration to the inlet concentration of platelets and we have incorporated the fact that $\boldsymbol{u} = \boldsymbol{0}$ on $S_\perp$. Similarly, the dimensionless flux of free platelets onto the pipe walls is given by

$$\hat{D}_p \nabla \phi_p \cdot \hat{\boldsymbol{n}} = \begin{cases} -\sigma_b \dfrac{\hat{\kappa}}{Re} \mathcal{E} \phi_p \phi_{vb}, & \text{(7.36a)} \\ -\sigma_b \dfrac{\hat{\kappa}}{Re} \mathcal{L} \phi_p \phi_{vb}, & \text{(7.36b)} \\ -\sigma_b \dfrac{\hat{\kappa}}{Re} \mathcal{L} \phi_p \phi_{vb} \left(1 - \dfrac{\phi_{pb}}{\mathcal{L} \phi_{vb}}\right). & \text{(7.36c)} \end{cases}$$

The initial conditions for the system at $t = 0$ are

$$\phi_v = 1,\ \phi_p = 1,\ \phi_{vb} = 1,\ \phi_{pb} = 0. \tag{7.37}$$

We can now contrast this dimensionless model under the lubrication scaling with the dimensionless model we analysed in Chapter 6. Firstly, in the Navier-Stokes equations (7.13) - (7.16), inertial terms are now premultiplied by the reduced Reynolds number $\epsilon^2 Re$, demonstrating that the small aspect ratio of the device demotes inertia compared to the arterial-scale device. In the equations for the free VWF and platelet concentrations, (7.18) and (7.19), diffusive effects in the cross-section are promoted compared to in Chapter 6. In the FENE-P equations, (7.22) - (7.27), since the axial velocity is larger than the cross-sectional fluid velocities, the key fluid gradients which

deform the protein are the cross-sectional gradients of the axial velocity. Furthermore, the cross-sectional gradients of the axial velocity are an order of magnitude larger than the convective forces in (7.22) - (7.27). Hence, in this device, the VWF protein extension is dominated by the fluid extension forces rather than advection.

7.4.2 Integrated transport equations

We will analyse the free VWF and platelet transport equations (7.18) and (7.19) in the small, reduced shear Péclet number regime so we anticipate that the leading-order concentrations will be functions of z only. Hence, we now derive a conservation equation for the free VWF and platelet which will be used to determine their leading order concentrations. We detail this for the platelet transport equation only for brevity. We first integrate the transport equation (7.19) over the cross-section of the pipe $V_\perp$, giving

$$\frac{\hat{\kappa}}{Re}\frac{\partial}{\partial t}\int_{-1}^{1}\int_{-s}^{s}\phi_p\,dxdy+\int_{-1}^{1}\int_{-s}^{s}\nabla_\perp\cdot\left(\boldsymbol{u}_\perp\phi_p-\frac{\hat{D}_p}{\epsilon^2}\nabla_\perp\phi_p\right)\,dxdy \\ +\frac{\partial}{\partial z}\int_{-1}^{1}\int_{-s}^{s}\left(w\phi_p-\hat{D}_p\frac{\partial\phi_p}{\partial z}\right)\,dxdy-\frac{\partial s}{\partial z}\int_{-1}^{1}\left[\hat{D}_p\frac{\partial\phi_p}{\partial z}\right]_{-s}^{s}\,dy=0, \quad (7.38)$$

where we have used Leibniz' integral rule to exchange integration with the axial and time derivatives which produces the final term in (7.38). We directly integrate the second double integral in (7.38), rather than using the divergence theorem, since the normal to $V_\perp$ is not equal to the normal to the three dimensional surface of the microfluidic device which is defined

$$\boldsymbol{n}=\begin{cases}\pm\boldsymbol{j} & \text{on } y=\pm1,\\ \pm\left(\boldsymbol{i}-\epsilon\dfrac{\partial s}{\partial s}\boldsymbol{k}\right) & \text{on } x=\pm s,\end{cases} \quad (7.39)$$

which has magnitude

$$|\boldsymbol{n}|=\begin{cases}1 & \text{on } y=\pm1,\\ \left(1+\epsilon^2\left(\dfrac{\partial s}{\partial z}\right)^2\right)^{1/2} & \text{on } x=\pm s,\end{cases} \quad (7.40)$$

such that the outward unit normal to the pipe is defined $\hat{\boldsymbol{n}} = \boldsymbol{n}/|\boldsymbol{n}|$. Evaluating the second double integral in (7.38) we have

$$\frac{\hat{\kappa}}{Re}\frac{\partial}{\partial t}\int_{-1}^{1}\int_{-s}^{s}\phi_p\,dxdy + \frac{\partial}{\partial z}\int_{-1}^{1}\int_{-s}^{s}\left(w\phi_p - \hat{D}_p\frac{\partial\phi_p}{\partial z}\right)\,dxdy + \int_{-1}^{1}\left[-\frac{\hat{D}_p}{\epsilon^2}\nabla_\perp\phi_p + \frac{\partial s}{\partial z}\hat{D}_p\frac{\partial\phi_p}{\partial z}\right]_{-s}^{s}dy + \int_{-s}^{s}\left[-\frac{\hat{D}_p}{\epsilon^2}\nabla_\perp\phi_p\right]_{-1}^{1}dx = 0. \quad (7.41)$$

The integrands in (7.41) are equal to the flux into the pipe surface multiplied by $|\boldsymbol{n}|/\epsilon$, hence applying the flux boundary condition (7.35a), we have

$$\frac{\hat{\kappa}}{Re}\frac{\partial}{\partial t}\int_{-1}^{1}\int_{-s}^{s}\phi_p\,dxdy + \frac{\partial}{\partial z}\int_{-1}^{1}\int_{-s}^{s}\left(w\phi_p - \hat{D}_p\frac{\partial\phi_p}{\partial z}\right)\,dxdy = -\epsilon|\boldsymbol{n}|\sigma_b\frac{\hat{\kappa}}{Re}\int_{S_\perp}\mathcal{E}\phi_v\phi_{pb}\,dS. \quad (7.42)$$

and similarly for the free VWF concentration we have

$$\frac{\hat{\kappa}}{Re}\frac{\partial}{\partial t}\int_{-1}^{1}\int_{-s}^{s}\phi_v\,dxdy + \frac{\partial}{\partial z}\int_{-1}^{1}\int_{-s}^{s}\left(w\phi_v - \hat{D}_v\frac{\partial\phi_v}{\partial z}\right)\,dxdy = -\epsilon|\boldsymbol{n}|\sigma_b\frac{\hat{\kappa}}{Re}\int_{S_\perp}\mathcal{E}\phi_p\phi_{vb}\,dS, \quad (7.43)$$

which we have derived from (7.18) using boundary condition (7.36a). We now examine the values of the model parameters in this lubrication regime.

7.5 Parameter values

The dimensionless parameters for the device geometry and the fluid flow, their definitions, and their values in the microfluidic *in vitro* setup are shown in Table 7.3. We also list the order of these values in the *in vitro* setup compared to ϵ. It is useful to define the reduced Brownian Péclet numbers for VWF and platelets as $\epsilon^2 Pe_v$ and $\epsilon^2 Pe_p$ which determine the strength of axial advection to cross-sectional diffusion. The reduced shear Péclet number is $\epsilon^3 Pe_{\mathrm{sh}}$, where the additional power of ϵ arises from the scaling of the shear rate.

The reduced Brownian Péclet numbers are both large, of $O(\epsilon^{-2})$, which demonstrates that Brownian diffusion is subdominant to fluid transport. The reduced shear Péclet number is 11.1, which is also large but smaller than the Brownian Péclet numbers. This suggests that in the microfluidic system, the transport of platelets and VWF is dominated by fluid advection with platelets and VWF accumulating in

a diffusive boundary layer on the pipe walls. Analysing this boundary layer would require solving a lubrication-type problem at higher-order to determine the velocity components in all three dimensions. This would then be coupled to a two-dimensional boundary layer problem on all the walls of the domain for the concentration of free platelets and VWF. As a result, this regime would be more computationally complex than the full scale arterial simulations carried out in Chapter 6.

However, if the aspect ratio of the pipe were reduced by a third, then the reduced shear Péclet number would be small. The small reduced shear Péclet number limit is significantly more tractable and we are able to develop a reduced, one dimensional model. Since we are close to this regime experimentally, we choose to examine the regime where $\epsilon^3 Pe_{\text{sh}} = O(\epsilon)$. Hence, we define $Pe_{\text{sh}} = \epsilon^{-2} Pe_0$ and take $Pe_0 = O(1)$. In this analysis, we take the orders of all other geometry and flow parameters to be as close to their orders in the *in vitro* setup as possible. We list our assumptions of the parameter orders in the last column of Table 4.1. Following these scalings, we define the scaled Reynolds number $Re = \epsilon^{-1} Re_0$ where Re_0 is of $O(1)$.

The six unknown dimensionless parameters are listed in Table 7.4. To balance elastic forces on the right-hand side of (7.22) - (7.27) with fluid shear forces on the left-hand side, we assume that $\xi = O(\epsilon^2)$. We scale the VWF unfolding rate such that $\hat{\gamma}^*$ is of $O(\epsilon^{-1})$ to balance our scaling of the shear rate. We assume all other parameters are of $O(1)$. This is a valid assumption for the VWF extensibility parameter L since *in vitro*, VWF has been observed to extend to up 20 times its original length, which is of $O(1)$ [98]. Since we have scaled the Reynolds number with ϵ^{-1}, the timescale of platelet-VWF binding is longer than the timescale of fluid advection such that $\hat{\kappa}/Re$ is of $O(\epsilon)$. The assumed order of all model parameters is listed in Table 7.4.

We proceed by determining the leading-order system as $\epsilon \to 0$. We derive this system using the binding rates proportional to VWF extension as the other cases can be readily recovered from this one, by inserting the alternative binding models defined in (7.6c) and (7.6b) into the leading-order, integrated conservation equation free platelets and PDE for bound platelet deposition, which we derive in Section 7.6.2.

Name	Param.	Def.	Val. *in vitro*	In model
Aspect Ratio	ϵ	h/l	3.1×10^{-3}	$O(\epsilon)$
Reduced Reynolds	$\epsilon^2 Re$	$h^2 U\rho/l\mu$	0.33	$O(\epsilon)$
Reduced shear Péclet	$\epsilon^3 Pe_{\text{sh}}$	h^3/lk_{sh}	11.1	$O(\epsilon)^*$
Reduced VWF Brownian Péclet	$\epsilon^2 Pe_v$	Uh^2/lD_v	5.9×10^5	$O(\epsilon^{-2})$
Reduced Platelet Brownian Péclet	$\epsilon^2 Pe_p$	Uh^2/lD_p	1.85×10^6	$O(\epsilon^{-2})$
Inlet conc. ratio	σ_v	ϕ_{vi}/ϕ_{pi}	2.1×10^{-3}	$O(\epsilon)$
Stenosis length	$\hat{l}_1$	l_1/l	0.23	$O(1)$
Tapering length	$\hat{l}_2$	l_2/l	0.08	$O(1)$
Minimum width	$\hat{d}_2$	d_2/h	10	$O(1)$
Maximum width	$\hat{d}_1$	d_1/h	1	$O(1)$

Table 7.3: Known dimensionless parameters for the model using values from the microfluidic *in vitro* setup in Table 7.1 and blood shown in Table 7.2. In the last column we list the assumed order of the parameters in the model. These are as close as possible to the *in vitro* parameters, except for the reduced shear Péclet number, marked with a star, which is reduced.

Name	Param.	Def.	In model
VWF relaxation parameter	ξ	$\alpha\mu/l^2\rho$	$O(\epsilon^2)$
VWF unfolding threshold	$\hat{\gamma}^*$	$\gamma^* l^2\rho/\mu$	$O(\epsilon^{-1})$
VWF-platelet binding rate	$\hat{\kappa}$	$\kappa\phi_{pi} l^2\rho/\mu$	$O(1)$
VWF extension parameter	$\hat{\beta}$	$\beta\mu/l^2\rho$	$O(1)$
VWF maximum extension	L	-	$O(1)$
VWF small relaxation time	δ	-	$O(1)$
Bound VWF concentration ratio	σ_b	$\phi_{vbi}/l\phi_{pi}$	$O(1)$

Table 7.4: Unknown model parameters, their definitions relative to dimensional equivalents and the assumptions about their order.

7.6 Leading-order model

We now determine the leading-order dynamics of the system using the assumptions on fluid transport equations listed in Tables 7.3 and VWF and platelet binding parameters in Table 7.4.

7.6.1 Fluid flow

First, we consider the fluid mechanics, recalling that the reduced Reynolds number is small. We expand the fluid variables such that $u \sim u_0$, $v \sim v_0$, $w \sim w_0$, $p \sim p_0$, as $\epsilon \to 0$, then using this expansion in Eqs. (7.13) - (7.16), the leading-order flow system reduces to the standard lubrication equations for slow flow in the domain V, namely

$$\frac{\partial u_0}{\partial x} + \frac{\partial v_0}{\partial y} + \frac{\partial w_0}{\partial z} = 0, \tag{7.44}$$

$$\frac{\partial p_0}{\partial x} = 0, \tag{7.45}$$

$$\frac{\partial p_0}{\partial y} = 0, \tag{7.46}$$

$$\frac{\partial^2 w_0}{\partial x^2} + \frac{\partial^2 w_0}{\partial y^2} = \frac{\partial p_0}{\partial z}. \tag{7.47}$$

The boundary conditions on the walls of the pipe $S_\perp$, (7.32), become

$$u_0 = 0, \ v_0 = 0, \ w_0 = 0 \quad \text{on } S_\perp \ \forall z. \tag{7.48}$$

By (7.45) and (7.46), the pressure is independent of the cross-sectional coordinates, and we can solve Eq. (7.47) using a cosine series expansion. We suppose that w_0 has a solution of the form

$$w_0(x, y, z) = \sum_{n>0, \text{ odd}}^{\infty} A_n(y, z) \cos\Big(\frac{n\pi x}{2s}\Big), \tag{7.49}$$

so that w_0 already satisfies $w_0 = 0$ on $x = \pm s$. Inserting Eq. (7.49) into (7.47), we have

$$\sum_{n>0, \text{ odd}}^{\infty} \cos\Big(\frac{n\pi x}{2s}\Big) \left[\frac{d^2 A_n}{dy^2} - \Big(\frac{n\pi}{2s}\Big)^2 A_n\right] = \frac{\partial p_0}{\partial z}, \tag{7.50}$$

where we require $A_n = 0$ on $y = \pm 1$ to satisfy the no-flux boundary condition (7.48). We thus obtain the following solution for the leading-order axial flow:

$$w_0(x, y, z) = \frac{16 s^2}{\pi^3} \frac{\partial p_0}{\partial z} \sum_{n>0, \text{ odd}}^{\infty} \frac{(-1)^{(n-1)/2}}{n^3} \cos\Big(\frac{n\pi x}{2s}\Big) \left(\frac{\cosh(n\pi y/2s)}{\cosh(n\pi/2s)} - 1\right). \tag{7.51}$$

We note that the terms in the solution (7.51) converge faster than the standard double cosine eigenfunction solution to (7.47) in a rectangle which converges $\sim n^2$ as $n \to \infty$.

To determine the leading-order axial pressure gradient, we integrate the continuity equation (7.44) in the cross-section of the pipe $V_\perp$. Since the cross-sectional flow

vanishes on the boundary, we deduce that the flux is constant in the pipe and equal to the inlet unit flux defined in (7.34). Hence,

$$\iint_{V_\perp} w_0 \, dxdy = 1. \tag{7.52}$$

We can then insert our solution for w_0 into Eq. (7.52), giving the following expression for the axial pressure gradient:

$$\frac{\partial p_0}{\partial z}\frac{128s^3}{\pi^5}\sum_{n>0,\text{ odd}}^{\infty}\frac{1}{n^5}\left(2s\tanh\left(\frac{n\pi}{2s}\right)-n\pi\right) = 1. \tag{7.53}$$

This determines the leading-order axial flow as a function of pipe width s and the cross-sectional coordinates. We now proceed by examining the transport of free VWF and platelets.

7.6.2 Free species transport

To determine the leading-order VWF and platelet system we examine the size of the Péclet numbers. Since the reduced Brownian Péclet numbers are of $O(\epsilon^{-2})$, Brownian motion for both species is considerably weaker than fluid advection. We have assumed that the reduced shear Péclet number is of $O(\epsilon)$, hence the cross-sectional shear-induced diffusion dominates over axial advection.

We expand the free and bound species concentrations as follows:

$$(\phi_v, \phi_p, \phi_{pb}, \phi_{vb}) \sim (\phi_{v0}, \phi_{p0}, \phi_{pb0}, \phi_{vb0}) \text{ as } \epsilon \to 0. \tag{7.54}$$

Inserting these expansions into Eq. (7.18) and (7.19), we find that at leading-order diffusion dominates in the cross-section, which gives the following system:

$$\nabla_\perp \cdot (\dot{\gamma}_0 \nabla_\perp \phi_{v0}) = 0, \tag{7.55}$$

$$\nabla_\perp \cdot (\dot{\gamma}_0 \nabla_\perp \phi_{p0}) = 0, \tag{7.56}$$

where the leading-order shear rate $\dot{\gamma}_0$ depends only on the leading-order axial velocity through the expression

$$\dot{\gamma}_0 = \sqrt{\left(\frac{\partial w_0}{\partial x}\right)^2 + \left(\frac{\partial w_0}{\partial y}\right)^2}. \tag{7.57}$$

Since we have scaled the Reynolds number with ϵ, the flux of free species on the walls in (7.35a) and (7.36a) are now proportional to $\epsilon\sigma_b\hat{\kappa}/Re_0$. Hence, at leading-order, we have no diffusive flux on the walls of the domain, obtaining instead homogeneous Neumann boundary conditions on $S_\perp(z)$ for all z:

$$\nabla_\perp \phi_{v0} \cdot \hat{\boldsymbol{n}} = 0 \text{ on } S_\perp, \tag{7.58}$$

$$\nabla_\perp \phi_{p0} \cdot \hat{\boldsymbol{n}} = 0 \text{ on } S_\perp. \tag{7.59}$$

The shear rate becomes $O(\epsilon)$ in the centre of the pipe, $|\boldsymbol{x}_\perp| < \epsilon$. However, diffusive terms are promoted by $O(\epsilon^{-2})$. Hence, diffusive forces still dominate the dynamics in this region. This results in leading-order concentration solutions $\phi_{p0}(z)$ and $\phi_{v0}(z)$ that are independent of the cross-sectional coordinates x and y throughout the pipe.

We now insert the expansions for ϕ_v and ϕ_p into the conservation equations (7.42) and (7.43). We note that the axial shear diffusion is of $O(\epsilon)$ so that it is subdominant to fluid advection. Hence the leading-order conservation equations, in $z = [-1, 1]$, are

$$\frac{\partial}{\partial z}\left(\phi_{v0}\iint_{V_\perp} w_0 \, dxdy\right) + \frac{\hat{\kappa}\sigma_b\phi_{v0}}{Re_0}\int_{S_\perp} \mathcal{E}_0\phi_{pb0} \, dS = 0, \tag{7.60}$$

$$\frac{\partial}{\partial z}\left(\phi_{p0}\iint_{V_\perp} w_0 \, dxdy\right) + \frac{\hat{\kappa}\sigma_b\phi_{p0}}{Re_0}\int_{S_\perp} \mathcal{E}_0\phi_{vb0} \, dS = 0, \tag{7.61}$$

where $\mathcal{E}_0$ is the leading-order VWF extension and the normal metric $|\boldsymbol{n}|$ is not present as at leading-order the normal to $x = \pm s$ is equal to $\pm\boldsymbol{i}$. Using the flux conservation result (7.52) we have

$$\frac{\partial\phi_{v0}}{\partial z} + \frac{\hat{\kappa}\sigma_b\phi_{v0}}{Re_0}\int_{S_\perp} \mathcal{E}_0\phi_{pb0} dS = 0, \tag{7.62}$$

$$\frac{\partial\phi_{p0}}{\partial z} + \frac{\hat{\kappa}\sigma_b\phi_{p0}}{Re_0}\int_{S_\perp} \mathcal{E}_0\phi_{vb0} \, dS = 0. \tag{7.63}$$

These are coupled to the leading-order versions of (7.29a) and (7.30a), namely

$$\frac{\partial\phi_{vb0}}{\partial t} = 0, \tag{7.64}$$

$$\frac{\partial\phi_{pb0}}{\partial t} = \mathcal{E}_0\phi_{p0}\phi_{vb0}, \tag{7.65}$$

which hold on $S_\perp$, where the right-hand side of (7.64) is equal to zero because $\sigma_v = O(\epsilon)$. Hence on this timescale bound VWF remains at its initial values: $\phi_{vb0} = 1$, and the solution for the free VWF concentration, determined by (7.62), decouples from the remaining system for the free and bound platelet concentrations. Hence we

do not need to solve for ϕ_{v0} to determine the bound platelet deposition. The system consisting of (7.62) - (7.63) on $z = [-1, 1]$ and (7.64) - (7.65) on $S_\perp$ has boundary and initial conditions

$$\phi_{p0} = 1 \text{ at } z = -1, \tag{7.66}$$

$$\phi_{pb0} = 0 \text{ at } t = 0. \tag{7.67}$$

We then determine an analytical expression for the free platelet concentration to be given by

$$\phi_{p0}(z) = \exp\left(-\frac{\hat{\kappa}\sigma_b}{Re_0}\int_{-1}^{z}\int_{S_\perp(\hat{z})}\mathcal{E}_0\ dSd\hat{z}\right). \tag{7.68}$$

We note that the free platelet concentration is steady since the bound VWF concentration does not change on this timescale. Hence, it remains to solve a single PDE for the bound platelet concentration at each location on the wall $S_{\perp(z)}$, namely

$$\frac{\partial\phi_{pb0}}{\partial t} = \mathcal{E}_0\phi_{p0} = \mathcal{E}_0\exp\left(-\frac{\hat{\kappa}\sigma_b}{Re_0}\int_{-1}^{z}\int_{S_\perp(\hat{z})}\mathcal{E}_0\ dSd\hat{z}\right). \tag{7.69}$$

We now examine the VWF extension dynamics to determine $\mathcal{E}_0$.

7.6.3 VWF extension

We now determine the leading-order balance in the FENE-P equations (7.22) - (7.27). We recall that we selected the parameters in the shear-dependent relaxation time, (7.28), so that at high shear, the elastic forces in the FENE-P equations (7.22) - (7.27) balance with the shear forces. This led to the assumption, detailed in Section 7.5, that $\xi Re = O(\epsilon)$ and the definition $\xi = \epsilon^2\xi_0$. Furthermore, since we assumed that the VWF extensibility parameter L, which determines the maximum length of VWF, is of $O(1)$, we assume that the components of the configuration tensor also remain $O(1)$. Hence, expanding the configuration tensor $\boldsymbol{A} \sim \boldsymbol{A}_0$ as $\epsilon \to 0$, the FENE-P equations, (7.22) - (7.27), reduce at leading-order to an algebraic system as follows

$$fA_{xx,0} = a, \tag{7.70}$$

$$fA_{yy,0} = a, \tag{7.71}$$

$$2A_{xz,0}\frac{\partial w_0}{\partial x} + 2A_{yz,0}\frac{\partial w_0}{\partial y} = \frac{fA_{zz,0} - a}{\xi_0 Re_0\hat{\tau}(\dot{\gamma})}, \tag{7.72}$$

$$A_{yy,0}\frac{\partial w_0}{\partial y} = \frac{fA_{yz,0}}{\xi_0 Re_0\hat{\tau}(\dot{\gamma})}, \tag{7.73}$$

$$A_{xx,0}\frac{\partial w_0}{\partial x} = \frac{fA_{xz,0}}{\xi_0 Re_0\hat{\tau}(\dot{\gamma})}, \tag{7.74}$$

$$A_{xy,0} = 0, \tag{7.75}$$

where $a = L^2/(L^2 - 3)$ and $f = L^2/(A_{zz,0} + A_{yy,0} + A_{xx,0} - L^2)$. We define the leading-order protein length as

$$\mathcal{L}_0 = \frac{\sqrt{A_{xx,0} + A_{yy,0} + A_{zz,0}}}{\sqrt{3}}, \tag{7.76}$$

and the corresponding leading-order extension by $\mathcal{E}_0 = \mathcal{L}_0 - 1$. In this thin-film regime, the transport of the proteins is subdominant to extension so the proteins respond instantaneously to the changing fluid shear forces as they move through the pipe. Since the largest components of fluid shear are gradients of the axial flow in the cross-sectional directions, these are the only components which alter the VWF length and alignment at leading-order.

We can further interpret the leading-order system, (7.70) - (7.74), as follows. The proteins are sheared in the axial direction shown in Eqs. (7.72) - (7.74). This will cause an increase in their length and in the alignment of the proteins with the z-axis. In order to maintain the length of the protein below L, the protein will contract in the x- and y- direction as shown by Eqs. (7.70) and (7.71). By (7.75), $A_{xy,0} = 0$, which demonstrates that the protein alignment is randomly distributed in the (x, y) planes. From (7.70) and (7.71), the proteins contract equally in both x- and y- directions to maintain their length. This arises because we scaled both cross-sectional directions with ϵ.

It is interesting to note here the reduction of the FENE-P equations from a system of PDEs to an algebraic system arises because there is no diffusion in the FENE-P equation and advection is subdominant to fluid extension forces on the protein. Furthermore, since we only require the value of the leading-order VWF extension $\mathcal{E}_0$ on the walls of the pipe to determine how free platelets deposit using (7.69), we can solve (7.70) - (7.74) only on $S_\perp$.

To summarise, the leading-order system consists of the analytic expressions for the axial fluid flow w_0, (7.51), and pressure p_0, (7.53), and an algebraic system of five equations for the VWF configuration tensor $\boldsymbol{A}_0$: (7.70) - (7.74). The VWF length $\mathcal{L}_0$ and extension $\mathcal{E}_0$ can then be determined by (7.76). We have an algebraic equation for the concentration of free platelets at each axial position in the pipe $z = [-1, 1]$, given by (7.68), which is coupled to a PDE which determines the bound platelet concentration at each point on the pipe walls $S_\perp$, given by (7.69).

This system is significantly less complex than the original system of PDEs and can be readily solved numerically. We note that since the series solution for the axial flow is even in x and y and since $s(z)$ is even in z, the axial flow downstream of

the stenosis is equal to the flow upstream. Since the flow is even in all coordinates, the VWF extension is also even in x, y and z. Furthermore, since free platelets can deposit on all walls of the domain, (7.69) can be solved in a quarter of the domain $x > 0$, $y > 0$. We now present our numerical method for solving the coupled system.

7.6.4 Numerical solution

The leading-order model can be solved sequentially in $x > 0$, $y > 0$. We first evaluate the fluid solution, (7.51) and (7.53), then the VWF extension, (7.70) - (7.75), and then solve the platelet equations, (7.68) and (7.69).

We take the first 300 components of the series solution for the axial velocity and pressure, (7.51) and (7.53). As described in Appendix B.4, each term in the series solution for the axial velocity decays as $O(n^{-3})$ as $n \to \infty$, this results in an 0.27% error and an 0.014% error in the maximum values of $\partial w_0/\partial x$ and $\partial w_0/\partial y$ respectively when compared to truncating the series at 5000 terms.

We solve the FENE-P equations, (7.70) - (7.75), on the walls of the domain only since this is the only location where we need the solution to determine platelet deposition. We can simplify the system since $\partial w_0/\partial x = 0$ on the base of the domain and similarly $\partial w_0/\partial y = 0$ on the side walls of the domain. We then formulate the remaining system as a polynomial for $A_{zz,0}$, which we solve using *roots* in MATLAB, taking the only real solution. We validate this solution by noting that as $L \to \infty$ the FENE-P model reduces to the Oldroyd-B system which can be solved analytically. As described in Appendix B.4, our solution to the FENE-P model, (7.70) - (7.75), tends to this analytical solution as $L \to \infty$.

The free platelet solution, (7.69), is evaluated using numerical quadrature employing the MATLAB function *trapz*. We use 500 grid points to discretise the x- and y-dimensions and 1000 grid points in the z-dimension. We confirm that the quadrature achieves the known convergence of the trapezoidal rule in Appendix B.4. We solve the PDE for the bound platelets, (7.68), using MATLAB integrator *ode45* with absolute tolerance 10^{-6} and relative tolerance 10^{-3}, which are the default values. We examine the effect of varying these in Appendix B.4 but conclude that these values are sufficient as they give an error in the bound platelet concentration of 10^{-4} at $t = 21$ compared to using an absolute tolerance of 10^{-8} and relative tolerance of 10^{-5}.

The plan for the remainder of this chapter is as follows. In Section 7.7, we solve the model numerically for the binding dynamics proportional to VWF extension using the VWF unfolding parameters from Chapter 5, defined in Table 7.5, and all other parameters as in Table 7.3. We fix the initial bound VWF concentration such that

Name	Param.	Def. (if reduced)	Values
Reynolds Number	Re_0	Re/ϵ	$1.8 - 47$
Stenosis length	$\hat{l}_1$	-	0.23
Tapering length	$\hat{l}_2$	-	0.1 - 0.4
Minimum width	$\hat{d}_2$	-	10
Maximum width	$\hat{d}_1$	-	1
VWF relaxation parameter	ξ_0	ξ/ϵ^2	725
VWF extension threshold	$\hat{\gamma}_0^*$	$\hat{\gamma}^*\epsilon$	16.9
VWF platelet binding rate	$\hat{\kappa}$	-	$0.01 - 3.2$
VWF extension parameter	$\hat{\beta}$	-	3.8×10^{-4}
VWF maximum extension	L	-	16
Initial VWF concentration	σ_b	-	1
VWF small relaxation time	δ	-	10^{-2}

Table 7.5: Model parameters and definitions relative to dimensional equivalents. We use values selected in Chapters 5 and 6 for the VWF unfolding parameters.

$\sigma_b = 1$ and then we vary the binding rate $\hat{\kappa}$ from 0.1 to 3.2. We explore how the microfluidic device geometry and Reynolds number affect the VWF dynamics and platelet deposition in Section 7.8. In Section 7.9, we then examine how these results change when the different binding models are used. In Section 7.10 we then determine how *in vitro* data of VWF behaviour and thrombosis could be used to parameterise the model in the future.

7.7 Typical numerical results

Figure 7.7a - d shows the leading-order model solution with x- and y- directions scaled by ϵ to allow for easy comparison with Fig. 7.1. Figure 7.7a shows the leading-order prediction for the wall shear rate according to the analytical axial fluid solution (7.51), which illustrates that the wall shear rate is ten times larger in the stenosis than upstream. Fig. 7.7b shows the resulting VWF extension. The protein extends up to $\mathcal{E}_0 = 7$ in the stenosis where the shear rate is high, and remains globular, corresponding to $\mathcal{E}_0 = 0$, in the upstream and downstream regions of the pipe. We note that this differs from our previous examination of VWF dynamics in Chapter 6 in which advection transported extended proteins downstream of the stenosis.

The free platelets are shown in Fig. 7.7c at $t = 1$. The free platelet concentration is not reduced upstream of the stenosis as there is no deposition in this region. The

free platelet concentration then decreases up to 0.75 across the stenosis. The bound platelets on the wall of the domain at $t = 1$ are shown in Fig.7.7d. At this binding rate, the deposition follows the VWF extension pattern very closely with platelets deposited where VWF is extended but with more deposition at the start of the stenosis.

The time-dependent dynamics are shown in Fig. 7.8. We plot the average bound platelet concentration $\bar{\phi}_{pb0}$ defined as

$$\bar{\phi}_{pb0} = \iint_{V_\perp} \phi_{pb0} \, dxdy. \tag{7.77}$$

As discussed above for $t = 1$, bound platelets as shown in Fig. 7.8a deposit only where VWF is extended inside the narrowest part of the stenosis, marked with dashed lines, with slightly more deposited at the start of the stenosis. In Fig. 7.8b, the free platelet concentration in the pipe is steady as was noted in Section 7.6.2.

7.8 Thrombosis dependence on Reynolds number and geometry

We now explore how the Reynolds number and stenosis geometry alter the deposition patterns in the lubrication regime. In Fig. 7.9a we vary the scaled Reynolds number, Re_0 from 1.8 to 47, examining the bound platelet deposition which occurs at $t = 1$ in all cases. In the microfluidic device $Re_0 = 37.8$. We can see that as Re increases, more platelets are deposited and further upstream as the maximum shear rate increases in the pipe and the proteins unfold more.

In Fig. 7.9b we vary the stenosis angle, where a smaller value of $\hat{l}_2$ corresponds to a steeper stenosis. In this lubrication regime, decreasing stenosis angle does not increase the maximum shear rate in the pipe, instead the gradient of the shear rate in the axial distance increases. This is reflected in the average bound platelet concentrations shown in Fig. 7.9b, where for steeper stenosis the platelets are deposited further downstream but approximately the same amount of platelets are deposited in the centre of the stenosis for $z > -0.2$.

7.9 Exploration of binding models

We now explore how bound platelet deposition varies spatially and temporally when we consider the alternative binding models defined in Eqs. (7.30b) and (7.30c) while varying the binding rate $\hat{\kappa}$. We obtain the leading-order model for alternative binding models, defined in (7.30b) and (7.30c), by modifying the right-hand side of (7.68) and

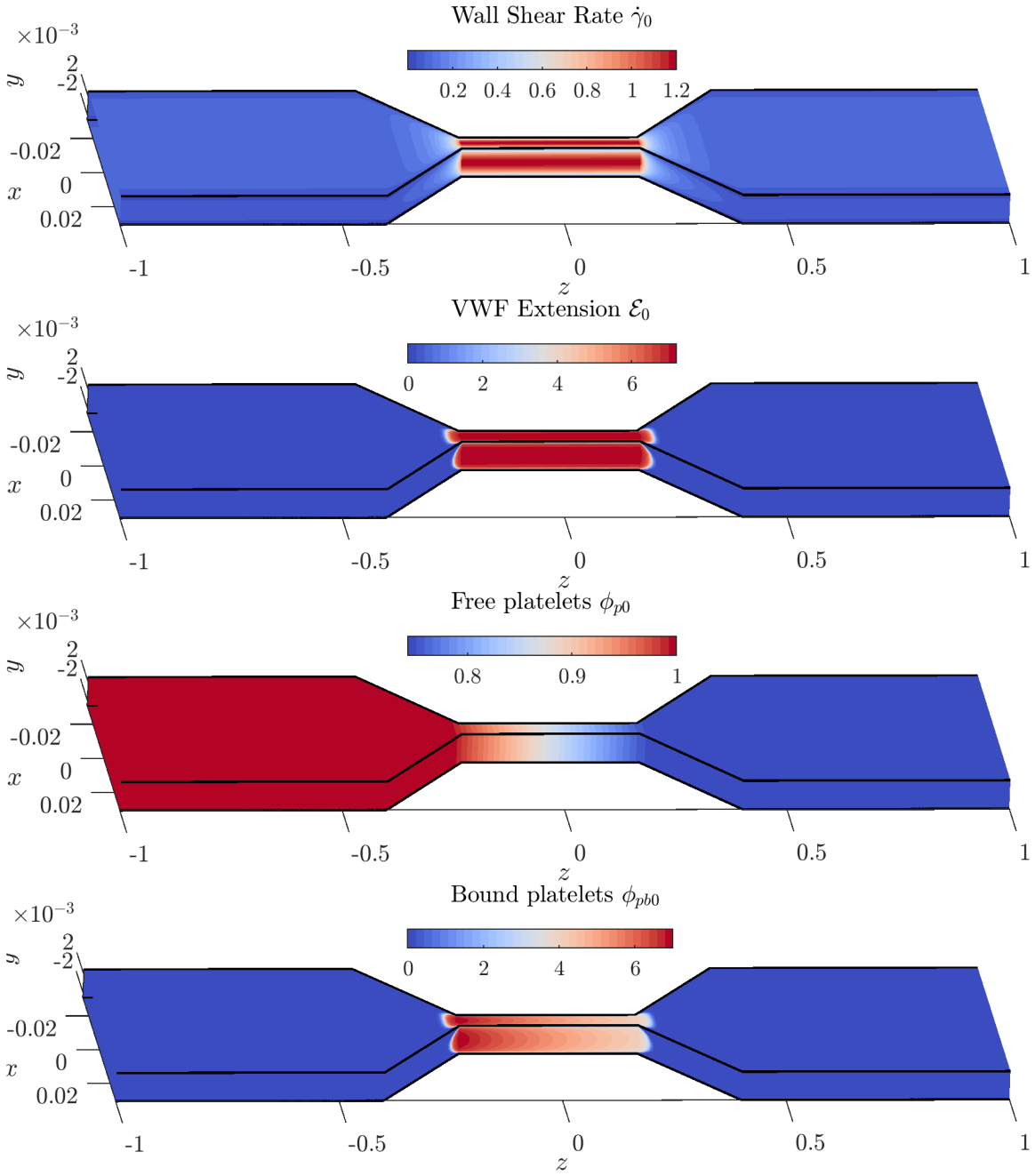

Figure 7.7: Solution of leading-order lubrication model, shown with x- and y- directions scaled by ϵ to allow for easy comparison with Fig. 7.1. (a) Wall shear rate is ten times higher in the stenosis than upstream. (b) VWF reaches its maximum extension $\mathcal{E}_0 = 7$ in the centre of the stenosis. The extension is symmetric around $z = 0$. (c) Free platelet concentration is shown at $t = 1$. The concentration is independent of cross-sectional coordinates and only reduces in the stenosis where binding occurs. (d) Bound platelet concentration at $t = 1$. Platelets deposit where VWF is extended, with more platelets deposited at the upstream edge of the stenosis. We have $Re_0 = 37.8$, $\hat{\kappa} = 1$, all other parameters are shown in Table 7.5.

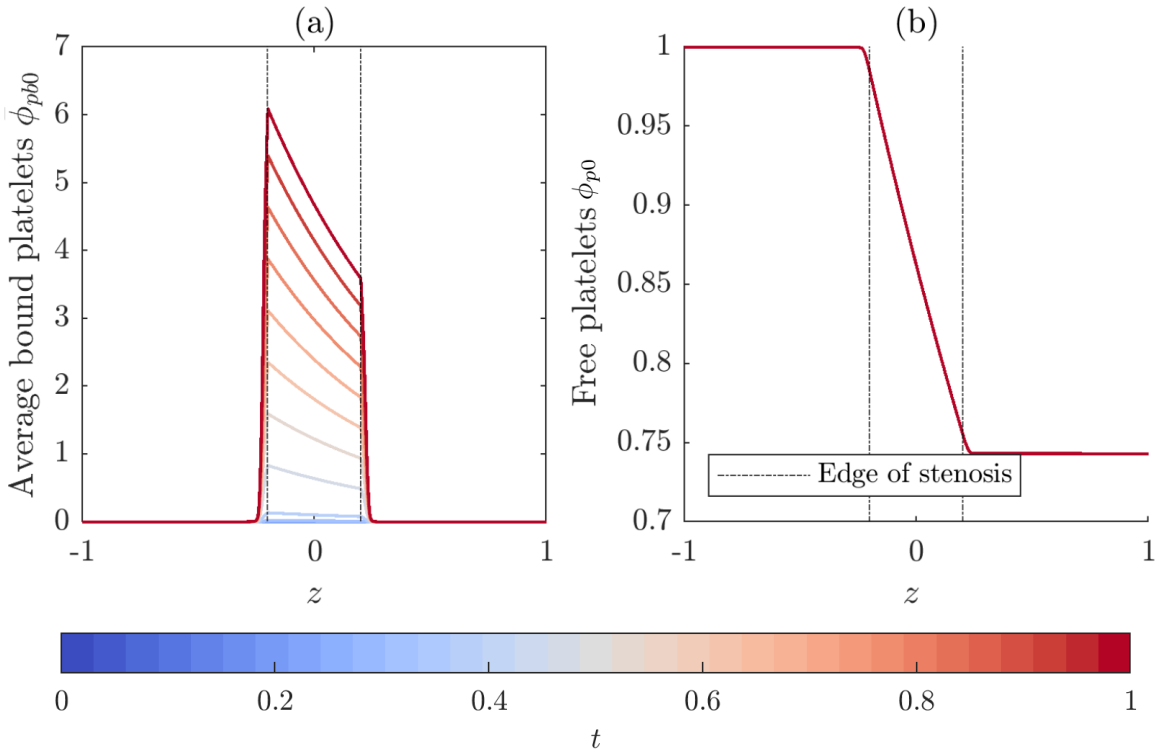

Figure 7.8: (a) The average bound platelet and (b) free platelet concentrations over time. The edge of the narrowest part of the domain is shown by the black dashed lines. Line colour defines the time of the solution according to the colour bar. Bound platelets accumulate where VWF is extended and more platelets are deposited at the upstream edge of the stenosis. Free platelet concentration reduces only inside the stenosis. At later times there are fewer free platelets as more are deposited. We have $Re_0 = 37.8$, $\hat{\kappa} = 1$, all other parameters are shown in Table 7.5.

(7.69). This is motivated by our *in vitro* data demonstrating that a small number of platelets are deposited outside of the stenosis region. Since we nondimensionalised on the timescale of platelet deposition to compare different binding rates, we consider deposition up to $t = 2\hat{\kappa}$ which is a fixed dimensional time period (which was selected to show saturation in Fig. 7.10c).

In the previous section we considered the dynamics where platelets bind proportional to VWF extension $\mathcal{E}$ with a binding rate $\hat{\kappa} = 1$. We now consider $\hat{\kappa}$ ranging from 0.01 to 3.2 for all the binding models. In Fig. 7.10a, binding proportional to VWF extension is shown for increasing binding rate. As the binding rate increases, the overall deposition increases. Furthermore, for $\hat{\kappa} \gtrsim 2$, the deposition is no longer uniform across the stenosis and platelets are deposited more at the start of the stenosis (black dashed line). Fig. 7.10b shows deposition proportional to VWF length $\mathcal{L}$ as defined in Eq. (7.30b). Since this allows platelets to deposit where $\mathcal{L} = 1$, we see a

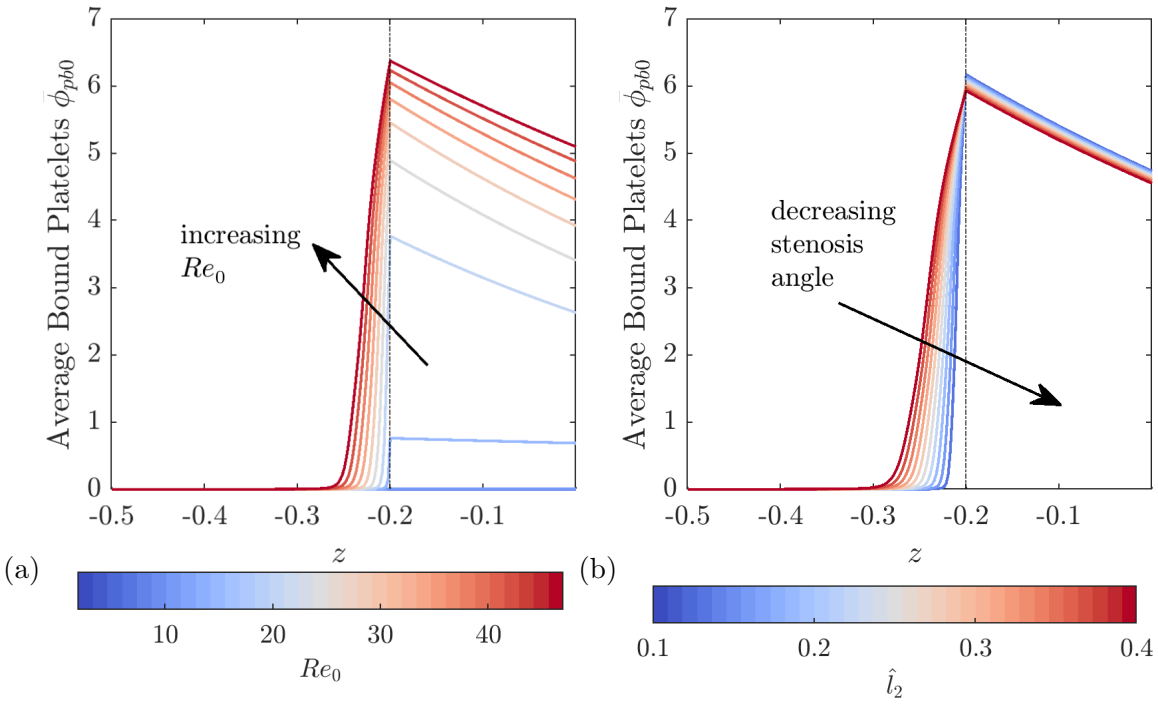

Figure 7.9: Average bound platelet concentration on the base obtained at $t = 1$. (a) Increasing the scaled Reynolds number Re_0 results in greater extension of VWF and more platelet deposition. (b) Increasing the stenosis angle, which corresponds to decreasing $\hat{l}_2$, results in platelet deposition further upstream as the wall shear rate required to unfold VWF occurs further downstream. In the lubrication regime, increasing the steepness does not increase the maximum shear rate, so all cases have $\max \phi_{pb} \approx 6$. In both cases we have $\hat{\kappa} = 1$ in (b) we have $Re_0 = 37.8$, all other parameters are shown in Table 7.5.

significant deposition of platelets upstream in $z < -0.2$. Upstream deposition results in fewer platelets depositing in the stenosis region for larger values of $\hat{\kappa}$, compared to Fig. 7.10a, as available free platelets are used up by the upstream deposition.

Finally, in Fig. 7.10c we plot the bound platelet concentration when the saturating binding model, defined in (7.6c), is used. In this case, binding is limited by the available space on the existing bound VWF. Since we do not have deposition of bound VWF in the leading-order model, this results in a maximum bound platelet concentration of $\phi_{pb0} = \mathcal{L}$. As the binding rate increases, the bound platelets reach this level more rapidly. This is in contrast to Fig. 7.10a and 7.10b where the binding is not limited to $\mathcal{L}$

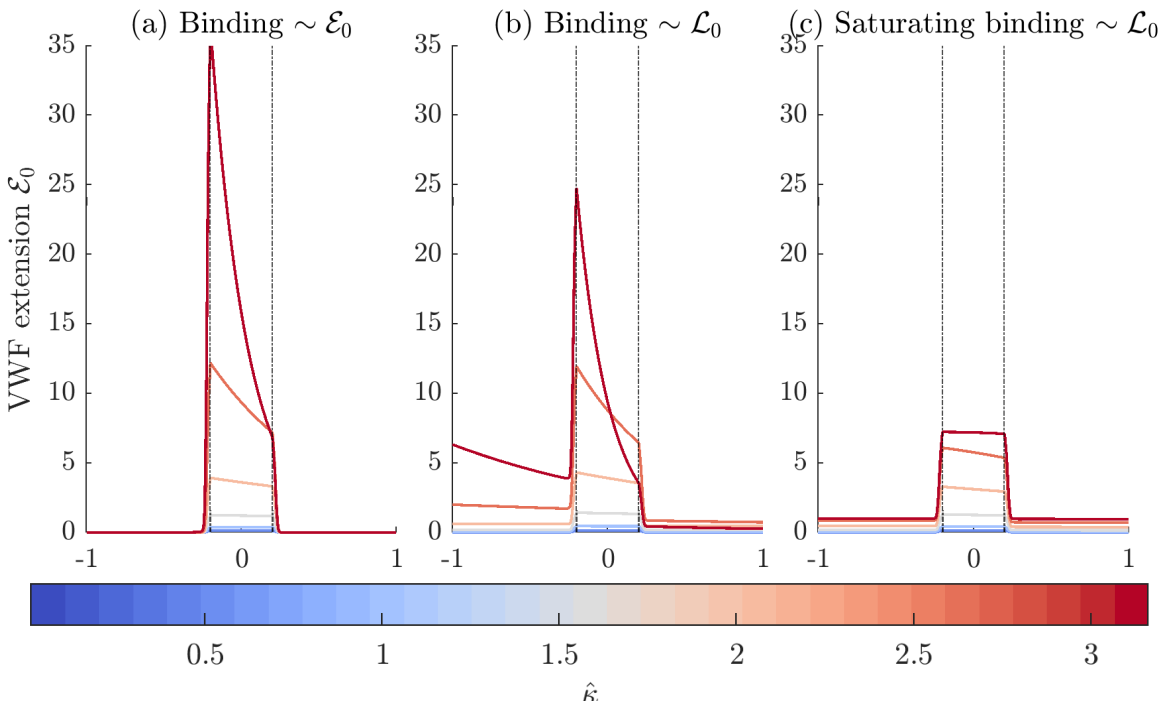

Figure 7.10: Comparison of platelet deposition for three cases of binding dynamics. We depict deposition at time $t = 2\hat{\kappa}$ so that we consider the same dimensional time period in each case. (a) Binding proportional to VWF extension $\mathcal{E}$ causes very large deposition in the stenosis which increases with the binding rate. (b) Binding proportional to VWF length $\mathcal{L}$ causes large deposition in the stenosis and upstream of the stenosis where the proteins are globular. (c) Saturating binding proportional to VWF extension $\mathcal{L}$ leads to deposition in which the maximum possible bound platelet concentration is $\phi_{pb} = \mathcal{L}$ which is obtained as $\hat{\kappa} \to 3.2$. We have $Re_0 = 37.8$, all other parameters are shown in Table 7.5.

7.10 Parameterisation through numerical optimisation

We recall that our model has seven unknown parameters: γ^*, β, α, L and δ, which characterise VWF's unfolding, as well as κ and ϕ_{vbi}, which determine the free platelet deposition to VWF. In Sections 7.7 - 7.9, we used values of these parameters which were qualitatively chosen in Chapters 5 and 6. In this section, we discuss how these model parameters could be determined using experimental data.

At the start of this chapter we discussed two existing types of experimental data: (i) VWF length at various shear rates which have been gathered by Lippok and coauthors and (ii) thrombosis data from a microfluidic device provided by our collaborators. In Section 7.5, we determined that in the microfluidic device used to gather thrombosis data, the reduced shear Péclet number for platelet transport is 11.1. In

this chapter, we analysed the model for the regime when the reduced shear Péclet number $\epsilon^2 Pe_{\text{sh}}$ is of $O(\epsilon)$. Hence, we recall that the reduced model in Section 7.6 is outside of the regime of the experiments used to gather thrombosis data. In this section, we discuss how model predictions can be compared to microfluidic data so that this method can be applied when future experimental data is available in the $\epsilon^3 Pe_{\text{sh}} = O(\epsilon)$ regime.

In this section, we use Lippok et al. VWF experimental data to determine γ^*, β, α, L, and δ. We then discuss how the microfluidic data could be used to find σ_b and $\hat{\kappa}$. We use the Lippok et al. experimental data since the Schneider et al. data sampled a limited number of shear rates and did not show saturation. We recall Lippok et al. estimated VWF cleavage as a function of the shear rate as

$$\kappa_{cleave}(\dot{\gamma}) = \frac{3.5 \times 10^{-3}}{1 - \exp((\dot{\gamma} - 5522)/1271)} \text{nM/s}. \tag{7.78}$$

Since the proteins were sheared in combination with an enzyme which cleaves VWF at an internal bond, usually hidden when the protein is globular, the authors assumed that VWF cleavage was proportional to VWF length. We can define the relative extension predicted by the Lippok fitting at the shear rate $\dot{\gamma}_i$ as $\tilde{\mathcal{E}}(\dot{\gamma}_i) = \kappa_{cleave}(\dot{\gamma}_i)/3.5 \times 10^{-3}\text{nM/s}$. If we define the solution of the FENE-P equation in two-dimensional shear flow at $\dot{\gamma}_i$ as $\mathcal{E}(\gamma_i)$, we can define the mean error made to Lippok fitting as

$$\epsilon_{VWF} = \frac{1}{N} \sum_{i=1}^{N} |\tilde{\mathcal{E}}(\dot{\gamma}_i) - \mathcal{E}(\dot{\gamma}_i)|, \tag{7.79}$$

where we use N discrete values of the shear rate between zero and $\dot{\gamma} = 10^5$. We can then use a minimisation algorithm to minimise the error from a suitable initial guess of the parameters. In this case, we estimate some of the initial parameters comparing the Lippok fitting to the VWF relaxation time. This gives initial values of $\beta = 2/1271$ and $\dot{\gamma} = 5522$. For the remaining parameters we use heuristic guesses at the values we used in Chapter 6 as these produced physically realistic results: $L = 16$, $\alpha = 9.3 \times 10^{-2}$, and $\delta = 10^{-4}$.

We can now seek a set of parameter values which minimise e_{VWF}. We use the gradient-based minimiser *fmincon* from MATLAB's optimisation toolbox. This evaluates the minimisation from a single initial condition using the gradient of the multidimensional parameter space to select the next parameter values in an iterative procedure. Since we have an estimate of several of the parameters, we expect the minimum found with a single initial condition will approximate the Lippok extension sufficiently. We will discuss alternative minimisation approaches in Section 7.11.

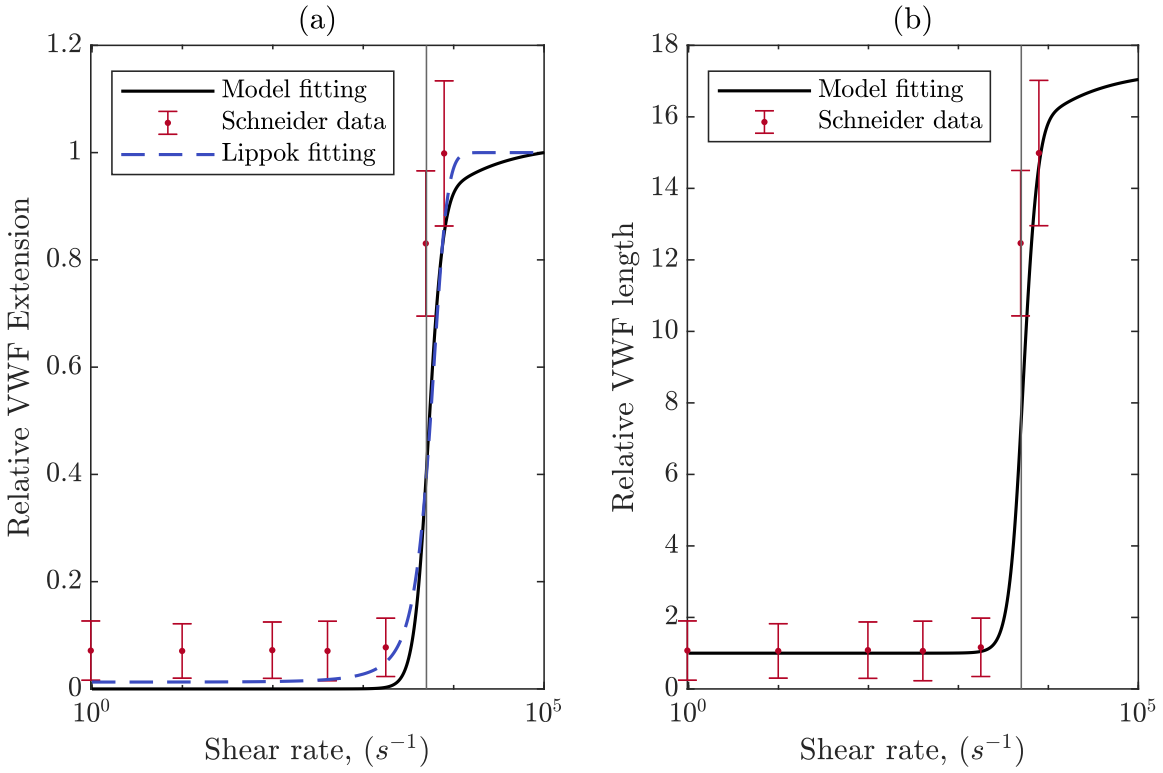

Figure 7.11: Best fit of model VWF behaviour in shear flow to the empirical fitting obtained by Lippok et al. [69]. We add the experimental data by Schneider et al. for comparison; however, this is not used in the fitting [98]. (a) The relative extension of VWF, (b) VWF length which is only available for the Schneider data set.

Using *fmincon*, we are able to obtain a minimum error $\epsilon_{VWF} = 0.078$ which corresponds to a mean error of 7.8%. In Fig. 7.11a, we show that the best fitting of the relative extension of the FENE-P model obtains a good quantitative and qualitative match to the Lippok fitting. This result also closely matches the relative extension obtained by Schneider et al., marked by the red bars in Fig. 7.11a, and the length by Schneider et al., shown in Fig. 7.11b.

Using these fitted VWF parameters, two unknown model parameters remain: the VWF-platelet binding rate $\hat{\kappa}$ and the relative initial concentration of VWF σ_b. We can use the microfluidic data to estimate these parameters. We need to define the error made relative to the *in vitro* microfluidic data. The binding rate primarily controls the amount of bound platelets deposited at each time rather than the location at which platelets bind. The latter is determined by the VWF extension. This motivates focusing on matching the maximum value of bound platelets at each time. Hence, we

can define an error metric as follows:

$$\epsilon_p = \frac{1}{N}\sum_{j=1}^{N} \frac{|\max(\tilde{\phi}_{pb}(z,t_j)) - \delta_p \max(\phi_{pb}(z_i,t_j))|}{|\max \tilde{\phi}_{pb}(z,t_j)|}, \tag{7.80}$$

where $\tilde{\phi}_{pb}$ is the experimental data and δ_p is the parameter which converts bound platelet concentration to platelet fluorescence. With a low-dimensional parameter space, a grid search where one parameter is held fixed and the other parameter is varied becomes tractable. As a representative example we fix $\sigma_b = 1$ and evaluate the error for $\hat{\kappa} \in [10^{-2}, 10^2]$. We note we cannot consider $\hat{\kappa} > 10^2$ as this would modify the leading order flux boundary conditions for the free species concentrations defined in (7.58) and (7.59). The minimum error we can obtain with this metric is $\epsilon_{p1} = 0.09$ (9% mean error), which is obtained using binding proportional to VWF extension. The best value of the binding rate is $\hat{\kappa} = 0.6$, for which the model solution is shown in Fig. 7.12b compared to the *in vitro* data in Fig. 7.12a.

The best fitting obtains a qualitatively similar shape to the microfluidic data, and we are able to obtain a quantitatively similar maximum platelet deposition in the stenosis. However, since we have binding proportional to VWF extension we do not have any platelet depoition for $z < -0.25$. This qualitative match to the *in vitro* data in the stenosis, is surprising since our analysis of the platelet transport assumed a smaller value of the reduced Péclet number than *in vitro*. This is likely because the VWF unfolding parameters have been determined accurately using the Lippok et al. data which then allows us accurately capture the qualitative shape of the deposition, despite the transport dynamics being in a slightly different regime.

7.11 Discussion

In this chapter, we analysed our model for the initial stages of high shear thrombosis in a rectangular microfluidic stenosis geometry. We exploited the small aspect ratio of the device and analysed the system using lubrication theory. The leading-order reduced model consists of an analytical solution for the axial fluid velocity and pressure gradient, an algebraic system of equations for the VWF extension, an analytical expression for free platelets, and a single PDE which determines the bound platelet concentration at each location on the walls. This is a significant reduction in model complexity compared to the full model analysed in Chapter 6.

We used this reduced model to explore the effect of pipe geometry and Reynolds number on VWF behaviour. In the lubrication limit, VWF advection is subdominant

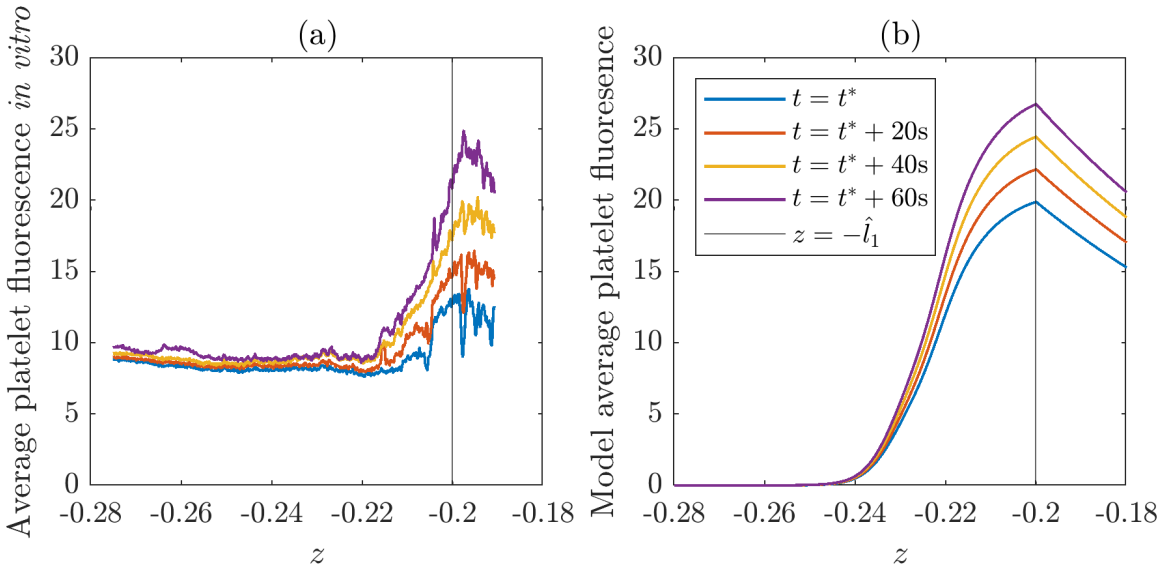

Figure 7.12: Comparison of the (a) *in vitro* microfluidic platelet deposition data to (b) the best fitting obtained using binding proportional to VWF extension with $\hat{\kappa} = 0.6$.

to shear and elastic forces. Hence, VWF extension at the wall is determined by the local fluid gradients at each point. Since the flow is symmetric in x, y and z, VWF extension is also symmetric in all coordinates, and the region where VWF is extended simply corresponds to the region of highest shear rate: the narrowest part of the pipe. The shear rate increases in the pipe as the Reynolds number increases and the profile of the shear rate is determined by the geometry of the pipe; for instance, steeper stenoses have larger axial gradients in the shear rate.

We constructed a reduced model motivated by the need to determine VWF unfolding parameters, the VWF platelet binding rate, and the initial concentration of bound VWF. In this chapter, we presented the data gathered by our collaborators on thrombosis in a microfluidic device. We analysed five experimental repeats of thrombosis with a single flow rate and in a single geometry. Through image analysis, we constructed average platelet fluorescence data sets for each repeat and determined the first time when the clot in the device embolises. This allowed us to bound the validity of the model comparison as we do not include clot growth in our model and thus cannot examine dynamics close to embolism. In this chapter, we also examined existing data for VWF dynamics in suspension, focusing on the data of Lippok et al. for VWF cleavage in flow [69].

To parameterise the model we used the Lippok et al. data to determine five VWF unfolding parameters: α, γ^*, β, δ and $\mathcal{L}$ by minimising the distance of the FENE-P model solution in 2D shear flow to the empirical fitting. We obtained a good quantita-

tive match to the Lippok et al. data for VWF extension and also obtains a reasonable quantitative match to the smaller Schneider et al. dataset for VWF length. We then presented a framework for determining the VWF binding rate $\hat{\kappa}$ and initial bound VWF concentration σ_b using microfluidic data. This could be done by comparing the maximum value of platelet deposition over time. To test this framework, we compared our model solution to the data even though we analysed the model for the reduced Péclet number being small, whereas the experiments had a reduced Péclet number of 11.1. We were able to achieve a qualitative match to the trend of platelet deposition seen *in vitro* which is likely since the VWF parameters, which primarily control deposition location in the stenosis, were accurately determined.

To accurately determine the remaining model parameters in the future, it would be ideal to obtain a greater number of experimental microfluidic repeats. As reflected in the large values of the standard deviation in the microfluidic data, the median calculated from five experimental repeats is not an accurate depiction of the average behaviour of thrombosis in this device. Furthermore, even with an accurate estimate of average behaviour at a single flow rate, it would be beneficial to gather data on thrombosis at different flow rates or in different device geometries. More data would allow us to test the predictive capacity of the model with calibrated parameters.

Motivated by the trends in the microfluidic data, in this chapter we considered two additional binding models for platelet deposition. Firstly, binding proportional to VWF length, which allowed platelets to deposit in the upstream and downstream regions of the pipe with significant accumulation at the inlet of the pipe. Secondly, we considered a saturating form of binding. In this case, deposition was limited by the available bind sites on bound VWF which we modelled as the product of VWF length and bound VWF concentration, $\phi_{vb}\mathcal{L}$. This produced a small, uniform amount of deposition in the inlet regions of the pipe, and deposition in the pipe stenosis was limited to the maximum value of $\phi_{vb}\mathcal{L}$. We expect that in future analysis of this model, the saturating binding will be best able to describe *in vitro* thrombosis data as it is the only binding model which can produce a uniform thin layer of platelets in the upstream region of the pipe.

Chapter 8

Conclusion

We conclude this thesis by discussing the successes and limitations of the mathematical models we have developed and analysed. In addition we consider the insight they can offer into the haemodynamic processes and some valuable extensions that could be made to this work.

8.1 Summary of work

We have developed two mathematical models for the transport and deposition of species in blood vessels: firstly the cell delivery model - a model for the delivery of magnetically tagged stem cells under the action of an external magnet in a single vessel and secondly the thrombosis model - a model for the initial stages of high-shear thrombosis. Each model focuses on a different physiological process within blood vessels. However, both follow a unified approach of considering the transport dynamics of dilute species determined by interactions with red blood cells, the vessel walls and the fluid flow. We used a combined analytical and numerical approach to analyse these models. Large-scale simulations were used to gain insight into regimes where analytical approaches were not possible. These simulations were complemented with the use of lubrication theory which allowed us to develop reduced models more amenable to rapid numerical solution and therefore more extensive parameter space exploration.

In Chapter 2, we outlined the development of the cell delivery model. This model extends the existing continuum models of nanoparticle delivery to focus on the capture of cells [46, 92]. We modelled the accumulation of the cells on the channel wall through the growth of a solid cell aggregate which eventually obstructs the flow in the channel. The cell aggregate grows due to cell arrival, and cells are removed from the aggregate by surface erosion and extravasation through the channel wall. Development and

design of this model benefited from collaboration with researchers in regenerative medicine at the University of Birmingham, notably Prof. Alicia El Haj. Their *in vitro* work demonstrated that the efficacy of magnetic targeting is significantly reduced by the presence of RBCs. In addition, they have found that the safety of the therapy relies on the minimisation of unsafe aggregation of stem cells in vessels near the target site. Therefore the key objective of Chapters 2 - 4 was to determine the effect of RBCs on the stem cells and whether cell aggregation can be minimised.

In Chapter 3, we analysed the cell delivery model numerically using flow and magnetic parameters from Prof. El Haj group's *in vitro* setup. For the delivery of a bolus of stem cells we found that initially cells are rapidly captured, then erosion becomes significant as the aggregate obstructs the channel and finally the cells leave the channel by extravasation. We demonstrated that the model is able to reproduce trends shown *in vitro*: (i) fewer stem cells are captured when higher percentages of RBCs are present; and (ii) increasing the magnetic field strength increases capture. In this chapter we also outlined the importance of aggregate minimisation effects namely: aggregate erosion and cell extravasation. The magnitude of these two effects determines the level of occlusion present in the channel, which is a key aspect requiring regulation to ensure the safety of the therapy.

Motivated by the need to explore the model parameter space more easily, in Chapter 4, we considered the cell delivery model in regimes where the magnet radius is much larger than the pipe diameter. This allowed us to analyse the system with lubrication theory. We explored the model in two distinguished limits: when the reduced Péclet number is small and when it is large. The latter case extends the work of Richardson et al. [92], on the large Péclet number delivery of magnetic nanoparticles, by including an evolving aggregate boundary. Using these reduced cell delivery models, in each regime we numerically established fittings which quantify the bounds on safe magnetic field strengths which can be used for a given flow rate, erosion strength and extravasation strength.

In the second half of this thesis we developed and analysed our thrombosis model. In Chapter 5, we presented a model for the dynamics of shear-sensitive blood protein VWF, which we modelled using a dilute limit of the viscoelastic fluid model FENE-P with a modified relaxation time. This represents the first continuum model of the protein VWF to mechanistically describe its behaviour in response to flow. The resulting protein model was combined with a model for the initial stages of thrombosis in a three dimensional pipe, which consists of advection-diffusion equations modelling

the transport of platelets and VWF in blood and temporal partial differential equations that model the evolution of bound platelets and bound VWF on the pipe walls. We followed the structure of the existing models of thrombosis, e.g. [105, 118], by tracking the free and bound species, however our model did not include any growth of the clot.

Our thrombosis model was developed in collaboration with Prof. Netanel Korin's Cardiovascular Laboratory at Technion. Existing treatments for arterial thrombosis can damage areas of the vasculature outside the vessel with the clot which can cause complications of excess internal bleeding. Our model aims to aid the development of targeted methods of delivering drugs to clots, including shear-sensitive capsules which allow the drugs to be delivered directly to the clot location. These methods require an understanding of the location of clot formation and the interplay between fluid flow, the protein VWF and platelets in diseased arteries.

Prof. Korin provided us with *in vitro* data of VWF deposition in an arterial-scale, stenosed pipe and data of platelet deposition within a microfluidic device capable of recreating arterial-level shear rates. These experiments and datasets motivated the choice of model geometries in both Chapter 6 and 7. In Chapter 6, we analysed our thrombosis model in an axisymmetric arterial-scale pipe. We matched the model parameters as far as possible to the arterial experiments. Through numerical simulations we explored the dynamics of VWF and platelets in the complex flows that occur in large devices at large Reynolds numbers. We demonstrated that the rate of deposition of platelets is determined by the ratio of VWF length and Reynolds number. VWF length is a saturating function of the Reynolds number. We found that for $Re \lesssim 350$, VWF is globular and deposition is slow, then at $Re \approx 350$, VWF extends and the deposition rate increases, then for $Re \gtrsim 350$, VWF has reached its maximum length and the deposition rate decreases as the fluid speed increases. We determined that the deposition rate determines the deposition location, with platelet deposition occurring further upstream when the rate is highest, at $Re \approx 350$. In this chapter, we increased the Péclet numbers associated with VWF and platelet transport to carry out simulations using the finite element method.

In Chapter 7, we examined our thrombosis model in a rectangular microfluidic geometry designed to match the device used to gather *in vitro* clotting data. We used image analysis to obtain quantitative data of platelet deposition within the rectangular device from five *in vitro* experimental repeats. We then analysed the model using lubrication theory exploiting the small ratio between the device height and its length. This allowed us to analytically determine the leading-order axial

flow and pressure gradient in the device. The FENE-P equations for VWF were reduced to an algebraic system for the extension, demonstrating that the protein responds instantaneously to the local flow in this regime. We then used existing data of VWF dynamics to parameterise our modified FENE-P model, which produced a good quantitative agreement to the experimental shear flow dynamics of the protein. In this chapter we analysed the most tractable regime for the transport equations of VWF and platelets, where the reduced Péclet number is small. This differs from the regime of the microfluidic experiments where the reduced Péclet number is 11.1. However analysing the simpler regime where the reduced Péclet number is small allowed us to develop a method for comparing the microfluidic data to the model predictions which could feasibly be used following future *in vitro* experiments

8.2 Future work

There are several possible extensions to the work in this thesis, either through further analysis of the existing models, improvements in model parameterisation or through the inclusion of extra physical effects into the models. We now summarise the key extensions of each type in the following three subsections.

8.2.1 Further analysis

The main challenge we faced in the analysis of the models within this thesis was that the Péclet numbers associated with the transport of dilute species in blood are typically very large. To remedy this in Chapters 3 and 6 we artificially reduced the size of the Péclet numbers to solve the models numerically. This will have likely underestimated the amount of accumulation which occurs on pipe walls. In the future, work could be done to adapt the finite element method schemes used in these chapters to utilise discontinuous elements and thus solve PDEs which are close to hyperbolic [34]. Alternatively, the trajectories of the cells or proteins could be solved for using Lagrangian particle tracking using the numerical solutions of the fluid flow, thus eliminating the need to study a large Péclet number advection-diffusion problem.

Asymptotic analysis is a powerful complementary approach to examine the boundary layer which forms on the stenosis wall in Chapter 6. In this region, normal diffusion would balance axial fluid transport, leading to a boundary layer problem similar to the Graetz problem of flow over a heated plate. This would require a semi-numerical solution as the fluid flow and FENE-P equations must still be solved numerically. However, this approach would break down at the fluid stagnation point

where the flow separates behind the stenosis. In this region, diffusion would be significant in both axial and normal dimensions and the problem would again require a full numerical solution, although over a much smaller domain than the full problem.

In Chapter 4, we used lubrication theory to analyse our cell delivery model in the large Péclet number regime for one case of aggregate growth parameters. This led to a boundary layer of cell concentration forming on the growing aggregate, where flux from the channel balanced flux into the aggregate. Since the aggregate growth parameters are unknown, analysing this model for a wider range of aggregate growth parameters would allow this analysis to be used in the future if model parameters are quantified. In Chapter 7, we used lubrication theory to develop a reduced thrombosis model. However, even in the lubrication regime the reduced Péclet number was more than order unity. Hence we analysed the reduced thrombosis model in a regime which differed from the microfluidic dataset. The analysis of the large reduced Péclet number regime for the reduced thrombosis model would require the solution a higher-order lubrication type problem to determine the cross-sectional flow components. Despite the computational complexity, as this is the regime for which we currently have experimental data it would be a valuable addition to this work.

8.2.2 Parameter estimation

The predictive results of the cell delivery model developed in Chapters 2 - 4 are only qualitative at this stage. In order to make quantitative predictions we would need to estimate the model parameters associated with aggregate growth, fluid erosion and extravasation. These parameters could be estimated using *in vitro* models that have been developed, e.g. [19, 55], which quantify and visualise extravasation of cells or the effect of the magnetic force on extravasation speed [79]. Similarly, the *in vitro* setup, which was used to gather the data in Chapter 3, could be employed to determine the stem cells' susceptibility to erosion by varying flow rates over pre-captured cells. Quantification of these parameters would allow the model to provide a prediction of aggregation dynamics, providing insight into the dosage levels required to ensure that stem cell aggregation is kept within safe limits while maintaining therapeutic efficacy.

A significant portion of Chapter 7 was devoted to estimating the unknown model parameters in the thrombosis model. As we have previously discussed, in order to better estimate the model parameters associated with platelet dynamics we would need to potentially analyse the model in the large Péclet regime and also gather experimental data of thrombosis for a wider range of flow rates and geometries. This would allow us to estimate parameters and robustly test the modelling predictions.

8.2.3 Model extensions

The mathematical models' developed in this thesis aim to capture the key physical processes of the underlying biological system in idealised geometries. These simplifying assumptions have limitations, and there are a number of potential important physical effects which should be included in future studies of these models. For example, in the magnetic stem cell model we assumed unaggregated stem cells are dilute and therefore neglected their effect on the fluid flow. The inclusion cell volume would add a force on the fluid, which could slow down the flow and change cell capture dynamics. Previous models have examined the similar problem of the forces which magnetic nanoparticles have on fluid flow [20, 44]. This was noted to have the potential to induce mixing in extreme cases [44]. As well as this, our model did not include the magnetic interaction between the internal nanoparticles in each cell and between neighbouring cells. The construction of a continuum representation for the effect of these interactions on a density field of superparamagnetic NPs is an open problem.

A further limitation to consider is that the stem cell aggregate modelled in Chapter 2 - 4 assumes that the aggregated cells are solid. This assumption neglects to account for internal flow. The true aggregate of stem cells at the magnet is likely to be porous rather than solid and RBCs may also be accidentally captured adding further heterogeneity to the mass. Porous heterogenous clot formation has been studied in the context of thrombosis, where interclot flow along with RBC entrapment have been shown to be essential in understanding clot stability and possible fracture [28, 120]. Examining the internal aggregate structure and tracking the RBC distribution explicitly would be a valuable next step for the model. Another piece of extension work would be to focus the model on more aspects of *in vivo* delivery, for example the model could be extended to delivery over a vessel network or considering a range of physiological flow rates. In these extensions, the reduced models presented in Chapter 4 could be employed in each branch of the network to reduce computational complexity.

In Chapter 7, we examined several models for VWF-platelet binding dynamics in the thrombosis model. The bonds between VWF and platelets can unbind during the early stages of thrombosis [26]. *In vitro* work demonstrated that platelets can roll over the surface of VWF nets, binding and unbinding as they move [26]. This temporal binding was included in the continuum model from Du et al. [29] and resulted in the embolism of small pieces of the edges of the clot. The binding was assumed to remain for 0.5 s [26]. In our current model we assume that the bonds are not temporal. This binding and unbinding property could be examined by including an advection term

in the bound platelet PDE which would be proportional to the wall shear stress at that location. This could be used to determine if the initial location prediction is a reliable predictor of final clot location.

As detailed in Chapter 1, our collaborators have carried out *in vitro* experiments in this arterial device examining the deposition of VWF in the absence of platelets. Their results showed that VWF deposition is not uniform as we assumed in our model. With VWF deposition being localised in to the flow separation point at for a stenosis of height $h = 0.6$ but no localisation for a stenosis of height $h = 0.75$. Examining VWF binding dynamics with collagen in order to examine these results would be a valuable extension to the model, although this would add further model parameters and constitutive relations to be validated.

The thrombosis model developed in Chapters 5 - 7, aims to predict thrombus location using initial dynamics. Models which include the full thrombosis cascade have demonstrated that the initial location does broadly indicate the final thrombus location [29]. However, during the rapid thrombus growth seen in the later stage of thrombosis platelets are deposited preferentially in lower shear regions. As a result the initial location may not be sufficient to determine the location required for targeted thrombolytic drugs. The model presented in Chapters 5 - 7 could be readily extended to consider the later stages of thrombosis. Inclusion of thrombus growth via either an empirical growth law, as in Chapter 2 of this thesis or in [9, 77], would allow the model to include growth while remaining tractable.

A key property of the FENE-P equation, discussed in Chapter 5, is its ability to reproduce the known dependency of VWF on the flow structure. In Chapter 5 we demonstrated that the protein unfolds at a lower shear rate in elongational flow compared to shear flow. In this chapter, we used the solution of the FENE-P model at the wall to describe the length of VWF. Since the flow at the wall is predominantly shear flow, the elongational vs shear flow structure dependence of the FENE-P equation was not apparent in the results demonstrated in Chapters 6 or 7. Elongational aspects of the flow could become significant to platelet deposition if a number of extensions were considered to the model for example hysteresis, whereby the proteins relax back to their original length over a longer timescale than extension. This would mean that the proteins could retain extension as a result of elongational flows away from the walls of the pipe at the beginning of the stenosis. A key process to accurately model in this case would be the translation of VWF across fluid streamlines. VWF translation in pipe flow was examined using discrete mathematical models by Rack et al. who found that its ability to translate depended on both the RBC concentration

and the length of VWF [89]. In our model, we included shear-induced diffusion which models collisions with RBCs, but this was neglected in Chapter 6 in the numerical solution of the model to maintain tractability.

In conclusion, in this thesis we have developed novel mathematical models to examine blood flow dynamics in single vessels and the deposition of transported species to vessel walls. Through the collaboration with experimental biological researchers we identified the key aspects of delivery which are not well understood that mathematical models are able to help explore. In this thesis we have delivered mechanistic insight through the combination of large scale numerical simulations and exploitation of lubrication theory where possible. Finally, we have developed parameterisation frameworks which will enable these models to be used as predictive tools in the future.

Appendices

Appendix A

Weak form of thrombosis system

In this section we detail the weak form of the thrombosis model which we implemented in Chapter 6. This section follows the notation and schemes detailed in the *Automated solution of differential equations by the finite element method: The FEniCS book* by Log et al. [71]. We recall we are solving the steady Navier-Stokes (6.8) and (6.9), steady FENE-P equation (6.10) and time-dependent transport equations (6.14) and (6.13). We define the domain as Ω with the inlet denoted as Γ_i, the walls of the channel denoted Γ_w, the outlet denoted Γ_o and the centre of the channel Γ_c. The system is then defined in Ω

$$\nabla \cdot \boldsymbol{u} = 0, \tag{A.1}$$

$$Re\, \boldsymbol{u} \cdot \nabla \boldsymbol{u} = -\nabla p + \nabla^2 \boldsymbol{u}, \tag{A.2}$$

$$\boldsymbol{u} \cdot \nabla \boldsymbol{A} - \boldsymbol{A} \cdot \nabla \boldsymbol{u} - \nabla \boldsymbol{u}^T \cdot \boldsymbol{A} - D\nabla^2 \boldsymbol{A} = -\frac{1}{\xi Re \hat{\tau}(\dot{\gamma})}(f(\boldsymbol{A})\boldsymbol{A} - a\boldsymbol{I}), \tag{A.3}$$

$$\frac{\hat{\kappa}}{Re}\frac{\partial \phi_v}{\partial t} + \nabla \cdot (\boldsymbol{u}\phi_v - D\nabla \phi_v) = 0, \tag{A.4}$$

$$\frac{\hat{\kappa}}{Re}\frac{\partial \phi_p}{\partial t} + \nabla \cdot (\boldsymbol{u}\phi_p - D\nabla \phi_p) = 0, \tag{A.5}$$

where we have included the numerical diffusion in (A.3) - (A.5) with $D = 10^{-3}$. This has boundary conditions

$$w = \left(1 - r^2\right), \quad u = 0, \quad \boldsymbol{A} = \boldsymbol{A}_{in}(r), \quad \phi_v = 1, \quad \phi_p = 1 \quad \text{on} \quad \Gamma_i,$$

$$\hat{\boldsymbol{n}} \cdot \boldsymbol{\sigma} \cdot \hat{\boldsymbol{n}} = 0, \quad u = 0, \quad \nabla \phi_p \cdot \hat{\boldsymbol{n}} = 0, \quad \nabla \boldsymbol{A} \cdot \hat{\boldsymbol{n}} = \boldsymbol{0}, \quad \nabla \phi_v \cdot \hat{\boldsymbol{n}} = 0 \quad \text{on} \quad \Gamma_0,$$

$$u = 0, \quad \frac{\partial w}{\partial r} = 0, \quad \nabla \phi_v \cdot \hat{\boldsymbol{n}} = 0, \quad \nabla \boldsymbol{A} \cdot \hat{\boldsymbol{n}} = \boldsymbol{0}, \quad \nabla \phi_p \cdot \hat{\boldsymbol{n}} = 0 \quad \text{on} \quad \Gamma_c,$$

$$\boldsymbol{u} = \boldsymbol{0}, \quad (\phi_p \boldsymbol{u} - D\nabla \phi_p) \cdot \hat{\boldsymbol{n}} = \sigma_b \frac{\hat{\kappa}}{Re} \phi_p \phi_{vb} \mathcal{E} \quad \text{on} \quad \Gamma_w,$$

$$\nabla \boldsymbol{A} \cdot \hat{\boldsymbol{n}} = \boldsymbol{0}, \quad (\phi_v \boldsymbol{u} - D\nabla \phi_v) \cdot \hat{\boldsymbol{n}} = \sigma_b \frac{\hat{\kappa}}{Re} \phi_v \phi_{pb} \mathcal{E} \quad \text{on} \quad \Gamma_w.$$

We solve the system sequentially, first the Navier-Stokes equations, then the FENE-P equation, then the time dependent transport equations. We seek a solution to the Navier Stokes equations where $\boldsymbol{u}$ exists in a vector space $\boldsymbol{H}^1$, equipped with an inner product and the pressure exists in a scalar function space of square integrable functions on V: Q. We add further restrictions on the space by prescribing that our solutions must satisfy the Dirichlet conditions on the appropriate boundaries. This gives the function spaces as follows

$$\boldsymbol{u} \in V \subset \boldsymbol{H}_0^1(\Omega, \mathbb{R}^2) = \{\boldsymbol{u} \in \boldsymbol{H}^1(\Omega) \ : \ \boldsymbol{u} = \boldsymbol{0} \text{ on } \Gamma_w\}, \tag{A.6}$$

$$p \in Q \subset L_0^2(\Omega) = \{p \in L^2(\Omega) : p = 0 \text{ on } \Gamma_o\}, \tag{A.7}$$

The mixed space for the system $(\boldsymbol{u}, p)$ is constructed $W = V \times Q$. We now define test variables $(\boldsymbol{v}, q) \in W$ and multiply (A.2) by $\boldsymbol{v}$ and (A.1) by q to construct the weak formulation of the problem, as follows

$$\int_\Omega q \nabla \cdot \boldsymbol{u} \ d\Omega = 0, \tag{A.8}$$

$$\int_\Omega (Re\, \boldsymbol{u} \cdot \nabla \boldsymbol{u} + \nabla p - \nabla^2 \boldsymbol{u}) \cdot \boldsymbol{v} \, d\Omega = 0. \tag{A.9}$$

Integrating the last term in (A.9) by parts we obtain

$$\int_\Omega Re\, (\boldsymbol{u} \cdot \nabla \boldsymbol{u}) \cdot \boldsymbol{v} d\Omega + \int_\Omega (\nabla \boldsymbol{u} - p\boldsymbol{I}) \cdot \nabla \boldsymbol{v} d\Omega - \int_{\delta\Omega} \boldsymbol{v} (\nabla \boldsymbol{u} - p\boldsymbol{I}) \cdot \boldsymbol{n} \, dS = 0,$$

where $\delta\Omega$ is the boundary of Ω, and $\boldsymbol{n}$ is the outward pointing unit normal vector. Since we either have no stress or Dirichlet boundary conditions on all boundaries, the boundary term vanishes. We then add (A.8) and (A.10) to arrive at the weak form of Navier-Stokes as follows

$$\int_\Omega [Re\, (\boldsymbol{u} \cdot \nabla \boldsymbol{u}) \cdot \boldsymbol{v} d\Omega - (\nabla \boldsymbol{u} - p\boldsymbol{I}) \cdot \nabla \boldsymbol{v} + q \nabla \cdot \boldsymbol{u}] \ d\Omega = 0.$$

We solve this system using Taylor-Hood elements, second-order Lagrange elements for the velocity components and first-order Lagrange elements for the pressure.

For the FENE-P equations we seek a solution $\boldsymbol{A}$ where each entry of the tensor e.g. A_{rr} is in the following function space

$$A_{rr} \in Q \subset L_0^2(\Omega) = \{A_{rr} \in H^1(\Omega) : A_{rr} = A_{rr,i} \text{ on } \Gamma_i\}, \tag{A.10}$$

Since the FENE-P equations are comprised of four coupled advection-diffusion-reaction equations, we state the weak form for A_{rr} for brevity. We take a test function in Q and multiply the A_{rr} equation from (A.3).

$$\int_\Omega \left[-(\boldsymbol{u} A_{rr} - D \nabla A_{rr}) \cdot \nabla q + \left(-2A_r \frac{\partial u}{\partial r} - 2A_{rz} \frac{\partial w}{\partial r} + \frac{(f A_{rr} - a)}{\xi Re \hat{\tau}(\dot{\gamma})} \right) q \right] \ d\Omega = 0,$$

where we have integrated by parts to obtain the first term. Similarly the weak form for the time-dependent platelet and VWF transport equations are

$$\int_\Omega \frac{\partial \phi_v}{\partial t} q_2 - (\boldsymbol{u}\phi_v - D\nabla\phi_v)\cdot\nabla q_2 + \int_{\delta\Omega} \sigma_b \frac{\hat{\kappa}}{Re}\phi_v\phi_{pb}\mathcal{E}q_2 \; d\Gamma_w = 0,$$
$$\int_\Omega \frac{\partial \phi_p}{\partial t} q_3 - (\boldsymbol{u}\phi_p - D\nabla\phi_v)\cdot\nabla q_3 + \int_{\delta\Omega} \sigma_b \frac{\hat{\kappa}}{Re}\phi_p\phi_{vb}\mathcal{E}q_2 \; d\Gamma_w = 0,$$

where q_2 and q_3 are test functions in the following spaces

$$q_i \in Q \subset L_0^2(\Omega) = \{q_i \in H^1(\Omega) : q = 0 \text{ on } \Gamma_i\}, \tag{A.11}$$

and we define ϕ_{pb} and ϕ_{vb} as functions in $L^2(\Omega)$ with zero at all nodes aside from the nodes on Γ_w, where we track their values over time.

Appendix B

Numerical validation

This appendix details the numerical validation for all schemes in this thesis in the order they appear.

B.1 Validation of magnetic stem cell delivery COMSOL method

In this section we detail the numerical validation of the scheme in Chapter 3, which consists of quasi-steady Stokes equations (3.1) and (3.2), an advection diffusion equation for cell concentration (3.3), the growth of the aggregate defined by Eq. (3.13). We first detail our approximation of the flux condition Eq. (3.10) and then detail mesh convergence tests.

B.1.1 Regularised Heaviside functions

The flux condition for the cells, Eq. (3.10), requires three Heaviside functions. Defining the numerical approximation to the Heaviside function by $\tilde{\mathcal{H}}$ this is implemented as follows

$$\chi(c-\tilde{c})^{+} - \gamma\mu\left(\tau - \frac{\tilde{\tau}}{\mu}\right)^{+}\mathcal{H}(h) \approx \chi(c-\tilde{c})\tilde{\mathcal{H}}(c-\tilde{c})^{+} - \gamma\mu\left(\tau - \frac{\tilde{\tau}}{\mu}\right)\tilde{\mathcal{H}}\left(\tau - \frac{\tilde{\tau}}{\mu}\right)\tilde{\mathcal{H}}(h). \quad \text{(B.1)}$$

We use the inbuilt function *flc1hs*(x,δ) in COMSOL [21] which has continuous first derivative and is defined as a fifth order polynomial. The function is equal to zero for $x < -\delta$ and one for $x > \delta$. This is illustrated in Fig. B.1 for varying δ. Since we need to avoid the approximate Heaviside function having positive values for any $x < 0$, as this would allow effects such as erosion to occur when there is no aggregate, we chose

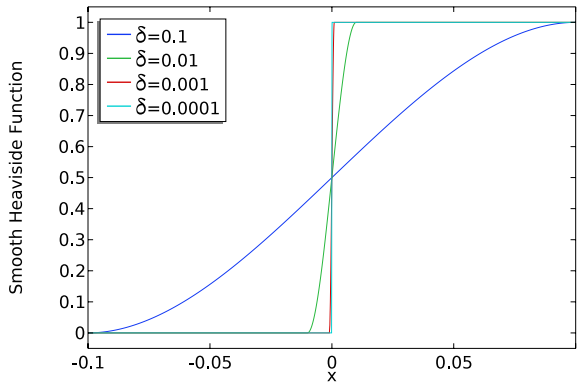

Figure B.1: Plot of the regularised heaviside function *flc1hs*(x, δ) for decreasing δ, as $\delta \to 0$ the regularised function tends to the analytic Heaviside function.

to use the Heaviside function shifted by δ such that it is equal to zero for $x < 0$ and one for $x > 2\delta$. We chose to use $\delta = 0.1$, which attains a maximum error of $< 10^{-3}$ in the aggregate height compared to using $\delta = 10^{-4}$.

B.1.2 Mesh convergence tests

To ensure our mesh is suitably fine we construct a mesh with finer elements near the boundary then reduce the total number of elements while maintaining this structure. We compare the solution obtained on meshes with increasing resolution to a reference solution obtained on a mesh with $m = 13758$ elements. We use a mesh which has $n = 4202$ elements which achieves $\leq 1.59\%$ (as shown in Figures B.2a and B.2b) percentage error compared to the reference solution, in all variables. We note that we restrict our study to values of $\gamma \leq 0.1$ since the coupling of the fluid shear to the moving boundary makes the problem stiff, hence we restrict gamma to ensure reasonable convergence (poor convergence shown in Fig B.3 for $\gamma = 0.5$).

B.2 Reduced models of magnetic stem cell delivery: numerical validation

This section details the numerical validation for the two numerical schemes used in Chapter 4.

B.2.1 Small Péclet number solution

This section validates the numerical scheme to solve the advection-diffusion equation (4.50) coupled to an PDE which governs aggregate height and (4.58), defined in

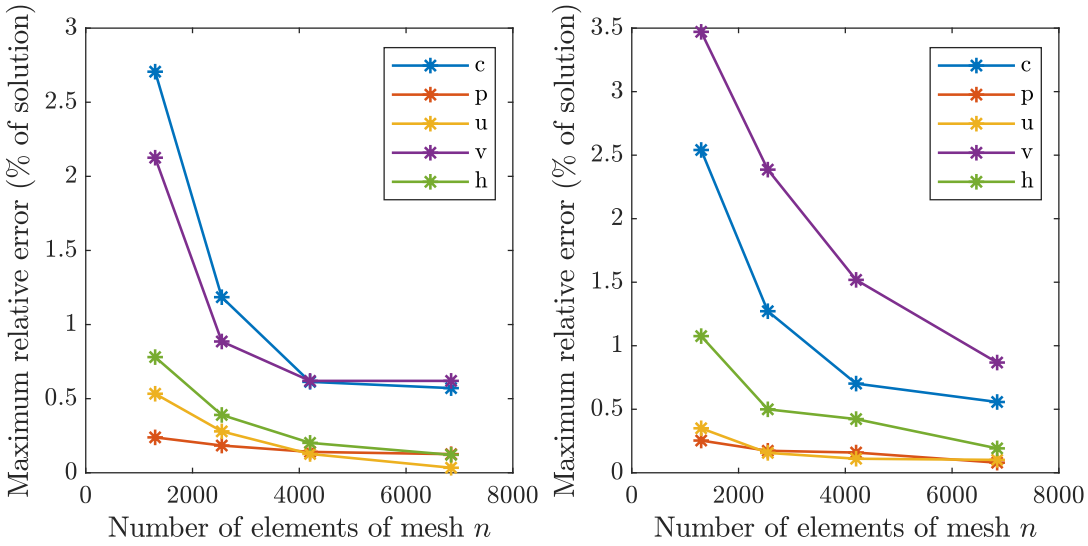

Figure B.2: Percentage error of each variable relative to the maximum value of that variable. (a) Parameters: $\beta = 210$, $\gamma = 0$, $\kappa_1 = 0$. (b) Parameters: $\beta = 210$, $\gamma = 0.1$, $\kappa_1 = 0.1$. The third mesh provides $< 1.59\%$ change in all variables.

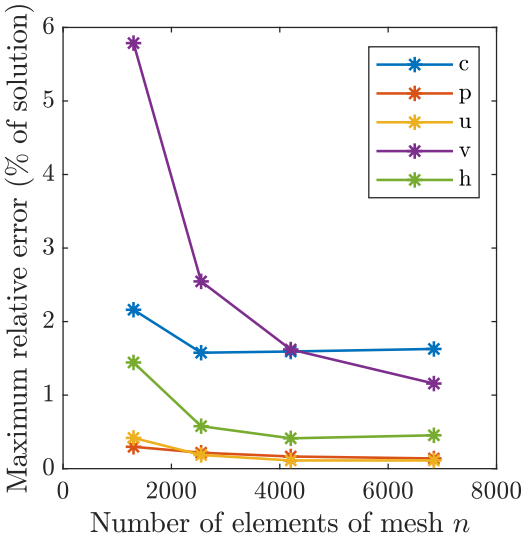

Figure B.3: Percentage error of each variable relative to the maximum value of that variable. Parameters: $\beta = 210$, $\gamma = 0.5$, $\kappa_1 = 0.1$. The solution does not have good convergence properties as γ is larger,so we restrict the value of γ considered to achieve better stability properties.

Section 4.6, Chapter 4. In this solution we smooth the positive part functions using tanh functions as in Chapter 3. To validate the accuracy of our implementation we consider a test case of the PDE when we have no deposition of stem cells and no aggregate growth. In this case we have the following PDE for c_0

$$\frac{\partial}{\partial x}\left(c_0\eta_0\left(\overline{u_0}+\frac{\hat{\beta}}{\mu}\overline{u_{m0}}\right)-\frac{\eta_0\overline{\dot{\gamma}_0}c_{0,x}}{Pe_0}\right)=0, \tag{B.2}$$

with the width averaged quantities given by

$$\overline{u_{m0}}=\frac{-x}{(1+x^2)^2}, \quad \overline{u_0}=\frac{4}{6}, \quad \overline{\dot{\gamma}_0}=1. \tag{B.3}$$

and $\eta_0 = 2$ for all time. We then solve (B.2) in Mathematica using the numerical ODE solver *NDSolve*. The solution is shown in Fig. B.4a. We then compare the value of maximum stem cell concentration obtained by our MATLAB numerical scheme. In Fig. B.4b we can see as $N \to \infty$ we have $1/N$ convergence, as expected from the first order finite difference approximation we have used. In Chapter 4 we take $N = 400$, shown in red.

We now examine a general case when we allow the aggregate to grow. We confirm the accuracy of the spatial discretisation used in the advection-diffusion by comparing the stem cell concentration obtained at $t = 10$ calculated using varying grid sizes. We compare to a reference solution calculated with $N = 4000$. We calculate the maximum error obtained at every point in the coarser grid using that point in the fine solution. This avoids the use of interpolation. The error is shown in Fig. B.5, again this demonstrates that we obtain the $1/N$ convergence for the solution.

We compare the value of the average bound platelet solution obtained at $t = 10$ varying the absolute and relative tolerances. We use the default values of absolute tolerance 10^{-4} and relative tolerance 10^{-4}, which achieve a maximum error of 1×10^{-4} compared to the solution obtained using an absolute tolerance 10^{-9} and relative tolerance 10^{-8}. This is shown in Table B.1.

B.2.2 Large Péclet number solution

This section details the analysis of the numerical scheme in Section 4.7, Chapter 4 to solve the leading-order system given by (4.64) and (4.87). We examine the explicit Euler timestepping scheme for various fixed timesteps, comparing the error obtained at $t = 0.5$ to the solution using $\delta t = 10^{-5}$ in Table B.2. In Chapter 4 we use $\delta t = 10^{-2}$ which obtains a maximum error of 10^{-3} in the aggregate height compared to using $\delta t = 10^{-5}$. This was calculated for the case $\hat{\beta}_0 = 1$ and $\hat{\kappa}_0 = 0$.

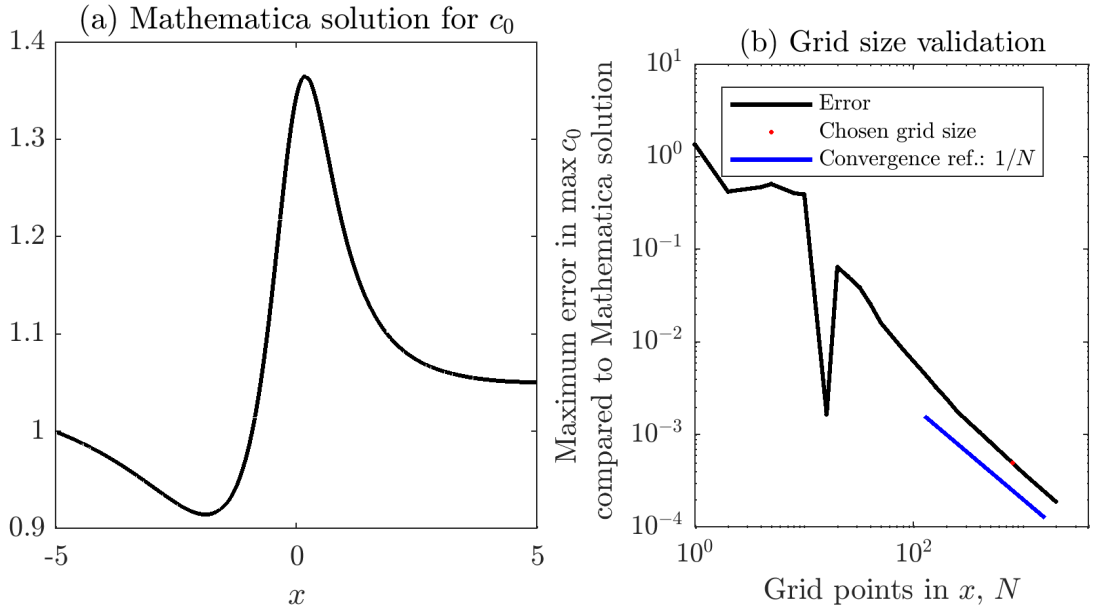

Figure B.4: (a) Mathematica solution for stem cell concentration PDE in test case. (b) Error made in the maximum value of the stem cell concentration obtained using our numerical method compared to the Mathematica solution. Convergence reference shown in blue.

Rel. Tolerance	Absolute tolerance					
	10^{-3}	10^{-4}	10^{-5}	10^{-6}	10^{-7}	10^{-8}
10^{-1}	0.012	0.012	0.012	0.012	0.012	0.012
10^{-2}	0.0053	0.0053	0.0053	0.0053	0.0053	0.0053
10^{-3}	0.0053	0.0053	0.0053	0.0053	0.0053	0.0053
10^{-4}	0.0003	0.00011	0.00011	0.00011	0.00011	0.00011
10^{-5}	0.0003	0.00012	6×10^{-5}	6×10^{-5}	6×10^{-5}	6×10^{-5}
10^{-6}	0.0003	0.00012	1.9×10^{-5}	1.1×10^{-5}	1.1×10^{-5}	1.1×10^{-5}
10^{-7}	0.0003	0.00012	2.7×10^{-5}	7.9×10^{-6}	6.6×10^{-6}	6.6×10^{-7}

Table B.1: Error analysis of ODE15s solver, varying the absolute and relative tolerances. We compare the maximum error made in the stem cell concentration at the final time $t = 10$ compared to a solution calculated with absolute tolerance 10^{-9} and relative tolerance 10^{-8}. In Chapter 4 we use absolute tolerance 10^{-4} and relative tolerance 10^{-4}.

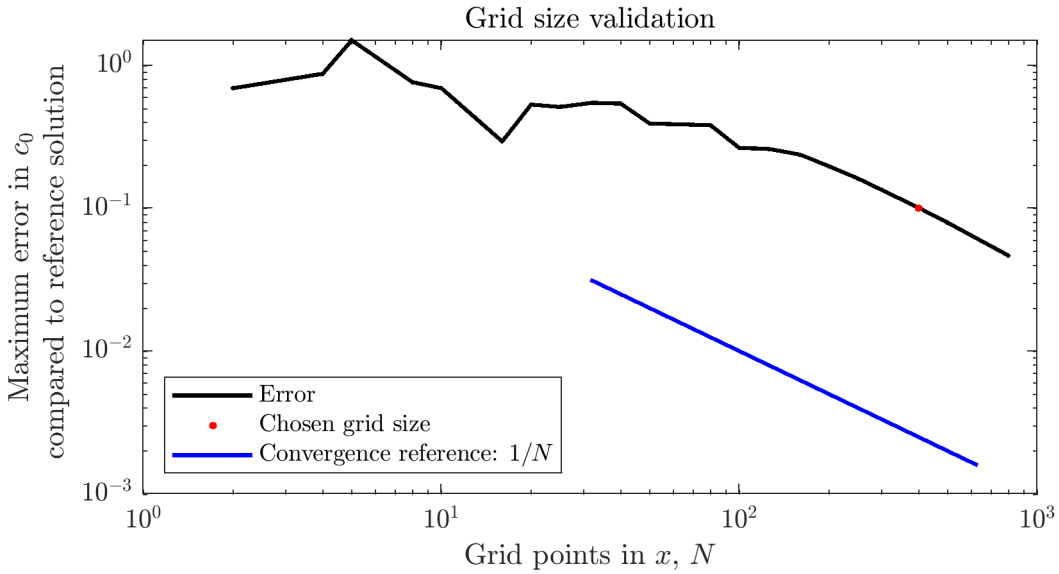

Figure B.5: Analysis of the finite difference used to calculate the stem cell concentration in Section 4.6, Chapter 4. We compare the error made in the quadrature to a fine solution where $N = 4000$. We use $N = 400$, marked in red, in Chapter 4.

Timestep δt	10^{-1}	10^{-2}	10^{-3}	10^{-4}
Maximum error	0.038	0.0051	0.00058	0.00052

Table B.2: Timestepping error analysis for explicit Euler scheme in Chapter 4, Section 4.7. Error made in the maximum aggregate height at $t = 0.5$ compared to using $\delta t = 10^{-5}$.

Table B.3 shows a comparison of tolerances which are used to define the initial position of the dividing trajectory and when we terminate the solution. We compare a range of tolerances from $0.32 - 0.0042$ to the case when we use a tolerance of 10^{-3}, again for the case $\hat{\beta}_0 = 1$ and $\hat{\kappa}_0 = 0$ at $t = 0.5$. We find that a tolerance of 0.018 achieves a maximum error of 10^{-2}, so we use this value in Chapter 4.

We compare the error of the solution obtained for varying grid number of axial grid points in for the same parameter test case: $\hat{\beta}_0 = 1$ and $\hat{\kappa}_0 = 0$ at $t = 0.5$. We compare the error in the solution to the case when $N = 5 \times 10^5$. In Chapter 4 we use $N = 1000$ which obtains a maximum error of 10^{-3} compared to the finer grid. We note that the error always occurs at the location of the discontinuity in the aggregate height due to the discontinuous outer stem cell solution. However the maximum aggregate height obtained for both $N = 1000$ and $N = 5 \times 10^5$ are equal to machine precision.

Boundary layer tolerance	0.32	0.075	0.018	0.0042
Maximum error	0.3418	0.2082	0.0178	0.0356

Table B.3: Varying the numerical approximation of the boundary layer tolerance for (4.64) in Chapter 4. Maximum error is calculated relative to the solution when the tolerance is 10^{-3}

B.3 Arterial thrombosis system validation

We now detail the analysis of the numerical method used to solve the arterial thrombosis system in Chapter 6. We examine mesh convergence for all PDEs (Navier-Stokes (6.8) and (6.9), FENE-P equation (6.10) and transport equations (6.14) and (6.13)); we examine the domain length required for the solution of the Navier-Stokes equations to fully contain the recirculaion zone; we examine the timestep required for the transport equations. Finally we examine the step size required in the numerical continuation of the FENE-P equation.

B.3.1 Mesh convergence

We first construct an initial mesh that is finer closer to the boundary $r = R(z)$, using GMSH's background mesh functionality. Next, we carry out subsequent refinements on the mesh using the FEniCS *refine* function which splits each mesh edge into two edges. We solve the PDEs on each level of refinement. We examine the change in the maximum velocity for the Navier Stokes equations, the maximum extension for the FENE-P equations and the maximum concentrations of VWF and platelets at $t = 0.1$ for the transport equations. We use the mesh achieved with three consecutive mesh refinements that has approximately 10^4 elements. When compared our reference mesh (constructed with five refinements), our chosen mesh achieves a maximum relative error of 0.02% on all variables. We show the convergence of a selection of variables in Fig B.6a for reference.

B.3.2 Timestepping analysis

To determine the timestep requirement in the transport equations we solve the system until $t = 0.15$ using steps of $\delta t = 0.1,\ 0.05,\ 0.01,\ 0.005, 0.001,\ 0.0005$, and compare the maximum error in free and bound platelet concentrations on the base of the domain obtained at the final time to that obtained using $\delta t = 10^{-4}$. We use $\delta t = 0.005$ in simulations in this chapter as this achieves a relative error of 0.1% compared to

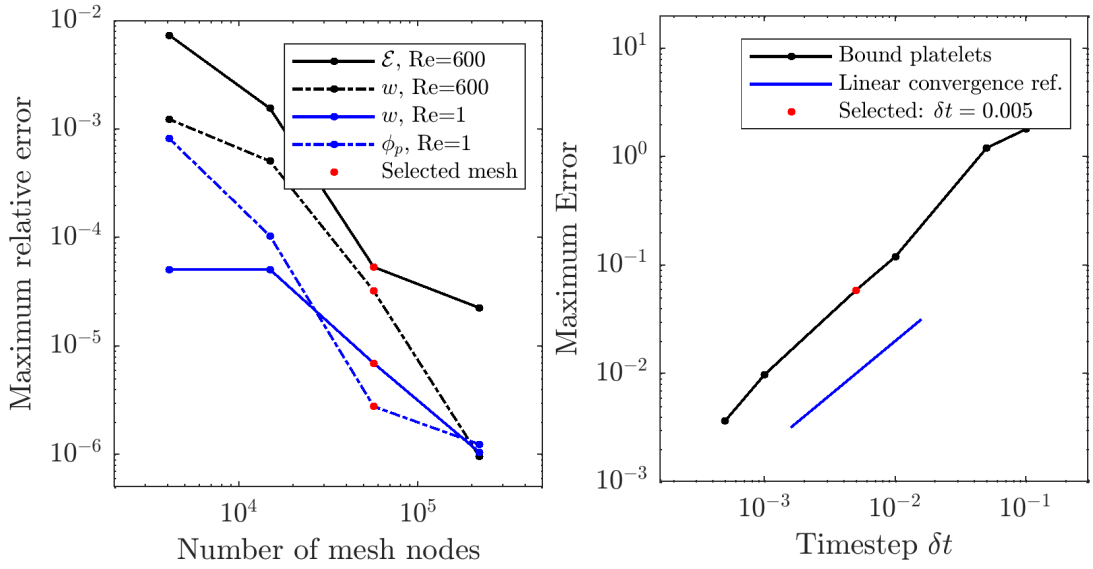

Figure B.6: (a) Relative error in maximum extension of the FENE-P equation for increasing numbers of mesh refinements at $Re = 500$, mesh level three obtains 0.01% relative error. (b) Transport timestepping analysis: platelet equations a timestep of $\delta t = 0.005$ achieves $< 0.1\%$ error compared to a timestep of $\delta t = 10^{-4}$. Parameters: $l = 30$, $\hat{h} = 0.5, \hat{l}_1 = 0,\ \hat{l}_2 = 1.5$.

the smaller timestep. This is shown in Fig. B.6b, along with confirmation that the scheme achieves a linear convergence as δt decreases, as expected.

B.3.3 Domain length analysis

We examine the domain length requirement for the full recirculation zone to be included in the domain. We quantify this using the number of separation points in the flow, for $\hat{h} = 0.5$ a domain length of $l = 30 + \hat{l}_1 + \hat{l}_2$ is required to contain the recirculation zone fully.

B.3.4 Numerical continuation

The Navier Stokes equations can be solved at Reynolds numbers up to 500 without numerical continuation, as the relative maximum error in the solution when numerical continuation is used is 10^{-13}. Hence we use an initial guess of zero for all variables in the the Newton solver for Navier Stokes.

The FENE equation is solved using numerical continuation in the Reynolds number. We use steps of 12, as is the largest step size for which the Newton solver converges. Decreasing step size does not increase the accuracy of the solution.

B.4 Microfluidic thrombosis system validation

This section details the numerical valiation of the scheme in Chapter 7 to solve the leading-order system consists of the analytic expressions for the axial fluid flow w_0, (7.51), and pressure p_0, (7.53), and an algebraic system of five equations for the VWF configuration tensor $\boldsymbol{A}_0$: (7.70) - (7.74), an algebraic equation for the concentration of free platelets given by (7.68) and the bound platelet concentration given by (7.69).

To validate our solution of the microfluidic thrombosis system we first compare our leading order fluid solution, (7.51), and (7.53) to the solution of Stokes flow obtained using commercial finite element software COMSOL in an identical geometry. We do this for a straight channel and a stenosed channel. The percentage error in the leading order axial flow, pressure gradient and shear rate are shown in Table B.5. It is clear that in a straight pipe the solution matches the COMSOL solution up to 0.01%. We use this to infer that our computation of the series solution is accurate. Compared to the solution in the stenosed pipe the solution only matches the COMSOL solution up to 0.1%. We assume that this is since the COMSOL solution struggles to solve the system accurately in pipes with very small aspect ratios.

We now determine the appropriate point to truncate the series solutions, (7.51), and (7.53). We compare the maximum value obtained in the shear stress components on the base and walls of the pipe to the maximum value obtained when we truncate the series solution at $N = 5000$. This is shown in Fig. B.7. We use $N = 300$ in Chapter 7, which is marked in red. This gives us an 0.27% error and an 0.014% error in the maximum values of $\partial w_0/\partial x$ and $\partial w_0/\partial y$ respectively when compared to truncating the solutions at $N = 5000$.

We solve the leading order FENE-P equations on the walls and the base of the pipe separately. On the base of the pipe $\partial w_0/\partial x = 0$ the leading order system is

$$fA_{xx} = a, \tag{B.4}$$

$$fA_{yy} = a, \tag{B.5}$$

$$2A_{yz}\frac{\partial w_0}{\partial y} = \frac{fA_{zz} - a}{\xi_0 Re\hat{\tau}_0(\dot{\gamma})}, \tag{B.6}$$

$$A_{yy}\frac{\partial w_0}{\partial y} = \frac{fA_{yz}}{\xi_0 Re\hat{\tau}_0(\dot{\gamma})}, \tag{B.7}$$

$$A_{xz} = 0. \tag{B.8}$$

This can be formed into a cubic equation for A_{zz}. We can compare the numerical calculation of A_{zz} to solution of the Oldroyd-B model in which $f = 1$ and $a = 1$. The

	Absolute tolerance					
R. tol.	10^{-3}	10^{-4}	10^{-5}	10^{-6}	10^{-7}	10^{-8}
10^{-1}	0.038	0.072	0.040	0.079	0.044	0.24
10^{-2}	0.0032	0.0032	0.0035	0.0029	0.0036	0.0029
10^{-3}	0.00057	0.00039	0.00037	0.00037	0.00039354	0.00032
10^{-4}	3.45×10^{-5}	2.10×10^{-5}	2.33×10^{-5}	1.37×10^{-5}	1.05×10^{-5}	1.28×10^{-5}
10^{-5}	1.96×10^{-5}	3.37×10^{-6}	4.93×10^{-6}	1.27×10^{-6}	2.21×10^{-6}	1.43×10^{-6}

Table B.4: Error analysis of ODE45 solver, varying the absolute and relative tolerances. We compare the maximum error made in the average bound platelets at the final time compared to a solution calculated with absolute tolerance 10^{-8} and relative tolerance 10^{-6}.

three diagonal components of $\boldsymbol{A}$ for the Oldroyd-B model are

$$A_{xx} = 1, \tag{B.9}$$

$$A_{yy} = 1, \tag{B.10}$$

$$A_{zz} = 2\left(\xi_0 Re\hat{\tau}_0(\dot{\gamma})\frac{\partial w_0}{\partial y}\right)^2 + 1. \tag{B.11}$$

A comparison of the numerical solution of the FENE-P equation to the Oldroyd-B model are shown in Fig. B.8. We can see for the FENE-P solution tends to the Oldroyd-B solution as $L \to \infty$, confirming that we have correctly solved the cubic equation.

We confirm the accuracy of the quadrature used to calculate the free platelets within the PDE, (7.69), by comparing the initial free platelet concentration calculated using varying grid sizes. In all cases we have $2N_z = N_x$ and compare to a reference solution calculated with $N_x = 2000$. We calculate the maximum error obtained at every point in the coarser grid using that point in the fine solution. This avoids the use of interpolation. The error is shown in Fig. B.9. As $N_x \to \infty$ we obtain the known convergence rate N_x^{-2}, of the trapezoidal rule which is illustrated by the blue reference line. In Chapter 7 we use $N_x = 500$.

We compare the value of the average bound platelet solution obtained at $t = 21$ varying the absolute and relative tolerances. We compare the maximum error made in the average bound platelets at the final time compared to a solution calculated with absolute tolerance 10^{-8} and relative tolerance 10^{-6}. This justifies using the default values of absolute tolerance 10^{-6} and relative tolerance 10^{-3}, as it gives an error of 3.7×10^{-4} compared to the solution obtained using smaller tolerances, as shown in Table B.4.

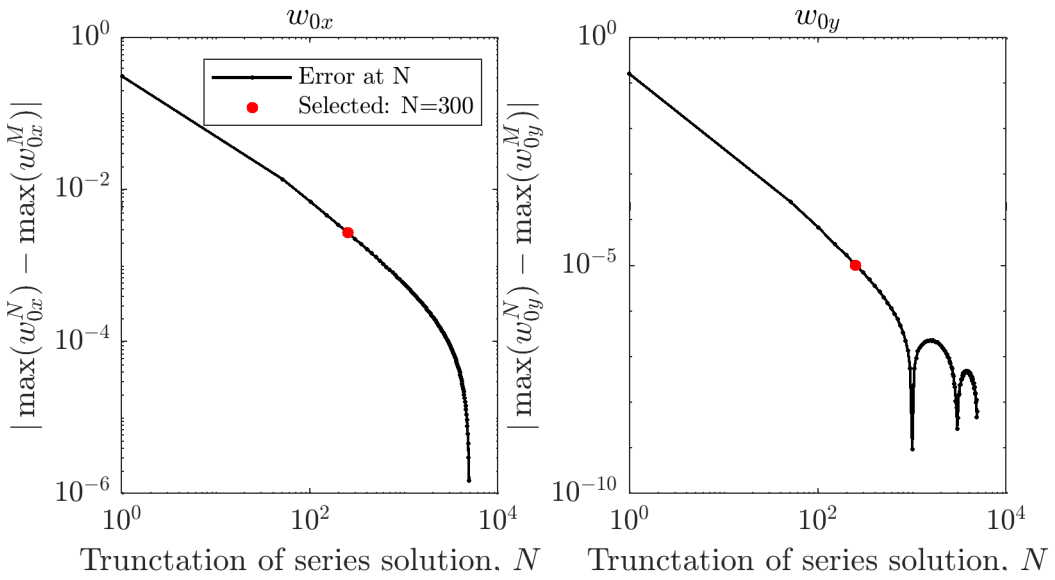

Figure B.7: Error in the maximum values of the shear stress on the base (left) and the walls (right) compared to the value obtained when the series are truncated at $N = 5000$. We use $N = 300$ in Chapter 7, marked in red.

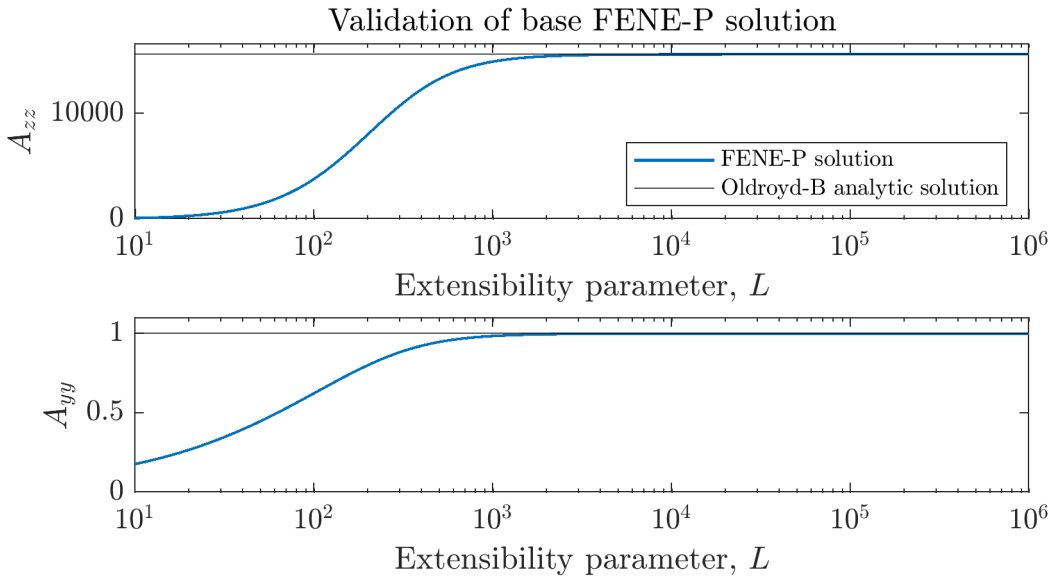

Figure B.8: Comparison of the solution of the FENE-P equation on the wall of the pipe to the analytic Oldroyd-B solution as the extensibility parameter increases. We can see the FENE-P solution tends to the Oldroyd-B soltuion as $L \to \infty$.

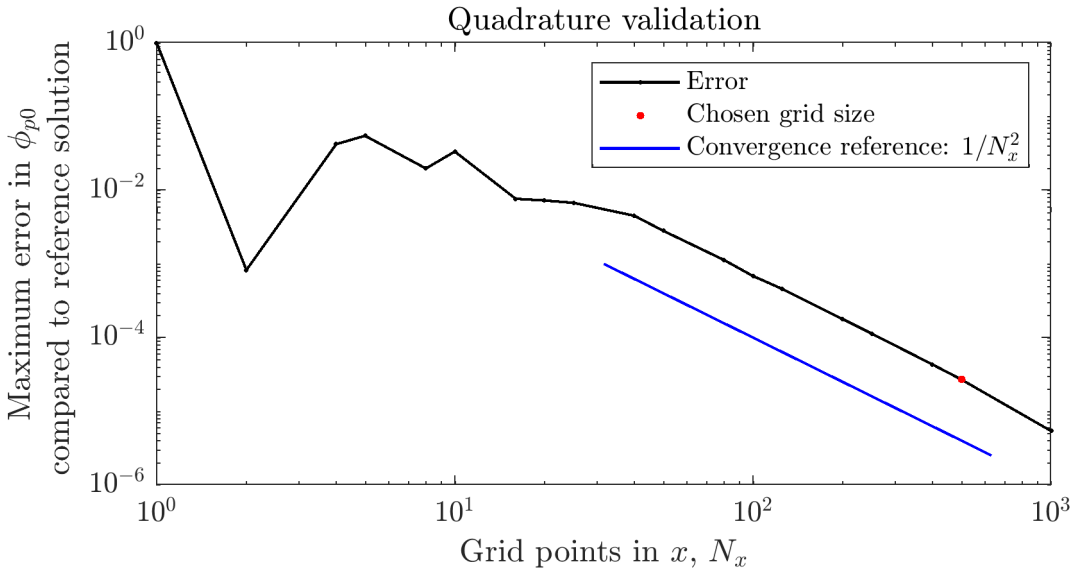

Figure B.9: Analysis of the quadrature step used to calculate the free platelet concentration. We compare the error made in the quadrature to a fine solution where $N_x = 2000$. We can see as $N_x \to \infty$ we have $1/N_x^2$ convergence, as expected from the trapezoidal rule. We use $N_x = 500$, marked in red, in Chapter 7.

Case	Aspect ratio	Percentage error		
		Error $p_{0,z}$	Error w_0	Error $\dot{\gamma}_0$
Straight pipe	0.61	-5×10^{-3}	-1.9×10^{-3}	1.3×10^{-2}
Straight pipe	0.006	-3.2×10^{-2}	-4.6×10^{-2}	3.5×10^{-1}
Stenosed pipe	0.006	1.0×10^{-2}	5.1×10^{-1}	-9.1×10^{-1}

Table B.5: Error of our analytic series solution compared to COMSOL solution of stokes flow

Appendix C

Top Boundary Layer

This section details boundary layer analysis which is used to derive boundary condition for the outer problem in the large Péclet number regime in Chapter 4. We define a boundary layer coordinate $\tilde{y} = (y-1)/\delta$ with $\delta \ll 1$, such that $\tilde{y} \to -\infty$ matches into the outer domain. In the boundary layer (4.29) is defined as follows

$$\epsilon \frac{\partial c}{\partial t} + \frac{\partial}{\partial x}\left(\left(\delta\tilde{u} + \epsilon\hat{\beta}_0\tilde{v}_m\right)c - \frac{\epsilon^3\dot{\gamma}}{Pe_0}\frac{\partial c}{\partial x}\right) + \frac{\partial}{\partial \tilde{y}}\left(\left(\delta\tilde{v} + \frac{\hat{\beta}_0}{\delta}\tilde{v}_m\right)c - \frac{\epsilon\dot{\gamma}}{\delta^2 Pe_0}\frac{\partial c}{\partial \tilde{y}}\right) = 0, \tag{C.1}$$

where we have rescaled the fluid velocities in the boundary layer such that $u = \delta\tilde{u}$ and $v = \delta^2\tilde{v}$. The magnetic velocities in this boundary layer are defined by

$$\tilde{u}_m = \frac{-x}{((\epsilon(1+\delta\tilde{y})+\epsilon+1)^2+x^2)^2}, \quad \tilde{v}_m = \frac{-(\epsilon(1+\delta\tilde{y})+\epsilon+1)}{((\epsilon(1+\delta\tilde{y})+\epsilon+1)^2+x^2)^2}. \tag{C.2}$$

Eq. C.1 has a no-flux boundary condition on $\tilde{y} = 0$ as follows

$$\left(\delta^2\tilde{v} + \hat{\beta}_0\tilde{v}_m\right)c - \frac{\epsilon\dot{\gamma}}{\delta Pe_0}\frac{\partial c}{\partial \tilde{y}} = 0. \tag{C.3}$$

At leading-order, we expand $c = c_0 + ...$ and balance normal diffusion with normal magnetic advection which gives $\delta = \epsilon$. Hence we have the following equation for c_0

$$\frac{\partial}{\partial \tilde{y}}\left(\hat{\beta}_0\tilde{v}_{m0}c_0 - \frac{\dot{\gamma}_0}{Pe_0}\frac{\partial c_0}{\partial \tilde{y}}\right) = 0, \tag{C.4}$$

where $\tilde{v}_{m0} = -x^{-4}$, with boundary condition

$$\hat{\beta}_0\tilde{v}_{m0}c_0 - \frac{\dot{\gamma}_0}{Pe_0}\frac{\partial c_0}{\partial \tilde{y}} = 0 \text{ on } \tilde{y} = 0. \tag{C.5}$$

This has solution

$$c_0(x,\tilde{y}) = A(x)\exp(-g(x)\tilde{y}), \tag{C.6}$$

with $g(x) = \beta_0|v_{m0}|Pe_0/\dot{\gamma}_0$. As $\tilde{y} \to -\infty$ $c_0 \to \infty$, hence to match with the solution in the outer which is constant we must have $A(x) = 0$. This yields the zero boundary condition on $y = 1$ for the outer problem in Section 4.7.

Bibliography

[1] S. G. Advani and C. L. Tucker III. The use of tensors to describe and predict fiber orientation in short fiber composites. *Journal of Rheology*, 1987.

[2] M. S. Alnæs, J. Blechta, J. Hake, A. Johansson, B. Kehlet, A. Logg, C. Richardson, J. Ring, M. E. Rognes, and G. N. Wells. The FEniCS project version 1.5. *Archive of Numerical Software*, 2015.

[3] M. S. Alnæs, A. Logg, K. Mardal, O. Skavhaug, and H. P. Langtangen. Unified framework for finite element assembly. *International Journal of Computational Science and Engineering*, 2009.

[4] M. S. Alnæs and K. Mardal. On the efficiency of symbolic computations combined with code generation for finite element methods. *ACM Transactions on Mathematical Software*, 2010.

[5] M. S. Alnæs and K. Mardal. SyFi and SFC: Symbolic finite elements and form compilation. In *Automated solution of differential equations by the finite element method*. Springer, 2012.

[6] L. H. Arroyo and R. T. Lee. Mechanisms of plaque rupture: mechanical and biologic interactions. *Cardiovascular Research*, 1999.

[7] Y. Asaad, M. Epshtein, A. Yee, and N. Korin. The flow dependent adhesion of von Willebrand factor (VWF)-A1 functionalized nanoparticles in an *in vitro* coronary stenosis model. *Molecules*, 2019.

[8] I. M. Barbash, P. Chouraqui, J. Baron, M. S. Feinberg, S. Etzion, A. Tessone, L. Miller, E. Guetta, D. Zipori, L. H. Kedes, R. A. Kloner, and J. Leor. Systemic delivery of bone marrow–derived mesenchymal stem cells to the infarcted myocardium. *Circulation*, 2003.

[9] D. L. Bark and D. N. Ku. Wall shear over high degree stenoses pertinent to atherothrombosis. *Journal of Biomechanics*, 2010.

[10] G. K. Batchelor. *An Introduction to Fluid Dynamics*. Cambridge University Press, 2000.

[11] P. C. Bean and J. D. Livingston. Superparamagnetism. *Journal Applied Physics*, 1959.

[12] J. F. Bentzon, F. Otsuka, R. Virmani, and E. Falk. Mechanisms of plaque formation and rupture. *Circulation Research*, 2014.

[13] P. Biller and F. Petruccione. The flow of dilute polymer solutions in confined geometries: a consistent numerical approach. *Journal of Non-Newtonian Fluid Mechanics*, 1987.

[14] R. Bird, P. Dotson, and N. Johnson. Polymer solution rheology based on a finitely extensible bead-spring chain model. *Journal of Non-Newtonian Fluid Mechanics*, 1980.

[15] D. Brooks, J. Goodwin, and G. Seaman. Interactions among erythrocytes under shear. *Journal of Applied Physiology*, 1970.

[16] R. Byron, R. C. Armstrong, and O. B. Hassager. *Dynamics of polymeric liquids. Vol. 1: Fluid mechanics*. Wiley, 1987.

[17] R. Byron, C. F. Curtiss, R. C. Armstrong, and O. B. Hassager. *Dynamics of polymeric liquids, Volume 2: Kinetic theory*. Wiley, 1987.

[18] L. D. C. Casa, D. N. Ku, and G. W. Woodruff. Thrombus formation at high shear rates. *Annual Review of Biomedical Engineering*, 2017.

[19] M. B. Chen, J. A. Whisler, J. Fröse, C. Yu, Y. Shin, and R. D. Kamm. On-chip human microvasculature assay for visualization and quantification of tumor cell extravasation dynamics. *Nature Protocols*, 2017.

[20] E. M. Cherry and J. K. Eaton. A comprehensive model of magnetic particle motion during magnetic drug targeting. *International Journal of Multiphase Flow*, 2014.

[21] COMSOL Multiphysics® v. 5.4. COMSOL AB, Stockholm, Sweden.

[22] P. F. Costa, H. J. Albers, J. E. Linssen, H. H. Middelkamp, L. Van Der Hout, R. Passier, A. Van Den Berg, J. Malda, and A. D. Van Der Meer. Mimicking arterial thrombosis in a 3D-printed microfluidic *in vitro* vascular model based on computed tomography angiography data. *Lab on a Chip*, 2017.

[23] F. R. Da Cunha and E. J. Hinch. Shear-induced dispersion in a dilute suspension of rough spheres. *Journal of Fluid Mechanics*, 1996.

[24] M. J. Davies and A. Thomas. Thrombosis and acute coronary-artery lesions in sudden cardiac ischemic death. *New England Journal of Medicine*, 1984.

[25] S. M. Devine, A. M. Bartholomew, N. Mahmud, M. Nelson, S. Patil, W. Hardy, C. Sturgeon, T. Hewett, T. Chung, W. Stock, D. Sher, S. Weissman, K. Ferrer, J. Mosca, R. Deans, A. Moseley, and R. Hoffman. Mesenchymal stem cells are capable of homing to the bone marrow of non-human primates following systemic infusion. *Experimental Hematology*, 2001.

[26] S. M. Dopheide, M. J. Maxwell, and S. P. Jackson. Shear-dependent tether formation during platelet translocation on von Willebrand factor. *Blood, The Journal of the American Society of Hematology*, 2002.

[27] C. F. Driscoll, R. M. Morris, A. E. Senyei, K. J. Widder, and G. S. Heller. Magnetic targeting of microspheres in blood flow. *Microvascular Research*, 1984.

[28] J. Du and A. L. Fogelson. A two-phase mixture model of platelet aggregation. *Mathematical Medicine and Biology*, 2018.

[29] J. Du, D. Kim, G. Alhawael, D. N. Ku, and A. L. Fogelson. Clot permeability, agonist transport, and platelet binding kinetics in arterial thrombosis. *Biophysical Journal*, 2020.

[30] E. C. Eckstein, D. G. Bailey, and A. H. Shapiro. Self-diffusion of particles in shear flow of a suspension. *Journal of Fluid Mechanics*, 1977.

[31] A. J. El Haj, J. R. Glossop, H. S. Sura, M. R. Lees, B. Hu, S. Wolbank, M. van Griensven, H. Redl, and J. Dobson. An *in vitro* model of mesenchymal stem cell targeting using magnetic particle labelling. *Journal of Tissue Engineering and Regenerative Medicine*, 2015.

[32] A. W. El-Kareh and L. G. Leal. Existence of solutions for all deborah numbers for a non-newtonian model modified to include diffusion. *Journal of Non-Newtonian Fluid Mechanics*, 1989.

[33] A. M. Elhfnawy, P. U. Heuschmann, M. Pham, J. Volkmann, and F. Fluri. Stenosis length and degree interact with the risk of cerebrovascular events related to internal carotid artery stenosis. *Frontiers in Neurology*, 2019.

[34] A. Ern and J. Guermond. *Theory and practice of finite elements.* Springer, 2004.

[35] R. Fahraeus and T. Lindqvist. The viscosity of the blood in narrow capillary tubes. *American Journal of Physiology-Legacy Content*, 1931.

[36] A. Federici, E. Berntorp, and C. Lee. The 80th anniversary of von Willebrand's disease: history, management and research. *Haemophilia*, 2006.

[37] A. J. Friedenstein, K. V. Petrakova, A. I. Kurolesova, and G. P. Frolova. Heterotopic transplants of bone marrow. *Transplantation*, 1968.

[38] H. Fu, Y. Jiang, D. Yang, F. Scheiflinger, W. P. Wong, and T. A. Springer. Flow-induced elongation of von Willebrand factor precedes tension-dependent activation. *Nature Communications*, 2017.

[39] M. Furlan. Von Willebrand factor: Molecular size and functional activity. *Annals of Hematology*, 1996.

[40] E. P. Furlani and E. J. Furlani. A model for predicting magnetic targeting of multifunctional particles in the microvasculature. *Journal Magnetism and Magnetic Matter*, 2007.

[41] E. P. Furlani and K. C. Ng. Analytical model of magnetic nanoparticle transport and capture in the microvasculature. *Physical Review E*, 2006.

[42] C. Geuzaine and J.-F. Remacle. Gmsh: A 3-d finite element mesh generator with built-in pre-and post-processing facilities. *International Journal for Numerical Methods in Engineering*, 2009.

[43] J. C. Gill, J. Endres-Brooks, P. J. Bauer, W. J. Marks, and R. R. Montgomery. The effect of ABO blood group on the diagnosis of von Willebrand disease. *Blood*, 1987.

[44] J. Gómez-Pastora, I. H. Karampelas, X. Xue, E. Bringas, E. P. Furlani, and I. Ortiz. Magnetic bead separation from flowing blood in a two-phase continuous-flow magnetophoretic microdevice: theoretical analysis through computational fluid dynamics simulation. *The Journal of Physical Chemistry C*, 2017.

[45] P. D. Goodman, E. T. Barlow, P. M. Crapo, S. F. Mohammad, and K. A. Solen. Computational model of device-induced thrombosis and thromboembolism. *Annals of Biomedical Engineering*, 2005.

[46] A. D. Grief and G. Richardson. Mathematical modelling of magnetically targeted drug delivery. *Journal of Magnetism and Magnetic Materials*, 2005.

[47] D. J. Griffiths. *Introduction to electrodynamics*. Prentice Hall, 1999.

[48] R. R. Hansen, A. A. Tipnis, T. C. White-Adams, J. Di Paola, and K. B. Neeves. Characterization of collagen thin films for von Willebrand factor binding and platelet adhesion. *Langmuir*, 2011.

[49] J. W. Haverkort, S. Kenjeres, and C. R. Kleijn. Computational simulations of magnetic particle capture in arterial flows. *Annals of Biomedical Engineering*, 2009.

[50] M. Herrchen and H. C. Öttinger. A detailed comparison of various FENE dumbbell models. *Journal of Non-Newtonian Fluid echanics*, 1997.

[51] J. S. Horner, M. J. Armstrong, N. J. Wagner, and A. N. Beris. Measurements of human blood viscoelasticity and thixotropy under steady and transient shear and constitutive modeling thereof. *Journal of Rheology*, 2019.

[52] J. Huang, R. W. Lyczkowski, and D. Gidaspow. Pulsatile flow in a coronary artery using multiphase kinetic theory. *Journal of Biomechanics*, 2009.

[53] T. J. R. Hughes, W. K. Liu, and T. K. Zimmermann. Lagrangian-Eulerian finite element formulation for incompressible viscous flows. *Computer Methods in Applied Mechanics and Engineering*, 1981.

[54] T. K. Jain, M. K. Reddy, M. A. Morales, D. L. Leslie-Pelecky, and V. Labhasetwar. Biodistribution, clearance, and biocompatibility of iron oxide magnetic nanoparticles in rats. *Molecular Pharmaceutics*, 2008.

[55] J. S. Jeon, I. K. Zervantonakis, S. Chung, R. D. Kamm, and J. L. Charest. In vitro model of tumor cell extravasation. *PLoS ONE*, 2013.

[56] H. Karcher, J. Lammerding, H. Huang, R. T. Lee, R. D. Kamm, and M. R. Kaazempur-Mofrad. A three-dimensional viscoelastic model for cell deformation with experimental verification. *Biophysical journal*, 85(5):3336–3349, 2003.

[57] T. J. Kean, P. Lin, A. I. Caplan, and J. E. Dennis. Mscs: delivery routes and engraftment, cell-targeting strategies, and immune modulation. *Stem Cells International*, 2013.

[58] S. Kenjereš and B. W. Righolt. Simulations of magnetic capturing of drug carriers in the brain vascular system. *International Journal of Heat and Fluid Flow*, 2012.

[59] D. Kim, C. Bresette, Z. Liu, and D. N. Ku. Occlusive thrombosis in arteries. *APL Bioengineering*, 2019.

[60] D. A. Kim and D. N. Ku. Structure of shear-induced platelet aggregated clot formed in an *in vitro* arterial thrombosis model. *Blood Advances*, 2022.

[61] J. A. Kim, H. J. Lee, H. Kang, and T. H. Park. The targeting of endothelial progenitor cells to a specific location within a microfluidic channel using magnetic nanoparticles. *Biomedical Microdevices*, 2009.

[62] R. C. Kirby. Algorithm 839: FIAT, a new paradigm for computing finite element basis functions. *ACM Transactions on Mathematical Software (TOMS)*, 2004.

[63] R. C. Kirby. Fiat: numerical construction of finite element basis functions. In *Automated solution of differential equations by the finite element method*. Springer, 2012.

[64] J. Kitayama, A. Hidemura, H. Saito, and H. Nagawa. Shear stress affects migration behavior of polymorphonuclear cells arrested on endothelium. *Cellular Immunology*, 2000.

[65] N. Korin, M. Kanapathipillai, B. D. Matthews, M. Crescente, A. Brill, T. Mammoto, K. Ghosh, S. Jurek, S. A. Bencherif, D. Bhatta, A. U. Coskun, C. L. Feldman, D. D. Wagner, and D. E. Ingber. Shear-activated nanotherapeutics for drug targeting to obstructed blood vessels. *Science*, 2012.

[66] P. G. Kyrtatos, P. Lehtolainen, M. Junemann-Ramirez, A. Garcia-Prieto, A. N. Price, J. F. Martin, D. G. Gadian, Q. A. Pankhurst, and M. F. Lythgoe. Magnetic tagging increases delivery of circulating progenitors in vascular injury. *JACC: Cardiovascular Interventions*, 2009.

[67] M. M. Larimi, A. Ramiar, and A. A. Ranjbar. Numerical simulation of magnetic nanoparticles targeting in a bifurcation vessel. *Journal of Magnetism and Magnetic Materials*, 2014.

[68] D. Leighton and A. Acrivos. The shear-induced migration of particles in concentrated suspensions. *Journal of Fluid Mechanics*, 1987.

[69] S. Lippok, M. Radtke, T. Obser, L. Kleemeier, R. Schneppenheim, U. Budde, R. R. Netz, and J. O. Rädler. Shear-induced unfolding and enzymatic cleavage of full-length VWF multimers. *Biophysical Journal*, 2016.

[70] Z. Liu, J. R. Clausen, R. R. Rao, and C. K. Aidun. Nanoparticle diffusion in sheared cellular blood flow. *Journal of Fluid Mechanics*, 2019.

[71] A. Logg, K. Mardal, G. N. Wells, et al. *Automated Solution of Differential Equations by the Finite Element Method*. Springer, 2012.

[72] A. S. Lübbe, C. Bergemann, W. Huhnt, T. Fricke, H. Riess, J. W. Brock, and D. Huhn. Preclinical experiences with magnetic drug targeting: tolerance and efficacy. *Cancer Research*, 1996.

[73] A. S. Lübbe, C. Bergemann, H. Riess, F. Schriever, P. Reichardt, K. Possinger, M. Matthias, B. Dörken, F. Herrmann, R. Gürtler, P. Hohenberger, N. Haas, R. Sohr, B. Sander, A. J. Lemke, D. Ohlendorf, W. Huhnt, and D. Huhn. Clinical experiences with magnetic drug targeting: a phase I study with 4'-epidoxorubicin in 14 patients with advanced solid tumors. *Cancer Research*, 1996.

[74] N. T. Luu, G. E. Rainger, and G. B. Nash. Kinetics of the different steps during neutrophil migration through cultured endothelial monolayers treated with tumour necrosis factor-α. *Journal of Vascular Research*, 1999.

[75] A. Marcinkowska-Gapińska, J. Gapinski, W. Elikowski, F. Jaroszyk, and L. Kubisz. Comparison of three rheological models of shear flow behavior studied on blood samples from post-infarction patients. *Medical & Biological Engineering & Computing*, 2007.

[76] H. Markides, O. Kehoe, R. H. Morris, and A. J. E. Haj. Whole body tracking of superparamagnetic iron oxide nanoparticle-labelled cells – a rheumatoid arthritis mouse model. *Stem Cell Research & Therapy*, 2013.

[77] M. Mehrabadi, L. D. Casa, C. K. Aidun, and D. N. Ku. A predictive model of high shear thrombus growth. *Annals of Biomedical Engineering*, 2016.

[78] J. P. Müller, S. Mielke, A. Löf, T. Obser, C. Beer, L. K. Bruetzel, D. A. Pippig, W. Vanderlinden, J. Lipfert, R. Schneppenheim, et al. Force sensing by the vascular protein von willebrand factor is tuned by a strong intermonomer interaction. *Proceedings of the National Academy of Sciences*, 113(5):1208–1213, 2016.

[79] M. Muthana, S. D. Scott, N. Farrow, F. Morrow, C. Murdoch, S. Grubb, N. Brown, J. Dobson, and C. E. Lewis. A novel magnetic approach to enhance the efficacy of cell-based gene therapies. *Gene Therapy*, 2008.

[80] N Casson. A flow equation for pigment-oil suspensions of the printing ink type. *Rheology of Disperse Systems*, 1959.

[81] A. T. O'Byrne. *Re-entrant corner flows of Oldroyd-B fluids*. PhD thesis, University of Bath, 2010.

[82] F. Peyvandi, I. Garagiola, and L. Baronciani. Role of von willebrand factor in the haemostasis. *Blood Transfusion*, 9(Suppl 2):s3, 2011.

[83] S. V. Pislaru, A. Harbuzariu, R. Gulati, T. Witt, N. P. Sandhu, R. D. Simari, and G. S. Sandhu. Magnetically targeted endothelial cell localization in stented vessels. *Journal of the American College of Cardiology*, 2006.

[84] A. S. Popel and G. Enden. An analytical solution for steady flow of a quemada fluid in a circular tube. *Rheologica acta*, 1993.

[85] A. R. Pries, D. Neuhaus, and P. Gaehtgens. Blood viscosity in tube flow: dependence on diameter and hematocrit. *American Journal of Physiology-Heart and Circulatory Physiology*, 1992.

[86] A. R. Pries, T. W. Secomb, and P. Gaehtgens. Biophysical aspects of blood flow in the microvasculature. *Cardiovascular Research*, 1996.

[87] B. Purnode and M. Crochet. Polymer solution characterization with the FENE-P model. *Journal of Non-Newtonian Fluid Mechanics*, 1998.

[88] D. Quemada. Rheology of concentrated disperse systems II. A model for non-newtonian shear viscosity in steady flows. *Rheologica Acta*, 1978.

[89] K. Rack, V. Huck, M. Hoore, D. A. Fedosov, S. W. Schneider, and G. Gompper. Margination and stretching of von Willebrand factor in the blood stream enable adhesion. *Scientific Reports*, 2017.

[90] S. Rafii and D. Lyden. Therapeutic stem and progenitor cell transplantation for organ vascularization and regeneration. *Nature Medicine*, 2003.

[91] J. M. Rallison and E. J. Hinch. Do we understand the physics in the constitutive equation? *Journal of Non-Newtonian Fluid Mechanics*, 1988.

[92] G. Richardson, K. Kaouri, and H. Byrne. Particle trapping by an external body force in the limit of large Péclet number: applications to magnetic targeting in the blood flow. *European Journal of Applied Mathematics*, 2010.

[93] D. Richter, G. Iaccarino, and E. S. Shaqfeh. Simulations of three-dimensional viscoelastic flows past a circular cylinder at moderate reynolds numbers. *Journal of Fluid Mechanics*, 2010.

[94] B. E. Rittman. The effect of shear stress on biofilm loss rate. *Biotechnology and Bioengineering*, 1982.

[95] Z. M. Ruggeri. Von Willebrand factor: looking back and looking forward. *Thrombosis and haemostasis*, 2007.

[96] J. E. Sadler. Biochemistry and genetics of Von Willebrand factor. *Annual Review of Biochemistry*, 1998.

[97] D. Saintillan and M. J. Shelley. Theory of active suspensions. In *Complex Fluids in biological systems*. Springer, 2015.

[98] S. Schneider, S. Nuschele, A. Wixforth, C. Gorzelanny, A. Alexander-Katz, R. Netz, and M. F. Schneider. Shear-induced unfolding triggers adhesion of von Willebrand factor fibers. *Proceedings of the National Academy of Sciences*, 2007.

[99] L. A. Segel and G. H. Handelman. *Mathematics applied to continuum mechanics*. SIAM, 2007.

[100] J. G. Shake, P. J. Gruber, W. A. Baumgartner, G. Senechal, J. Meyers, J. M. Redmond, M. F. Pittenger, and B. J. Martin. Mesenchymal stem cell implantation in a swine myocardial infarct model: engraftment and functional effects. *The Annals of Thoracic Surgery*, 2002.

[101] S. Sharma, V. Katiyar, and U. Singh. Mathematical modelling for trajectories of magnetic nanoparticles in a blood vessel under magnetic field. *Journal of Magnetism and Magnetic Materials*, 2015.

[102] C. Siediecki, B. J. Lestini, K. Kottke-Marchant, S. J. Eppell, D. L. Wilson, and R. E. Marchant. Shear-dependent changes in the three-dimensional structure of human von Willebrand factor. *Blood*, 1996.

[103] C. E. Sing and A. Alexander-Katz. Elongational flow induces the unfolding of von Willebrand factor at physiological flow rates. *Biophysical Journal*, 2010.

[104] D. E. Smith, H. P. Babcock, and S. Chu. Single-polymer dynamics in steady shear flow. *Science*, 1999.

[105] E. N. Sorensen, G. W. Burgreen, W. R. Wagner, and J. F. Antaki. Computational simulation of platelet deposition and activation: I. model development and properties. *Annals of Biomedical Engineering*, 1999.

[106] T. A. Springer. Von Willebrand factor, Jedi knight of the bloodstream. *Blood*, 2014.

[107] B. E. Strauer and R. Kornowski. Stem cell therapy in perspective. *Circulation*, 2003.

[108] R. Sureshkumar and A. N. Beris. Effect of artificial stress diffusivity on the stability of numerical calculations and the flow dynamics of time-dependent viscoelastic flows. *Journal of Non-Newtonian Fluid Mechanics*, 1995.

[109] C. Taylor and P. Hood. A numerical solution of the Navier-Stokes equations using the finite element technique. *Computuational Fluids*, 1973.

[110] M. L. Turgeon. *Clinical hematology: theory and procedures*. Lippincott Williams & Wilkins, 2005.

[111] M. Viceconti, F. Pappalardo, B. Rodriguez, M. Horner, J. Bischoff, and F. M. Tshinanu. *In silico* trials: Verification, validation and uncertainty quantification of predictive models used in the regulatory evaluation of biomedical products. *Methods*, 2021.

[112] Y. Wang, M. Morabito, X. F. Zhang, E. Webb, A. Oztekin, and X. Cheng. Shear-induced extensional response behaviors of tethered von Willebrand factor. *Biophysical Journal*, 2019.

[113] J. M. Wardlaw, V. Murray, E. Berge, and G. J. del Zoppo. Thrombolysis for acute ischaemic stroke. *Cochrane Database of Systematic Reviews*, 2014.

[114] S. Waters, L. Schumacher, and A. El Haj. Regenerative medicine meets mathematical modelling: developing symbiotic relationships. *NPJ Regenerative Medicine*, 2021.

[115] G. Weibrich, W. K. Kleis, M. Kunz-Kostomanolakis, A. H. Loos, and W. Wagner. Correlation of platelet concentration in platelet-rich plasma to the extraction method, age, sex, and platelet count of the donor. *International Journal of Oral & Maxillofacial Implants*, 2001.

[116] M. K. Wells, D. C. Winter, A. W. Nelson, and T. C. McCarthy. Blood velocity patterns in coronary arteries. *Journal of Biomechanical Engineering*, 1977.

[117] C. Wilhelm, L. Bal, P. Smirnov, I. Galy-Fauroux, O. Clément, F. Gazeau, and J. Emmerich. Magnetic control of vascular network formation with magnetically labeled endothelial progenitor cells. *Biomaterials*, 2007.

[118] W. T. Wu, M. Zhussupbekov, N. Aubry, J. F. Antaki, and M. Massoudi. Simulation of thrombosis in a stenotic microchannel: The effects of VWF-enhanced shear activation of platelets. *International Journal of Engineering Science*, 2020.

[119] Y. Wu, P. Hsu, C. Tsai, P. Pan, and Y. Chen. Significantly increased low shear rate viscosity, blood elastic modulus, and RBC aggregation in adults following cardiac surgery. *Scientific Reports*, 2018.

[120] Z. Xu, N. Chen, M. M. Kamocka, E. D. Rosen, and M. Alber. A multiscale model of thrombus development. *Journal of the Royal Society Interface*, 2008.

[121] B. P. Yawn, W. L. Nichols, and M. E. Rick. Diagnosis and management of von Willebrand disease: guidelines for primary care. *American Family Physician*, 2009.

[122] K. Yeleswarapu, M. Kameneva, K. Rajagopal, and J. Antaki. The flow of blood in tubes: theory and experiment. *Mechanics Research Communications*, 1998.

[123] E. Yeo, H. Markides, A. Schade, A. Studd, J. Oliver, S. Waters, and A. El Haj. Experimental and mathematical modelling of magnetically labelled mesenchymal stromal cell delivery. *Journal of the Royal Society Interface*, 2021.

[124] H. Zafar, F. Sharif, and M. J. Leahy. Measurement of the blood flow rate and velocity in coronary artery stenosis using intracoronary frequency domain optical coherence tomography: Validation against fractional flow reserve. *IJC Heart & Vasculature*, 2014.

[125] H. Zhang, L. R. Moore, M. Zborowski, P. S. Williams, S. Margel, and J. J. Chalmers. Establishment and implications of a characterization method for magnetic nanoparticle using cell tracking velocimetry and magnetic susceptibility modified solutions. *The Analyst*, 2005.

[126] M. Zhussupbekov, R. Mendez Rojano, W. Wu, M. Massoudi, and J. F. Antaki. A continuum model for the unfolding of von Willebrand factor. *Annals of Biomedical Engineering*, 2021.

[127] A. Zydney and C. K. Colton. Augmented solute transport in the shear flow of a concentrated suspension. *PCH. Physicochemical hydrodynamics*, 1988.